# *Different Shapes of Menisci Emerging during Evaporation: Picolitre Droplets Showing Diversities in Cylindrical Wells.*

ZHIDA HUANG

# Different Shapes of Menisci Emerging during Evaporation: Picolitre Droplets Showing Diversities in Cylindrical Wells

**Zhida Huang**

A Thesis presented for the degree of
Doctor of Philosophy


Department of Chemistry
Durham University
United Kingdom
Apr 2023

# Declaration

The work in this thesis is based on research carried out at the Department of Chemistry, Durham University, United Kingdom. No part of this thesis has been submitted elsewhere for any other degree or qualification and it is all my own work unless referenced to the contrary in the text.

# Acknowledgements

I sincerely acknowledge all the members of the group and my supervisors Colin and Philip for the assistance and kindness they have provided during my days in Durham. I also really appreciate the badminton club of CSSA at Durham University for the exciting games they organised of which I have enjoyed much.

I am also really grateful to Dan and Halim for carefully reviewing this work and the lovely talk during the viva and to Robert for being the Independent Chair for the viva!

# Contents

**Declaration** **ii**

**Acknowledgements** **iii**

**List of Symbols** **vii**

**1 Introduction** **1**

1.1 Motivation for the Project . . . . . 3

1.2 Ink-jet Printing . . . . . 4

1.3 Droplet Evaporation . . . . . 7

1.3.1 Surface Tension and Laplace Pressure . . . . . 10

1.3.2 Marangoni Flow . . . . . 12

1.4 Printed Droplets Evaporating in a Well . . . . . 16

**2 Experimental Setup and Analysis Method** **24**

2.1 Fabrication of Substrates . . . . . 24

2.2 Experimental Setup . . . . . 26

2.3 Three-beam Interference . . . . . 29

2.4 Profile Reconstruction and its Geometrical Features . . . . . 40

2.4.1 Profile Reconstruction . . . . . 41

2.4.2 Geometrical Features of a Droplet Profile . . . . . 44

2.5 Error Analysis of Binary Solvent Systems . . . . . 51

**3 Pure Solvents: W/U/C-shaped Profiles 55**

3.1 Evaporation Rate of a Pure Solvent Droplet in a Cylindrical Well . . 57

3.2 Lubrication Approximation . . . . . 61

3.3 C-shaped Profile . . . . . 65

3.3.1 Definition of C-shaped Profiles . . . . . 65

3.3.2 Experimental Results of a C-shaped Profile . . . . . 67

3.4 U-shaped Profile . . . . . 71

3.4.1 What is a U-shaped Profile? . . . . . 71

3.4.2 Experimental Results of a U-shaped Profile . . . . . 73

3.5 W-shaped Profile . . . . . 75

3.5.1 What is a W-shaped Profile? . . . . . 75

3.5.2 Experimental Results of a W-shaped Profile . . . . . 78

3.6 Comparison between W/U/C-shaped Profiles . . . . . 81

3.6.1 Profiles with Different Values of $\Omega$ . . . . . 82

3.6.2 U-shaped Profiles with Different Values of $\Omega$ . . . . . 87

3.6.3 U-shaped Profiles with Similar Values of $\Omega$ . . . . . 93

3.7 Effectiveness of $\Omega$ . . . . . 97

3.7.1 Profiles of Different Solvents . . . . . 98

3.7.2 The Impact from Temperature on Profiles . . . . . 104

**4 Binary Solvents: New Profiles and its Features 109**

4.1 Evaporation Rate of a Binary Mixture Droplet in a Cylindrical Well 110

4.1.1 Evaporation of n-Butanol and n-Butyl Acetate . . . . . 118

4.2 New Profiles Emerging from Binary Droplets . . . . . 122

4.2.1 Bell-shaped Profile . . . . . 122

4.2.2 M-shaped profile . . . . . 126

4.2.3 Spreading profile . . . . . 131

4.2.4 Lopsided profile . . . . . 134

4.3 Non-ideal Binary Droplets . . . . . 138

4.4 Doughnut Profile after Touch-down . . . . . 147

**5 Conclusion** **149**

5.1 Conclusion . . . . . 149

5.2 Future Work . . . . . 151

**1 Appendix** **171**

1.1 Three-beam Interference . . . . . 171

1.2 Geometrical Features of a Profile . . . . . 181

1.3 Evaporation Rate of a Binary Droplet . . . . . 201

# List of Symbols

**Chapter 1**

| | |
|---|---|
| $\gamma_{CIJ}$ | Continuous inkjet printing |
| $Re$ | Reynolds number |
| $We$ | Weber number |
| $Oh$ | Ohnesorge number |
| $Ca$ | Capillary number |
| $L$ | Characteristic length in a dimensionless number |
| $U$ | Characteristic velocity in a dimensionless number |
| $\gamma$ | Surface tension of liquid-air interface / N $m^{-1}$ |
| $\mu$ | Viscosity / Pa s |
| $CCA$ | Constant contact angle |
| $CCR$ | Constant contact radius |
| $\theta$ | Contact angle of a droplet / $^\circ$ |
| $m$ | mass / kg |
| $\frac{dm}{dt}$ | mass changing rate / kg $s^{-1}$ |
| $R_c$ | The gas constant 8.314 kg $m^2$ $s^{-2}$ $K^{-1}$ mol |
| $T_c$ | Thermodynamic temperature / K |

| | |
|---|---|
| $M_w$ | Molecular weight of a substance / kg mol$^{-1}$ |
| $p_v$ | Vapour pressure of a liquid / Pa |
| $D$ | Diffusion coefficient / m$^2$ s$^{-1}$ |
| $r_p$ | Principal radius of a spherical droplet / m |
| $c_0$ | Vapour concentration close to a droplet surface / kg m$^{-3}$ |
| $C_{ap}$ | Capacitance of the lens in Picknett and Bexon's theory |
| $r_l$ | The radius of the contact area between a droplet and a substrate |
| $FEM$ | Finite element method |
| $RH$ | Relative humidity |
| $c_v$ | Saturated vapour concentration of a substance / kg m$^{-3}$ |
| $\mathbf{J}$ | Diffusion flux / m$^2$/s |
| $\mathbf{r}$ | Position vector |
| $\mathbf{c}$ | The vapour concentration of an evaporating droplet |
| $\rho$ | Density / kg m$^3$ |
| $u$ | Velocity of the flow in a liquid phase / m s$^{-1}$ |
| $u_r$ | Radial velocity profile / m s$^{-1}$ |
| $h$ | Altitude in a cylindrical coordinate system / m |
| $h_{r=0}$ | Height of a droplet at the centre of a well / m |
| $t$ | Time / s |
| $\gamma_{lv}$ | Surface tension of liquid-vapour interface / N m$^{-1}$ |
| $\gamma_{ls}$ | Surface tension of liquid-solid interface / N m$^{-1}$ |
| $\gamma_{sv}$ | Surface tension of solid-liquid interface / N m$^{-1}$ |
| $H$ | Mean curvature of a surface at a point / m$^{-1}$ |
| $p$ | Pressure / Pa |
| $A$ | the Helmholtz free energy / J |
| $G$ | the Gibbs free energy / J |
| $W$ | the work done to an object / J |
| $\eta$ | chemical potential / J |

| | |
|---|---|
| $s$ | the area of a surface / $m^2$ |
| $T$ | Temperature / K |
| $v$ | Volume / $m^3$ |
| $p_L$ | the Laplace pressure / Pa |
| $\nu$ | Kinematic viscosity / $m^2$ $s^{-1}$ |
| $Ma$ | the Marangoni number |
| $Ma_T$ | the thermal Marangoni number |
| $D_T$ | Thermal diffusivity / $m^2$ $s^{-1}$ |
| $Ma_c$ | the solutal Marangoni number |
| $\epsilon$ | Aspect ratio of an object, such as a droplet or a cylindrical well |
| $\phi$ | Volume fraction of a solvent in the mixture |
| $\phi_1$ | Volume fraction of solvent 1 in the mixture |
| $\phi_2$ | Volume fraction of solvent 2 in the mixture |
| $OLED$ | Organic light-emitting diodes |
| $PVA$ | Polyvinyl acetate |
| $H_0$ | Depth of a cylindrical well $\mu$m |
| $R_0$ | Radius of a cylindrical well $\mu$m |
| $dV/dt$ | Evaporation rate $m^3$/s |
| $E_0$ | Evaporation rate per area m/s |
| $I$ | Light intensity |
| $UV$ | Ultraviolet |
| $ITO$ | Indium tin oxide |
| $IPA$ | Isopropanol or 2-propanol |
| $EC$ | 2-methoxy-1-methylethyl acetate |
| $2D$ | 2-dimensional |
| $3D$ | 3-dimensional |
| $\sigma$ | the standard deviation of the Gaussian distribution |
| $\psi$ | the mean or expectation of the Gaussian distribution |

**Chapter 2**

| | |
|---|---|
| $\mathcal{R}$ | Real part of a function |
| $\mathbf{A}$ | A complex vector with Cartesian rectangular components |
| $\mathbf{A}^\star$ | Conjugate of a complex vector $\mathbf{A}$ |
| $n$ | refractive index |
| $c$ | velocity of light in the vacuum, 299,792,458 m/s |
| $\varepsilon_l$ | dielectric constant |
| $\mu_l$ | magnetic permeability |
| $\Upsilon$ | Visibility of the fringes |
| $\mathbf{E}$ | Electric field vector |
| $T$ | Period of a field |
| $\omega$ | Frequency of a field; $\omega = 2\pi/T$ |
| $\mathbb{R}$ | The set of all real numbers |
| $T$ | Transmission |
| $R$ | Reflection |
| $R_{DA}$ | Reflection from air-droplet interface |
| $R_{ID}$ | Reflection from droplet-ITO interface |
| $R_{GI}$ | Reflection from ITO-glass interface |
| $I$ | Light intensity |
| $I_A$ | Light intensity of the transmission at air-droplet interface |
| $I_D$ | Light intensity of the transmission at droplet-ITO interface |
| $I_I$ | Light intensity of the transmission at ITO-glass interface |
| $I_{DA}$ | Light intensity of the reflection from air-droplet interface |
| $I_{ID}$ | Light intensity of the reflection from droplet-ITO interface |
| $I_{GI}$ | Light intensity of the reflection from ITO-glass interface |
| $I_\alpha$ | Light intensity of the three-beam interference fringes |
| $J$ | Light intensity of an interference term |
| $J_{AD}$ | Light intensity of interference term from air-droplet interface |

| | |
|---|---|
| $J_{DI}$ | Light intensity of interference term from droplet-ITO interface |
| $J_{IG}$ | Light intensity of interference term from ITO-glass interface |
| $\delta$ | Phase difference |
| $\delta_{DA}$ | Phase difference of interference term from air-droplet interface |
| $\delta_{ID}$ | Phase difference of interference term from droplet-ITO interface |
| $\delta_{GI}$ | Phase difference of interference term from ITO-glass interface |
| $\Delta s$ | Difference of optical path |
| $\lambda$ | Wavelength of a light wave in vacuum |
| $\mathcal{T}_{12}$ | Transmissivity of a light beam from medium 1 to medium 2 |
| $\mathcal{R}_{12}$ | Reflectivity of a light beam from medium 1 to medium 2 |
| $\mathcal{T}_{GI}$ | Transmissivity of a light beam from glass to ITO |
| $\mathcal{R}_{GI}$ | Reflectivitya of light beam from glass to ITO |
| $\mathcal{T}_{ID}$ | Transmissivity of light beam from ITO to droplet |
| $\mathcal{R}_{ID}$ | Reflectivity of light beam from ITO to droplet |
| $\mathcal{T}_{DA}$ | Transmissivity of light beam from droplet to air |
| $\mathcal{R}_{DA}$ | Reflectivity of light beam from droplet to air |
| $h_{ITO}$ | Thickness of ITO layer / m |
| $h_{droplet}$ | Thickness of a droplet / m |
| $n_{ITO}$ | Refractive index of ITO layer |
| $n_{droplet}$ | Refractive index of a droplet |
| $\lambda_0$ | Wavelength of the light source in the setup (470 nm) |
| $h_{ITO}$ | Thickness of ITO layer /m |
| $\Delta h$ | Height difference between two nearest bright fringes or dark fringes |
| $u$ | Angular position or as the azimuth in a cylindrical coordinate system |
| $r$ | Cylindrical axis in a cylindrical coordinate system |
| $\mathbf{h}$ | the map $\mathbf{h} : U(r,t) \rightarrow R^3$, which represents the parametrisation of the surface$\mathbf{h}$(t,r) |

**Chapter 3**

$\Omega$ The parameter explained in Chapter 3 which is the product of $\epsilon^4\gamma/\mu E_0$

$l_c$ The capillary length

$g$ Gravity acceleration constant / $m^2/s$

$\mathbf{J}$ Diffusion flux / $mol/m^3$

$\mathbf{J}_m$ Diffusion flux counted in mass / $kg/m^3$

$r'$ Non-dimensionalised scale of $r$

$h'$ Non-dimensionalised scale of $h$

$p'$ Non-dimensionalised scale of $p$

$u'$ Non-dimensionalised scale of $u$

$w'$ Non-dimensionalised scale of $w$

$t'$ Non-dimensionalised scale of $t$

$H'$ Non-dimensionalised scale of $H$

$t_0$ the initial moment to count the evaporation process of a droplet /s

$t_{flat}$ the moment when the height of a droplet at the centre is equal to the host well /s

$t_d$ the moment when a droplet touches down at the base of its host well /s

$t_f$ the moment when a droplet dries up in a well /s

$\tau'$ the characteristic time

$k_1$ The first principal curvature of a surface at a / $m^{-1}$

$k_2$ The Second principal curvature of a surface at a point / $m^{-1}$

$K$ Gaussian curvature of a surface at a point / $m^{-2}$

$H$ Mean curvature of a surface at a point / $m^{-2}$

item[$RH$] Relative humidity

$\Pi$ Disjoining pressure / Pa

$T_{sub}$ Temperature of a substrate / $^o$C

**Chapter 4**

$n_1$ Refractive index of solvent 1

$n_2$ Refractive index of solvent 2

$n_{12}$ Refractive index of a mixture containing solvent 1 and solvent 2

$n_{12}^0$ Refractive index of a mixture at the initial moment

$\Psi$ The product of Lorentz-Lorenz

$\psi_1$ Volume fraction of component 1

$\psi_2$ Volume fraction of component 2

$\Delta h_a$ Height difference between two nearest bright fringes or dark fringes counted in the refractive index of a binary solvent mixture at the initial stage

$\Delta h_b$ Height difference between two nearest bright fringes or dark fringes counted in the refractive index of the less volatile solvent in a binary mixture

$\xi$ Error in analysing a binary solvent mixture

$\mathbf{J}$ Diffusion flux mol/m$^3$

$\mathbf{J}_{m1}$ Diffusion flux counted in mass of component 1 / kg/m$^3$

$\mathbf{J}_{m2}$ Diffusion flux counted in mass of component 2 / kg/m$^3$

$D$ Diffusion coefficient in air

$D_1$ Diffusion coefficient of solvent 1

$D_2$ Diffusion coefficient of solvent 2

$D_m$ Diffusion coefficient of a mass flux

$c_m$ Concentration distribution of a substance counted in mass

$R_0$ Radius of a droplet

$\theta$ Contact angle of a droplet

$P_1$ One of the coefficients of Eq 4.1.25 to calculate the evolution of $x_1$

$P_2$ One of the coefficients of Eq 4.1.25 to calculate the evolution of $x_1$

$Q$ One of the coefficients of Eq 4.1.25 to calculate the evolution of $x_1$

$\mathbf{N}$ The number density of particles

$M_{w1}$ Molecular weight of solvent 1 in a binary mixture

$M_{w2}$ Molecular weight of solvent 2 in a binary mixture

$p_v$ Vapour pressure of a liquid

$p_{v1}$ Partial vapour pressure of solvent 1 in a binary mixture

$p_{v2}$ Partial vapour pressure of solvent 2 in a binary mixture

$p_{v1}^0$ Vapour pressure of solvent 1 / Pa

$p_{v2}^0$ Vapour pressure of solvent 2 / Pa

$n_{m1}$ The amount of substance of solvent 1 in a binary mixture

$n_{m2}$ The amount of substance of solvent 2 in a binary mixture

$n_{m1}^0$ The amount of substance of solvent 1 in a binary mixture at initial moment $t_0$ / mol

$n_{m2}^0$ The amount of substance of solvent 2 in a binary mixture at initial moment $t_0$ / mol

$n_{m1}^t$ The amount of substance of solvent 1 in a binary mixture at the moment $t$ / mol

$n_{m2}^t$ The amount of substance of solvent 2 in a binary mixture at the moment $t$ / mol

$x_1$ Mole fraction of solvent 1 in a binary mixture

$x_2$ Mole fraction of solvent 2 in a binary mixture

$c_{v1}$ Saturated vapour concentration of solvent 1 of a binary mixture

$c_{v2}$ Saturated vapour concentration of solvent 2 of a binary mixture

$R_h$ Relative concentration of a substance in its vapour phase to the saturated vapour concentration of the substance; for example, if the substance is water, $R_h$ denotes the relative humidity of the surroundings

$R_{h1}$ Relative concentration of solvent 1 in a binary mixture in its vapour phase to the saturated vapour concentration of the substance

$R_{h2}$ Relative concentration of solvent 2 in a binary mixture in its vapour phase to the saturated vapour concentration of the substance

# CHAPTER 1

# Introduction

This work is to investigate the evaporation of a printed droplet in a cylindrical well so as to understand the evolution of height profile of the droplet and the possible reasons for the appearance of a dynamic meniscus.

The experiment setup developed for the study is illustrated in Chapter 2 where I also illustrate the procedures for fabricating thin cylindrical wells, which means the depth of a well is far smaller than its radius. The procedures are illustrated with an example. Here, the photolithography with SU-8 as the photoresist was conducted with the assistance from Michael Cooke at the Department of Engineering at Durham University. In addition, a method to reconstruct a profile is described in Chapter 2 as well, which is applied to analyse the results collected from the setup.

The results of pure solvent droplets are presented in Chapter 3 in which three different shapes of menisci, W-shaped profiles, U-shaped profiles and C-shaped profiles, emerged when picoliter droplets evaporated in cylindrical wells with the aspect ratios, depth against radius, ranging between 0.013 to 0.04. W-shaped profile is a kind of profile appearing when the height at the centre is a local peak which remains until a droplet touches down at the base; U-shaped profile has a flat area near the centre when a droplet is about to touch down; in addition, C-shaped profile is the

profile which behaves like the normal meniscus resembling a spherical cap until the touch-down moment, forcing the droplet to break up at the centre. The evolution of mean curvature of a profile is applied to distinguish a W-shaped profile and a U-shaped profile from a C-shaped profile.

Evaporation rates agreed with the theoretical prediction by Hu and Larson [1] [2]. In addition, a parameter involving evaporation rate, surface tension, viscosity and the aspect ratio of a well, defined as $\Omega$ in this work, is shown to be effective to predict a shape emerging from a pure droplet evaporating in a cylindrical well.

In Chapter 4, I analyse the error in the experiments of binary solvents due to the preferential evaporation. Furthermore, I deduce the evaporation rate of a binary solvent, assuming that the vapour pressures of the components obey Raoult's law; the results show that the mole fraction evolves with time following a logistic-curve-like manner (a sigmoid function). Based on the expression of the evaporation rate, the sign of $d\gamma/dt$ is applied to predict the four new profiles of menisci emerging during the evaporation of a binary droplet, namely bell-shaped profile, lopsided profile, M-shaped profile and spreading profile. Lopsided profile is the only spontaneous symmetry-breaking profile found in this work and it only occurs when $d\gamma/dt < 0$ under which condition bell-shaped profiles may appear; on the other hand, M-shaped profiles and spreading profiles occur when $d\gamma/dt > 0$.

Moreover, binary droplets of the non-ideal binary systems of toluene and n-butanol with different concentrations were investigated, in which case the more volatile solvent changes from n-butanol to toluene when the concentration of n-butanol rises since there is a positive deviation of the binary system from Raoult's law; and, therefore, the direction of the Marangoni flow also changes, leading to the change of profiles from M-shaped profiles, to bell-shaped profiles or even lopsided profiles.

The results prove that changing the concentration of a component in a non-ideal binary system may also change the direction of the solutal Marangoni flow; in consequence, it is critical to quantitatively control the exact concentrations of components and the non-ideality of a solvent system may eventually turn out to be a surprising merit if the mechanism of an evaporation process and the interaction

among components are well learnt.

## 1.1 Motivation for the Project

This study concentrates on the evaporation of a picolitre droplet, the volume of which ranges from 20 pl to 50 pl, printed in a cylindrical well whose shape is still one of the most widely-used patterns in the field of printed electronics, rigid [3] [4] or flexible [5] [6] [7] [8], such as high-tech chips [9] [10], batteries [11] [12], sensors [13] [14] [15] and light-emitting devices including organic [16] [17] and non-organic ones [18] [19] [20].

Inkjet-printing is forecast to be a game changer in the industry of additive manufacturing by the middle of the 21st century [21] [22] [23], as the desired pattern can be modified any time before printing which is an improvement on its competitive rivals, namely photolithography and vacuum evaporation working with heavy and rigid metal masks [24] [24] [25]. What is more, ink-jet printing is a material-saving method and the ability of fabricating a device with the lowest amount of by-products, such as toxic chemicals, has shown to have a promising future [26] [27]. Even though the precision of inkjet printing has reached a satisfying degree to place a picolitre droplet into a micro-sized pattern [28] [29] [30], it probably cannot ignore the other significant procedure, evaporation of the printed droplets, which is even more important in developing a long-desired flat layer [30] [31] [32]. Hence, how to exploit the natural power, evaporation, which is the foundation of the next generation of manufacturing methods, particularly of ink-jet printing, is critical in both academia and industry.

The fabrication of printed electronics for high-tech chips usually involves printing a specific ink onto a well-patterned substrate [33] [34]. Uniformity of a deposited layer plays a vital role in the quality and efficiency of a device [35] [36]. For instance, a sharp notch or hill on a printed layer will always lead to a relatively low breakdown voltage of a diode, so that its performance is limited [37] [38] [39]. Thus, how to avoid an uneven layer from printing is the cornerstone to ameliorate the unsatisfactory performance of a device such as low lifespan, and extend the technology for further

applications [40] [41].

Understanding the evaporation process inside a cylindrical well which is one of the most widely-used patterns and also bears the merit of axisymmetry to avoid the influence from an irregular edge, lays the foundation to research the evaporation in wells with more complex geometrical features. The solvent systems including pure solvent, binary solvents, ternary solvents and polymer solution, are designed to research the evolution of height profiles and the shapes of a deposit from polymer solution pure or mixed solvents. Surfactant is widely-used to control the flatness of a layer, because of the solutal Marangoni effect induced by the surface tension gradient [42] [43] [44] [45]; however, in an electronic device, the existence of surfactants may introduce the adverse effects on its performance and hinder the deposition of the next layer during fabrication. Therefore, in this project, I attempt to understand the evaporation process of a printed droplet so that the amounts of the components added to control the ultimate profiles in industry can be limited to the least amount.

## 1.2 Ink-jet Printing

Inkjet printing is usually applied to fabricate electronic devices, because of the precise location of droplets on a substrate and the capability to jet the droplets with the same volumes. There are two kinds of printing methods, continuous inkjet printing, CIJ printing, and drop-on-demand inkjet printing, DOD printing [30] [46] [47] [48]. Continuous inkjet printing generates droplets continuously which form a thin stream at the early stage, appears to be a wavy profile later and, eventually, breaks into a series of liquid beads due to the Rayleigh-Plateau instability [46] [49]. In order to improve the efficiency of printing, continuous inkjet printer has a gutter to collect the ink where the droplets are not designed to lay on a substrate, and recycle the ink back into the print head [50].

For drop-on-demand printing, droplets printed by a DOD printer are squeezed out from a nozzle on a print head in which ink chamber has a piezo-electric actuator driven by different voltage waveforms to control the volumes and the frequencies of printed droplets [51] [52]. Therefore, a line of droplets may have different volumes

depended on the intention to print and the property of an ink. Once the wave form is tuned to perform a task, a piezoacoustic actuator will oscillate to produce an extra pressure in the ink chamber so that droplets near a print head are jetted down, breaking through the Laplace pressure at the surface [53] [54]. However, not all liquid is suitable to be printed with a DOD printer; whether a liquid is printable is not only up to the liquid itself but also the property of a printer such as the radius of the nozzle, the area and frequency of a piezoacoustic actuator, the size of an ink chamber and the design of pipes.

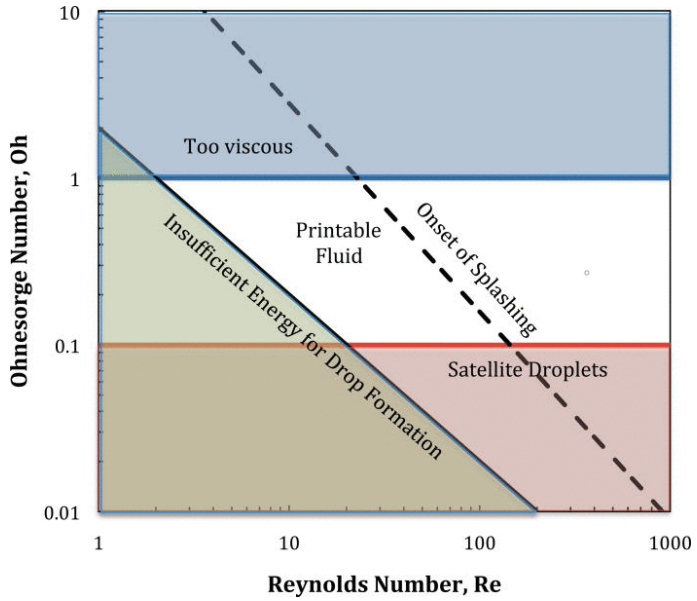


Figure 1.1: Schematic diagram showing different regimes for stable operation of drop-on-demand inkjet printing: the droplets located in the blue regime are too viscous to print, while in the red regime are often jetted with satellite droplets as the droplets experience Rayleigh-Plateau instability; the regime beyond the dashed line suggests that the droplets splash when jetted from a print head while in the yellow region the droplets may not be jetted at all as the pressure induced by a piezoacoustic actuator is not great enough to form a droplet [55]. (Reprinted with the kind permission from Annual Review of Fluid Mechanics who holds the copy right).

Considering that the behaviours of droplets formed near a print head depend on the fluid mechanical features of the droplets, four dimensionless numbers, the Reynolds number, the Weber number, the Ohnesorge number and the capillary

number, are applied to describe if an ink is printable or not.

$$Re = \frac{LU\rho}{\mu} = \frac{inertial\,force}{viscous\,force} \tag{1.1}$$

$$We = \frac{\rho U^2 L}{\gamma} = \frac{inertial\,force}{capillary\,force} \tag{1.2}$$

$$Oh = \frac{\mu}{\sqrt{\rho\gamma L}} = \frac{\sqrt{We}}{Re} \tag{1.3}$$

$$Ca = \frac{\mu U}{\gamma} = \frac{We}{Re} \tag{1.4}$$

The Reynolds number, $Re$, shown in Eq 1.1 in which $U$ and $L$ are characteristic velocity and length, respectively, while $\mu$ is the dynamic viscosity of a droplet, describes the ratio of inertial to viscous forces [56] [57]. The Weber number, $We$, describes the ratio of inertial to capillary forces, as is shown in Eq 1.2 in which $\gamma$ is the surface tension of a droplet [58]. The Ohnesorge number shown in Eq 1.3 reflects the competition between viscous timescale and the capillary timescale [30] and is independent of the driving conditions as the characteristic velocity is cancelled out. The capillary number, $Ca$, presented in Eq 1.4, expresses the ratio of viscous to capillary forces [59] [60]. In DOD printing, the characteristic velocity of a droplet is the velocity when it is jetted out from a print head; the characteristic length is the radius of a droplet rather than the radius of nozzle although the size and shape of a nozzle together with the waveform to determine the volume of a droplet.

The diagram in Fig 1.1 shows if an ink is printable by the ratio of $Oh$ and $Re$ [55]. Alternatively, one can calculate the values of $We$ and $1/Oh$, which is also denoted as Z constant [61] [62], to deduce the performance of an ink when it is printed. Also, in Fig 1.1, the value of $Oh$ in the blue regime is larger than 1 which indicates viscous force may hinder the generation of a droplet near a nozzle; however, when $Oh$ is less than 1, satellite droplets may appear [63]. In addition, when a droplet locates in the area above the dashed line in Fig 1.1, where $Oh \geq 50Re^{4/5}$, it may splash when droplets land on a substrate. On the other hand, when $Oh \leq 0.5Re$, droplets will be not jetted out from a print head as the pressure difference inside a chamber is not large enough for a droplet to overcome surface tension [64] [65]. Thus, in the regime where an ink is printable, the range of its $Oh$ is $0.5Re \leq Oh \leq 50Re^{4/5}$ in

which $Oh \in [0.1, 1]$.

## 1.3 Droplet Evaporation

The evaporation of a droplet printed in a well or on a flat substrate is the other essential procedure, besides printing, for fabricating printed electronics [66] and plays a significant role in developing a long-desired flat layer.

When a coffee droplet dries on a flat substrate, it leaves a coffee ring as the coffee particles carried by the internal flow move towards the contact line and accumulate there [67] [68]. Evaporation of a sessile droplet occurs most rapidly near the contact line when the contact angle is less than 90° [1] [67] [69]; thus, an internal flow, also deemed as capillary flow [67] [70], moves towards the contact line to compensate the mass loss and also to maintain the cap-like shape due to the dominance of surface tension.

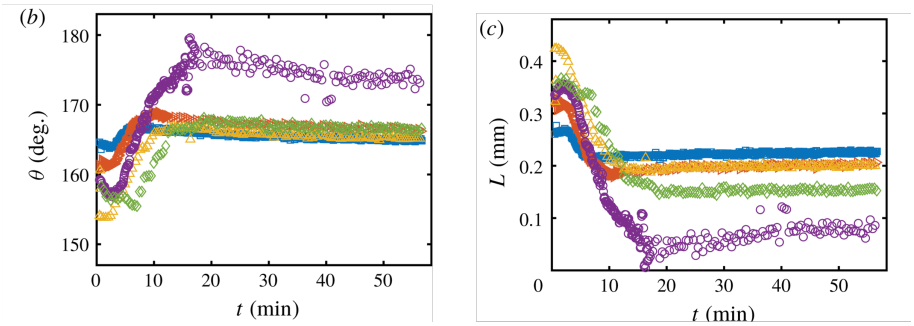


Figure 1.2: The results of the contact angle and radius of the droplets containing water and ethanol measured by Tan and his co-workers: the volume ratios of the blue, red, yellow, purple, green dots are 70:30, 60:40, 50:50, 40:60 and 30:70, respectively, where 70:30 means water takes up 70% in volume. Purple dots, whose volume ratio is 40:60, show that the contact radius and the contact angle are changing simultaneously before t = 20 min [71](Reprinted with the kind permission from Journal of Fluid Mechanics who holds the copy right).

For pure droplets, there are two limiting modes of evaporation: constant contact angle, CCA, and constant contact radius, CCR [72] [73]. Regarding the CCA mode, the contact angle of a droplet, $\theta$, remains unchanged while the contact radius, which is the distance between the centre of a droplet and its contact line, shrinks during evaporation; when a droplet evaporates with the contact line pinned and the contact

angle decreasing, the droplet evaporates in the mode of constant contact angle. Depending on the property of a liquid and substrate, a pure droplet may experience two different modes during the evaporation. However, for a binary droplet or a droplet with even more complex components, the contact angle and the radius of a droplet may change simultaneously - one example is shown in Fig 1.2 - thanks to the selective evaporation occurring which gives rise to the Marangoni flow [71] [74].

Morse *et al* investigated the evaporation of small iodine spheres in air experimentally the volume of which was at the millimetre scale [75] in 1910; while in 1918 Irving Langmuir illustrated the evaporation rate of the spheres 1.5:

$$-\frac{dm}{dt} = \frac{4\pi r_p D M_w p_v}{R_c T_c} \tag{1.5}$$

where $r_p$ is the principal radius of a droplet which is assumed as a spherical cap.

Picknett and Bexon pointed out two evaporation modes of a droplet when gravity was negligible, CCA and CCR; in addition, assuming that the liquid-air interface of a droplet was a spherical cap and an evaporation process was diffusion-limited, the evaporation rates of the two modes were [72]:

$$-\frac{dm}{dt} = 2\pi D c_0 C_{ap} \tag{1.6}$$

where $C_{ap}$ are

$$\frac{C_{ap}}{r_p} = 0.6366\theta + 0.09591\theta^2 - 0.061440\theta^3 \quad 0 \leq \theta < 0.175 \tag{1.7}$$

$$\frac{C_{ap}}{r_p} = 0.00008957 + 0.6333\theta + 0.1160\theta^2 - 0.08878\theta^3 + 0.01033\theta^4 \quad 0.175 \leq 0 \leq \pi \tag{1.8}$$

where $C_{ap}$ and $r_p$ are the capacitance of the lens and the radius of a spherical droplet, respectively.

The results from Eq 1.6−1.8 were shown to predict the evaporation rate of a droplet in the different modes [76] [77]. However, when a droplet evaporates on a substrate, it may obey the mode of constant contact radius first, and once the contact

angle reaches the receding angle, the droplet switches to the mode of constant contact angle while evaporating.

The assumption that the evaporation of a droplet is diffusion-limited was also applied in the work by Hu and Larson [1] [2], in which the evaporation of a sessile droplet was investigated experimentally and theoretically and computed with the finite element method, FEM [1]. The results in their research were well-matched with the experiment that water droplet was chosen to investigate, although the initial contact angle of the droplets ranged from 0 to $\pi/2$.

$$-\frac{dm}{dt} = \pi r_l D(1 - RH)c_v(0.27\theta^2 + 1.3) \tag{1.9}$$

$$-\frac{dm}{dt} = 2\pi r_l D(1 - RH)c_v \quad \theta \sim \pi/2 \tag{1.10}$$

$$-\frac{dm}{dt} = 4r_l D(1 - RH)c_v \quad \theta \sim 0 \tag{1.11}$$

where $RH$ is the relative humidity of the atmosphere surrounding a droplet and $c_v$ is the saturated vapour concentration of a substance which is water in this case.

In spite of the constant value of evaporation rate, evaporative flux is not evenly distributed on a surface. Because of the strength difference of a flux over the liquid-vapour interface, a radial flow is generated to make up for the loss near the contact line, moving from the point where the flux is the least acute to the point where the flux occurs most severely [69] [78] [79] [80]. Such capillary flow mechanism for a ring-shape deposit was reported by Deegan and his co-workers in 1997 [67]; moreover, they also pointed out that if a droplet had high viscosity, the viscous force may prevent a droplet from maintaining its equilibrium shape in that the capillary flow was hindered [81].

When the evaporation of a droplet reaches the steady state, the transient term in the diffusion equation may be neglected, reducing the diffusion equation to a Laplace equation for the concentration in the vapour phase: 1.12 [78] [2] [82] [83].

$$D\partial_t c = \Delta c = 0 \tag{1.12}$$

Furthermore, Hu and Larson investigated the evolution of sessile droplets whose contact lines were pinned at different contact angles, 20°, 30° and 40° [2]. Evaporation was also assumed as diffusion limited with the parabolic approximation for the profiles of water droplets. The lubrication approximation was also applied to achieve the parabolic radial velocity profiles [84]. The results from their analysis, Eq 1.13−1.14, show that the height at the centre depends on the evaporation rate of a droplet, and decreases linearly with time.

$$u_{h(r,t)} = \frac{\partial h}{\partial t} + \frac{J(r,t)}{\rho} \tag{1.13}$$

$u_{h(r,t)}$ is the velocity profiles in Hu and Larson's theory [2]

$$\frac{dh}{dt}_{r=0} = \frac{2}{\rho \pi r_l^2} \frac{dm}{dt} \tag{1.14}$$

For a droplet which evaporates under the limit of vapour diffusion, the pressure over the droplet is key to analyse the evaporation rate and its internal flow. The pressure at the liquid-vapour interface induced by the liquid-vapour interfacial tension, $\gamma_{lv}$ or simply $\gamma$, which is always parallel to the interface, is also called the Laplace pressure [85].

As regards the internal flow inside a sessile droplet whose aspect ratio is small, which means $\epsilon \ll 1$, there is a shear stress between the adjacent layers in which the flow in a layer moves horizontally, whereas the permeation occurs at a thin ribbon on the top border where the boundary limits a flow moving and forces it to join the next layer. The illustration of the terraced structure of the internal flow inside a sessile droplet is presented in Fig 1.3 [86], which is mostly applied in the numerical simulation to investigate the internal flow within an evaporating droplet.

### 1.3.1 Surface Tension and Laplace Pressure

Surface tension is a force to minimise the surface area of a droplet so as to reach its smallest surface-to-volume ratio [87] [85], and describes the amount of the work needed to change the area of a surface, Eq 1.15, which is identical to the change in

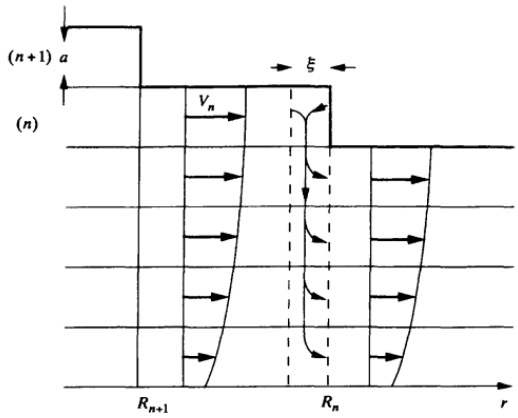


Figure 1.3: The terraced structure of the internal flow in a sessile droplet with the aspect ratio $\epsilon \ll 1$: the internal flow is parallel to the substrate while the permeation only occurs at a thin ribbon whose width is assumed as $\xi$; also, $n$ is the $nth$ terrace; $a$ is the height of the $(n+1)th$ terrace while $R_n - R_{n+1}$ is the length of the nth terrace; $V_n$ is the velocity profile at the terrace $n$ [86]. (Reprinted with the kind permission from Soft Interfaces - The 1994 Dirac Memorial Lecture who holds the copy right)

the Helmholtz energy with the shift of surface area under a constant temperature and volume, as given in Eq 1.16 [88].

$$dW = \gamma ds \tag{1.15}$$

$$\gamma = \frac{\partial A}{\partial s}_{T,V,n} \tag{1.16}$$

$$p_L = 2\gamma H \tag{1.17}$$

where $W$ denotes the work needed to change the shape of a droplet and $H$ is the mean curvature at a point of a surface. In the case of a spherical cap, $H$ is the reverse of the radius.

Thanks to surface tension, a pressure arises over the interface of droplet, the Laplace pressure shown in Eq 1.17, maintaining the shape to be a spherical cap when gravity is negligible. When placed in a capillary tube, the liquid inside also appears to be a spherical cap which is also called meniscus [89] [90]; however, whether a meniscus is a concave or convex hinges on the wetting between a liquid and container. If a profile is regarded as a spherical cap, the Laplace pressure on the surface will

be equal at any point, in which case the Laplace pressure does not contribute to the internal flow. However, we may notice the

When there is an internal flow in a droplet, the viscous force competes against surface tension, as is described by the capillary number, $Ca$ in Eq 1.4. Viscous force is to obstruct an internal flow moving in a liquid droplet and its strength is usually characterised by dynamic viscosity, $\mu$, which is the proportion between the shear stress and the velocity gradient in a droplet [91] [92]; the kinematic viscosity, $\nu = \mu/\rho$, is also used to describe the degree of a viscous force.

The height-averaged radial velocity profile of a droplet evaporating on a substrate due to the capillary flow is well approximated by lubrication approximation, when the aspect ratio of the droplet is small, namely $\epsilon \ll 1$, as is shown in Eq 1.18 [74] [93] [94] [95] where the derivative of pressure along the radial direction indicates the strength of a capillary flow which is contributed by evaporation and the Laplace pressure at the liquid-vapour interface.

$$\overline{u}_{r,ca} = \frac{h^2}{3\mu}\frac{\partial p}{\partial r} \tag{1.18}$$

### 1.3.2 Marangoni Flow

If a droplet has more than one component or is subjected to a drastic thermal change during evaporation, therefore, unreasonable to neglect the thermal effect, the Marangoni effect will play a crucial role in the internal flow of a droplet [96] [97] [98] [99].

Marangoni flows are caused by surface tension gradient along the surface of a profile which can be induced by a temperature gradient, thermal Marangoni effect [101] [102], the selective evaporation of a solvent in a multi-component droplet, solutal Marangoni effect [74] [103] [104], or the existence of surfactant, solutal Marangoni effect as well [105] [106] [107] [108] although sometimes it is also called surfactant Marangoni effect.

There may appear different kinds of Marangoni flows competing against each other, such as the evaporation of whisky droplet on a substrate which shows two

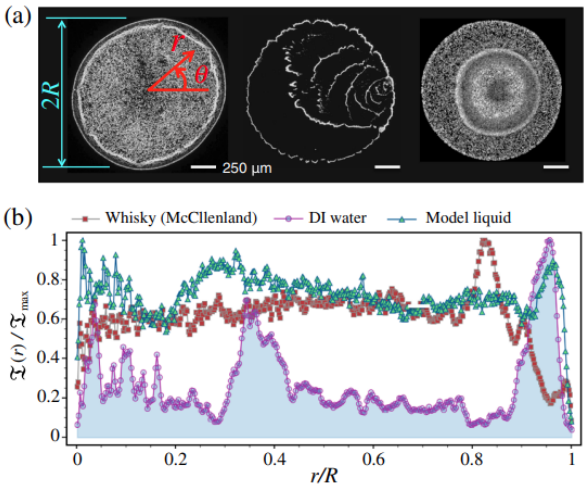


Figure 1.4: The experiment results of the whisky, water and model liquid in Kim *et al*'s work: the deposit of water shows a ring-like deposit when dries up; however, in the whisky droplet and the model liquid, the deposits are flatter than the deposit of water, which shows that the solutal Marangoni flows due to the selective evaporation and the existence of the surfactants can flatten the deposit [100]. (Reprinted with the kind permission from Physical Review Letters who holds the copy right)

kinds of Marangoni effects, namely solutal Marangoni flow and surfactant Marangoni flow [100]. Owing to the preferential evaporation of ethanol in the whisky droplet, the concentration of ethanol was lower at the contact line than that at the centre of the droplet, leading to the solutal Marangoni flow moving towards the contact line; however, as the surfactant accumulated near the contact line and the wind-down of the solutal Marangoni flow grew obvious, the surfactant Marangoni effect became to dominate, generating the surfactant Marangoni flow moving towards the centre of the droplet; later, with the depletion of ethanol in the droplet, the impact of the solutal Marangoni effect became weaker and was conquered by the capillary flow due to evaporation, bringing the the direction of the internal flow from the centre to the contact line again; finally, after the internal flow changed twice, it left a relatively flat deposit, as is shown in Fig 1.4.

Not only does the Marangoni flow change the deposit of a colloidal droplet [109] [110] [111], but also the spreading process [74] [112] [113], since the advancing and receding contact angles for binary or ternary droplets are mainly up to the compositions near the contact line which change rapidly as the evaporation occurs and the vapour field evolves quickly [106] [114].

The Marangoni number, $Ma$, compares the gradient of surface tension in a droplet, with the viscous force and diffusion [30] [115].

$$Ma = \frac{\Delta\gamma L}{\mu D} \tag{1.19}$$

The definition of the Marangoni number may vary with the specific conditions [116] [117]; The Marangoni number due to the preferential evaporation or a temperature gradient are defined as solutal Marangoni number and thermal Marangoni number.

Solutal Marangoni number, $Ma_c$:

$$Ma_c = \frac{d\gamma}{dc}\frac{h\Delta c}{\mu D} \tag{1.20}$$

where $\Delta\gamma$ is the gradient of surface tension and is represented by the the sensitivity of surface tension to the concentration difference of a component in a mixture droplet, while $h$ is the height on a height profile at a point [118] [119].

Thermal Marangoni number, $Ma_T$:

$$Ma_T = \frac{d\gamma}{dT}\frac{h\Delta T}{\mu D_T} \tag{1.21}$$

where $d\gamma/dT$ describes the sensitivity of surface tension of a droplet to temperature and $\Delta T$ is the temperature difference in an area, while $D_T$ is the thermal diffusivity of the liquid.

The Marangoni effect in solvent mixtures results in the Marangoni flow whose direction depends on the difference of the surface tension. When the more volatile solvent in a binary droplet has the lower surface tension, the surface tension at the contact line is larger than that near the centre, leading to the Marangoni flow moving towards the contact line from the centre, as is illustrated in Fig 1.5a; however, if the more volatile solvent has the higher surface tension, the surface tension gradient points to the centre from the contact line, as is shown in Fig 1.5b. Therefore, the value of the Marangoni number should also indicate the direction of the Marangoni

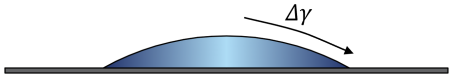


(a) The gradient of surface tension pointing towards the contact line of a binary droplet when the more volatile solvent has the lower surface tension.

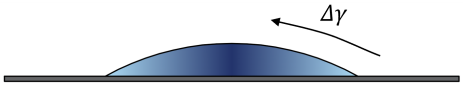


(b) The gradient of surface tension pointing towards the centre of a binary droplet when the more volatile solvent has the higher surface tension.

Figure 1.5: Two cases of the Marangoni flow: when the more volatile solvent has the lower surface tension, the Marangoni flow is moving towards the contact line of a binary droplet, while if the more volatile solvent has the higher surface tension, the Marangoni flow is moving towards the centre, the result of which is to further mix the components in a binary droplet; in the figures, the darker a region is, the higher the surface tension at this region will be.

flow. The Marangoni number for a binary droplet counted in the more volatile solvent is shown in Eq 1.22.

$$Ma_{c,1} = \frac{d\gamma}{dc_1} \frac{h\ \Delta c_1}{\mu D_1} \tag{1.22}$$

where the subscripts of $Ma$, $c$ and $D$ denote the Marangoni number, concentration and the diffusivity of the more volatile solvent defined as solvent 1. $\Delta c_1$ represents the concentration difference of the more volatile solvent at the contact line, $r = r_l$, and the centre $r = 0$, namely $\Delta c_1 = c_{1,r_l} - c_{1,0}$, which is always negative for the more volatile solvent.

When $d\gamma/dc_1$ is positive, it means the more volatile solvent has the higher surface tension than the other one so that the value of the Marangoni number counted in the more volatile solvent is negative, namely $Ma_{c,1} < 0$, and the Marangoni flow moves to the centre; on the other hand, when the more volatile solvent has the lower surface tension, the Marangoni number counted in the more volatile solvent is positive, namely $Ma_{c,1} > 0$, the direction of the Marangoni flow is from the centre to the contact line.

With the lubrication approximation in the cylindrical coordinates and the as-

sumption that the aspect ratio of a droplet is small ($h/R << 1$), we have

$$\frac{\partial h}{\partial t} = \frac{-1}{r}\frac{\partial (r h u_a)}{\partial r} - \mathbf{J}\cdot\mathbf{n} \tag{1.23}$$

where $\mathbf{J}$ is the total evaporative flux and $u_a$ is the height-averaged velocity defined as [74]

$$u_a = \frac{h^2}{3\mu}\frac{\partial p}{\partial r} + \frac{h}{2\mu}\frac{\partial \gamma}{\partial r} \tag{1.24}$$

in which the first term is due to the Laplace pressure and the second is the Marangoni flow

$$u_{Ma_c} = \frac{h}{2\mu}\frac{d\gamma}{d\phi_1}\frac{\partial \phi_1}{\partial r} \tag{1.25}$$

where $u_{Ma_c}$ is defined in component 1

$$u_{Ma_c} = \begin{cases} u_{Ma_c} > 0 & d\gamma/d\phi_1 < 0 \\ u_{Ma_c} < 0 & d\gamma/d\phi_1 > 0 \end{cases} \tag{1.26}$$

where $\phi_1$ is the volume fraction of the more volatile solvent. In the case that the more volatile solvent has the higher surface tension, $d\gamma/d\phi_1 > 0$, $u_{Ma_c}$ appears to be negative; when the more volatile solvent has the lower surface tension, that is $d\gamma/d\phi_1 < 0$, $u_{Ma_c}$ is positive. The speed of the Marangoni flow, $u_{Ma_c}$, is height-averaged as the aspect ratio is very small [74] [95].

## 1.4 Printed Droplets Evaporating in a Well

For practical purposes, such as printed electronics [120] [121] [122], fabricating biosensors [123] [124] or DNA chip manufacturing [125] [126] [127] [128], droplets are printed or jetted by a pipette on a patterned area. When a droplet evaporates in a well, the contact line is pinned at the brim of a well. In consequence, the evaporation process follows the mode of constant contact line until the droplet touches

down at the base of a well; since then, a new contact line emerges at the base and recedes towards the brim.

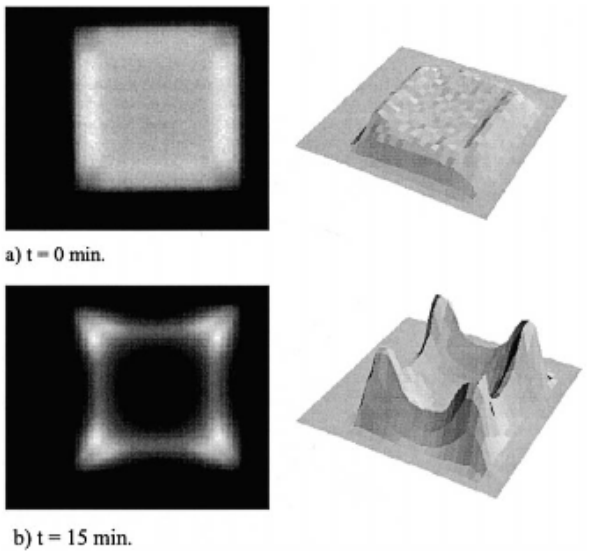


Figure 1.6: The experiment results of glycol/water droplet, whose volume ratio is 9:1, evaporating in a cuboid well the depth and length of which are 6 $\mu$m and 200 $\mu$m, respectively: a). the initial moment, $t = 0$, of the evaporation process when the droplet filled up the well; b). at the moment $t = 15$ min when the droplet was pinned at the brims while the main body was below the depth of the well, forming a cuboid concave in the centre [129]. (Reprinted with the kind permission from Sensors and Actuators A: Physica who holds the copy right)

As the contact line of a printed droplet in a well is pinned, the coffee-ring effect plays a significant role while the droplet dries up, although the exact shapes may hinge on the shape of wells. For polygonal shapes, the droplets will be pinned at the brims until it dries out; after the touchdown moment, the majority of the droplets stay near the corners [129] [130] [131] [132]. For circular wells, like cylindrical wells or spherical wells, there is no sharp corner on the contact line, so that the shapes appear to have circular symmetry.

When a water droplet seeded with micro-spheres with the initial volume of 37.7 nl approximately, evaporated in a cylindrical well, whose radius and depth were 500 $\mu$m and 48 $\mu$m, respectively, the micro-spheres were piled near the border of the well once the droplet dried up [133], forming a ring-like shape in the well; in addition, the liquid-vapour interface, also deemed as a meniscus, remained a spherical-cap shape, with or without the particles, until the droplet touched down at the base;

also, the height at the centre decreased linearly while the droplet evaporated, as if the droplet had been placed on a substrate [133] [134].

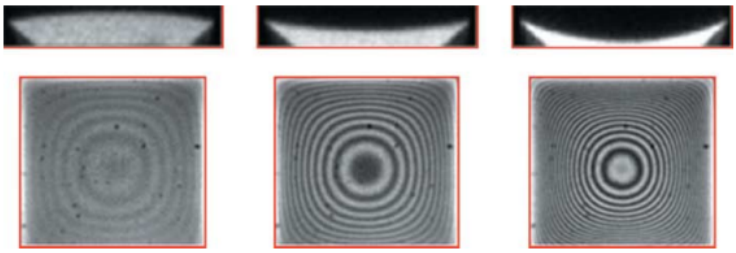

Figure 1.7: The experiment results of an ethylene glycol droplet, evaporating in a truncated square pyramid well, the width at the top, depth and the tilt angle of which are 200 $\mu$m, 20 $\mu$m and 54.7°: the top bars are the confocal images of the profile at different times, $t = 53$ s, $t = 97$ s and $t = 164$ s; **bottom-left** shows the fringe pattern of the ethylene glycol droplet at the moment $t = 53$ s when the droplet fills up the well; **bottom-middle** shows the fringe pattern of the ethylene glycol droplet at the moment $t = 97$ s when the droplet forms a concave meniscus in the well; **bottom-right** shows the fringe pattern of the ethylene glycol droplet at $t = 164$ s when the droplet is about to touch down at the base of the well [135]. (Reprinted with the kind permission from Journal of Microscopy who holds the copy right)

The same evolution of a meniscus also occurred in a truncated cone well [136], in which case the diameter of the top was 1.38 mm, larger than that of the bottom, 0.77 mm, while the height of the reservoir was 2.2 mm, leading to the initial volume of a water droplet being 0.65 $\mu$l. The shapes of the menisci at different moments remained spherical caps before the droplet touched down at the base; likewise, in their work, the shape of a meniscus resembled to a spherical cap while the droplet receded towards the brim of the reservoir.

In a cuboid well with the width and length both being 200 $\mu$m and the depth being 6 $\mu$m, the evaporation of glycol droplets and the binary droplets containing water and glycol also showed cap-like shapes in the main bodies near the centre even though there were irregular shapes near the edges of the cuboid well due to the sharp corners [129].

Like what happened in a cuboid well, the same phenomena occurred in a truncated square pyramid with the length at the top, depth and the tilt angle being 200 $\mu$m, 20 $\mu$m and 54.7°, respectively [135]. An ethylene glycol evaporating in

one of the truncated square pyramid wells was researched with an epi-illumination microscope to achieve confocal images which showed the side-view of the meniscus, shown in the top bar in Fig 1.7, and an interferometry recording the fringe pattern to reconstruct the profile during evaporation, presented in the lower bar in Fig 1.7.

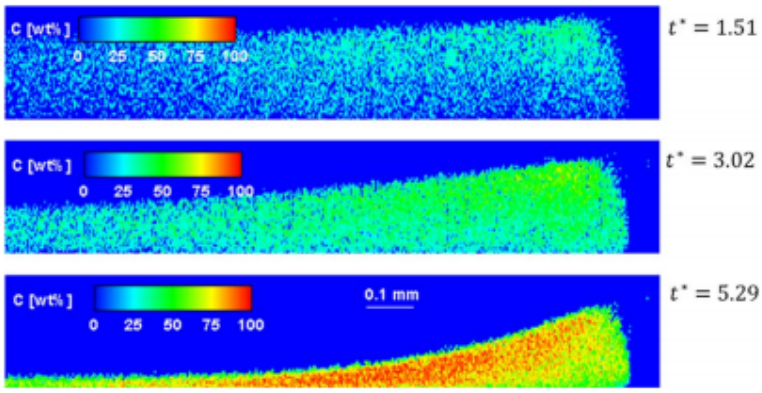


Figure 1.8: The Laser Induced Fluorescence result concentration distribution of PVA solution with the initial concentration being $20wt\%$, evaporating in a cuboid well, the width and depth of which are 7.00 mm, 1.26 mm: the top bar is at the moment $t^* = 1.51$ when the concentration of PVA is highest near the brim thanks to the evaporation of water occurring fastest at the brim; the middle bar presents the result at the moment $t^* = 3.02$ when the concentration of PVA is still highest at the brim; the bottom bar shows that PVA is the densest near the centre at the moment $t^* = 5.29$ rather than the brim [137]. $t^* = t\ u_{avg}/h(t)$ with $u_{avg}$ denoting the average evaporation induced velocity. (Reprinted with the kind permission from Physics of Fluids who holds the copy right)

Babaie and his co-workers investigated the velocity profile of a droplet containing PVA, polyvinyl alcohol, evaporating in a cuboid well [138] [139]. Although the volume of the wells used in their study were at micro-litre scale, 39.2 $\mu$l, when the depth is 0.8 mm and the length and width of the well were both 7 mm, there was still a vortex arising near the brim when the ratio of the depth versus the length is over 0.3. In addition, the appearance of a vortex also depends on the viscosity of a solution, which also indicates that viscosity plays an important role in the internal flow during evaporation. Also, they showed that the higher concentration of PVA was, whose molecular weight was 6000 g/mol and 80% hydrolysed, the higher initial viscosity would be and the less stronger the vortex to the Marangoni effect was. In the middle of evaporation, the concentration of PVA was the highest near the

contact line or the brim, but the concentration at the centre became the highest when the droplet touched down , as was shown in Fig 1.8 [137] [140]. The concentration gradient in the droplet also led to the emergence of the solutal Marangoni flow which flowed to the centre at the moment $t^* = 3.02$ as water evaporated more rapidly at the contact line; however, the Marangoni flow moved towards the brim at the moment $t^* = 5.29$ when there was no water left at the centre.

Rieger *et al*. investigated the evaporation of ethylene glycol droplets in the cylindrical wells with the depth being 6 $\mu$m and the radii being 50, 75, 100 and 150 $\mu$m, respectively, in which the shapes of the menisci at different moments were all well-fit with spherical caps and there was a linear relation between the evaporation rate and the radius of a cylindrical well [141]; moreover, the height evolution at the centre, $h_{r=0}$, decreased linearly like an evaporating sessile droplet [1] [78]; and, the theoretical evaporation rate in the wells were proved to follow the same rule of pure sessile droplets [141].

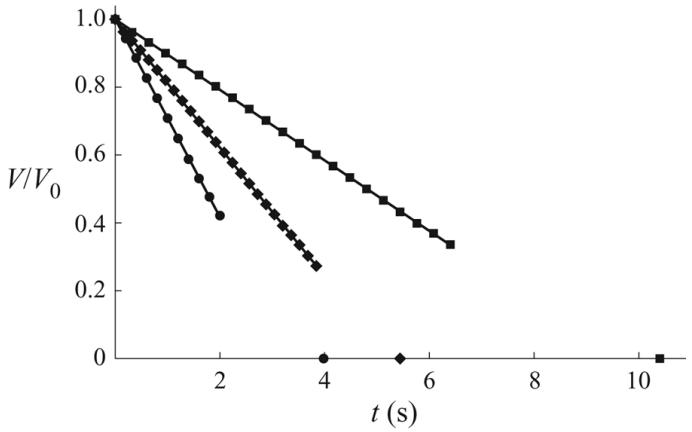


Figure 1.9: The experiment results of methyl benzoate droplets evaporating in the cylindrical wells, the depth and radii of which are 2.38 $\mu$m ,1.87 $\mu$m and 2.39 $\mu$m, 29 $\mu$m, 50 $\mu$m and 75 $\mu$m, respectively: in the three wells, the volumes of methyl benzoate droplets decreased linearly with time [142]. (Reprinted with the kind permission from Journal of Fluid Mechanics who holds the copy right)

D'Ambrosio *et al*. researched the evaporation of picoliter droplets in cylindrical wells with the radii being 29 $\mu$m, 50 $\mu$m and 75 $\mu$m respectively, while the depths of the wells were 2 $\mu$m approximately; in addition, they developed a model to predict the profiles and regarded the mean curvature of the free surface of the droplet as a constant [142]. The evaporation rates were constant before the touch-down moment

and the height profiles at the centre decreased linearly, presented in Fig 1.9. The experimental results agreed with their model, although the height profile in the theoretical part was not assumed to be a spherical cap when $B \neq 0$:

$$h = A\, r^2 + B\, log\, r + C \tag{1.27}$$

where A, B, C are constants and determined by the boundary conditions in the model.

Apart from shallow cuboid square or cylindrical wells, stadium-shaped wells are also common in industry, the evaporation phenomena in which were investigated experimentally by Kazmierski [143] and theoretically by Dam and Kuerten [122] and Kajiya *et al* [120]. The results show that for wells without sharp edges, the profiles of the menisci due to the Marangoni effect, thermal or solutal, will behave differently from a spherical cap, such as a dimple in the middle or an M-shaped profile (a local minimum at the centre resembling to the capital 'M') when droplets touch down [120] [144]. In short, geometrical features of a well play an important role in evaporation and the components in a droplet will also contribute to the deformation of a profile drastically.

Similar to a droplet evaporating on a substrate with its contact line pinned, the evaporation rate of a droplet in a circular well is highest near the brim of a well [142]. Also, the internal flow was shown to be the strongest near the brim [141], when the Marangoni flow was absent. As a result, surface tension over a droplet dominates the shape, leading to the profile at different moments until touch-town appearing to be a spherical cap, if droplets are at nanolitre or even picolitre scale.

For polygonal prisms, in the case of gravity-free, the main bodies of menisci near the centres appear to be spherical caps, although there are singularities at the corners [145]. As is shown in Fig 1.10, the menisci are no longer spherical caps. Therefore, calculating the evaporation rate experimentally from an interferometry inevitably comprises of the error from the asymmetry. What may prove even worse is that the geometry singularity at the corners may introduce the highest evaporation flux on a surface which could give rise to the temperature gradient at the brims

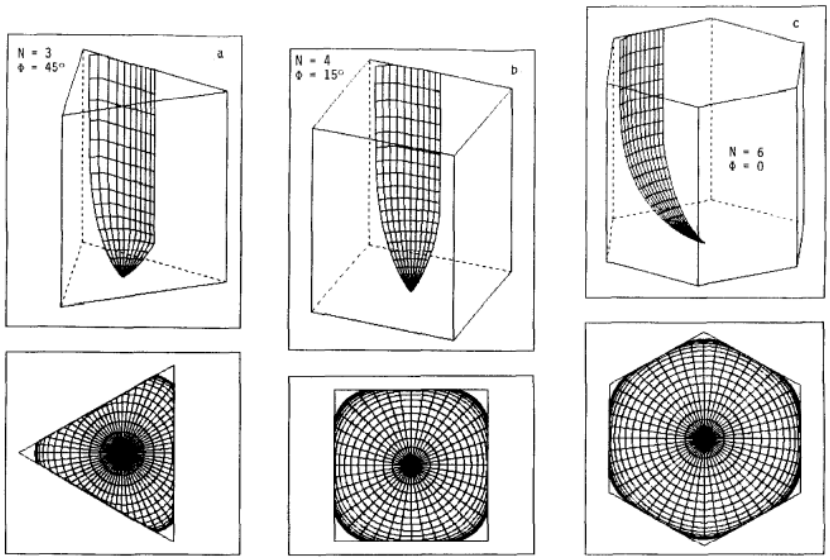


Figure 1.10: The menisci of equilateral triangular, square, and hexagonal prism, when the contact angle is assumed to be 45°: the results in the top bar are the 3-D results of the menisci while the bottom bar is the menisci from the top view, which shows that the profile near the centres are part of hemispheres [145]. (Reprinted with the kind permission from Journal of Colloid and Interface Science who holds the copy right)

so that the thermal Marangoni effect may further complicate the already involved issue; thus, cylindrical wells are great candidates to experimentally investigate the behaviour of a droplet evaporating in a patterned area.

Regarding to evaporation rate, the experiment results show that a pure droplet in a cylindrical well behaves like a droplet placed on a substrate with the contact line pinned with a constant evaporation rate [141] [142] [146], as is given in Eq 1.28 which assumes water as the droplet; however, there may appear a little deviation when a droplet touches down; since then, a new contact line has emerged at the base of the host well.

$$-\frac{dm}{dt} = 4R_0D(1 - RH)c_v \qquad \theta \sim 0 \tag{1.28}$$

where $R_0$ is the radius of a cylindrical well.

As in the case of sessile droplets, the evaporation flux diverges at a contact line giving rise to a capillary flow moving from the centre to the contact line to com-

pensate the loss of liquid. Although the meniscus of a liquid droplet in a cylindrical well appears to be a spherical cap like a droplet on a substrate, the meniscus will turn to be concave down when the height at the centre is lower than the depth of a well [147].

# CHAPTER 2

# Experimental Setup and Analysis Method

The solvents in this study are purchased from Aldrich or Flurochem without further purification. Picolitre droplets are printed in cylindrical wells with different aspect ratios by a printhead from Microfab, the orifice of which is 30.0 $\mu$m. The cylindrical wells are designed in house and fabricated with the assistance from Michael Cooke at the Department of Engineering. The radii of the wells in this study are 30.0 $\mu$m, 50.0 $\mu$m and 75.0 $\mu$m respectively, while the depths of the wells range from 1.20 $\mu$m to 3.12 $\mu$m.

## 2.1 Fabrication of Substrates

The substrates used in this study are processed with photolithography carried out at the Department of Engineering Durham University, on ITO-coated glasses provided by Visiontek Systems Ltd.. The width and thickness of the square glass are 50 mm and 1.1 mm, respectively; while the thickness of the ITO layer is only 50 nm which is only coated on one side of the glass. Photolithography is a process used to micro-fabricate the desired pattern on a thin substrate. The photomasks, shown in Fig 2.1, applied during the photolithography were designed by Teresa Colosimo and

Figure 2.1: Photomasks for developing patterns of cylindrical wells. (left, centre and right are for fabricating wells with radius 75.0 $\mu$m, 30.0 $\mu$m and 50.0 $\mu$m, respectively.)

fabricated by Micro Lithography Services Ltd.. To develop cylindrical wells with the photomasks, SU-8, a negative photoresist, is chosen to undertake the UV-light exposure procedure.

With different spinning rates to spread SU-8 on an ITO-coated glass and the control of the exposure time, cylindrical wells with the same radius, but different depths are patterned on an ITO-coated glass. Similar procedures are conducted for different photo masks so that cylindrical wells with different radii are fabricated.

Here we illustrate an example of the photolithography process, from which the cylindrical wells, with depth and radius being 2.93 $\mu$m and 75.0 $\mu$m respectively, are patterned on ITO-coated glasses.

An ITO-coated glass substrate is carefully cleaned in a sonicator, in which the substrate is entirely immersed in IPA and ultra-pure water for 10 min, respectively. Once a glass is thoroughly cleaned and purged with nitrogen flow, electric resistance of the glass on each side is measured to find the ITO side of the glass.

To develop the SU-8 on the ITO side, first, the glass is pre-baked at 95 °C for 5 min to improve the wettability of the ITO layer so that the photoresist is easier to spread; second, the photoresist-loaded glass is transferred to a spin coater, the spinning rates of which are set at 500 rpm for 10 s and 3000 rpm for 60 s, respectively. After being covered with the photoresist, the glass is baked again at 95 °C for 1 min; afterwards, the glass is exposed under UV light for 10 s, the intensity of which is set at 140 mJ/s, to initialise the photo-chemical reaction inside the photoresist. In order to develop the pattern, the exposed glass is placed in EC solvent, the developer

for SU-8, for 1 min, before it is rinsed with IPA. Having been purged with nitrogen flow, the patterned glass then is baked at 200 °C for 10 min.

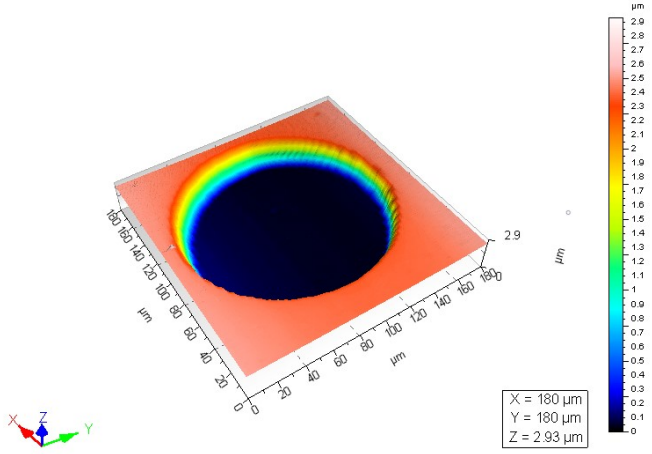


Figure 2.2: A 3D result of a cylindrical well measured by the profiler, KLA (Tencor P-6 Stylus): the depth of the well is 2.93 $\mu$m approximately.

Depths and radii of the wells are measured with the profiler by KLA (Tencor P-6 Stylus) and are further confirmed with the interferometer applied in this study. One of the 3D result is achieved by scanning a whole cylindrical well such that the contour of the well can be reconstructed, as is shown in Fig 2.2.

According to the procedure shown above, the depth of a well is either controlled by the duration and intensity of UV exposure or the spinning rate of a spin-coater. With the assumption that the ridge of a well is flat, we can compare the height at the ridge and the height at the bottom of a well to measure the depth of a well. The results that are collected by the profiler agree with the results measured with the inteferometer in the experimental setup presented in Sec 2.2. Therefore, the profiler is reliable to estimate the depth of cylindrical wells developed by photolithography.

## 2.2 Experimental Setup

Experiments are performed with the custom-built interferometer shown in Fig 2.3 to record a video of a picolitre droplet evaporating in a cylindrical well. The wavelength of the light source provided by (Thorlabs M470L3) is $\lambda_0 = 465$ nm; as a result, the height difference at a point between adjacent bright fringes is 0.167 $\mu$m

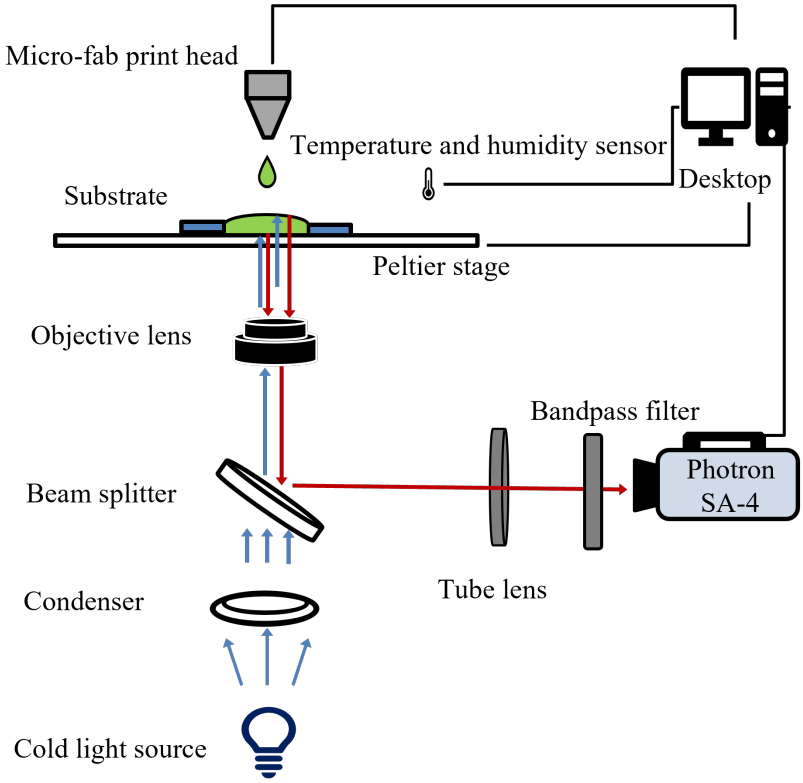


Figure 2.3: Experimental setup which contains a cold light source to provide the light beam with the wavelength at 465 nm, a condenser to transform the beam from a point source into a parallel one, a beam splitter to achieve the transmission from the condenser and reflect the interference to the high-speed camera, Photron SA-4, an objective lens so as to acquire the resolution at 0.400$\mu$m per pixel, a Peltier stage to maintain as well as change the temperature of a substrate which is patterned with cylindrical wells to hold the liquid droplet printed by a print head and a temperature and humidity sensor to record the ambient conditions.

approximately, according to $\Delta h = \lambda/(2n)$ where $n = 1.3941$ is the refractive index of n-butyl acetate [148]. A condenser is placed to convert the diverging beam from the cold light source into a parallel one, preparing the beam for interference. Transmitting the parallel beam from the condenser side and reflecting the interference at the tube lens side, a beam spiltter is necessary to compose the setup. Since the typical radius of a well is 75.0 $\mu$m, the objective lens is applied to improve the resolution to 0.400 $\mu$m per pixel. There is also a Peltier stage combined in the setup to maintain and change the temperature of a substrate in the range -10.00°C to 60.00°C so that experiments may be carried out at different temperatures.

The substrate is an ITO-coated glass patterned with cylindrical wells on the ITO side by photolithography. Picoliter droplets are generated with a print head

by MicroFab (MJ-ABP-01) whose diameter of orifice is 30.0 $\mu$m. The volume of a droplet ranges from 30.0 to 50.0 pl which may overfill a few wells with small aspect ratios. Therefore, I compare different shapes by choosing the initial moment $\tau^{'} = 0$ when the height at the centre is equal to the depth of a host well. The tube lens is set to produce the intermediate image, while the bandpass filter is to limit the band width of a beam, which obeys a normal distribution. The high-speed camera, Photron SA-4, collects the frames forming a video for further analysis.

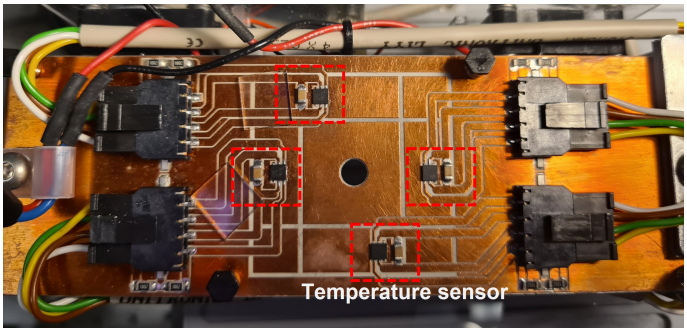


Figure 2.4: The Peltier stage to control the temperature of a substrate with four sensors set on its copper surface shown in the red dashed squares.

The wavelength of the cold light source provided is claimed to be 470 nm; however, the result of the wavelength distribution of the light source after passing through the band pass filter is well-fit by a Gaussian distribution with the standard deviation $\sigma = 3.98$ nm and the mean or expectation for the Gaussian distribution $\psi = 465$ nm, as is shown in Fig 2.5; meanwhile, the expression of the Gaussian distribution is given in Eq 2.2. The deviation induced by the distribution of the wavelength in the interference is analysed in Sec 2.3; the value of the deviation is 7.0 nm approximately, when the solvent is n-butyl acetate.

$$f(\lambda) = \frac{1}{\sigma\sqrt{2\pi}} e^{-\frac{1}{2}\left(\frac{\lambda-\psi}{\sigma}\right)} \tag{2.2.1a}$$

$$\sigma = 3.98nm \tag{2.2.1b}$$

$$\psi = 465nm \tag{2.2.1c}$$

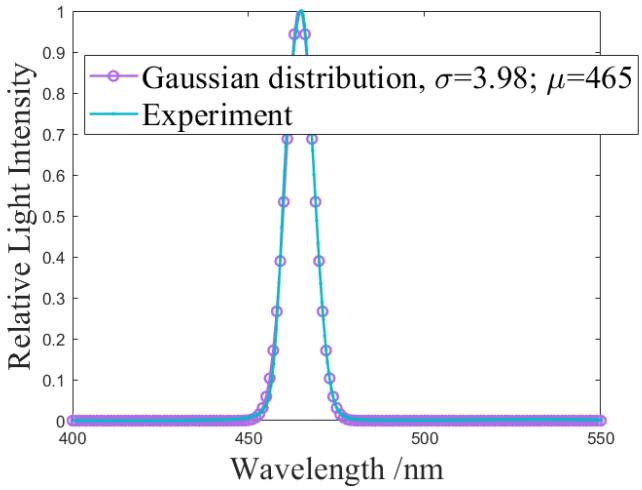


Figure 2.5: The light intensity distribution of the light source in the inteferometer shown in Fig 2.3, which is well-fit with a Gaussian distribution. The data was kindly provided by Teresa Colosimo.

## 2.3 Three-beam Interference

The interferometer in Fig 2.3 is developed to record the evolution of height profile of an evaporating picolitre droplet with the height ranging from 0 to 4 $\mu$m. The fringes are generated by the method of division of amplitude, which are the reflection beams in our case [148] [152]. Since there is a thin layer of ITO on the glass, the interference is the combination of three reflections at the interfaces between air and a droplet, $R_{AD}$, a droplet and the ITO film, $R_{DI}$, and the ITO film and the glass substrate $R_{IG}$, respectively, as is shown in Fig 2.6 where the radius and depth of a

| Material | Refractive index |
|---|---|
| n-Butanol | 1.3988 |
| n-Butyl acetate | 1.3941 |
| Pentyl acetate | 1.4023 |
| Toluene | 1.4961 |
| Anisole | 1.5174 |
| Mesitylene | 1.4994 |
| Methyl benzoate | 1.5164 |
| Benzyl alcohol | 1.5396 |
| ITO | 1.9842 |
| Glass | 1.5200 |
| Air | 1.0003 |

Table 2.1: Refractive indices [149] [150] [151]

well is 75.0 $\mu$m and 2.00 $\mu$m, respectively; and the height at the centre of a droplet is 3.00 $\mu$m. In addition, if a profile is a spherical cap, the principal curvatures are 3.55 $\times 10^{-4}$ $\mu m^{-1} \approx 0$. Therefore, it is reasonable to assume the reflection at the air-droplet interface is parallel to the reflections from the the droplet-ITO interface and the ITO-glass interfaces.

The refractive indices of the materials used in this study are shown in Table 2.1 which indicates phase change may occur at the interface of a liquid droplet and glass, if benzyl alcohol is chosen as the candidate solvent. Therefore, a major merit of the pre-laid ITO film is that the refractive index of ITO is 1.9842, higher than that of all the chemicals used in our study, so that the phase change is avoided.

However, the thin layer of the ITO film also contributes to the error since the fringes are in fact the combination of three beams in this scenario. To calculate the error, we have to understand what happens in three-beam interference.

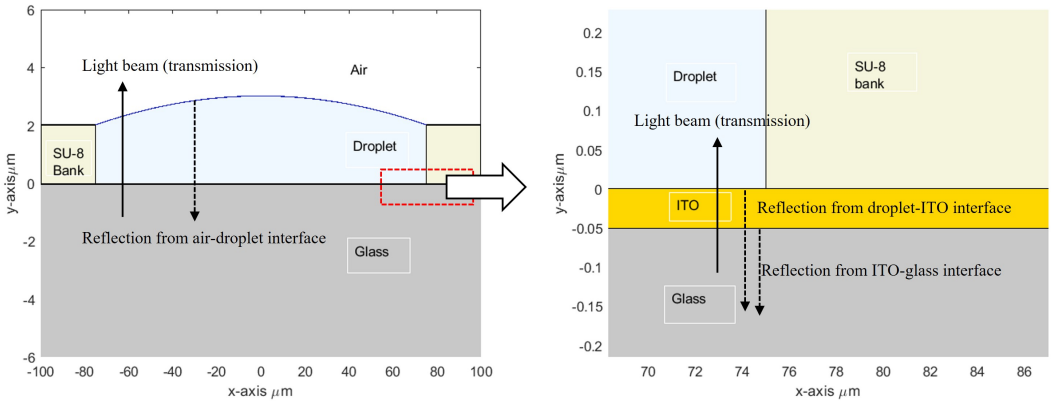


Figure 2.6: The illustration of three-beam interference: reflection beams are from the reflection at the air-droplet interface ( shown in the left sub-figure) and the reflections at the droplet-ITO interface and ITO-glass interface ( shown in the right sub-figure), respectively.

The definition of light intensity, I, is given in Eq 2.3.1, which shows that it is the time average of the amount of energy that crosses in unit time per unit area perpendicular to the direction of the energy flow [148]. In our case, the light intensity of the reflected beams is measured by a high speed camera in the same medium (air), shown in the experimental setup.

$$I=\frac{c}{4\pi}\sqrt{\frac{\varepsilon_l}{\mu_l}}\mathbf{E}^2 \tag{2.3.1}$$

where $\varepsilon_l$ and $\mu_l$ are dielectric constant and magnetic permeability, respectively, while $c$ and $E^2$ are the speed of light and the strength of an electric vector, respectively .

The electric vector of light is presented in Eq 2.3.2, in which $\mathbf{A}$ is a complex vector whose conjugate is $\mathbf{A}^\star$. The Cartesian rectangular components of $\mathbf{A}$ is listed in Eq 2.3.3, where $a_1$, $a_2$, $a_3$, $g_1$, $g_2$, and $g_3$ are functions of position. While taking the time average over a time period , $t^\star$, which is large compared to the period of a vector field $T = 2\pi/\omega$, $(t^\star \gg T)$ we can find the time-averaged electric energy density is reduced to Eq 2.3.5.

$$\mathbf{E}\left(\mathbf{r},t\right)=\mathcal{R}\left\{\mathbf{A}e^{-i\omega t}\right\}=\frac{1}{2}\left[\mathbf{A}\left(\mathbf{r}\right)e^{-i\omega t}+\mathbf{A}^\star\left(\mathbf{r}\right)e^{-i\omega t}\right] \tag{2.3.2}$$

$$\mathbf{A}\left(\mathbf{r}\right)=\left(A_x,A_y,A_z\right)=\left(a_1e^{ig_1(\mathbf{r})},a_2e^{ig_2(\mathbf{r})},a_3e^{ig_3(\mathbf{r})}\right) \tag{2.3.3}$$

$$\mathbf{E}^2=\frac{1}{4}\left(\mathbf{A}^2e^{-2i\omega t}+\mathbf{A}^{\star 2}e^{2i\omega t}+2\mathbf{A}\mathbf{A}^\star\right) \tag{2.3.4}$$

while taking the time average over an interval which is large compared with the period T

$$\left\langle\mathbf{E}^2\right\rangle=\frac{1}{2}\mathbf{A}\cdot\mathbf{A}^\star=\frac{1}{2}\left(\left|A_x\right|^2+\left|A_y\right|^2+\left|A_z\right|^2\right)=\frac{1}{2}\left(a_1^2+a_2^2+a_3^2\right) \tag{2.3.5}$$

where T is the period of a field and $\omega$ is the frequency. The real part is understood to represent the physical quantity.

Providing that there are three monochromatic waves, $\mathbf{E}_1$, $\mathbf{E}_2$ and $\mathbf{E}_3$, superposed at a point, say point B, the total electric field $\mathbf{E}_t$ at this point is

$$\mathbf{E}_t=\mathbf{E}_1+\mathbf{E}_2+\mathbf{E}_3 \tag{2.3.6}$$

$$\mathbf{E}_t^2=\mathbf{E}_1^2+\mathbf{E}_2^2+\mathbf{E}_3^2+2\mathbf{E}_1\cdot\mathbf{E}_2+2\mathbf{E}_1\cdot\mathbf{E}_3+2\mathbf{E}_2\cdot\mathbf{E}_3 \tag{2.3.7}$$

Thus, the light intensity at point B is

$$I_t = I_1 + I_2 + I_3 + J_{12} + J_{13} + J_{23} \tag{2.3.8}$$

$$I_i = \left\langle \mathbf{E}_i^2 \right\rangle \; i = 1, 2, 3 \tag{2.3.9}$$

$$J_{ij} = 2 \left\langle \mathbf{E}_i \cdot \mathbf{E}_j \right\rangle \tag{2.3.10}$$

where $J_{ij}$ denotes the interference term of wave i and wave j.

From Eq 2.3.8, we can find that in the case of three-beam interference, there are three interference terms generated between each two beams. The intensities of the interference terms are shown in Eq 2.3.10.

According to the expression of an electric vector field in Eq 2.3.2, the inner product of two electric vector fields is

$$\mathbf{E}_1 \cdot \mathbf{E}_2 = \frac{1}{2}\left[\mathbf{A}_1(\mathbf{r})\, e^{-i\omega t} + \mathbf{A}_1^{\star}(\mathbf{r})\, e^{i\omega t}\right] \cdot \frac{1}{2}\left[\mathbf{A}_2(\mathbf{r})\, e^{-i\omega t} + \mathbf{A}_2^{\star}(\mathbf{r})\, e^{i\omega t}\right] \tag{2.3.11}$$

$$= \frac{1}{4}\left(\mathbf{A}_1 \cdot \mathbf{A}_2 e^{-2i\omega t} + \mathbf{A}_1 \cdot \mathbf{A}_2^{\star} + \mathbf{A}_1^{\star} \cdot \mathbf{A}_2 + \mathbf{A}_1^{\star} \cdot \mathbf{A}_2^{\star} e^{-2i\omega t}\right) \tag{2.3.12}$$

If for wave k, its amplitudes at $x$, $y$ and $z$ directions are

$$A_{kx} = a_{k1} e^{i g_{k1}} \tag{2.3.13}$$

$$A_{ky} = a_{k2} e^{i g_{k2}} \tag{2.3.14}$$

$$A_{kz} = a_{k3} e^{i g_{k3}} \tag{2.3.15}$$

then the interference term between wave 1 and wave 2 is

$$J_{12} = 2\left\langle \mathbf{E}_1 \cdot \mathbf{E}_2 \right\rangle = \frac{1}{2}\left(\mathbf{A}_1 \cdot \mathbf{A}_2^{\star} + \mathbf{A}_1^{\star} \cdot \mathbf{A}_2\right) = \left(a_{11}a_{21} + a_{12}a_{22} + a_{13}a_{23}\right) cos\delta_{12} \tag{2.3.16}$$

where $\delta_{ij}$ is the phase difference of the corresponding components, the definition of which is shown below (m =1,2,3 denotes x, y and z direction, respectively):

$$\delta_{ij} = g_{im} - g_{jm} = \frac{2\pi}{\lambda}\Delta s_{ij} \tag{2.3.17}$$

where $\lambda$ is the wave length of a light source, while $\Delta s_{ij}$ is the difference of the optical path.

Since interference does not occur when two light beams polarise perpendicularly, when the waves propagate in the z-direction and are linearly polarised with their **E** vectors in the x-direction [148], we only need to consider the items $a_{11}$ and $a_{21}$ in Eq 2.3.16, that is

$$a_{12} = a_{22} = a_{13} = a_{23} = 0 \tag{2.3.18}$$

therefore,

$$J_{12} = a_{13}a_{23}cos\delta_{12} \tag{2.3.19}$$

where the subscripts of $J_{12}$ and $\delta_{12}$ represent the interference and the phase difference from wave 1 and wave 2, respectively.

Based on the definition of light intensity given in Eq 2.3.9 and 2.3.18, the light intensity of the interference term, $I_{12}$, is reduced to Eq 2.3.23.

$$I_1 = \frac{1}{2}a_{11}^2 \tag{2.3.20}$$

$$I_2 = \frac{1}{2}a_{21}^2 \tag{2.3.21}$$

$$J_{12} = a_{11}a_{21}cos\delta_{12} = 2\sqrt{I_1 I_2}cos\delta_{12} \tag{2.3.22}$$

$$I_{12} = I_1 + I_2 + 2\sqrt{I_1 I_2}cos\delta_{12} \tag{2.3.23}$$

Furthermore, the total light intensity at point B, $I_t$, due to three-beam interference, is the combination of the interferences between each two light beams, as is shown in Eq 2.3.8. Applying the result into Eq 2.3.23, the total intensity is then

$$I_t = I_1 + I_2 + I_3 + 2\sqrt{I_1 I_2}cos\delta_{12} + 2\sqrt{I_1 I_3}cos\delta_{13} + 2\sqrt{I_2 I_3}cos\delta_{23} \tag{2.3.24}$$

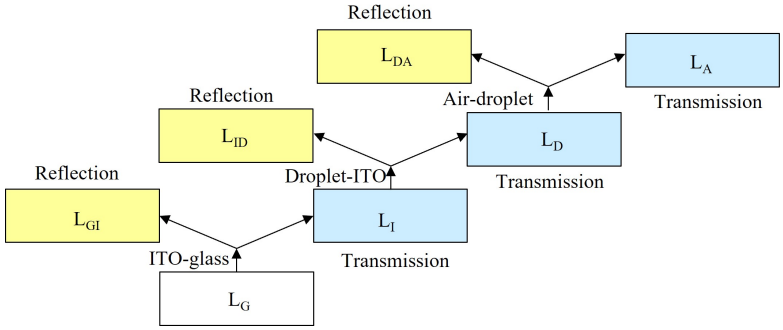


Figure 2.7: Transmissions and reflections at different interfaces: a light beam will transmit and reflect at a interface and the light intensities of the transmission and reflection are calculated with Eq 2.3.25 and Eq 2.3.26.

Here we define that the light intensity of the incident light beam which has travelled through the glass layer and is just about to incident on to the interface between the ITO and glass, as is shown in Fig 2.7, is $L_G$ and the light intensities of the transmitted light beams at ITO-glass, droplet-ITO and air-droplet interface are $L_I$, $L_D$ and $L_A$, respectively. In addition, the light intensities of the reflected beams at ITO-glass, droplet-ITO and air-droplet interface are $L_{GI}$, $L_{ID}$ and $L_{DA}$, respectively.

When a light beam reaches the interface between medium 1 and medium 2, occurring normal incidence, it may either proceed into medium 2 or propagate back into medium 1. The intensities of the transmission and reflection, which are also described as the reflectivity $\mathcal{R}_{12}$ and transmissivity $\mathcal{T}_{12}$, depend on the refractive indices of the media.

$$\mathcal{T}_{12} = \left(\frac{n-1}{n+1}\right)^2 \tag{2.3.25}$$

$$\mathcal{R}_{12} = \frac{4n}{(n+1)^2} \tag{2.3.26}$$

where

$$n = \frac{n_2}{n_1} \tag{2.3.27}$$

where $n_1$ is the refractive index of medium 1 and $n_2$ is the refractive index of medium 2.

| Interface | Reflectivity | Transmissivity |
|---|---|---|
| Glass-ITO | 0.017500 | 0.98250 |
| ITO-droplet | 0.030500 | 0.96950 |
| Droplet-air | 0.027000 | 0.97300 |
| Glass-droplet | 0.0020000 | 0.99800 |

Table 2.2: Reflectivities and transmissivities of the interfaces when n-butyl acetate is the droplet.

According to Eq 2.3.25−2.3.26 and the refractive indices given in Table 2.1, the reflectivities and transmissivities of the glass-ITO, ITO-droplet and droplet-air interface are calculated and listed in Table 2.2 when n-butyl acetate is the droplet. Also, in Table 2.2, it shows that the reflectivity of the glass-droplet interface is only 0.0020000, whereas that of the ITO-droplet is 0.030500, proving that the existence of ITO significantly enhances the reflectivity and decreases the differences of the reflectivities between the interfaces as well.

As the reflections in Fig 2.7 are from the same light source with the intensity of $L_G$, the light intensities of the reflected beams are

$$I_{GI} = I_G \mathcal{R}_{GI} \tag{2.3.28a}$$

$$I_{ID} = I_G \mathcal{T}_{GI} \mathcal{R}_{ID} \mathcal{T}_{GI} \tag{2.3.28b}$$

$$I_{DA} = I_G \mathcal{T}_{GI} \mathcal{T}_{ID} \mathcal{R}_{DA} \mathcal{T}_{ID} \mathcal{T}_{GI} \tag{2.3.28c}$$

where $\mathcal{R}$ and $\mathcal{T}$ are reflectivity and transmissivity of an interface with the subscripts of $I$, $G$ and $D$ meaning ITO, glass and droplet, respectively; the light intensities of the interference terms are

$$J_{GI-ID} = 2\sqrt{I_{GI} I_{ID}}\, cos\delta_{GI-ID} \tag{2.3.28d}$$

$$J_{GI-DA} = 2\sqrt{I_{GI} I_{DA}}\, cos\delta_{GI-DA} \tag{2.3.28e}$$

$$J_{ID-DA} = 2\sqrt{I_{ID} I_{DA}}\, cos\delta_{ID-DA} \tag{2.3.28f}$$

where the phase differences are

$$\delta_{GI-ID} = \frac{2\pi}{\lambda_0}\left(2n_{ITO}h_{ITO}\right) + \pi \tag{2.3.28g}$$

$$\delta_{GI-DA} = \frac{2\pi}{\lambda_0}\left(2n_{ITO}h_{ITO} + 2n_{droplet}h_{droplet}\right) + \pi \tag{2.3.28h}$$

$$\delta_{ID-DA} = \frac{2\pi}{\lambda_0}\left(2n_{droplet}h_{droplet}\right) \tag{2.3.28i}$$

An extra phase difference $\pi$ added in terms $\delta_{GI-ID}$ and $\delta_{GI-DA}$ is due to the optical properties of the media. When a light beam reflects normally from medium 1 to medium 2 which is assumed to be optically denser than medium 1, the phase differs from the transmission by $\pi$ [148] [152].

Most of the solvents, in this study are less optically denser than glass, so that the phase difference exists. However, when the liquid is benzyl alcohol, which is optically denser than glass, the phase difference will not occur at the interface of glass-droplet. Therefore, the existence of an ITO layer not only increases the reflectivity, but also keeps the values of the phase differences in Eq 2.3.28i.

| Reflection | Light intensity |
|---|---|
| Glass-ITO($I_{GI}$) | 0.018000 $I_G$ |
| ITO-droplet ($I_{ID}$) | 0.028500 $I_G$ |
| Droplet-air($I_{DA}$) | 0.025700 $I_G$ |

Table 2.3: Light intensities of the reflections when n-butyl acetate is the droplet.

According to Eq 2.3.24, the light intensity of three-beam interference fringes is

$$I_\alpha = I_{GI} + I_{ID} + I_{DA} + J_{GI-ID} + J_{GI-DA} + J_{ID-DA} \tag{2.3.29}$$

Given the expressions of the light intensities and phase differences of the reflec-

tions in Eq 2.3.28a−2.3.28i, the total light intensity in Eq 2.3.29, $I_\alpha$, becomes

$$\begin{aligned} I_\alpha = {} & I_G\mathcal{R}_{GI} + I_G\mathcal{T}_{GI}\mathcal{R}_{ID}\mathcal{T}_{GI} + I_G\mathcal{T}_{GI}\mathcal{T}_{ID}\mathcal{R}_{DA}\mathcal{T}_{ID}\mathcal{T}_{GI} + \\ & 2\sqrt{I_G\mathcal{R}_{GI}I_G\mathcal{T}_{GI}\mathcal{R}_{ID}\mathcal{T}_{GI}}\, cos\left[\frac{2\pi}{\lambda_0}\left(2n_{ITO}h_{ITO}\right) + \pi\right] + \\ & 2\sqrt{I_G\mathcal{R}_{GI}I_G\mathcal{T}_{GI}\mathcal{T}_{ID}\mathcal{R}_{DA}\mathcal{T}_{ID}\mathcal{T}_{GI}}\, cos\left[\frac{2\pi}{\lambda_0}\left(2n_{ITO}h_{ITO} + 2n_{droplet}h_{droplet}\right) + \pi\right] + \\ & 2\sqrt{I_G\mathcal{T}_{GI}\mathcal{R}_{ID}\mathcal{T}_{GI}I_G\mathcal{T}_{GI}\mathcal{T}_{ID}\mathcal{R}_{DA}\mathcal{T}_{ID}\mathcal{T}_{GI}}\, cos\left[\frac{2\pi}{\lambda_0}\left(2n_{droplet}h_{droplet}\right)\right] \end{aligned} \tag{2.3.30}$$

Having noticed that the height of a droplet at point B is falling monotonically as the droplet evaporates whilst the thickness of the ITO remains unchanged, I combine the first four items of Eq 2.3.30 together and denote it as $I_{\alpha 1}$ and the last two items as $I_{\alpha 2}$.

$$I_\alpha = I_{\alpha 1} + I_{\alpha 2} \tag{2.3.31}$$

$I_{\alpha 1}$ is a constant as the values of the items never change during evaporation.

$$\begin{aligned} I_{\alpha 1} = {} & I_G\left(\mathcal{R}_{GI} + \mathcal{T}_{GI}\mathcal{R}_{ID}\mathcal{T}_{GI} + \mathcal{T}_{ID}\mathcal{R}_{DA}\mathcal{T}_{ID}\mathcal{T}_{GI}\mathcal{T}_{GI}\right) \\ & - 2I_G\mathcal{T}_{GI}\sqrt{\mathcal{R}_{GI}}\mathcal{R}_{ID}cos\left[\frac{2\pi}{\lambda_0}\left(2n_{ITO}h_{ITO}\right)\right] \end{aligned} \tag{2.3.32}$$

but $I_{\alpha 2}$ depends on the height of a droplet

$$\begin{aligned} I_{\alpha 2} = {} & -2I_G\mathcal{T}_{GI}\mathcal{T}_{ID}\sqrt{\mathcal{R}_{GI}\mathcal{R}_{DA}}cos\left[\frac{2\pi}{\lambda_0}\left(2n_{ITO}h_{ITO} + 2n_{droplet}h_{droplet}\right)\right] + \\ & 2I_G\mathcal{T}_{GI}^2\mathcal{T}_{ID}\sqrt{\mathcal{R}_{ID}\mathcal{R}_{DA}}cos\left[\frac{2\pi}{\lambda_0}\left(2n_{droplet}h_{droplet}\right)\right] \\ = {} & \left\{-2I_G\mathcal{T}_{GI}\mathcal{T}_{ID}\sqrt{\mathcal{R}_{GI}\mathcal{R}_{DA}}cos\left[\frac{2\pi}{\lambda_0}(2n_{ITO}h_{ITO})\right] + 2I_G\mathcal{T}_{GI}^2\mathcal{T}_{ID}\sqrt{\mathcal{R}_{ID}\mathcal{R}_{DA}}\right\} \\ & cos\left[\frac{2\pi}{\lambda_0}\left(2n_{droplet}h_{droplet}\right)\right] + 2I_G\mathcal{T}_{GI}\mathcal{T}_{ID}\sqrt{\mathcal{R}_{GI}\mathcal{R}_{DA}}sin\left[\frac{2\pi}{\lambda_0}\left(2h_{ITO}n_{ITO}\right)\right] \\ & sin\left[\frac{2\pi}{\lambda_0}\left(2n_{droplet}h_{droplet}\right)\right] \\ = {} & Ncos\left[\frac{2\pi}{\lambda_0}\left(2n_{droplet}h_{droplet}\right) - \theta\right] \end{aligned} \tag{2.3.33}$$

where $N$ and $\theta$ are independent of $h_{droplet}$

$$N = \sqrt{\left\{-2I_G\mathcal{T}_{GI}\mathcal{T}_{ID}\sqrt{\mathcal{R}_{GI}\mathcal{R}_{DA}}cos\left[\frac{2\pi}{\lambda_0}(2n_{ITO}h_{ITO})\right] + 2I_G\mathcal{T}_{GI}^2\mathcal{T}_{ID}\sqrt{\mathcal{R}_{ID}\mathcal{R}_{DA}}\right\}^2 + \left\{2I_G\mathcal{T}_{GI}\mathcal{T}_{ID}\sqrt{\mathcal{R}_{GI}\mathcal{R}_{DA}}sin\left[\frac{2\pi}{\lambda_0}(2h_{ITO}n_{ITO})\right]\right\}^2} \tag{2.3.34}$$

$$\begin{aligned}\theta &= arctan\left\{\frac{2I_G\mathcal{T}_{GI}\mathcal{T}_{ID}\sqrt{\mathcal{R}_{GI}\mathcal{R}_{DA}}sin\left[\frac{2\pi}{\lambda_0}(2h_{ITO}n_{ITO})\right]}{-2I_G\mathcal{T}_{GI}\mathcal{T}_{ID}\sqrt{\mathcal{R}_{GI}\mathcal{R}_{DA}}cos\left[\frac{2\pi}{\lambda_0}(2n_{ITO}h_{ITO})\right] + 2I_G\mathcal{T}_{GI}^2\mathcal{T}_{ID}\sqrt{\mathcal{R}_{ID}\mathcal{R}_{DA}}}\right\} \\ &= arctan\left\{\frac{\sqrt{\mathcal{R}_{GI}}sin\left[\frac{2\pi}{\lambda_0}(2h_{ITO}n_{ITO})\right]}{-\sqrt{\mathcal{R}_{GI}}cos\left[\frac{2\pi}{\lambda_0}(2h_{ITO}n_{ITO})\right] + \mathcal{T}_{GI}\sqrt{\mathcal{R}_{ID}}}\right\}\end{aligned} \tag{2.3.35}$$

Therefore, the patterns of the fringes only rely on the phase in $I_{\alpha 2}$ presented in Eq 2.3.33. The condition for the bright fringes in three-beam interference is

$$\frac{2\pi}{\lambda_0}(2n_{droplet}h_{droplet}) - \theta = 2k\pi;\ \text{k=0}, \pm 1, \pm 2, \cdots; \tag{2.3.36}$$

this corresponds to droplet height of

$$h_{droplet} = \frac{(2k\pi + \theta)\lambda_0}{4\pi n_{droplet}};\ \text{k} = 0, \pm 1, \pm 2, \cdots; \tag{2.3.37}$$

while for the dark fringes, the condition is

$$\frac{2\pi}{\lambda_0}(2n_{droplet}h_{droplet}) - \theta = (2k+1)\pi;\ \text{k} = 0, \pm 1, \pm 2; \tag{2.3.38}$$

and the height of the droplet at this condition is

$$h_{droplet} = \frac{((2k+1)\pi + \theta)\lambda_0}{4\pi n_{droplet}};\ \text{k=0}, \pm 1, \pm 2; \tag{2.3.39}$$

The influence due to the ITO layer is included in $\theta$.

Moreover, the height difference at a point between the adjacent bright fringes is

$$\Delta h = \lambda_0 / 2 n_{droplet} = 167 \text{ nm} \tag{2.3.40}$$

if the wavelength of a light source is 465 nm and the droplet is n-butyl acetate. The results above show that the existence of the thin ITO layer has no impact on the period of the fringes; however, it shifts the first bright fringe by $\theta = 0.200$ which is 5.40 nm in the height, namely the first bright fringe appearing when the height is 5.40 nm instead of 0.

I have assumed the light source is monochromatic in Eq 2.3.40, but according to the result shown in Fig 2.5, the distribution of the light source is well-fit with the Gaussian distribution given in Eq 2.3.41.

$$f(\lambda) = \frac{1}{\sigma\sqrt{2}\pi} e^{\frac{-1}{2}\left(\frac{\lambda-\psi}{\sigma}\right)^2};\ \sigma = 3.98;\ \psi = 465 \tag{2.3.41}$$

To consider the influence from the distribution of wavelength of the light source on the light intensity of three-beam interference fringes, we should take the item $N$ in Eq 2.3.33 as the function of $\lambda$ and apply the distribution of wavelength, Eq 2.3.41 to Eq 2.3.33, leading to the light intensity function $L(\lambda)$ being

$$L(\lambda, h_{droplet}) = \int N(\lambda)\, cos\left[\frac{2\pi}{\lambda}\left(2 n_{droplet} h_{droplet}\right) - \theta(\lambda)\right] + I_{\alpha_1}(\lambda)\, d\lambda \tag{2.3.42}$$

Here I solve the integral in Eq 2.3.42 numerically in Matlab, shown in Appendix 1.1. From the properties of a normal distribution, the area of the light intensity in Fig 2.3.41 located within $(\psi - 3\sigma, \psi + 3\sigma)$ accounts for 99.74% of the entire region [153] [154]. Therefore, in the numerical analysis, the wavelength range of the light source is defined within $(453.06, 476.94)$ with the step set at 1 nm. The result, presented in Fig 2.8, shows that the offset due to the distribution of the light source is 7.00 nm approximately.

The values of the offset vary for different solvents, since they have different refractive indices and thus different light intensities of reflection and transmission which contribute to $I_{\alpha 1}$ and $I_{\alpha 2}$; however, the values are relatively small compared

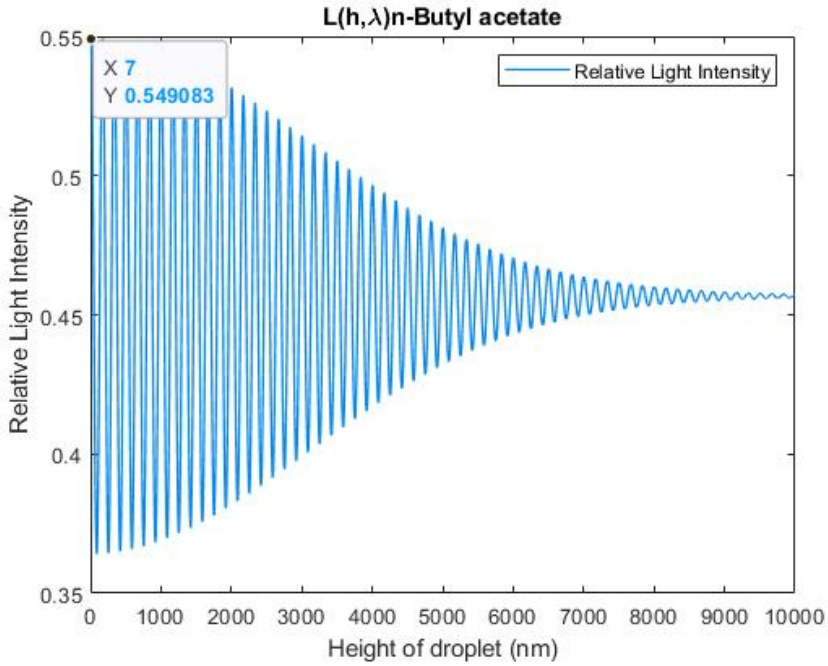


Figure 2.8: Numerical result of the light intensity of three-beam interference: the offset due to the distribution of the light source is 7.00 nm.

with the height difference between the adjacent bright fringes, 167 nm for n-butyl acetate, shown in Eq 2.3.40. Hence, it is reasonable to ignore the offset induced by the thin ITO layer.

## 2.4 Profile Reconstruction and its Geometrical Features

With the high-speed camera in our setup, an evaporation process is recorded at a specific frame rate depending on the evaporation rate of a liquid droplet and its volume and can be divided into a series of images. To compare the light intensity at the points of a selected line between the different images, an in-house Matlab programme was developed, with which the profile of droplet is reconstructed. It is reasonable to assume the profile of a pure liquid droplet to be axisymmetric when the atmosphere and temperature of the substrate remain steady; however, in the case of a mixture of binary solvent droplet or other more complex systems, such as polymer solution, to truly rebuild the profile, we should either choose the principal

directions of the profile as the scanning lines of analysis, if they exist, or analyse the whole region thoroughly.

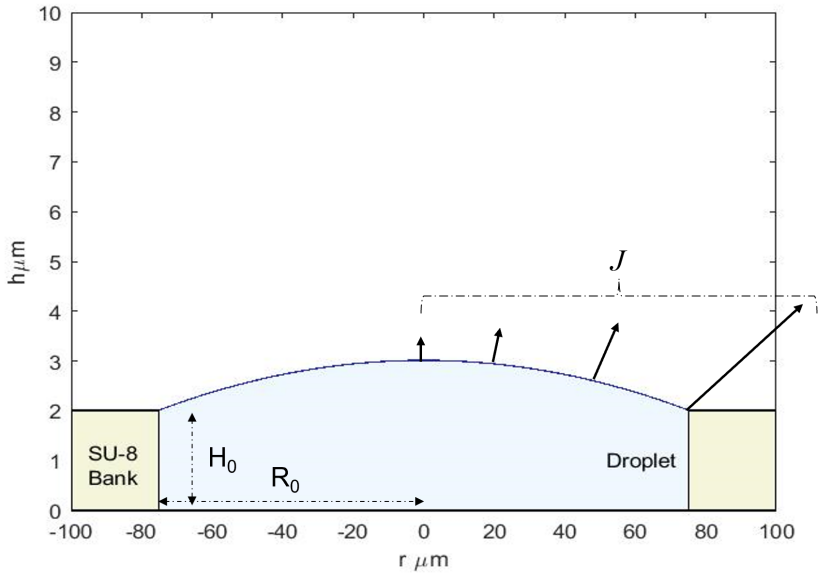


Figure 2.9: Schematic of an evaporating droplet with the coordinate applied in the study: the axis along the vertical direction is the axis of h and the axis along the horizontal direction is the axis of r, while $H_0$ and $R_0$ are the depth and radius of a well, respectively.

### 2.4.1 Profile Reconstruction

Because of the merit of the rotational symmetry of a cylinder with a flat base, during the evaporation of a picolitre droplet of pure solvent, the profile appears to be axisymmetric, so that we can facilitate the reconstruction of a profile by scanning the change of the light intensity on a line across the centre of the cylinder and rotating the height profile around h-axis, as shown in Fig 2.9−2.10 in which the yellow line represents the scanning direction and the green circle is the brim of the cylindrical well.

Once the scanning direction is chosen, the light intensity along this direction within the circle at different moments will be read. Based on the analysis in the preceding section, the change of light intensity at a point is well-fit with a sinusoidal function. Thus, by counting the number of peaks or valleys on a light intensity curve and taking into account the offset due to the influence from the thin ITO layers, the

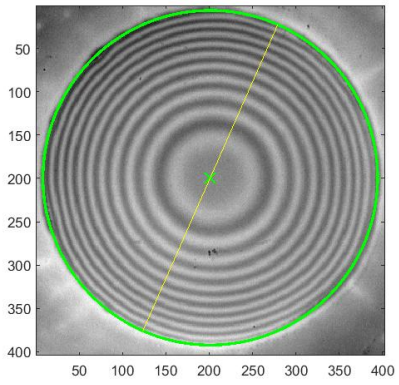


Figure 2.10: Line-scanning mode to reconstruct a profile: the yellow line inside the green circle, which is the brim of the cylindrical well, is a scanning line used to reconstruct the profile of this droplet.

height profile at a point is reconstructed.

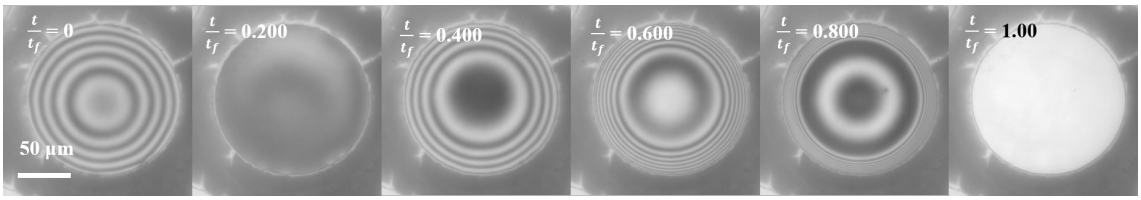


Figure 2.11: An example of a droplet evaporating in a cylindrical well: n-butanol droplet evaporating at the different moments, $t/t_f = 0$, 0.200, 0.400, 0.600, 0.800 and 1.00, respectively, where $t/t_f = 0 (t = 0)$ is the first moment when fringes are recognisable, while $t_f$ is the moment when a droplet dries up. The radius and depth of the cylindrical well are 75.0 $\mu$m and 1.53 $\mu$m, respectively.

The profiles of the droplet shown in Fig 2.11 are reconstructed and presented in Fig 2.12, for the case of an n-butanol droplet evaporating in a cylindrical well with the radius and depth being 75.0 $\mu$m and 1.53 $\mu$m, respectively.

In Fig 2.12, the red bold lines are the brims at either side, while the asterisks with different colours represent the profiles at different moments with a constant time interval. The data clearly illustrate that the emergence of a peak at the centre (the yellow asterisks in Fig 2.12), when the height at the centre is 0.40 $\mu$m.

An example of rebuilding a 3D contour of the W-shaped profile in Fig 2.12 is shown in Fig 2.13, at the time $t = t_d$ when the n-butanol droplet just touched down at the base of its host cylindrical well. As shown in Fig2.13, W-shaped profile has a peak at the centre $r = 0$ with a valley located in $0 < r < R_0$. More details of

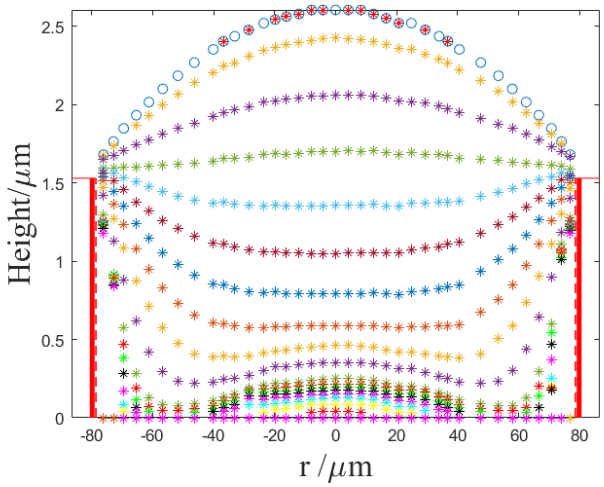


Figure 2.12: The 2D results of n-butanol droplet evaporating at different moments: the blue circle dots at the top is the height profile at the initial moment $t = 0$ and the red asterisks at the bottom is the result when the droplet is about to dry up; the time difference between the blue dots and the red asterisks is 0.1 ($t_d$) in which $t_d$ is the moment when the droplet touches down at the base.

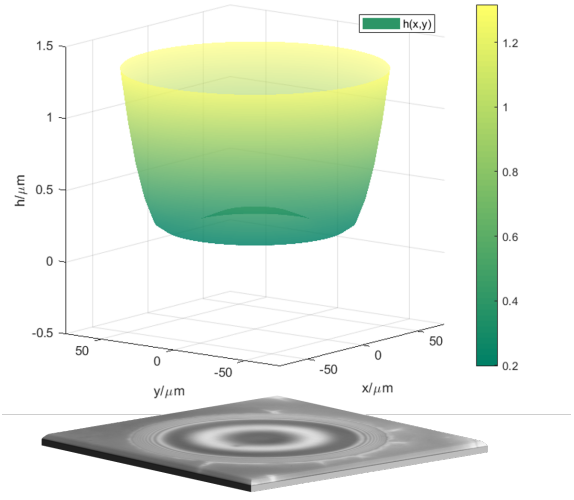


Figure 2.13: 3D visualisation of the n-butanol droplet at the touch-down moment, $t_d$, created by rotating the 2D line around the z-axis.

W-shaped profiles will be presented in Chpt 3 where I also illustrate the difference between a W-shaped profile and the other shapes.

Another way of displaying the evolution of a height profile at different moments is shown in Fig 2.14, where the surface of $\mathbf{h}(t, r)$ shows the evolution of a W-shaped profile in the region of $-R_0 < r < R_0$ until the touch-down moment.

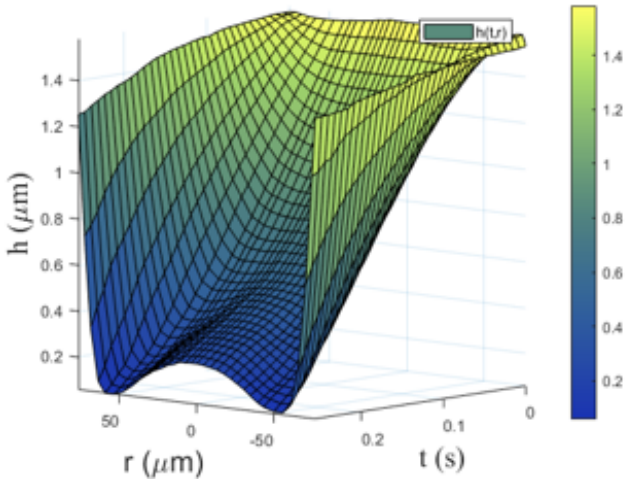


Figure 2.14: The height evolution of a n-butanol droplet, denoted as the surface of $\mathbf{h}(r, t)$.

### 2.4.2 Geometrical Features of a Droplet Profile

For pure solvent droplets, profiles appear to be axisymmetric when the thermal effect is absent and the container has circular symmetry; as a consequence, the profiles are similar to surfaces of revolution. To analyse the geometrical properties of a surface, the surface of revolution is first developed in a cylindrical coordinate system shown in Fig 2.15 where $u$ and $r$ are the azimuthal and cylindrical axis, respectively. The parametrisation of the surface of revolution, $\mathbf{h} = \mathbf{h}(r, u)$, is

$$\mathbf{h} = \begin{cases} x = r\ cosu & u \in [0, 2\pi) \\ y = r\ sinu & r \in [0, R_0] \\ z = h(r) & \end{cases} \tag{2.4.1}$$

where $h(r)$ is the expression of the rotating curve on the xy-plane.

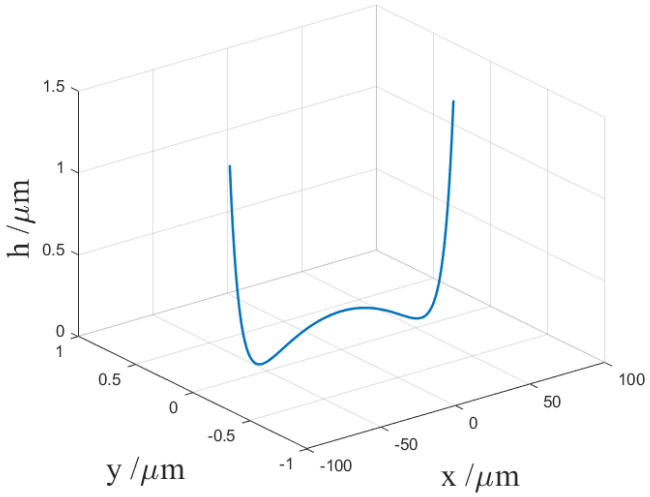


Figure 2.15: A cylindrical coordinate system applied to construct a surface of $\mathbf{h}\,(r, u)$: the transformation from a Cartesian coordinate system to the cylindrical coordinate system in the study.

From the parametrisation shown in Eq 2.4.1, the tangent vectors at a point are

$$\mathbf{h}_r = \Big(cos\ u,\ sin\ u,\ h^{'}\,(r)\Big) \tag{2.4.2a}$$

$$\mathbf{h}_u = (-r\ sin\ u,\ r\ cos\ u,\ 0) \tag{2.4.2b}$$

in which $\mathrm{h}^{'}\,(r)$ is the first derivative of $\mathrm{h}(r)$, while the outward-pointing unit normal vector of the surface is

$$\mathbf{N} = \frac{\mathbf{h}_r \times \mathbf{h}_u}{|\mathbf{h}_r \times \mathbf{h}_u|} = \frac{\big(-h^{'}\,(r)\,cos\ u, -h^{'}\,(r)\,sin\ u, 1\big)}{\left(1 + h^{'2}\,(r)\right)^{\frac{1}{2}}} \tag{2.4.2c}$$

Since the principal directions of the surface of revolution are along its meridians and parallels [155] [156], which are the lines of curvature of the surface, the principal curvatures, $k_1$ and $k_2$, of the surface are the normal curvatures along the meridians and parallels. The rotating curve itself in Fig 2.15 is a meridian of the surface of revolution; meanwhile, a cross-section on a surface parallel to the xy-plane is a parallel of the surface of revolution.

$$k_1 = \begin{cases} \frac{h'}{r\left(1+h'^2\right)^{1/2}} & r \neq 0 \\ h'' & r = 0 \end{cases} \tag{2.4.3a}$$

$$k_2 = \frac{h''}{\left(1+h'^2\right)^{3/2}} \tag{2.4.3b}$$

$$H = \frac{k_1 + k_2}{2} = \begin{cases} \frac{h'\left(1+h'^2\right)+rh''}{2r\left(1+h'^2\right)^{3/2}} & r \neq 0 \\ h'' & r = 0 \end{cases} \tag{2.4.3c}$$

$$K = k_1 k_2 = \begin{cases} \frac{h'h''}{r\left(1+h'^2\right)^2} & r \neq 0 \\ h''^2 & r = 0 \end{cases} \tag{2.4.3d}$$

$h'$and $h''$ are the first and second derivative of $h(r)$, respectively, while $H$ and $K$ are the mean curvature and Guassian curvature, respectively.

The aspect ratios of the cylindrical wells in this study range from 0.02 to 0.04, while the height of a droplet at a point evolves between 0 and 3 $\mu$m; therefore, the first derivative of $h\,(r)$, $dh/dr$, is at the scale of $5 \times 10^{-3}$ ,which is far smaller than 1, so that the values of $(1+h'^2)^{1/2}, (1+h'^2)^{3/2}$ and $(1+h'^2)^2$ can be approximately taken as 1 in my study, indicating that lubrication approximation is valid in the further analysis.

The signs of the principal curvatures are decided by the properties of a curve, such as slope and concavity that are the geometrical appearance of a function; in addition, the sign of mean curvature depends on the first and second derivative at a point. In the case of $r \neq 0$, the mean curvature is $(h'/r + h'')/2$ approximately; however, the mean curvature at the centre is always equal to $h''$ for pure droplet, as the first derivative is 0, leading to the result that the height profile at the centre always behaves like an umbilical point [155], where $k_1 = k_2$ holds, on a sphere, as long as it is axisymmetric.

Because of the axisymmetry of a cylindrical well, the profile from an evaporating droplet of pure solvent is axisymmetric if there is no thermal Marangoni effect [144]. In the following chapters, the different shapes of menisci of evaporating droplets in cylindrical wells with different aspect ratios are investigated with the perk of the

axisymmetry of a cylindrical well.

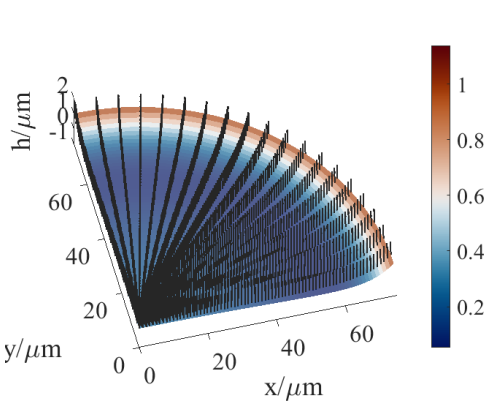


(a) Unit normal vectors on the surface shown in Fig 2.13.

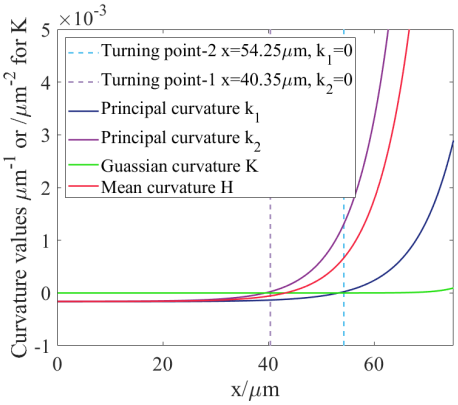


(b) Geometrical properties of the surface presented in Fig 2.13.

Figure 2.16: The normal vectors and the geometrical properties of the reconstructed surface shown in Fig 2.13: (a): normal vectors on the revolution surface (black arrows pointing upwards (from the liquid phase to its vapour phase); (b): geometrical features of a W-shaped profile - principal curvatures, mean curvature and Gaussian curvature - showing that there are three regions divided by the purple and blue dashed lines; the region on the left of the purple dashed line is the area where both principal curvatures are negative; the area in the middle between the dashed lines is where $k_1 < 0$ and $k_2 > 0$; meanwhile, the principal curvatures are both positive on the right of the blue dashed line.

The Laplace pressure is the pressure difference on the two sides of a curved surface [87] [157] [158] [159], and it is expressed as

$$p_L = -2\gamma H = \Delta p \tag{2.4.4}$$

where

$$\Delta p = p_{in} - p_{out} \tag{2.4.5}$$

Surface tension of a pure droplet is the same everywhere on the surface so that the value of mean curvature shows the direction of an internal flow caused by the Laplace pressure, which is proportional with mean curvature.

For example, the geometrical results of the surface presented in Fig 2.13 are given Fig 2.16 which shows the unit normal vectors of the surface in Fig 2.16a and the results of the curvatures in Fig 2.16b which shows two turning points in the range of

$0 \leq r \leq 75.0$ $\mu$m of $k_1$ and $k_2$, respectively; at the first turning point, $r = 40.3$ $\mu$m in Fig 2.16b is where $h'' = 0$ so that $k_2 = 0$, while at the second turning point, $r = 54.3$ $\mu$m, we have $h' = 0$, so that $k_1 = 0$ holds. The point where $H = (k_1 + k_2)/2 = 0$ is at $r = 43.1$ $\mu$m.

The change of the mean curvature on the W-shaped profile along the direction of r-axis shows that the pressure inside the droplet at the centre is largest, while it is the lowest at the brim of the host well. Hence, the pressure difference inside the droplet generates an internal flow, capillary flow, to resist the deformation of a W-shaped profile from a normal meniscus shape.

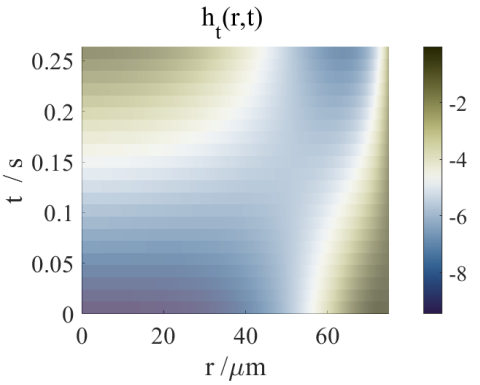


(a) The theoretical result of the first partial derivative of the surface $\mathbf{x}(t, r)$ at the direction of $t$.

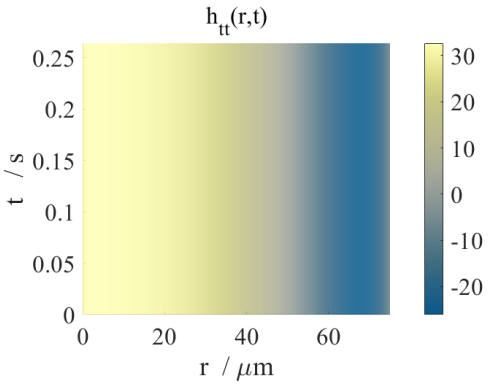


(b) The theoretical result of the second partial derivative of the surface $\mathbf{x}(t, r)$ at the direction of $t$.

Figure 2.17: The theoretical results of the reconstructed surface, $\mathbf{x}(t, r)$ in which $-R_0 \leq r \leq R_0$ and $0 \leq t \leq t_d$, shown in Fig 2.14: (a): the value of $\partial_t h$ increases from the centre to the brim at $t = 0$ s, but decreases from the moment $t = 0.13$ s which means the meniscus begins to be W-shaped with a dimple near the centre; (b): the values of $\partial_{tt} h$ at different locations stay unchanged as the profiles along the direction of t are best-fit with parabolas and it is 0 at the point $r = 51.1$ $\mu$m, suggesting that the height evolves linearly at this point.

Though the result shown above provides the geometrical features at a moment, to understand the evolution of a profile and achieve evaporation rate, the surfaces of $\mathbf{x}(t, r)$ of a profile is helpful. Owing to the axisymmetry, the function of a height profile is even, namely $h(r) = h(-r)$, so that the region where $r \geq 0$ $\mu$m is chosen to be researched. In addition, the derivative of the curvature of $\mathbf{x}(t, r)$ along the direction of $r$-axis at each point reflects the velocity field inside a droplet so that the experimental data can be connected with the simulation results when experiments,

such as particle-tracing velocity, are difficult to carry out. As regards lopsided profiles, $\mathbf{x}(t,r)$ on the principal directions may be critical to analyse so that the degree how askew a lopsided profile is, can be quantitatively understood.

Here I treat the function of $\mathbf{x}(t,r)$ as a regular surface to illustrate the method developed to analyse the non-axisymmetric profiles of binary solvent droplets in Chpt 4. The normal vector on the surface $\mathbf{x}(t,r)$ is only valid when the items $h_t^{'}$ and $h_r^{'}$ are non-dimensionalised, since they have different units .

First, the surface of $\mathbf{x}(t,r)$, as shown in Fig 2.14 is parameterised as

$$\mathbf{x} = \begin{cases} t = t \quad t \in [0, +\infty) \\ r = r \quad r \in [-R_0, R_0] \\ z = h\,(t,r) \end{cases} \tag{2.4.6}$$

the corresponding tangent vectors at $t$ and $r$ directions are

$$\mathbf{x}_t = \left(1, 0, h_t^{'}\right) \tag{2.4.7}$$

$$\mathbf{x}_r = \left(0, 1, h_r^{'}\right) \tag{2.4.8}$$

where $h_t^{'}$ denotes $\partial h/\partial t$, while $\mathrm{h}_r^{'}$ denotes $\partial h/\partial r$. And its normal vector is

$$\mathbf{N}_x = \frac{\left(-h_t^{'}, -h_r^{'}, 1\right)}{\left(1 + h_t^{'2} + h_r^{'2}\right)^{1/2}} \tag{2.4.9}$$

where the subscript, $x$, only denotes the surface that the unit normal vector belongs to. Therefore, according to the first and second fundamental forms of surfaces [155] [160], the mean curvature $H_x$ and Gaussian curvature $K_x$ are obtained as

$$H_x = \frac{1}{2}\nabla \cdot \frac{\nabla h}{\sqrt{1 + (\nabla h)^2}} \tag{2.4.10}$$

$$= \frac{\left(1 + h_t^{'2}\right)^2 h_{rr} + \left(1 + h_r^{'2}\right)^2 h_{tt} - 2h_t^{'}h_r^{'}h_{tr}}{2\left(1 + h_r^{'2} + h_t^{'2}\right)^{3/2}} \tag{2.4.11}$$

$$K_x = \frac{h_{tt}h_{rr} - h_{tr}^2}{\left(1 + h_r^{'2} + h_t^{'2}\right)^2} \tag{2.4.12}$$

where

$$h_{tt} = \frac{\partial^2 h}{\partial t^2} \qquad h_{tr} = \frac{\partial^2 h}{\partial r \partial t} \qquad h_{rr} = \frac{\partial^2 h}{\partial r^2} \tag{2.4.13}$$

The principal curvatures of the surface $\mathbf{h}(t, r)$ are given by

$$k_x = H_x \pm \sqrt{H_x^2 - K_x} \tag{2.4.14}$$

The subscript, $x$, in $H_x$, $K_x$ and $k_x$ only denotes the surface which these curvatures belong to, in order to distinguish the properties on the surface $\mathbf{x}$ from the surface $\mathbf{h}$. It can be seen that the numerator of Gaussian curvature is the Hessian matrix of $h(t, r)$, that is

$$\begin{vmatrix} h_{tt} & h_{tr} \\ h_{rt} & h_{rr} \end{vmatrix} \tag{2.4.15}$$

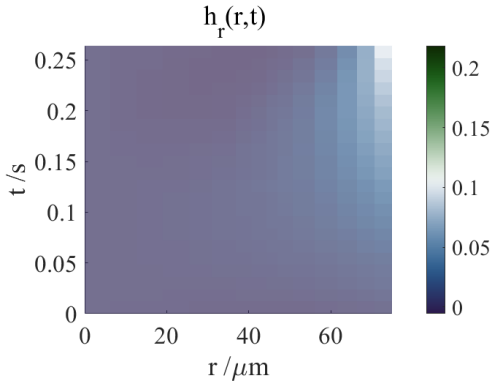


(a) The theoretical result of the first partial derivative of the surface $\mathbf{x}(t, r)$ on the direction of $r$.

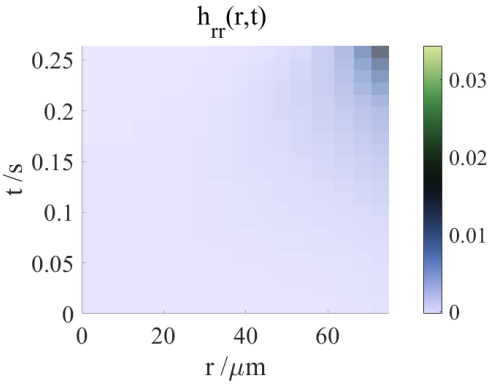


(b) The theoretical result of the second partial derivative of the surface $\mathbf{x}(t, r)$ on the direction of $r$.

Figure 2.18: The theoretical results of the reconstructed surface, $\mathbf{x}(t, r)$, shown in Fig 2.14: (a): the value of $\partial_r h$ at the majority points are small except at the area near the brim of the well where $r = 75.0$ $\mu$m, which shows that the influence of mean curvature on the internal flow is not negligible near the edge especially when the droplet is about to touch down; (b): the values of $\partial_{rr} h$ at the most places are small except near the brim of the well when the droplet is about to touch down.

The geometrical results of the surface, $\mathbf{x}(t, r)$, shown in Fig 2.14 are presented in Fig 2.18 and Fig 2.17. In Fig2.17a, $\partial_t h$ at the point $r = 0$ $\mu$m becomes smaller while the droplet is evaporating; however, as the droplet is pinned at the contact line, the

value of $\partial_t h$ around the point $r = 75.0$ $\mu$m is a constant; at the point $r \approx 50.0$ $\mu$m, the value of $\partial_t h$ almost stays the same value, $-5.00$ $\mu$m/s approximately, so that the decreasing tendency acts like a line, as is indicated in Fig 2.17b.

The partial derivatives along the direction of $r$ are shown in Fig 2.18. In Fig 2.18a, the value of $\partial_r h$ at $r = 0$ is zero since the centre is a local extrema for a W-shaped profile, but, according to the result, the value of $\partial_r h$ near the brim grows larger and larger as the droplet evaporates, which results from the dominance of surface tension and the depletion of the liquid in the well. The results of the second derivatives in Fig 2.18b suggest that the impact from the curvatures becomes stronger and stronger so that the Laplace pressure grow more and more powerful, while the droplet is evaporating.

The mean curvature and Gaussian curvature involve the calculations among the items: $h_r$, $h_t$, $h_{tr}$, $h_{rr}$ and $h_{tt}$. The method applied to analysis the surface $\mathbf{x}(t, r)$ may also be useful for the profiles which are non-axisymmetric.

For the curve $r = 0$ on the surface $\mathbf{x}(t, r)$, namely $\mathbf{x}(0, r)$, the curvatures of the curve along the r-direction are equal to the curvatures of the curves shown in the analysis of the surface $\mathbf{h}(r, u)$; and the curvature on the other direction, the direction of $t$, is the height changing tendency during the evaporation.

The value of evaporation rate $dV/dt$ is calculated by reconstructing a height profile at a moment and the ratio of volume against time.

$$\frac{dV}{dt} = \frac{\int_0^R 2\pi r h(r,t)\, dr}{\partial t} = \int_0^R 2\pi r \partial_t h(r,t)\, dr \tag{2.4.16}$$

Further analysis about evaporation rate is presented in Chpt 3.

## 2.5 Error Analysis of Binary Solvent Systems

The refractive index of a binary droplet changes as the components evaporate at different rates. In terms of a binary mixture, here I assume the refractive index remains unchanged while a binary droplet is evaporating. This assumption is reasonable for the mixtures containing the components with similar refractive indices,

such as toluene and mesitylene, whose refractive indices are 1.4961 and 1.4994 [149], respectively, as shown in Table 2.1; however, when the refractive index of each component differs at a significant level, further analysis of the error in experiment should be conducted.

As far as a binary mixture is concerned, the value $n_{12}$ from Eq 2.5.1 is generally regarded as the refractive index of the mixture [161] [162], which ranges between the refractive indices of solvent 1, $n_1$ ,and solvent 2, $n_2$ [148] [152].

To estimate the typical error in an analysis process of a binary mixture, solvent 2 is assumed to be the less volatile one in the mixture of solvent 1 and solvent 2. According to Lorentz-Lorenz equation [152]

$$n_{12} = \sqrt{\frac{2\Psi + 1}{1 - \Psi}} \tag{2.5.1}$$

where

$$\Psi = \frac{n_1^2 - 1}{n_1^2 + 2}(1 - \phi_2) + \frac{n_2^2 - 1}{n_2^2 + 2}\phi_2 \tag{2.5.2}$$

the refractive index of binary solvent can be calculated. For example, a binary solvent system contains 90.00% n-butanol and 10.00% mesitylene counted in mass has the refractive index of 1.408.

Because of the existence of preferential evaporation in a binary mixture, the refractive index becomes closer to the less volatile solvent generally, with the loss of the more volatile solvent near the contact line. If solvent 2, which is assumed to be the less volatile solvent, has larger refractive index than solvent 1, the refractive index of the mixture increases while evaporating. For example, in the binary mixture of n-butanol and mesitylene, as n-butanol evaporates faster than mesitylene, the refractive index of the mixture becomes closer to mesitylene, namely $n_2 - n_{12}$ growing smaller as the evaporation occurs, as shown in Fig 2.19 in which the brick red line is the refractive index at the initial moment.

The height difference between two nearest fringes is given in Eq 2.3.40. Therefore, the height difference between two nearest fringes counted in the refractive index of

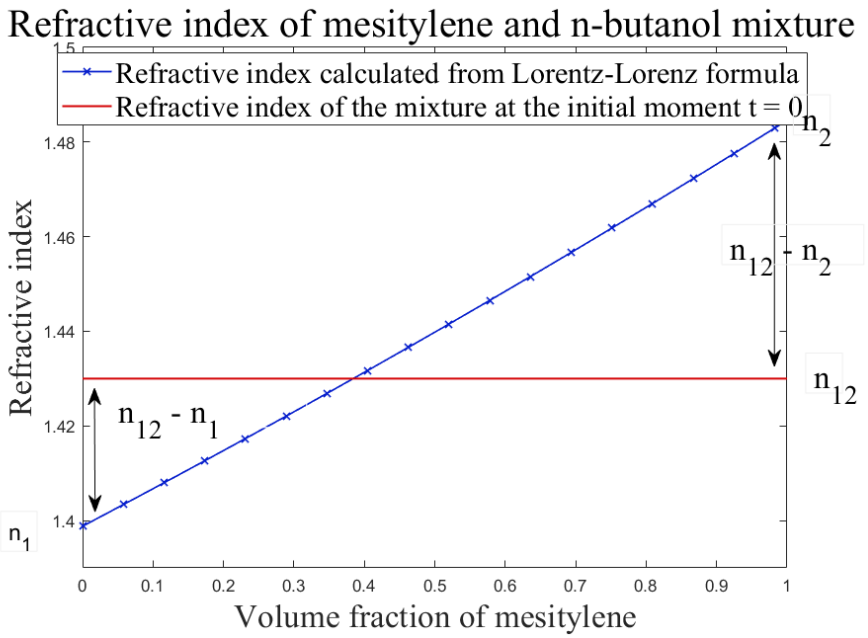


Figure 2.19: Refractive index of the binary mixture containing n-butanol and mesitylene.

a binary solvent mixture at the initial stage is $\Delta h_a$ as shown in Eq 2.5.3, while the height difference between two nearest fringes counted in the refractive index of the less volatile solvent in a binary mixture is $\Delta h_b$ presented in Eq 2.5.4.

The range of the error $\xi$ depends on the refractive index of a binary mixture at the initial moment and the refractive index of the less volatile component in it, as shown in Eq 2.5.5 which illustrates that the sign of $\xi$ hinges on the difference of refractive index between the solvents in a mixture. However, a negative error and a positive error with the same magnitude contribute the same extent so that we can only take the absolute value of the error to measure the degree of deviation.

$$\Delta h_a = \frac{\lambda_0}{2n_{12}^0} \tag{2.5.3}$$

$$\Delta h_b = \frac{\lambda_0}{2n_2} \tag{2.5.4}$$

$$\xi \leq \left|\frac{\Delta h_a - \Delta h_b}{\Delta h_a}\right| = \left|1 - \frac{n_{12}^0}{n_2}\right| \tag{2.5.5}$$

If a binary mixture contains 90.00% mesitylene and 10.00% n-butanol in mass, the height differences counted in the refractive index of the mixture at the initial stage, $\Delta h_a$, and the refractive index of mesitylene which is the less volatile solvent

in this case, $\Delta h_b$, respectively, are

$$\Delta h_a = \lambda_0 / 2 n_{12}^0 = 165.3\text{nm} \tag{2.5.6}$$

$$\Delta h_b = \lambda_0 / 2 n_2 = 155.1\text{nm} \tag{2.5.7}$$

Where $n_2$ and $n_{12}^0$ are 1.500 and 1.408, respectively. [149] Hence, the maximum of error, $\xi$, in the mixture of n-butanol and mesitylene is

$$\xi \leq \left| \frac{\Delta h_a - \Delta h_b}{\Delta h_a} \right| = 6.171\% \tag{2.5.8}$$

# CHAPTER 3

## Pure Solvents: W/U/C-shaped Profiles

In this chapter, the results of the evaporation of different pure droplets in cylindrical wells with different aspect ratios, including evaporation rate, shown in Sec 3.1, and the features of the height profiles, shown in Sec 3.3-3.5, illustrate the difference among W/U/C-shaped profiles. In addition, a parameter, $\Omega$, is proven effective to predict the shape of a profile.

In Sec 3.7.2, the impact from the temperature on the appearance of a profile, which is mainly due to the change of viscosity, surface tension and evaporation rate of a droplet, is investigated. The results show that the value of $\Omega$ increases with the rise of temperature; and droplets with C-shaped profiles are likely to show U-shaped profiles in the higher temperature, while U-shaped profiles tend to be W-shaped profiles.

All the substrates were cleaned with acetone, IPA and ultrapure water for 1 min, 5 min and 5 min, respectively, while they were placed in an ultrasonic bath, before use. The chemicals were purchased from Alfa Aesar or Aldrich and printed without further purification. The properties of the solvents in this chapter are given in Table 3.1 where the vapour pressure and diffusion coefficient in air are used to calculate the theoretical evaporation rate of a solvent, while the viscosity and surface tension

| Solvent | Viscosity mPa s | Surface tension mN/m | Vapour pressure kPa | Diffusion coefficient in air $\times 10^2 cm^2/s$ | Producer |
|---|---|---|---|---|---|
| n-Butanol | 2.54 | 24.93 | 0.86 | 8.61 | Sigma-Aldrich (99.9%) |
| n-Butyl acetate | 0.685 | 24.88 | 1.66 | 6.72 | Sigma-Aldrich (99.7%) |
| Pentyl acetate | 0.865 | 25.17 | 0.60 | 6.10 | Sigma-Aldrich (99.0%) |
| Toluene | 0.560 | 27.93 | 3.79 | 8.49 | Sigma-Aldrich (99.9%) |
| Anisole | 1.06 | 35.10 | 0.47 | 7.29 | Alfa Aesar (99.9%) |
| Mesitylene | 0.600 | 27.55 | 0.33 | 6.63 | Alfa Aesar (98.0%) |
| P-xylene | 0.603 | 28.01 | 1.19 | 6.70 | Alfa Aesar (99.9%) |
| Methyl benzoate | 1.88 | 37.17 | 0.05 | 6.47 | Sigma-Aldrich (99.0%) |

Table 3.1: Solvent properties including viscosity, surface tension, vapour pressure and diffusion coefficient in air. [149] [163]

are used to calculate the capillary number.

For a pure solvent, if the atmosphere is stable, which means no strong air flow over a droplet or acute temperature change on a substrate occurs in an experiment, there are three different sorts of shapes emerging, namely C-shaped profile, U-shaped profile and W-shaped profile; C-shaped profile is well-fit with a spherical cap and remains concave up at the centre of the well until the droplet touches down at the base at $r = 0$, and this shape is like a meniscus at the macroscopic scale. The U-shaped profile also keeps concave up till the droplet touches down at the centre of base, but the U-shaped profile has a flattened bottom like a round bowl. The W-shaped profile is concave down at the centre with two local minima in a cross section of the profile, showing the similarity to the appearance of the letter W.

Besides the appearance of the different profiles from the experiment result, in this chapter, a parameter, denoted as $\Omega$, interpreted as the scaled inverse capillary number [95], is also shown effective to predict the shapes of the different profiles. We show that a parameter $\Omega = \epsilon^4/Ca$, where $\epsilon$ is the aspect ratio of a well while $Ca$ is the capillary number, determines the profile of a droplet evaporating in a cylindrical well.

## 3.1 Evaporation Rate of a Pure Solvent Droplet in a Cylindrical Well

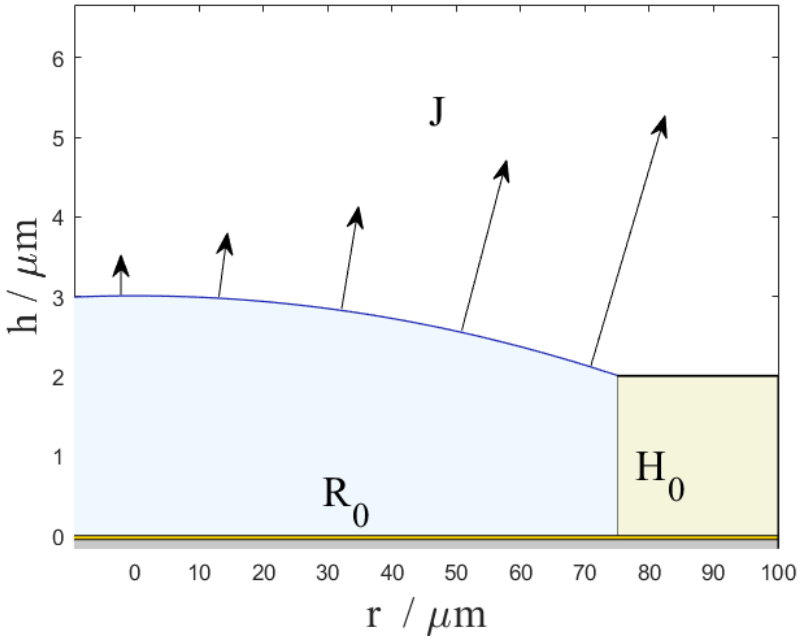


Figure 3.1: Schematic of an evaporating droplet in a well. $R_0$ and $H_0$ are the radius and depth of a cylindrical well, respectively, while $J$ is the evaporation flux from the liquid phase into the vapour phase.

We assume that the contact line of a droplet in a cylindrical well remains pinned at the brim of the well until the droplet touches down at the base. At this point, one, if the droplet touches down at $r = 0$, or two new contact lines, if it touches down at $r \neq 0$, emerge. These new contact lines change the profile of the evaporative flux [142].Despite being printed in a well, a droplet in a shallow well can be treated mathematically in the same way as a thin evaporating sessile droplet whose contact line is pinned at $r = R_0$.

Evaporation process is often taken as a matter flow diffusing along the direction of the normal vector on its surface, as explained by Fick's first law [87] [164]:

$$\mathbf{J} = -D\nabla N \tag{3.1.1}$$

$$\mathbf{J}_m = -D_m \nabla c_m \tag{3.1.2}$$

where $N$ is the number density of particles with units number per metre cubed [87], $D$ is the diffusion coefficient, $\mathbf{J}_m$, the unit of which is $\mathrm{kg{\cdot}m^{-2}{\cdot}s^{-1}}$, is the flux of matter counted in mass, $D_m$ is the diffusion coefficient counted in mass and $\nabla \mathrm{c}_m$ denotes the concentration gradient in a space, whose unit is $\mathrm{kg{\cdot}m^{-4}}$. The strength of a flux indicates how strong a diffusion process is and its direction is always pointing towards lower concentration, as indicated by the negative sign in Eq 3.1.2.

The evaporation rate can be defined as opposite number of the mass loss per unit time, $-dm/dt$, which can be expressed by a mass flux whose direction is from the liquid phase to the vapour phase on an interface along the normal vector; therefore, the flux counted in mass $\mathbf{J}_m$ travelling through the surface of a droplet is linked to the evaporation rate as

$$-\frac{dm}{dt} = \iint_S \mathbf{J}_m \cdot d\mathbf{S} = \iint_S \mathbf{J}_m \cdot \mathbf{n} dS \tag{3.1.3}$$

Inspired by the experiment of iodine spheres placed in air by Morse [75], Langmuir illustrated that the evaporation rate of a sphere was proportional to its radius as well as the vapour pressure and diffusion coefficient of the vapour and the inverse of the thermodynamic temperature of the atmosphere: [165]

$$-\frac{dm}{dt} = \frac{4\pi R D M_w p_v}{R_c T_c} \tag{3.1.4}$$

The result achieved by Langmuir is similar to Hu and Larson's conclusion [1] [2] which is deduced with the analytic theory and computed by finite element method, FEM. Hu and Larson investigated the evaporation rate of a water droplet with the shape analogous to a spherical cap and summarised the expressions of evaporation rates when the contact angles are $\pi/2$ and 0, respectively, as shown in Eq 3.1.5−3.1.6.

$$-\frac{dm}{dt} = 2\pi D \left(1 - R_h\right) c_v R_0 \qquad \theta \sim \frac{\pi}{2} \tag{3.1.5}$$

$$-\frac{dm}{dt} = 4D \left(1 - R_h\right) c_v R_0 \qquad \theta \sim 0 \tag{3.1.6}$$

where $c_v$ denotes the concentration by mass of the vapour phase at the liquid surface, and $R_c$ are gas constant. If the perfect gas law holds [87], then for a thin droplet whose contact angle is $\theta \sim 0$, Eq 3.1.6 becomes

$$c_v = \frac{p_v}{R_c T_c} M_w \tag{3.1.7}$$

$$-\frac{dm}{dt} = \frac{4D\,(1 - R_h)\,R_0\;p_v M_w}{R_c T_c} \qquad \theta \sim 0 \tag{3.1.8}$$

where $T_c$ is the temperature of atmosphere and $M_w$ is molecular weight. Written in the volume loss rate, evaporation rate is expressed as

$$-\frac{dV}{dt} = \frac{4D\,(1 - R_h)\,R_0\;p_v M_w}{R_c T_c\;\rho} \qquad \theta \sim 0 \tag{3.1.9}$$

for thin droplets placed on a flat substrate with its contact line pinned. Hence, the evaporation rate per area for a thin droplet with contact pinned is

$$E_0 = -\frac{dV}{dt}\frac{1}{\pi R_0^2} = \frac{4D\,(1 - R_h)\,p_v M_w}{R_c T_c\;\rho \pi R_0} \qquad \theta \sim 0 \tag{3.1.10}$$

where $R_c$, $R_0$ and $R_h$ are the gas constant, the radius of the well and the concentration of the substance in its vapour phase to the saturated vapour concentration. The value of $R_h$ is regarded 0 in my experiments and analysis as there is no source.

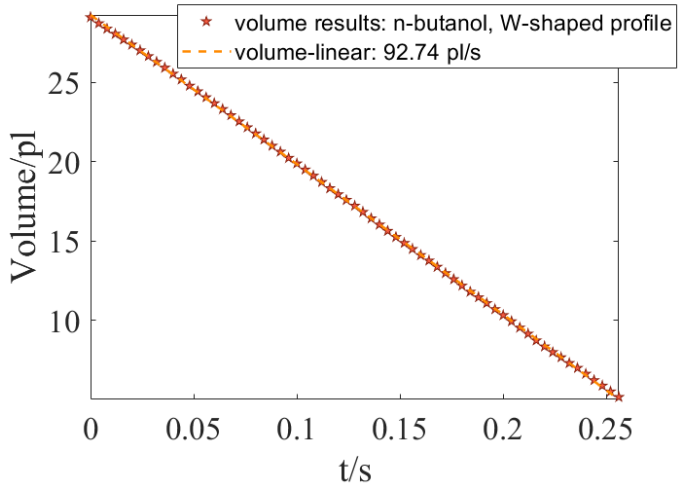


Figure 3.2: The volume change of an n-butanol droplet evaporating in a well with radius and depth being 75.0 $\mu$m and 1.53 $\mu$m, respectively.

For droplets evaporating in cylindrical wells, the experimental results verify that the evaporation rate of a droplet of pure solvent is constant; one of the examples is shown in Fig 3.2 in which the evaporation rate of n-butanol is at 94.7 pl/s.

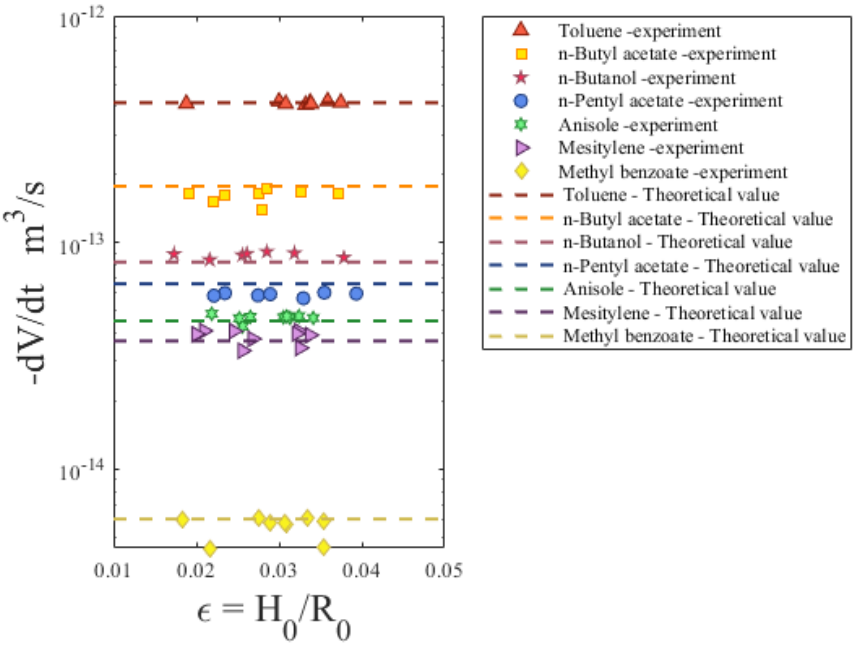


Figure 3.3: Evaporation rate of the solvents used in this chapter and its theoretical value calculated from Eq 3.1.9: theoretical prediction well-matched with its experimental results.

.

The theoretical results show that the depth of a well does not change the evaporation rate; however, the radius of a well significantly affect the evaporation rate; and fortunately the contact angle does not have much impact on the evaporation process in this work since the cylindrical wells are so thin with the aspect ratio less than 0.05.

To verify the theoretical evaporation rate shown in Eq 3.1.9, toluene, n-butyl acetate, n-butanol, pentyl acetate, anisole, mesitylene and methyl benzoate were chosen as the candidate solvents, the properties of which are shown in Table 3.1. The experimental results and the corresponding theoretical values are presented in Fig 3.3, which shows that the evaporation rate of these solvents in the wells with radius 75.0 $\mu$m are well-predicted by Eq 3.1.9, although there is some deviation for methyl benzoate (yellow diamonds) and n-butyl acetate (orange squares).

There are mainly two reasons for the deviation. First, evaporation is a process that reduces the temperature of a droplet since there exists expansion work arising from a change in volume decreasing the internal energy of the system, $\Delta U$ , which is connected with the temperature of a thermodynamic system, and the latent heat of the vaporisation of the liquid. The other reason is that the relative humidity may have an impact on a hydrophilic solvent such as n-butanol. However, the deviation between the theoretical prediction and the experiment remains negligible when the ranges of the ambient temperature and relative humidity, $RH$, are $21 \pm 0.5°C$ and $40\,\% \pm 0.5\,\%$, respectively.

## 3.2 Lubrication Approximation

According to the properties shown in Table 3.1 and the definition of the capillary length of a liquid, $l_c$ in Eq 3.2.1, the capillary lengths of the solvents range from 1.4 to 1.8 mm which is much higher than the depth or diameter of a cylindrical well in our experiment; therefore, the Laplace pressure, $p_L$, plays a vital role in evaporation and leads to the surface of a droplet remaining a cap-like shape when the influence from viscosity or gravity is negligible.

$$l_c = \sqrt{\frac{\gamma}{\rho g}} \tag{3.2.1}$$

where $\gamma$ and $\rho$ are the surface tension and density of a droplet, respectively, while $g$ denotes the acceleration due to gravity.

Considering that the aspect ratio of a well, $\epsilon \sim 2/75$, is much smaller than 1 and the inertial effect is negligible compared with viscous effect, $Re = \epsilon^2\,\rho\,u\,h/\mu \ll 1$, indicating that inertia is insignificant and the internal flow resembles to creeping flow [56] [74], it is reasonable to investigate the evaporation of a pure droplet in a

cylindrical well with the lubrication approximation [84].

$$\mu \frac{\partial^2 u}{\partial z^2} = \frac{\partial p}{\partial x} \tag{3.2.2}$$

$$\frac{\partial p}{\partial z} = 0 \tag{3.2.3}$$

$$\frac{\partial u}{\partial x} + \frac{\partial w}{\partial z} = 0 \tag{3.2.4}$$

or in the polar coordinate system as

$$\mu \frac{\partial^2 u}{\partial h^2} = \frac{\partial p}{\partial r} \tag{3.2.4}$$

$$\frac{\partial p}{\partial h} = 0 \tag{3.2.5}$$

$$\frac{1}{r}\frac{\partial (ru)}{\partial r} + \frac{\partial w}{\partial h} = 0 \tag{3.2.6}$$

To recover the characteristic properties of a system, the system is non-dimensionalised by

$$\left.\begin{array}{c} h' = \frac{h}{H_0} \quad r' = \frac{r}{R_0} \quad p' = \frac{\epsilon^3 R_0}{\mu E_0}(p - p_0) \\ u' = \frac{u}{U'} \quad w' = \frac{w}{\epsilon} \quad t' = \frac{U'}{R_0} t \end{array}\right\} \tag{3.2.7}$$

where $\epsilon = H_0/R_0$, the induced radial velocity is $U^{'} = E_0/\epsilon$, and $E_0$ is the average evaporation rate per area.

The Laplace pressure, $p_L = p - p_0$, is the only source of the pressure difference at the interface, relying on the surface tension of a liquid droplet as well as the mean curvature. The mean curvature in Eq 2.4.3c shows complexity along radius direction. Fortunately, as it is proved in Sec 2.4.2, the Laplace pressure at the centre of an axisymmetric droplet is $p_{L,r=0} = 2\gamma\ \partial^2 h/\partial r^2$; therefore, Eq 3.2.2 at the centre is non-dimensionalised to

$$\frac{\mu E_0}{\epsilon H_0^2}\frac{\partial^2 u'}{\partial h'^2} = 2\gamma \frac{H_0}{R_0^3}\frac{\partial^3 h'}{\partial r'^3} \tag{3.2.8}$$

since the pressure difference is caused by the Laplace pressure on the liquid-vapour interface. After moving the measurable items to the left hand side, Eq 3.2.8 turns

out as

$$\frac{E_0\mu}{\epsilon^4\gamma} = 2\frac{(\partial^3 h')/(\partial r'^3)}{\partial^2 u'/\partial h'^2} \tag{3.2.9}$$

$$\frac{1}{\Omega} = \frac{E_0\mu}{\epsilon^4\gamma} = Ca' \tag{3.2.10}$$

In this study, the item on the left hand side is defined as $1/\Omega$ which is also denoted as an enhanced droplet capillary number, $Ca'$ [93] [94], and is the combination of the properties of a well ($\epsilon$), the properties of a liquid ($\mu$ and $\gamma$) and the radius of a well ($E_0$ depends on the size of a well); while the item on the right hand side in Eq 3.2.9 suggests that the degree of $1/\Omega$ reflect the geometrical properties of a profile and the profile of its internal flow.

Here I choose $\Omega$, instead if $1.00/\Omega$, to compare the difference among profiles as is easier and more directly to notice the difference between 1.00 and 100 than the difference between 0.0100 and 1.00 although they represent the same difference of scale; also it is neater to have the figure 100 than 0.0100. Regarding the significant figure in the study, it is limited to 3 digits as the radius of a well measured by the profiler only bears 3 significant figures.

The value of $\Omega$, which also appeared in Kaplan and Mahadevan's work [95], reflects the competition between viscous forces and surface tension. Viscous force to drag fluid from moving is also known as internal friction opposing deformation of the liquid [56]; in the mean time, the pressure gradient over an interface due to surface tension drives the fluid moving towards an area with lower pressure.

With the non-dimensional scales shown in Eq 3.2.7, the velocity and the pressure are further deduced as

$$\frac{\partial u'}{\partial r'} = \frac{-h'^2}{3}\frac{\partial p'}{\partial r'} \tag{3.2.11}$$

$$p' = -\Omega\frac{1}{r'}\frac{\partial}{\partial r'}(r'\frac{\partial h'}{\partial r'}) \tag{3.2.12}$$

However, the velocity profile is too complicated to visualise in the experiment and the pressure on a surface is only possible to calculate from the curvature of a surface with a specific surface tension when droplet is at the scale of picoliter; hence,

this study mainly concentrates on the evolution of the height profile and attempts to find an effective way to predict the shape of a profile.

| Solvent | Viscosity mPa s | Surface tension mN/m | $-dV/dt$ pl/s | $R_0$ $\mu$m | $H_0$ $\mu$m | $\Omega$ | Profile |
|---|---|---|---|---|---|---|---|
| n-Butanol | 2.54 | 24.93 | 92.7 | 75.0 | 1.53 | 0.323 | W-shaped profile |
| n-Butanol | 2.54 | 24.93 | 92.6 | 75.0 | 2.63 | 2.83 | U-shaped profile |
| Methyl-benzoate | 1.88 | 37.17 | 4.57 | 75.0 | 2.66 | 124 | C-shaped profile |
| Mesitylene | 0.661 | 27.55 | 40.7 | 75.0 | 1.84 | 6.55 | U-shaped profile |
| Methyl-benzoate | 1.88 | 37.17 | 6.02 | 75.0 | 1.37 | 6.55 | U-shaped profile |
| n-Butyl-acetate | 0.690 | 24.88 | 65.9 | 50.0 | 1.77 | 6.80 | U-shaped profile |
| Mesitylene | 0.661 | 27.55 | 40.7 | 75.0 | 2.43 | 20.0 | U-shaped profile |

Table 3.2: Properties of n-butanol, n-butyl acetate and methyl benzoate and its host wells [149].

When the depth of a cylindrical well was 1.53 $\mu$m, the n-butanol droplet appeared to be a W-shaped profile; however, when the depth was 2.63 $\mu$m the profile was U-shaped; if methyl benzoate was chosen as the solvent in a cylindrical well with depth 2.66 $\mu$m, we found a C-shaped profile; U-shaped profiles from methyl benzoate, n-butyl acetate and mesitylene appeared when the values of its $\Omega$ were 6.60, 6.60, 20.0 and 6.80, respectively.

The experimental results suggest that the value of $\Omega$ is significantly linked to the evolution of a profile, as expected from the initial calculation shown above. Examples are given in Table 3.2: when $\Omega$ is 0.320 the profile is a W-shaped one; the U-shaped profile of n-butanol emerges at $\Omega = 2.80$, while the C-shaped profile appears at $\Omega = 124$. More details about the features of W-shaped profile, U-shaped profile and C-shaped profile are illustrated in the next few sections.

Apart from the comparison of the profiles with different shapes, the U-shaped profiles with $\Omega$ being 6.60 and 6.80 are chosen to consolidate the effectiveness of $\Omega$ in Sec 3.6.2, since the U-shaped profiles have the same evolution tendencies. More importantly, our experimental results of different solvents suggest that when $\Omega \leq 1.00$, a profile tends to be a W-shaped one and C-shaped profile emerges if $\Omega \geq 100$ , while U-shaped profiles is situated in the transition area between C-

shaped profile and W-shaped profile, with $1.00 \leq \Omega \leq 100$, as shown in Sec 3.7.1.

When a profile is identical to a spherical cap like a common meniscus does, defined as C-shaped profile in this study, $\partial^3 h'/\partial r'^3 = 0$ holds since the value of $\partial^2 h'/\partial r'^2$ is a constant anywhere at a moment; thus, $1/\Omega$ tends to be zero, namely a large value of $\Omega$, which reflects the extent of difference of a profile from a spherical cap. The larger the value of $\Omega$ is, the more similar a profile is to a spherical cap. On the other hand, $1/\Omega$ is associated with the viscous stress, $\mu\partial u/\partial r$, and ,therefore, $\partial w/\mu\partial h$ according to Eq 3.2.6.

Owing to $f_\tau = \mu\partial u/\partial h$ [56] [166] and $\partial f'_\tau/\partial h' = \mu\partial^2 u'/\partial h'^2 \sim 1/\Omega$, the value of $\Omega$ also represents the strength of a shear stress gradient, friction force [56], in an evaporating droplet. The larger an $\Omega$ is, the more uniform a shear stress will be.

The results listed in Table 3.2 are also further presented in Fig 3.21 in which W-region is where the profiles are W-shaped profile; U-region is mainly for profiles showing feature of a U-shaped profile, while C region is for profiles behaving like spherical caps. And the regions is divided by the evolution of the mean curvature of the profiles at the centre, $r = 0$, which will be shown in the next few sections.

## 3.3 C-shaped Profile

### 3.3.1 Definition of C-shaped Profiles

A spherical meniscus is usually found in a capillary tube when gravity is negligible and surface tension dominates which maintains the surface to reach the minimum area [88] [167]. Since the shape of a spherical meniscus and an offset C look alike, the menisci appearing to be spherical caps are named as C-shaped profile in this work. However, a C-shaped profile does not only emerge in a thin capillary tube, but also appears when a droplet evaporates in a thin shallow well [134] [141]. [142] [168].

Rieger and his colleagues reported C-shaped profiles of ethylene glycol droplets evaporating in the wells with depth being 6.0 $\mu$m and radii being 50 $\mu$m, 75 $\mu$m, 100 $\mu$m and 150 $\mu$m, respectively [141]; the corresponding values of $\Omega$ are 4295, 3038, 2026 and 1541.

All the $\Omega$'s are far larger than 1 while appearing C-shaped profiles, as we ex-

pected. They also found the height of a profile at the centre was best fit with a first-order polynomial and the evaporation rate of a ethylene glycol droplet was fixed during evaporation and increased linearly with the rise of the radius of a well. In addition, they pointed out that the linear dependency of evaporation rate on the radius of the well suggested the evaporation in a well was diffusion limited.

D'Ambrosio *et al.* also investigated C-shaped profiles of methyl benzoate droplets evaporating in the cylindrical wells with radii and depths being 29 $\mu$m, 50 $\mu$m and 75$\mu$m and 2.38 $\mu$m, 1.87 $\mu$m and 2.39 $\mu$m respectively [142]. However, in their work, the profiles are not assumed to be perfect spherical caps. Instead, they attempted to reconstruct the profiles with the amendment item $ln\, r$ in their height profile equations

$$h = c_1 r^2 + c_2 ln\ r + c_3 \tag{3.3.1}$$

where $r > 0$ and $c_1$, $c_2$ and $c_3$ are constants based on the initial and boundary conditions.

The values of $\Omega$ for the wells with the radii of 29 $\mu$m, 50 $\mu$m and 75 $\mu$m are 1518, 108 and 83 respectively. For the well with the largest radius, $r = 75$ $\mu$m, the profile appeared to deviate from a perfect spherical cap so that $c_2$ in their height profile equations in Eq 3.3.1, played a vital role in the result.

C-shaped profiles also found in the evaporation of water droplets in the well with depth and radius being 48 $\mu$m and 500 $\mu$m ,respectively [133]; furthermore, the results of Chen *et al*'s work showed that a water droplet seeded with microspheres of in a well left a ring-like deposit when the profiles were C-shaped during evaporation [168]. The ring-like deposit from a C-shaped profile suggests that the capillary flow was dominant in the internal flow.

However, it still remains unknown whether the profile of an evaporating droplet should leave a deposit with the similar shape; and, therefore, understanding the mechanism of the appearance of a profile lays the foundation for further manipulation of achieving a desired shape of a deposit.

### 3.3.2 Experimental Results of a C-shaped Profile

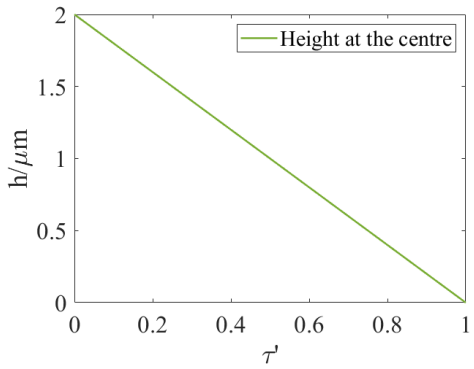


(a) The height at the centre of the C-shaped profile shown below decreasing linearly before touch-down.

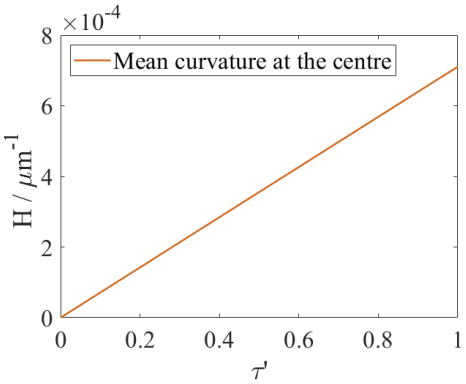


(b) The mean curvature increasing linearly at the centre of the C-shaped profile before touch-down.

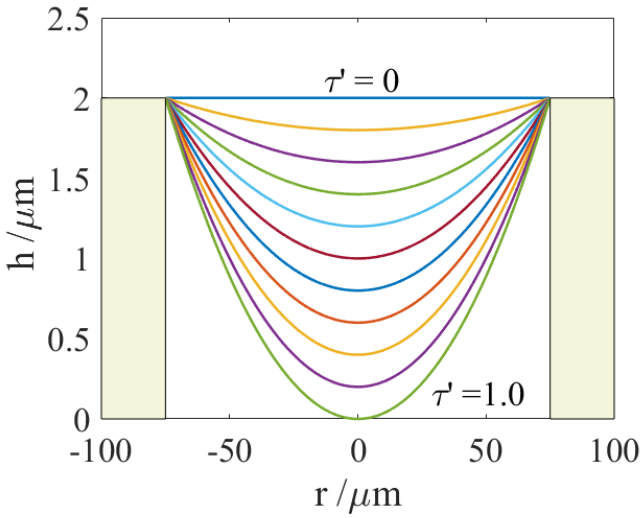


(c) The theoretical results of a C-shaped profile whose height at its centre decreases linearly with time counted by the characteristic time $\tau' = (t - t_{flat}) / (t_d - t_{flat})$ where $t_{flat}$ is the moment when the surface of a profile is a flat plane and equal to the depth of its host well.

Figure 3.4: The theoretical results of a C-shaped profile in which the radius and depth of the well are 75.0 $\mu$m and 2.00 $\mu$m, respectively.

The theoretical results of a droplet evaporating in a well with the radius and depth of the well being 75.0 $\mu$m and 2.00 $\mu$m, respectively, at different moments counted in the characteristic time $\tau'$, are presented in Fig 3.4c which shows the features of a C-shaped profile including:

(1) a profile remains spherical cap shape until it touches down;

(2) a droplet touches down at the base at the point $r = 0$ only;

(3) $h(r, t)$ decreases linear along the t-axis not just at $r = 0$ ;

(4) the mean curvature increases linearly with time. where $\tau' = (t - t_{flat})/(t_d - t_{flat})$ in which $t_{flat}$ and $t_d$ denote the moment when the profile of a droplet is flat and touches down at the base, respectively.

If a profile remains C-shaped until the touch-down moment with the height at the centre decreases linearly, which means the evaporation is diffusion-limited like what is reported in Rieger *et al*'s work [141], the mean curvature at the centre will rise linearly with time as is shown in Fig 3.4b.

Therefore, if a droplet evaporates in a cylindrical well with the process diffusion-limited, the evolution of the mean curvature at the centre is a sign to distinguish a C-shaped profile from the other two profiles, namely U-shaped profile and W-shaped profile.

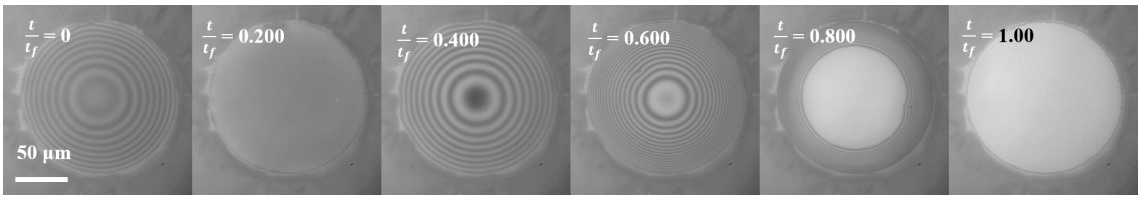


Figure 3.5: The evolution of methyl benzoate droplet, Ω of which is 124, at the different moments.

An example of the evolution of a C-shaped profile, details of which are in Table 3.2, is given in Fig 3.5 where $t_f$ is the duration of the evaporation process, also denoted as the final moment of an evaporation process and $t/t_f$ is the relative moment in the whole process.

The moment $t/t_f = 0$ is the initial moment of the evaporation, in which case the height at the centre of the droplet is higher than the depth of a well, leading to the shape to be a convex, while at the moment $t/t_f = 0.200$, the profile of a droplet is almost a flat plane whose height is nearly the same as the height of the well. Afterwards, the profile evolves like an expanding spherical cap with the height at the centre being the local minimum, as are shown at the moments $t/t_f = 0.400$ and $t/t_f = 0.600$; since the moment $t/t_f = 0.800$, the droplet has touched down at the base with a new contact line appearing in the centre and is receding towards the

brim of the well until it totally dries out at the moment $t/t_f = 1.00$.

According to the results by Rieger *et al*'s [141] and Hannah *et al*'s [142], the property of the base of a cylindrical well hardly contributes to the appearance of a profile before a droplet touches down; even so, the property of a base will influence the evaporation rate and the receding rate of the new contact line on the base, as is proven by Chen and his colleague [134] [168]. When a droplet touches down, the evaporation becomes more complex, as there is a new contact line expanding, which shifts the evaporation rate and is under the impact of the physico-chemical property of the base of a well. In addition, for the majority of an evaporation process in a well, the profile of a droplet is above the base and the deposit, if any, is mainly influenced by the profile before the touch-down moment. Therefore, the evolution of a profile before a droplet touches down is viewed as the core of an evaporation process in this study.

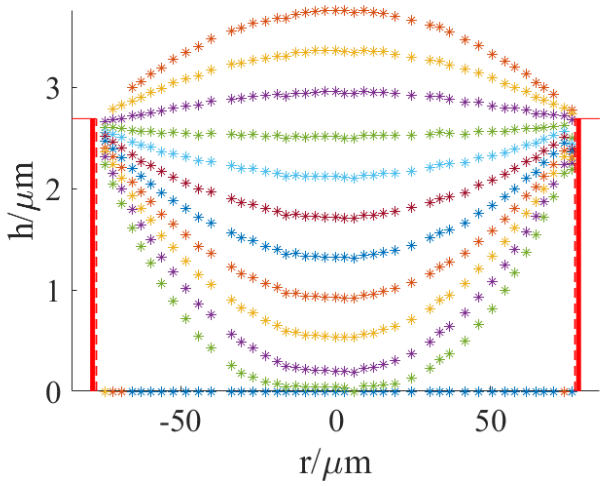


Figure 3.6: The profile of an evaporating methyl benzoate droplet in the well with depth and radius being 2.66 $\mu$m and 75.0 $\mu$m, respectively, while the value of $\Omega$ is 124.

The profile of a methyl benzoate droplet before the touch-down moment is presented in Fig 3.6. The red bold lines are the brim of the well. The top orange symbols in Fig are the result from the profile at the moment $\tau' = -0.466$, while the bottom green blue symbols represent the result at the moment $\tau' = 1.00$; the time difference is $0.147\tau'$ or 0.992 s.

The volume of the methyl benzoate droplet at different moments is shown in

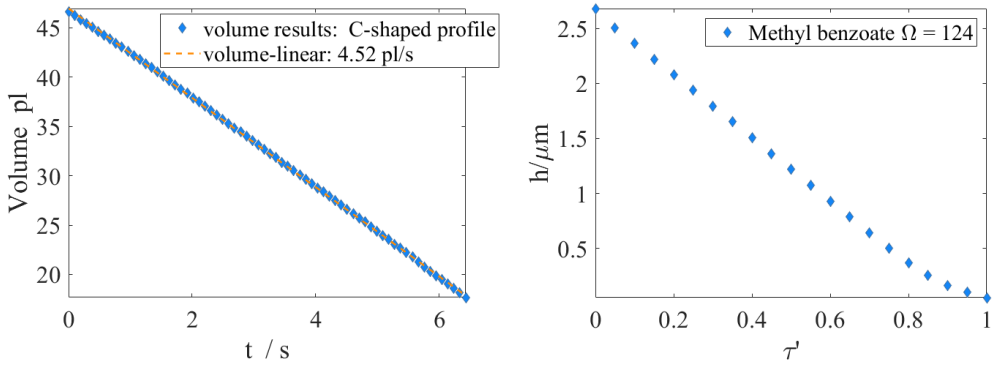


(a) The volume of the methyl benzoate droplet decreasing linearly with time at the rate of 4.57 pl/s.

(b) The height of the methyl benzoate droplet at the centre decreasing linearly with time before $\tau' = 0.900$.

Figure 3.7: The evolutions of the volume and height at the centre of methyl benzoate($\Omega = 124$).

Fig 3.7a which shows that the volume decreases linearly with time at the rate of 4.57 pl/s; therefore, the evaporation process is diffusion limited as Rieger *et al* or D'ambrosio *et al* found in their works [141] [142]. Also, the evolution of height at the centre is presented in Fig 3.7b, which shows that the height at the centre decreases linearly until the moment $\tau' = 0.900$ when the height at the centre is 0.160 $\mu$m; after then, the height falls less quicker than before, which may indicate that the viscous stresses become obvious that the liquid remain still. The other possible reason is that the disjoining pressure starts to make a difference; hence, it is reasonable to distinguish different shapes according to its behaviour by the moment $\tau' = 0.900$.

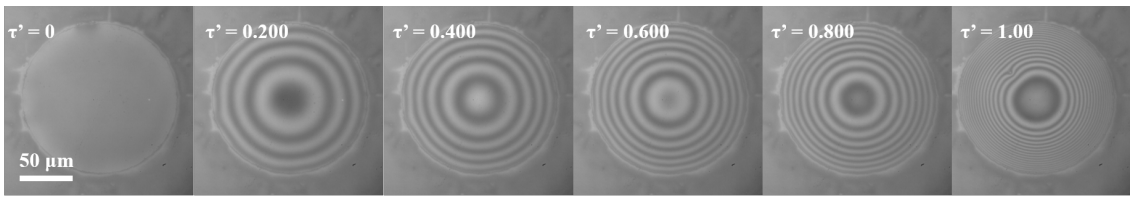


Figure 3.8: The experimental results of methyl benzoate with $\Omega$ of 124, shown in the characteristic time $\tau'$.

The experiment result of the droplet of methyl benzoate with $\Omega = 124$ is presented in Fig 3.8. At the moment $\tau' = 0$, the profile of the droplet is similar to a flat plane. The results at the different moments show that the profile evolves as an expanding spherical cap between the moments $\tau' = 0$ and $\tau' = 1.00$, so that the

droplet is under the dominance of surface tension as is indicated by its $\Omega$.

## 3.4 U-shaped Profile

### 3.4.1 What is a U-shaped Profile?

U-shaped profile shows a new sort of meniscus found during evaporation. At the early stage of evaporation, a U-shaped profile appears to be a spherical cap, but the height profile near the centre becomes flattened as the droplet thins at the centre; and, finally, when a droplet touches down, the touch-down area is a flattened bottom on the profile instead of a point at the centre $r = 0$.

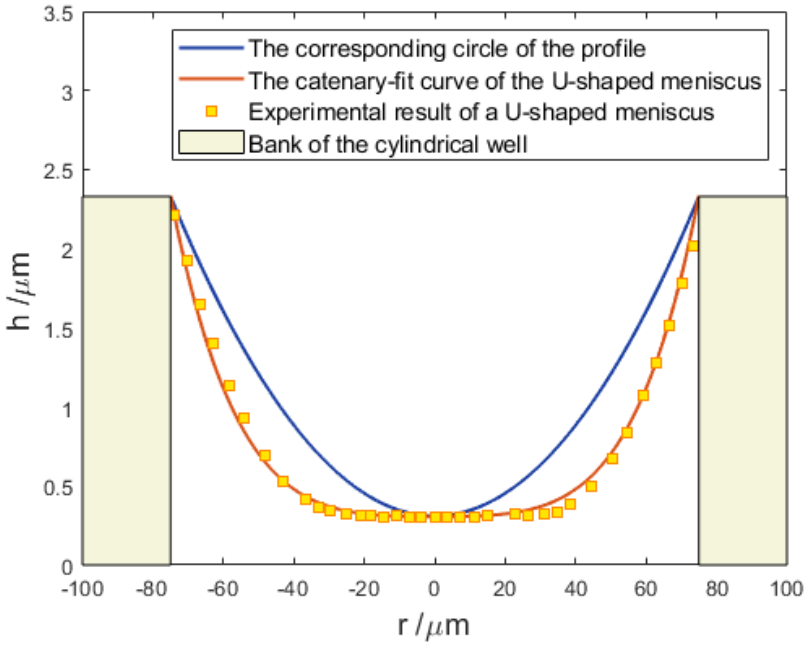


Figure 3.9: Illustration of the difference between a U-shaped meniscus and a spherical cap meniscus (a meniscus is a height profile at a moment): there is a flat bottom near the centre on the meniscus of the U-shaped profile (the orange curve and the yellow squares) of the n-butanol droplet at $\tau' = 0.729$ shown in Fig 3.12, while the meniscus of the corresponding C-shaped profile remains a spherical cap shape (the blue curve).

Consequently, one of the biggest differences between a U-shaped profile and a C-shaped profile is the existence of a flat bottom during evaporation, as is shown in Fig 3.9. The features of C-shaped profiles are demonstrated in the preceding

section which shows that the touch-down area of a C-shaped profile is only the point at $r = 0$; also the mean curvature at the centre increases linearly. Regarding a U-shaped profile, a flattened bottom near the centre $r = 0$ emerges before the droplet touches down and the flattened bottom grows larger while the droplet is evaporating. The radius of a flattened area reaches the maximum when the droplet touches down.

The difference between a C-shaped profile and U-shaped profile is usually clear-cut from the videos of profiles; but, sometimes, the flattened bottom only starts to grow when a droplet is about to touch down and the touch-down area is small when the value of $\Omega$ is large.

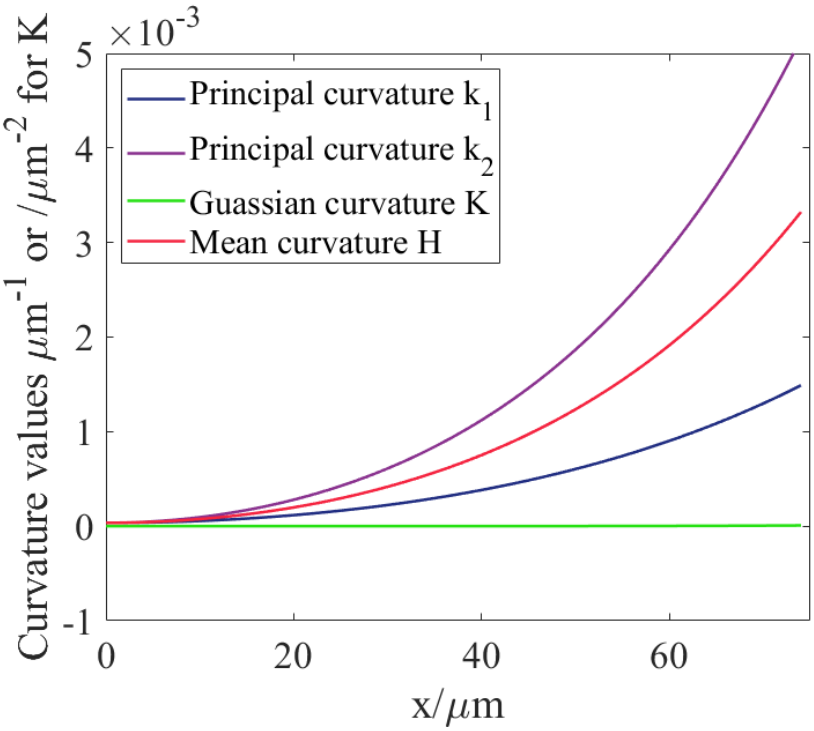


Figure 3.10: Geometrical features of the U-shaped meniscus shown in Fig 3.9.

The geometrical features of the U-shaped meniscus in Fig 3.9, is presented in Fig 3.10. The U-shaped meniscus has a flat bottom near the centre with the mean curvature rising monotonically with r. Based on the definition of the Laplace pressure shown in Eq 2.4.4, the Laplace pressure of the U-shaped meniscus, shown in Fig 3.9, decreases along the the direction of r. In the coordinates developed in Chapter 2, the Laplace pressure is $p_L = p_{in}$ - $p_{out}$. Therefore, that the Laplace pressure at the

centre is larger than that at the brim, suggests that the inner pressure at the centre is larger than that at the brim and the inner pressure decreases monotonically along the direction of r-axis.

With the assistance from the Laplace pressure due to the mean curvature on the U-shaped meniscus, the internal flow moves towards the brim of a well.

Experiments in Sec 3.7.1 show that a U-shaped profile appears when the value of $\Omega$ ranges from 1 to 100. When the value of $\Omega$ is close to 100, U-shaped profile appears late and may only emerge when the droplet is about to touch down. However, it still touches down in an area, though it is relatively small, instead of a point; If the value of $\Omega$ is close to the other end, 1, the U-shaped meniscus of a U-shaped profile appears early and may have a wide bottom near the centre.

### 3.4.2 Experimental Results of a U-shaped Profile

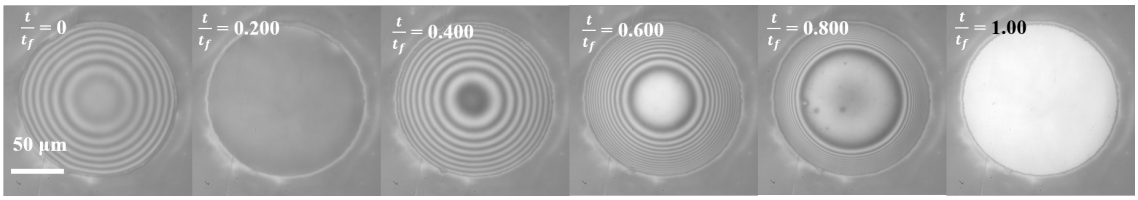


Figure 3.11: Bottom-view images of the n-butanol droplet showing a U-shaped profile with $\Omega = 2.83$, at the different moments.

Four examples of U-shaped profiles are given in Table 3.2. One of them is the n-butanol droplet ($\Omega$=2.83) evaporating in the cylindrical well with radius and depth being 75.0 $\mu$m and 2.63 $\mu$m, respectively. The bottom-view images of the n-butanol droplet evaporating in the well are presented in Fig 3.11, which show that at $t/t_f = 0.600$ a flat bottom developed at the central area and when the droplet was about to touch down, the flat bottom grew wide and extended to two thirds of the entire area at the moment $t/t_f = 0.800$.

In addition, the height profile of the U-shaped profile before touch-down is shown in Fig 3.12, in which the time difference is $0.135\tau'$. The height profiles of the n-butanol droplet are spherical caps at the early stage until the light blue symbols ($\tau = 0.189$), but it becomes flatter later in the process. The purple symbols near the bottom between the yellow symbols and the red symbols, are at the moment

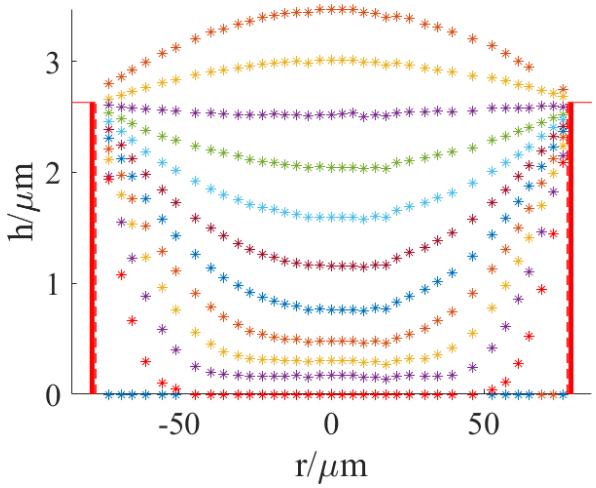


Figure 3.12: The evolution of n-butanol droplet, whose shape of profile is U-shaped with $\Omega = 2.83$.

$\tau' = 0.865$ when the droplet is about to touch down and the flat region locates at $-40.0\ \mu\text{m} \leq r \leq 40.0\ \mu\text{m}$ which grows to $-51.0\ \mu\text{m} \leq r \leq 51.0\ \mu\text{m}$ when the droplet touches down as shown in the red symbols near the bottom in Fig 3.12. The time difference between each height profile is $0.135\tau'$ or 0.058 s.

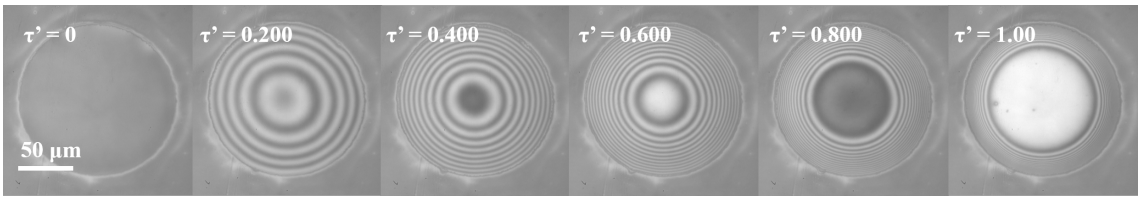


Figure 3.13: Different moments of the n-butanol droplet, $\Omega = 2.83$, counted in $\tau'$.

The experimental result of the n-butanol droplet counted in the characteristic time $\tau'$ is presented in Fig 3.13 which begins at the moment when the height at the centre is equal to the depth of its host well, $\tau' = 0$, and ends at the time when the droplet touches down at the base, $\tau' = 1.00$.

Until $\tau' = 0.400$, the meniscus behaves like a spherical cap and the height at the centre decreases linearly, as shown in Fig 3.14b. The profile near the centre becomes flattened since the moment $\tau' = 0.600$; meanwhile, the height at the centre seems to follow a new linearly decreasing mode but not as fast as it does between the moment $\tau' = 0$ and $\tau' = 0.400$. In the end, the flattened area grows to be the largest accounting for $0.462 \approx (51.0/75.0)^2$ of the total area ,at the moment $\tau' = 1.00$.

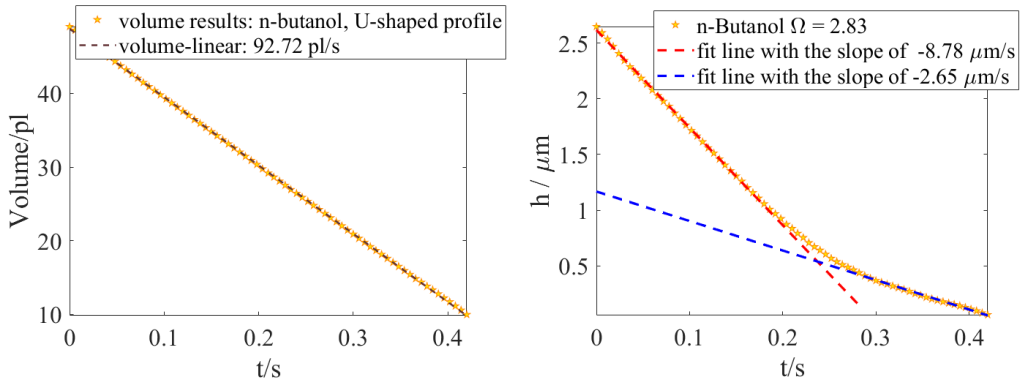


(a) The volume of the n-butanol droplet with $\Omega = 2.83$. decreasing at the rate of 92.7 pl/s.

(b) The height of the n-butanol droplet at the centre decreasing linearly before $t = 0.18$s and after $t = 0.28$s .

Figure 3.14: The volume change and the evolution of the height at the centre of the n-butanol droplet showing U-shaped profile until it touches down.

The evaporation rate of the n-butanol droplet is 92.6 pl/s before it touches down as is shown in Fig 3.14a. Although the volume changes linearly with time, indicating the evaporation of the U-shaped profile is diffusion limited as observed in C-shaped profiles, the height at the centre of the droplet only falls linearly at the rate of 8.76 $\mu$m/s before $\tau' = 0.450$ approximately and the declining tendency seems to fall into the other linear mode at the rate of 2.65$\mu$m/s from the moment $\tau' = 0.600$ as shown in Fig 3.14b.

## 3.5 W-shaped Profile

### 3.5.1 What is a W-shaped Profile?

A W-shaped profile can be found from the evaporation of a pure droplet in a cylindrical well with small aspect ratio. The meniscus of a U-shaped profile may appear to be a spherical cap at the early stage of the evaporation; likewise, the meniscus of a W-shaped profile can also seem to be a spherical cap at the beginning of the evaporation. In addition, during evaporation, the meniscus of a W-shaped profile may also show a flat bottom near the centre for a few moments as U-shaped profiles do; however, the centre will turn out to be a local peak while the droplet evaporates, which is different from U-shaped profiles. And, the local peak near the centre re-

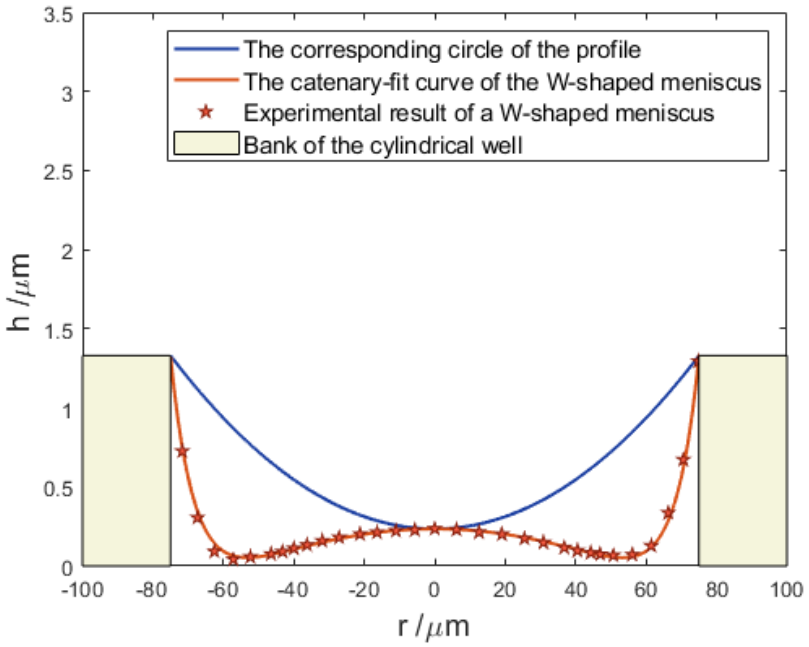


Figure 3.15: Illustration of the difference between the meniscus of a W-shaped profile and its corresponding spherical cap meniscus: a local peak arises near the centre, forming a dimple on the W-shaped meniscus (the orange curve and the red pentagrams) of the n-butanol droplet at $\tau' = 0.854$ shown in Fig 3.18; in addition, the local minimum appears at 52.0 $\mu$m in this example rather than at the centre.

mains until the droplet of W-shaped profile dries out. Therefore, the evolution of the geometrical features at the centre, such as mean curvature, is critical to distinguish a W-shaped profile from others.

The difference between a W-shaped meniscus and a spherical cap is shown in Fig 3.15, in which the local minima are located at $\pm 52.0$ $\mu$m rather than at the centre $r = 0$, which is the major difference between a W-shaped meniscus and a C-shaped meniscus. Also, in the centre of the W-shaped meniscus, there is a local convex (a dimple); meanwhile, there is a concave-up located in the region 41.3 $\mu$m $\leq r \leq$ 75.0 $\mu$m, indicating that the mean curvature along the direction of r-axis changes sign from negative to positive, which is different from C-shaped meniscus or U-shaped meniscus.

The experimental results show that once a profile from the evaporation of a pure droplet has W-shaped meniscus, the W-shaped meniscus will remain and evolve further to a curvier one; thus, in this study, if a profile shows a W-shaped meniscus during evaporation before $\tau' = 0.900$, the profile is defined as a W-shaped profile.

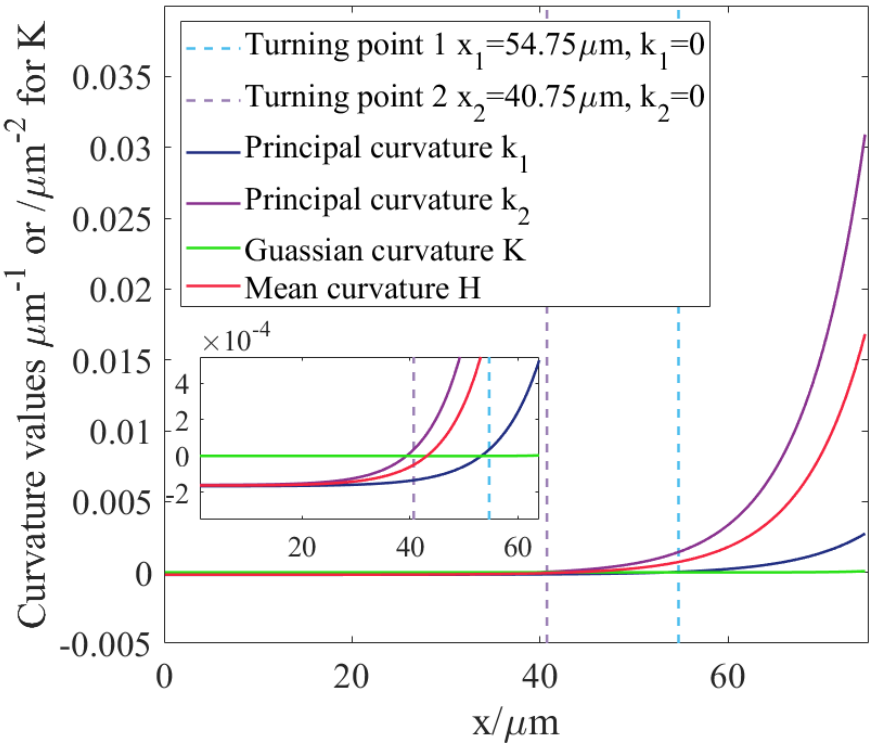


Figure 3.16: The geometrical features of the W-shaped meniscus shown in Fig 3.15.

The W-shaped meniscus still bears the property of axisymmetry, here the analysis is simplified to where 0 $\mu$m $\leq r \leq$ 75.0 $\mu$m. The geometrical features of the W-shaped meniscus shown in Fig 3.15, is presented in Fig 3.16, where the mean curvature of the W-shaped meniscus increases from a negative value to a positive value. The principal curvatures increases monotonically from negative to positive although they increases in different rates. When the first principal curvature is zero, $k_1 = 0$, the point where $x_1 \approx 54.8$ $\mu$m is the turning point of the curve of the W-shaped meniscus in Fig 3.15; when the second principal curvature is zero, $k_2 = 0$, the point where $x_2 \approx 40.8$ $\mu$m is the inflection point of the curve of the W-shaped meniscus. Furthermore, the point where the mean curvature is zero is located at $x_2 < x_3 < x_1$, between the purple dashed line and the blue dashed line in Fig 3.16.

The first principal curvature, $k_1$, increases from -1.60 $\times$ $10^{-4}\mu m^{-1}$ at the centre $r = 0$ $\mu$m to 0.00281 $\mu m^{-1}$ at $r = 75.0\mu$m, while the second principal curvature, $k_2$, increases from -1.60 $\times$ $10^{-4}$ $\mu m^{-1}$ to 0.033 $\mu$m. Therefore, the second principal dominates near the contact line, but both principal curvatures are negative and have

the same value near the centre. The first principal reaches zero at the point $x_1 = 54.8\mu$m and the second principal is zero at the point $x_2 = 40.8\mu$m; hence, the point where the mean curvature is zero is located at the region $40.8\mu\text{m} < x_3 < 54.8\mu\text{m}$. The Gaussian curvature is positive in two regions: where $x < 40.8\mu$m or $x > 54.8$ $\mu$m holds, but it becomes negative in the region where $40.8\mu\text{m} < x < 54.8$ $\mu$m, while in U-shaped profiles or C-shaped profiles the Gaussian curvature never grows to be zero at any moment.

According to the definition of the Laplace pressure, $p_L = p_{in} - p_{out} = -2\gamma H$, the inner pressure in the region where $0 \leq r < x_3$ is larger than that of the outside, $p_{out} = p_0$, and falls along the direction of r-axis like U-shaped profiles do.

### 3.5.2 Experimental Results of a W-shaped Profile

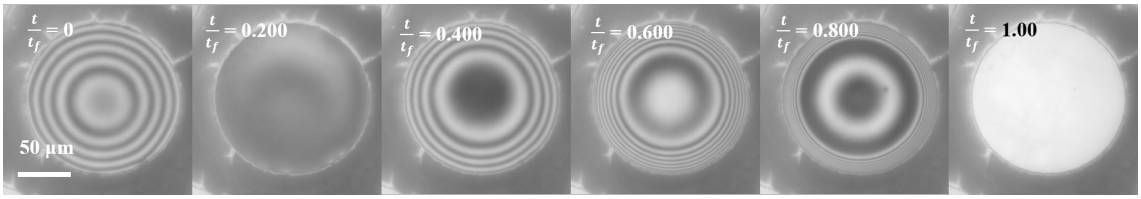


Figure 3.17: Bottom-view images of an n-butanol droplet showing W-shaped profile, $\Omega = 0.323$.

Bottom-view images of the W-shaped profile with $\Omega = 0.323$, see Table 3.2 for details, is presented in Fig 3.17, in which we can find a small dimple near the centre at the moment $t/t_f = 0.600$, since then the height at the centre keeps a local maximum until the droplet touches down at the point $r \approx 50.7$ $\mu$m; afterwards, two new contact lines appear on the base, one for the inner droplet and the other for the liquid which still sticks to the brim of the well. One of the new contact lines is the contact line of the newly-generated droplet, receding towards the centre of the well like a sessile droplet on a flat plane; the other contact line moves towards the brim of the well and acts like the new contact lines emerging in a C-shaped profile or a U-shaped profile when it touches down at the base.

The height profile of the W-shaped profile aforementioned with $\Omega = 0.323$ is presented in Fig 3.18. Likewise, the height profile is reconstructed before the touch-down moment shown in Fig 3.18.

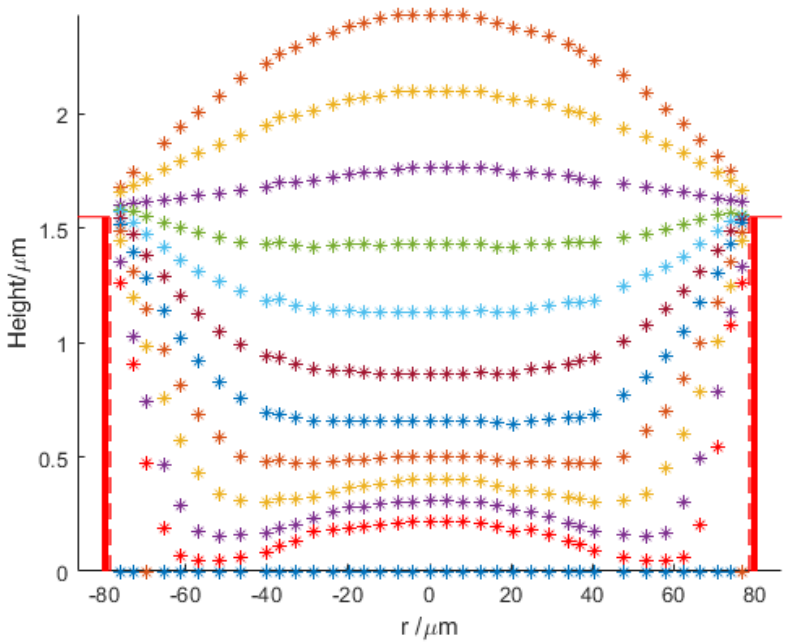


Figure 3.18: The evolution of the W-shaped profile of a n-butanol droplet with $\Omega = 0.323$.

The meniscus of the profile resembles to a spherical cap until $\tau' = -0.170$, the purple symbols; however it turns to be a flat bottom from $\tau' = 0.123$, the light blue symbols, and the flat bottom grows to the largest at $\tau' = 0.415$, the dark blue symbols; afterwards, there is a dimple turning up, the height of which is higher than 0.510 $\mu$m at the centre, at $\tau' = 0.561$ (the orange symbols) and growing to the largest scale when the droplet touches down (the red symbols).

In spite of showing a W-shaped meniscus during evaporation, the volume of the W-shaped profile of n-butanol still changes linearly with time before the droplet touches down. In Fig 3.20a, it shows that the evaporation rate is at 92.7 pl/s which is almost the same as the droplet of n-butanol showing U-shaped profile in the last section; for a W-shaped profile, the evaporation process is still diffusion limited.

The evaporation of the W-shaped profile counted in $\tau'$ is shown in Fig 3.19. Since the evaporation rate does not change until a pure droplet touches down, it is reasonable to set the initial moment at the moment when the height at the centre is equal to the depth of the well, in order to compare different profiles with the same initial conditions. At $\tau' = 0$, the height at the centre is equal to the depth of well, though it is a local peak. However, the local peak becomes the local valley

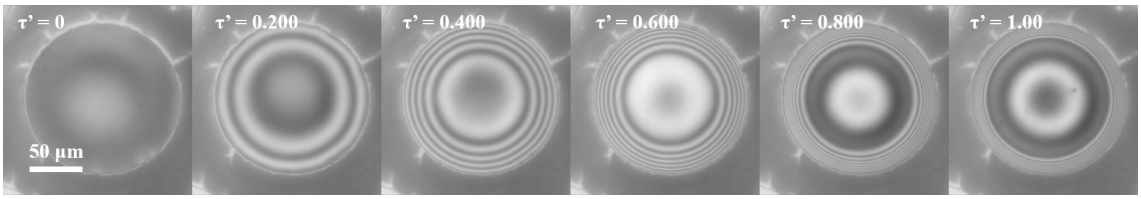


Figure 3.19: The evolution of a n-butanol droplet, whose Ω is 0.323, counted in $\tau'$.

at the moment $\tau' = 0.200$ when the droplet at the centre is similar to a spherical cap. Afterwards, the area near the centre becomes flattened, resemble a U-shaped meniscus; after then, the flat bottom only exists until $\tau' = 0.600$, at which moment there is a local peak (dimple) appearing in the centre. The dimple bears similarity to a spherical cap with the concave-down side filled with liquid, as shown at the moment $\tau' = 0.800$. When the droplet touches down, the inner droplet splits from the rest , moves towards the centre of the well and behaves as a sessile droplet.

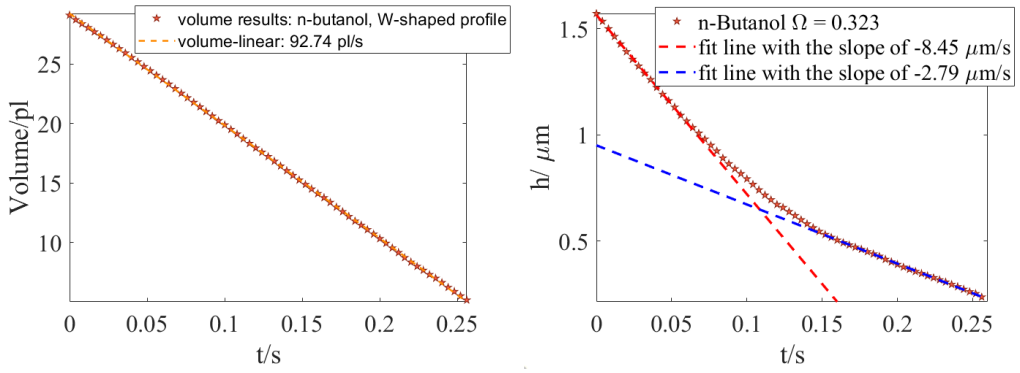


(a) The volume of the n-butanol droplet with Ω = 0.323 decreasing at the rate of 92.7 pl/s.

(b) The height of the n-butanol droplet at the centre decreasing linearly before $t = 0.07$s and after $t = 0.15$s.

Figure 3.20: The volume change of the n-butanol droplet and the evolution of the height at the centre counted in $\tau'$ and real scale.

As in a U-shaped profile, the height at the centre of the W-shaped profile declines non-linearly overall (Fig 3.20b). However, the height falls linearly just before $\tau' = 0.200$, the experiment result of which is shown in Fig 3.19, indicating that the meniscus is similar to a spherical cap at the moment. After then, the height at the centre falls more and more slowly, which is due to the appearance of the flat bottom near the centre, generating a U-shaped meniscus, seems to follow the other linear decrease at the moment $\tau' = 0.710$ and touches down at the base with the height

at the centre equal to 0.236 $\mu$m. When the droplet touches down, the height at the centre is 0.241 $\mu$m and the inner droplet behaves like a sessile droplet.

## 3.6 Comparison between W/U/C-shaped Profiles

In the preceding sections, three different profiles are reported with the geometrical features. Also, a parameter, $\Omega$, is developed preliminarily to predict the shape of a profile from the evaporation of a pure droplet in a cylindrical well.

In Sec 3.6.1, the profiles showing different shapes with different $\Omega$'s are compared under the non-dimensionalised scale to illustrate the difference among them and how to distinguish the shapes, while in Sec 3.6.2 the U-shaped profiles bearing different values of $\Omega$, with the different sizes of the flat bottoms near the centre are compared, which shows that the smaller the value of $\Omega$ is, the more flattened the bottom of a U-shape profile near the centre will be. In Sec 3.6.3, three U-shaped profiles with similar values of $\Omega$ are compared to further verify that the value of $\Omega$ alone determines the droplet profiles.

In addition, the evolutions of the mean curvatures at the centre also present different tendencies for different shapes. The mean curvature at the centre changes linearly with time for C-shaped profiles; however, the mean curvatures of U-shaped profiles at the centre only change linearly with time at the early stage, since U-shaped profiles show spherical menisci before the flat bottoms arise the moment of which is denoted as the flat moment, $\tau'_{flat}$. W-shaped profiles shows two sign changes of the mean curvature at the centre due to the appearances of dimples.

The values of the $\Omega$'s of the profiles selected in this section are shown in Fig 3.21 where in the light blue region is $\Omega < 1.00$, the jade region is $1 < \Omega < 100$ and the orange region is $\Omega < 100$, while at the borders, the blue dashed line is where $\Omega = 1.00$ separating the W-region and U-region and the red dashed line is where $\Omega = 100$ dividing U-region and C-region. The light blue dash-dotted line represents the points at which $\Omega = 6.55$

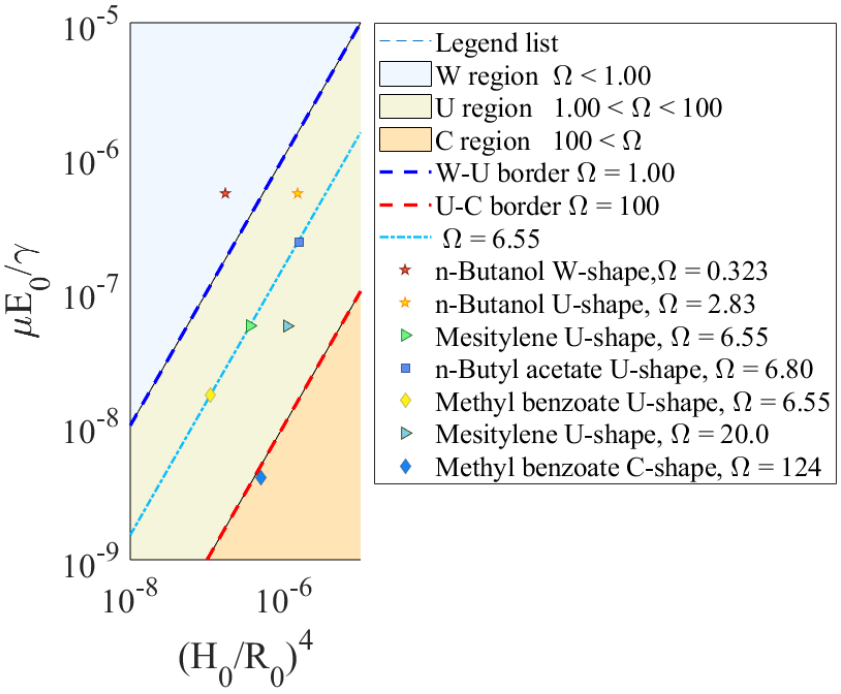


Figure 3.21: The values of Ω's of different profiles shown in Table 3.2 and selected to compare in this section.

.

### 3.6.1 Profiles with Different Values of Ω

The features of different profiles are presented in the last section; therefore, in the subsection, the attention only goes to the difference among them instead of the similarities such as the linear change of the volume against time.

The U-shaped profile of n-butanol droplet with $\Omega = 2.83$ in Fig 3.22b, has a flat bottom near the centre at the moment $\tau' = 0.400$, while the C-shaped profile still remains a spherical cap and the W-shaped profile is about to show a dimple; after then, the flat bottom in the U-shaped profile grows wider at the moment $\tau' = 0.800$ and reaches the base when the flat bottom grows to its largest size. However, for the W-shaped profile, the dimple becomes larger and larger from the moment $\tau' = 0.600$ and separates from the liquid near the brim at $\tau' = 1.00$. The C-shaped profile remains a spherical cap and has the only minimum at the centre.

The profiles of the experiments shown in Fig 3.22 are reconstructed in Fig 3.23 where the time difference between the nearest curves in each figure is set at $0.200\tau'$ so that the curve at the top is at the moment $\tau' = 0$, while at the bottom is $\tau' = 1.00$.

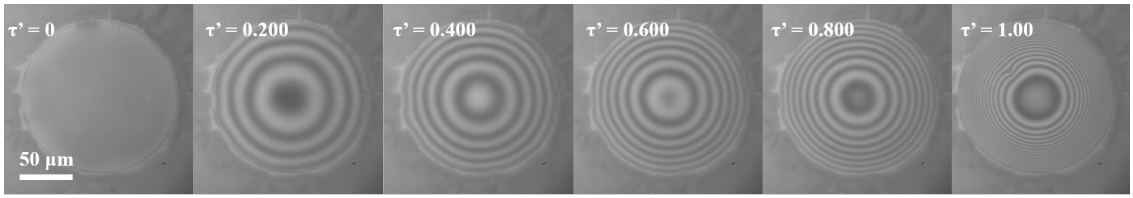


(a) C-shaped profile of the methyl benzoate droplet with $\Omega = 124$.

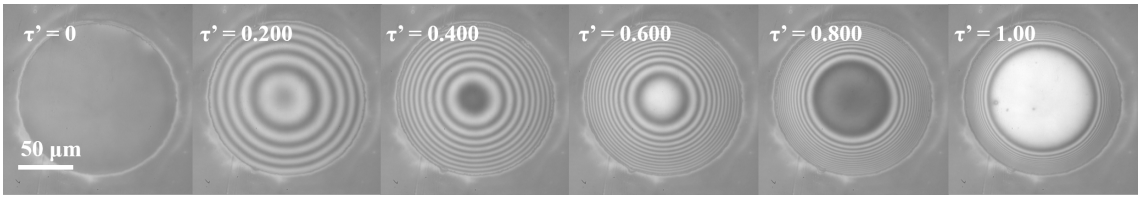


(b) U-shaped profile of the n-butanol droplet with $\Omega = 2.83$.

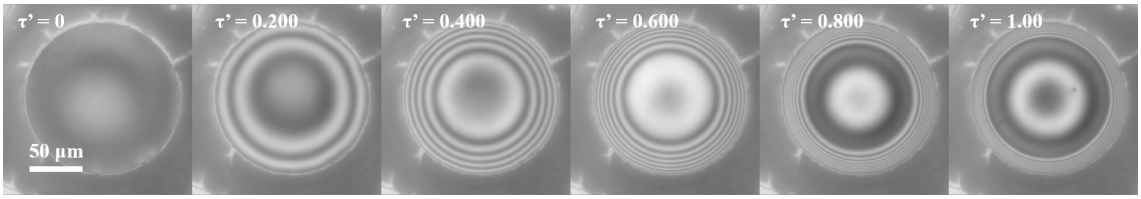


(c) W-shaped profile of the n-butanol droplet with $\Omega = 0.323$.

Figure 3.22: Bottom-view results of the W/U/C-shaped profiles of methyl benzoate and n-butanol droplets evaporating in the wells with aspect ratios being 1.37/75.0, 2.63/75.0 and 1.53/75.0, respectively.

The blue diamonds in Fig 3.23a are the profile of methyl benzoate with $\Omega = 124$, and resemble a spherical cap at each moment; the yellow stars in Fig 3.23b are the U-shaped profile of n-butanol whose $\Omega$ is 2.8, and the flat bottom on the meniscus arises at the moment $\tau' = 0.400$ and touches down at $\tau' = 1.00$ with the size of the flat bottom being $-0.574 < r' < 0.595$.

The W-shaped profile of n-butanol in Fig 3.23c has a dimple at the initial moment $\tau' = 0$, but the dimple soon turns to be a flat bottom ranging from $r' = -0.380$ to $r' = 0.391$ at the moment $\tau' = 0.200$ and the flat bottom grows to the size of $-0.441 < r' < 0.452$ at the moment $\tau' = 0.400$. Afterwards, a small dimple appears at $\tau' = 0.600$ within the region $-0.441 < r' < 0.452$ and reaches to the size of $-0.618 < r' < 0.634$ at the moment $\tau' = 0.800$; when the droplet touches down, the dimple ranges from $r' = -0.690$ to $r' = 0.711$, taking 70.1% of the total area.The combination of the profiles presented in Fig 3.23d directly illustrates the difference among them.

The evolutions of the mean curvature are presented in Fig 3.24. The mean curvature of the C-shaped profile of methyl benzoate (blue diamonds) rises linearly with time, although there is a turning point at the moment $\tau' = 0.941$ when the height at the centre is so thin that the disjoining pressure may not be negligible any more [169].

The U-shaped profile of n-butanol shows the same linear rise as the C-shaped profile does, until the moment $\tau' = 0.471$; since then there is a flat bottom appearing near the centre, as is already shown in Fig 3.22b and Fig 3.23b, and the mean curvature begins to drop from the moment $\tau' = 0.521$, but still remains positive until the moment $\tau' = 0.783$ when the height at the centre is 0.210 $\mu$m approximately.

The mean curvature at the centre for the W-shaped profile of n-butanol has two turning points on the curve as well, shown in the red stars in Fig 3.24. Since the experimental results show that there is a dimple near the centre at the initial moment, presented in Fig 3.22b and Fig 3.23b, the mean curvature at the centre rises from a negative value $H' = -5.34 \times 10^{-5}$ $\mu\text{m}^{-1}$ to the only peak, $H' = 8.00 \times 10^{-5}$ $\mu\text{m}^{-1}$, at the moment $\tau' = 0.272$; afterwards, the mean curvature begins to fall due to the appearance of a flat bottom near the centre, but is still positive until the

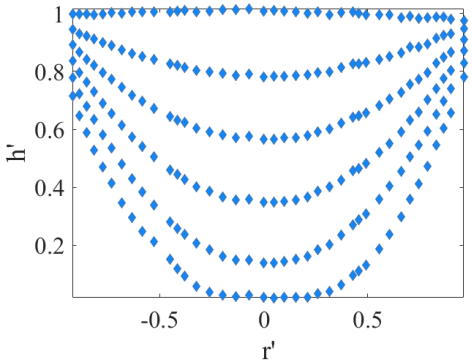


(a) C-shaped profile of the methyl benzoate droplet: $\Omega = 124$.

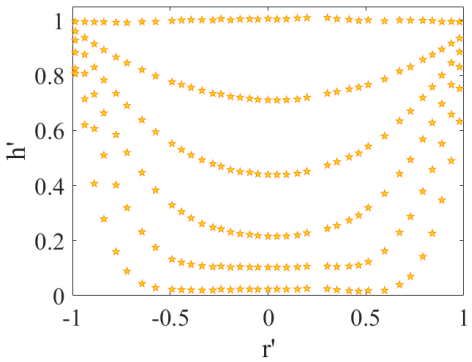


(b) U-shaped profile of the n-butanol droplet: $\Omega = 2.83$.

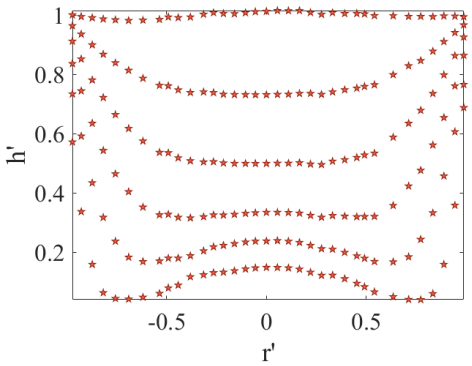


(c) W-shaped profile of the n-butanol droplet: $\Omega = 0.323$.

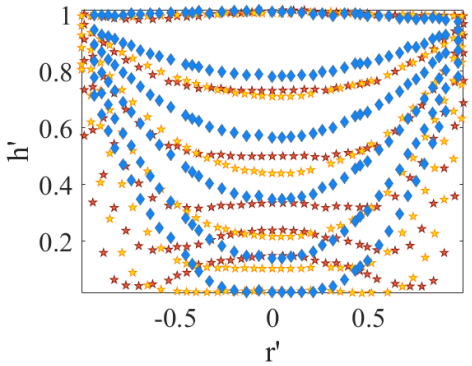


(d) The comparison of the profiles shown above.

Figure 3.23: Reconstructed profiles of the droplets shown in Fig 3.22, presented under the non-dimensionalised scales: the blue diamonds are the methyl benzoate droplet with $\Omega = 124$, while the yellow stars and the red stars are n-butanol droplets with $\Omega = 2.83$ and $\Omega = 0.323$, respectively.

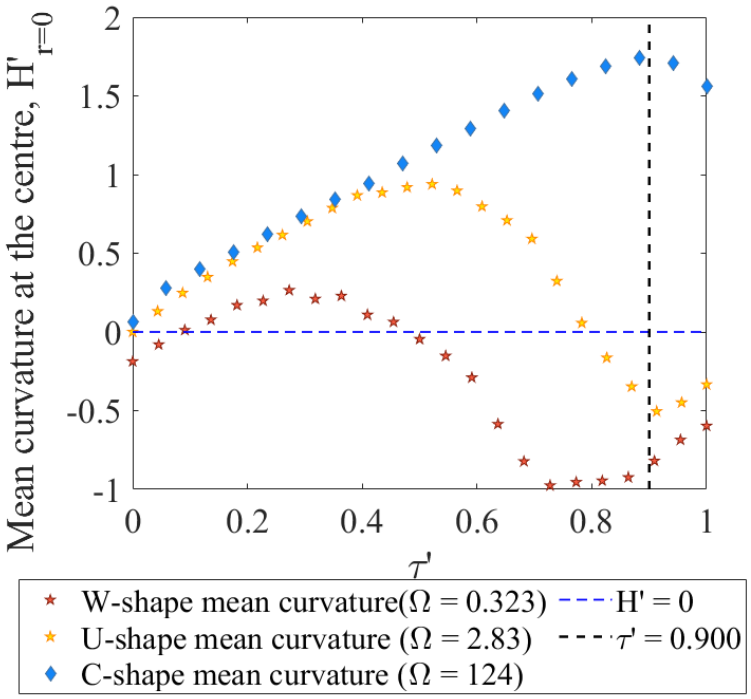


Figure 3.24: The mean curvatures of the profiles at the centre under the non-dimensionalised scales.

moment $\tau' = 0.500$ when a dimple starts to grow at the centre; however, the value of the mean curvature reaches the negative peak at $\tau' = 0.727$ when the dimple is at its curviest state and the inner pressure at the centre also reaches the highest value; after $\tau' = 0.864$, the mean curvature almost increases linearly again until the droplet touches down, suggesting that the dimple evolves like an expanding spherical cap.

On the other hand, apart from the evolution of mean curvature, the height at the centre also shows different falling tendencies of the profiles with different shapes.

In Fig 3.25a, the height at the centre for the C-shaped profile of methyl benzoate, shown in the blue diamonds, falls linearly until the moment $\tau' = 0.941$, indicating the meniscus remains a spherical cap at each moment before then. The yellow stars are the height at the centre of the U-shaped profile of n-butanol with $\Omega = 2.83$, showing the linear decrease until the moment $\tau' = 0.485$ as the meniscus remains a spherical cap; afterwards, the height profile evolves non-linearly until the moment $\tau' = 0.689$, indicating the flat bottom near the centre grows wider and wider; the other linear decrease arises from then and continues until $\tau' = 1.00$, which is not seen in the C-shaped profile.

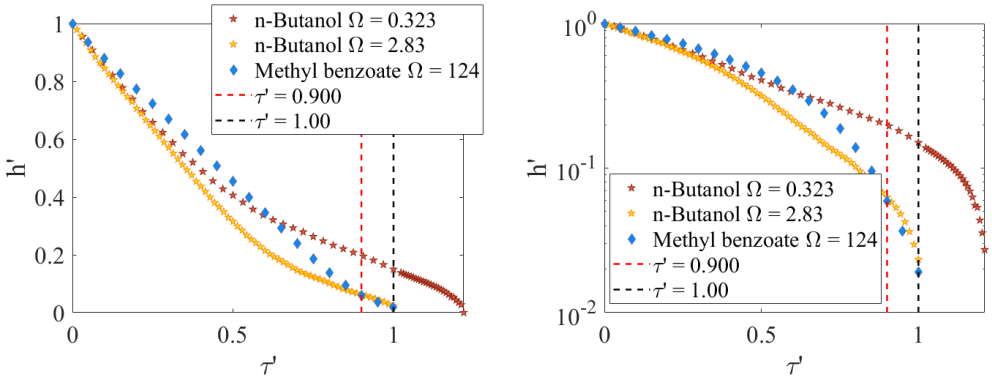


(a) The evolutions of the height at the centre of the W/U/C-shaped profiles.

(b) The results of the profiles plotted in the semi-logarithmic scales.

Figure 3.25: The evolutions of the height at the centre of the three profiles: the blue diamonds, yellow stars and red stars are the results of methyl benzoate ($\Omega = 124$), n-butanol ($\Omega = 2.83$) and n-butanol($\Omega = 0.323$), respectively.

The red stars in Fig 3.25 are the evolution of the height at the centre of the W-shaped profile of n-butanol with $\Omega = 0.323$. The decline tendency of the red stars has a inflection point at the touch-down moment $\tau' = 1.00$, suggesting that the evolution of a profile is different once a droplet touches down. Although both of the n-butanol droplets (the yellow stars and red stars) show the non-linear evolutions, the heights at the centre almost decrease at the same rate during $0.671 < \tau' < 1.00$ , as shown in Fig 3.25a. In addition, the red stars in the semi-logarithmic plot in Fig 3.25 illustrates that the height at the centre of the W-shaped profile evolves following the rule of $h' = e^{2.3[(h'_d-1)\tau'+1]}$.

### 3.6.2 U-shaped Profiles with Different Values of Ω

Three U-shaped profiles with different values of Ω are chosen to compare and verify the effectiveness of Ω on the prediction of a profile from the evaporation of a pure droplet printed in a cylindrical well. The details of the U-shaped profiles are also given in Table 3.2, which shows that the n-butanol droplet has $\Omega = 2.83$, one of the mesitylene droplets has smaller Ω, 6.55, and the other mesitylene droplet has the larger Ω, 20.0.

In Fig 3.26, the experimental results of the U-shaped profiles are presented under the characteristic time. The features of the n-butanol droplet with $\Omega = 2.83$ is given

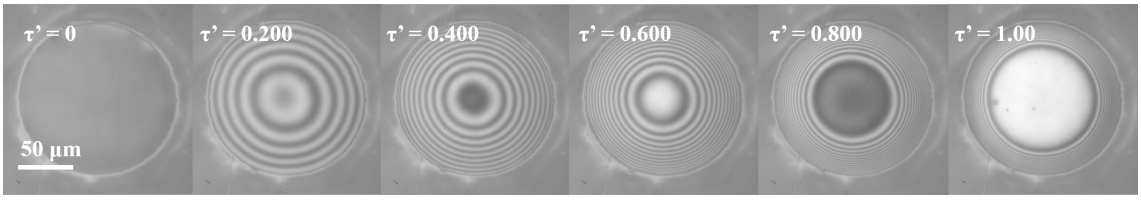


(a) U-shaped profile of the n-Butanol droplet with $\Omega = 2.83$.

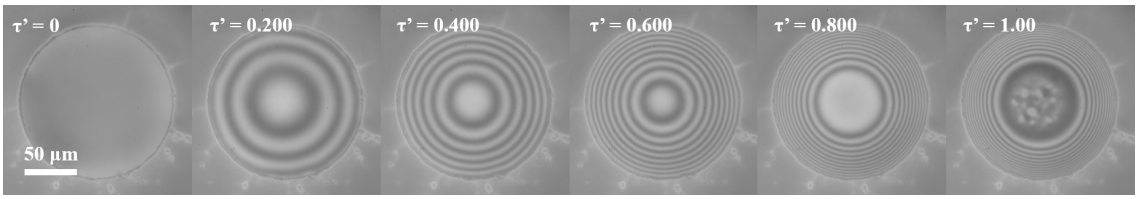


(b) U-shaped profile of the mesitylene droplet with $\Omega = 6.55$.

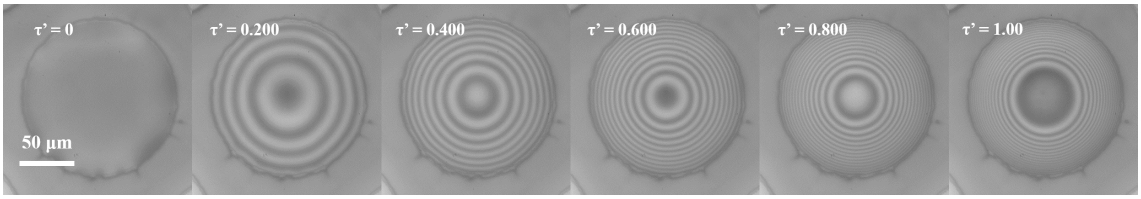


(c) U-shaped profile of the other mesitylene droplet with $\Omega = 20.0$.

Figure 3.26: Bottom-view results of the U-shaped profiles of n-butanol droplet and mesitylene droplets evaporating in the wells with aspect ratios being 2.63/75.0, 1.84/75.0 and 2.43/75.0, respectively.

in the last subsection, showing that the flat bottom arises at the moment $\tau' = 0.400$. The U-shaped profile of mesitylene with $\Omega = 6.55$ has a rather large flat bottom at the moment $\tau' = 0.800$, but not as large as the flat bottom appearing on the n-butanol droplet at the same time; when the mesitylene droplet with $\Omega = 6.55$ touches down, the touch down area is also smaller than that of the droplet of n-butanol.

As for the mesitylene droplet with $\Omega = 20.0$, the flat bottom near the centre only begins to appear at the moment $\tau' = 0.800$ and is the smallest one among the U-shaped profiles shown at the same moment; however, the flat bottom of the mesitylene droplet with $\Omega = 20.0$, keeps evolving and almost has the same size as that of the U-shaped profile of n-butanol at the moment $\tau' = 0.400$, shown in Fig 3.27a.

The profiles at the different moments in Fig 3.26 are reconstructed in Fig 3.27 where the results demonstrate that the smaller the value of $\Omega$ is, the earlier a flat bottom will arise near the centre. The yellow stars are the menisci of the U-shaped

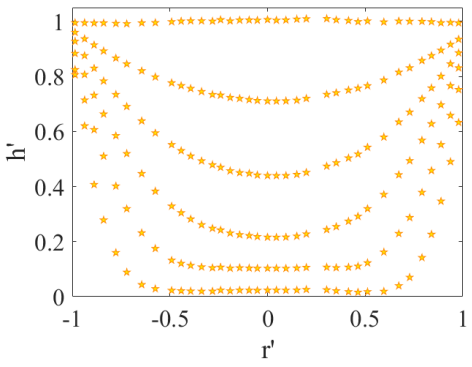


(a) U-shaped profile of the n-butanol droplet with $\Omega = 2.83$.

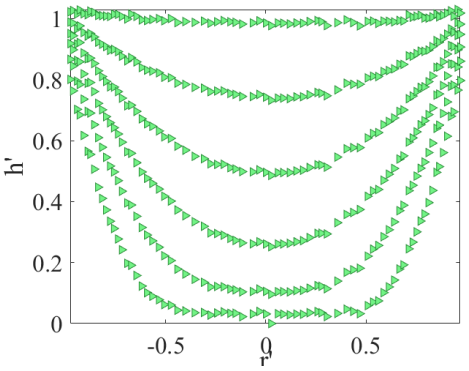


(b) U-shaped profile of the mesitylene droplet with $\Omega = 6.55$.

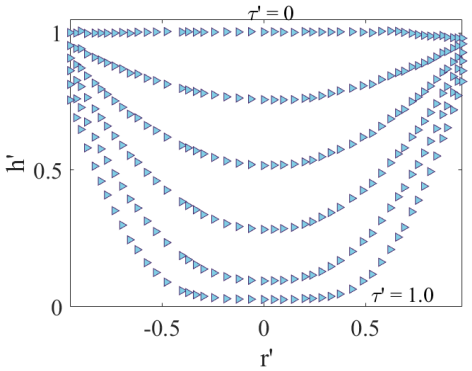


(c) U-shaped profile of the mesitylene droplet with $\Omega$ =20.0.

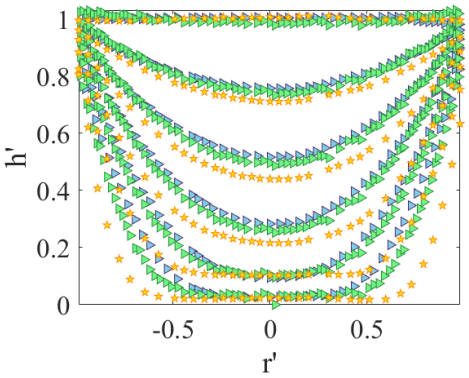


(d) The comparison of the U-shaped profiles.

Figure 3.27: Reconstructed U-shaped profiles shown in Fig 3.26, presented under the non-dimensionalised scales: the yellow stars are the n-butanol droplet with $\Omega = 2.83$, the green triangles are the the mesitylene droplet with $\Omega = 6.55$, and the blue triangles are the mesitylene droplet with $\Omega = 20.0$.

profiles of the n-butanol droplet with $\Omega = 2.83$. The green triangles are the U-shaped profile of mesitylene droplet, in which case $\Omega = 6.55$, evaporating in the cylindrical well with the radius and depth being 75.0 $\mu$m and 1.84 $\mu$m, respectively. A flat bottom first appears at the moment $\tau' = 0.600$ within the area of $-0.178 < r' < 0.184$ and grows to $-0.475 < r' < 0.508$ when the droplet touches down; in addition, the flat bottom appears later than the U-shaped profile of the n-butanol droplet does.

The other case of the U-shaped profile of mesitylene has $\Omega = 20.0$, shown in the blue triangles in Fig 3.27c. The mesitylene droplets have the identical evaporation rate, although the radius and depth of the well in this case are 75.0 $\mu$m and 2.43 $\mu$m, respectively, which is 0.590 $\mu$m deeper than that of the U-shaped profile with $\Omega = 6.55$. As a result, the blue triangles has a flat bottom at the moment $\tau' = 0.800$ ranging from $r' = -0.246$ to $r' = 0.236$, which is the smallest among the U-shaped profiles; after then, the flat bottom becomes slightly wider at the moment $\tau' = 1.00$, in the area $-0.402 < r' < 0.373$, but is still the tiniest one among them when the droplets touch down. Also, the comparison of the U-shaped profiles is shown in Fig 3.31d.

The evolutions of the mean curvature at the centre for the U-shaped profiles also show different features, as presented in Fig 3.28. The U-shaped profile of n-butanol, in the yellow stars, rise linearly until $\tau' = 0.471$, shows the turning point at $\tau' = 0.521$ and turns to be negative at the point $\tau' = 0.826$, although it increases to $H' = -0.333$ at $\tau' = 1.00$, after reaching the negative peak at $\tau' = 0.913$.

The green triangles representing the evolution of mean curvature at the centre for the U-shaped profile of mesitylene with $\Omega = 6.55$, show a similar linear rise with other profiles including C-shaped profile of methyl benzoate whose $\Omega$ is 124, indicating the meniscus resemble to a spherical cap until $\tau' = 0.556$ before it reaches the turning point at $\tau' = 0.667$; afterwards, the mean curvature drops as the result of the appearance of a flat bottom at the centre; however, the mean curvature only turns to be negative at the moment $\tau' = 0.960$ approximately.

The other case of mesitylene with $\Omega = 20.0$ are presented in the blue triangles in Fig 3.28. The rises linearly as well until the moment $\tau' = 0.667$ when a flat bottom

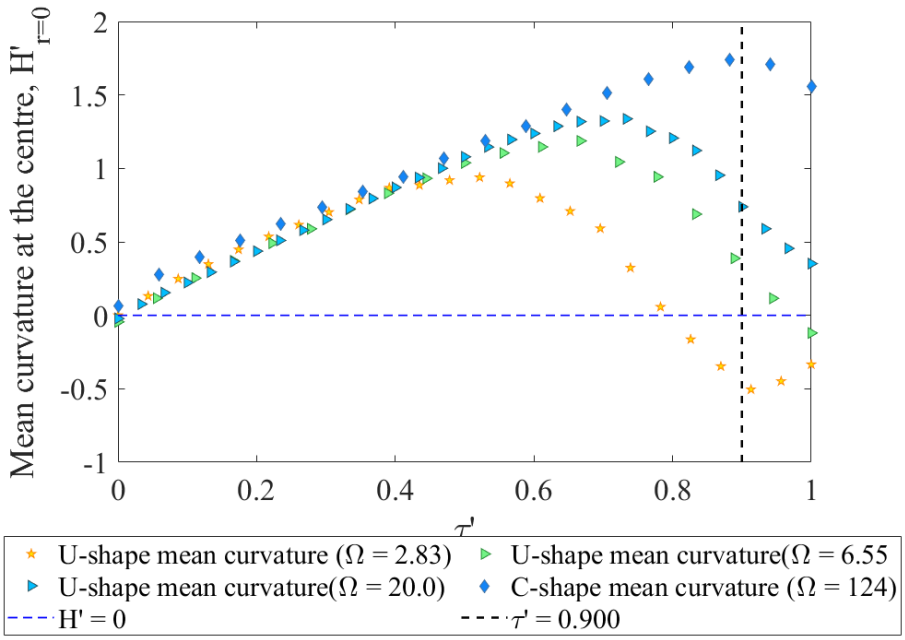


Figure 3.28: The evolutions of the mean curvature at the centre of the U-shaped profiles and the C-shaped profile of methyl benzoate.

begins to appear; the flat bottom grows slowly, as indicated by the experimental results in Fig 3.26c and Fig 3.27c, almost at the same rate as the mesitylene droplet with $\Omega = 6.55$. Unlike what happens to the two other U-shaped profiles, the mean curvature never turns to be negative, and the duration of a spherical-like meniscus is $0.667\tau'$, the longest among all of them.

In conclusion, the mean curvature of all the U-shaped profiles increases linearly at the same rate initially, though the linear increase ends at different moment.

On the other hand, the heights at the centre for the U-shaped profiles also show different features, although the U-shaped profiles of mesitylene bears similarities as shown in Fig 3.29.

The height at the centre of the mesitylene droplet with $\Omega = 6.55$ is shown in the green triangles, decreasing linearly until the moment $\tau' = 0.667$ when the mean curvature also begins to deviate from the linear rise as the appearance of the flat bottom at the centre. Afterwards, the height at the centre falls following the other linear mode of decrease from the moment $\tau' = 0.767$ when $h' = 0.118$.

The blue triangles are the height at the centre of the mesitylene droplet with

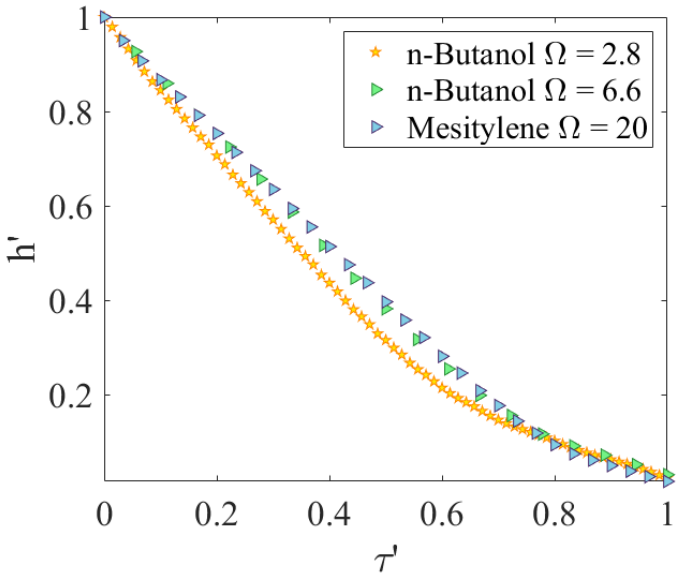


Figure 3.29: The evolutions of the height at the centre of the U-shaped profiles.The yellow stars, green triangles blue triangles are n-butanol droplet with $\Omega = 2.83$, mesitylene droplet with $\Omega = 6.55$ and the other mesitylene droplet with $\Omega = 20.0$, respectively.

$\Omega = 20.0$, which decreases linearly at the same rate as the other mesitylene droplet with $\Omega = 6.6$ (green triangles) shows, until the moment $\tau' = 0.667$ when the mean curvature shown in Fig 3.28 deviates from the linear rise. Likewise, the height follows the other mode of linear decrease from the moment $\tau' = 0.800$ when $h' = 0.094$.

All the height curves at the centre, $h(0, t)$, of the U-shaped profiles show linear falls until the moment when flat bottoms at the centre arise, although the durations and rates of the linear falls may differ. However, the height curves follow the other linear decrease and the results suggest that all three height curves almost show the same rate of the decrease when the droplets are about to touch down.

The same tendencies of the height curves at the centre of the U-shaped profiles consolidate the distinction of U-shaped profiles from W-shaped profiles and C-shaped profiles. On the other hand, height curves at the centre of U-shaped profiles also show diversities on the decreasing rate and difference of the moment when it enters the second sort of linear decrease.

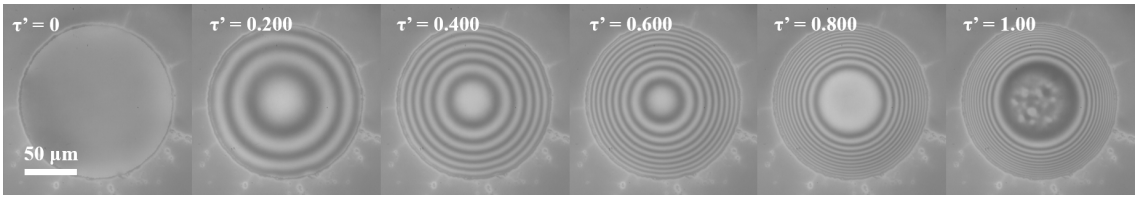


(a) U-shaped profile of the mesitylene droplet with $\Omega = 6.55$.

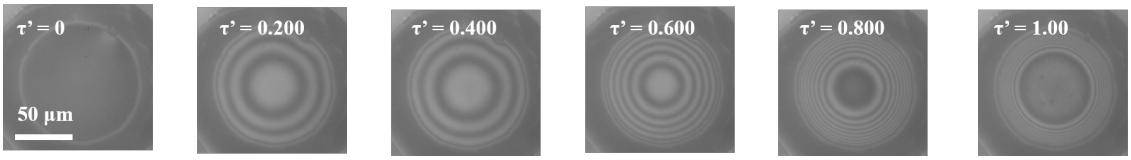


(b) U-shaped profile of the n-butyl acetate droplet with $\Omega = 6.80$.

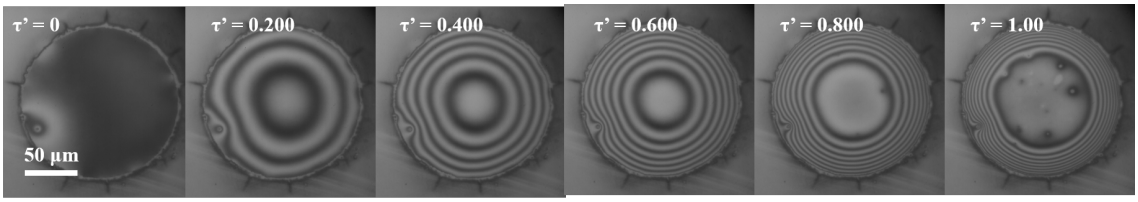


(c) U-shaped profile of the methyl benzoate droplet with $\Omega = 6.55$.

Figure 3.30: Comparisons of the U-shaped profiles of mesitylene droplet, n-butyl acetate droplet and methyl benzoate droplet evaporating in the wells with aspect ratios being 1.84/75.0, 1.77/50.0, and 1.37/75.0, respectively.

### 3.6.3 U-shaped Profiles with Similar Values of $\Omega$

As shown in the preceding sections that different values of $\Omega$ indicate different evolution tendencies, namely a large $\Omega$ suggesting a C-shaped profile, a small $\Omega$ linking to a W-shaped profile, here the profiles with the similar $\Omega$'s are presented to further prove the effectiveness of the parameter $\Omega$. The solvents chosen at this section are mesitylene, n-butyl acetate and methyl benzoate. More details about the host wells and the properties of the solvents are given in Table 3.2. To test the influence from the radius on the shape, the radius of the host well for n-butyl acetate is 50.0 $\mu$m whereas the radii of the two other cases are 75.0 $\mu$m.

The experimental results of the three U-shaped profiles with the similar $\Omega$'s are given in Fig 3.30 which show that the U-shaped profiles experience the identical evolutions with flat bottoms appearing at the moment $\tau' = 0.600$, in spite of the smaller radius of the well in the case of n-butyl acetate presented in Fig 3.30b. The methyl benzoate droplet in Fig 3.30c evaporates at the rate of 6.02 pl/s, but the shape of profile appears to be a U-shaped one when the depth and radius of the well

are 1.37 $\mu$m and 75.0 $\mu$m, respectively. Despite few particles, the profile still shows a flat bottom at the moment $\tau' = 0.600$ and evolves similarly with two other cases.

The results shown in Fig 3.30 are analysed as the profiles shown in Fig 3.31, where the green triangles, blue squares and yellow diamonds are the height profiles of the mesitylene droplet with $\Omega = 6.55$, the n-butyl acetate droplet with $\Omega = 6.80$ and the methyl benzoate droplet with $\Omega = 6.55$, respectively. The symbols at the top are the menisci at the moment $\tau' = 0$, while the symbols at the bottom are at $\tau' = 1.00$.

The results in Fig 3.31a, Fig 3.31b and Fig 3.31c of the U-shaped profiles, show the similarities among the evaporation process of the droplets, including the fact that flat bottoms first appear at the moment $\tau' = 0.600$ and reach its largest scale at $\tau' = 1.00$ almost accounting for half of the total area.

The flat bottom appears on the meniscus of the n-butyl acetate with $\Omega = 6.80$ at $\tau' = 0.600$, within the area $-0.196 < r' < 0.164$; soon the flat bottom grows to $-0.377 < r' < 0.345$ at $\tau' = 0.800$; finally, when the droplet touches down, the flat bottom is situated in the area $-0.515 < r' < 0.536$.

Similarly, Fig 3.31c shows that the moment of the emergence of a flat bottom on the meniscus of the methyl benzoate droplet is at $\tau' = 0.600$, presented in the yellow diamonds, taking up $-0.168 < r' < 0.196$; at $\tau' = 0.800$, the size of the flat bottom is $-0.270 < r' < 0.310$; in the end, the flat bottom accounts for half of the total area approximately, located in $-0.481 < r' < 0.499$.

The green triangles are the result of the mesitylene droplet with $\Omega = 6.55$, more details of which has shown in the last section. Briefly, the flat bottom arises at the moment $\tau' = 0.600$, taking up the area $-0.178 < r' < 0.184$ and grows to $-0.278 < r' < 0.303$ and $-0.475 < r' < 0.508$ at the moments $\tau' = 0.80$ and $\tau' = 1.0$, respectively.

In conclusion, the reconstructed profiles show that the U-shaped profiles having the similar values of $\Omega$s, experience the identical evolution during evaporation. Fig 3.31d, showing the similar menisci at each moment, is drawn to compare the U-shaped profiles directly. The evolutions of the mean curvature at the centre, $H'$, are presented in Fig 3.32. The green triangles again are the result of the mesitylene

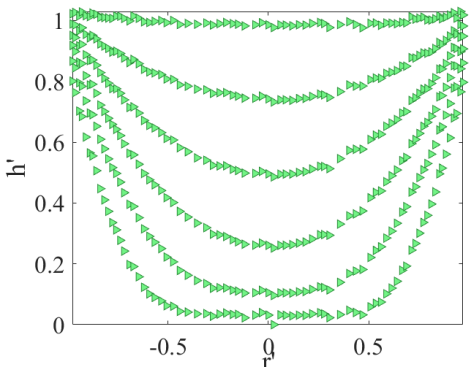


(a) U-shaped profile of the mesitylene droplet with $\Omega = 6.55$.

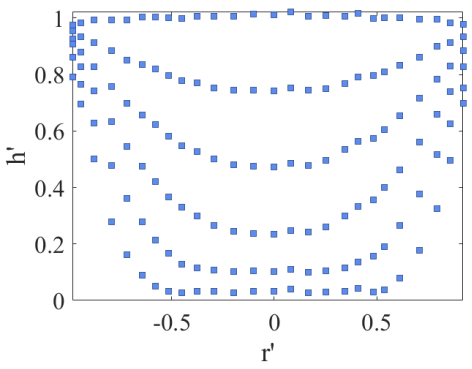


(b) U-shaped profile of the n-butyl acetate droplet with $\Omega = 6.80$.

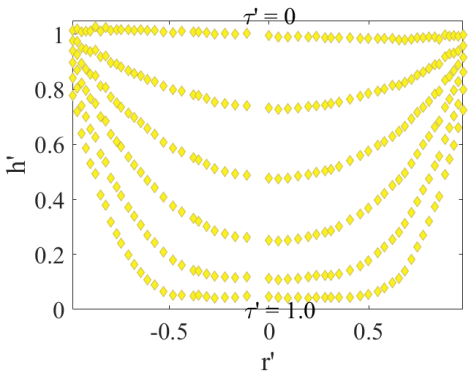


(c) U-shaped profile of the methyl benzoate droplet with $\Omega = 6.55$.

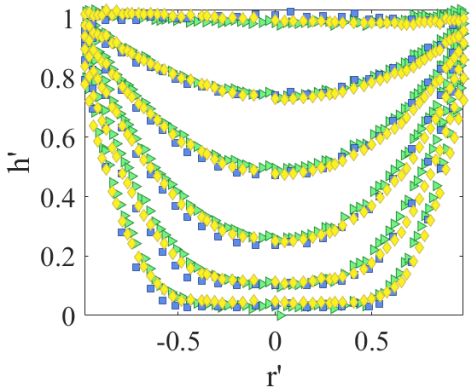


(d) The comparison of the U-shaped profiles with similar $\Omega$'s.

Figure 3.31: Reconstructed U-shaped profiles shown in Fig 3.30, presented with the non-dimensionalised scales.

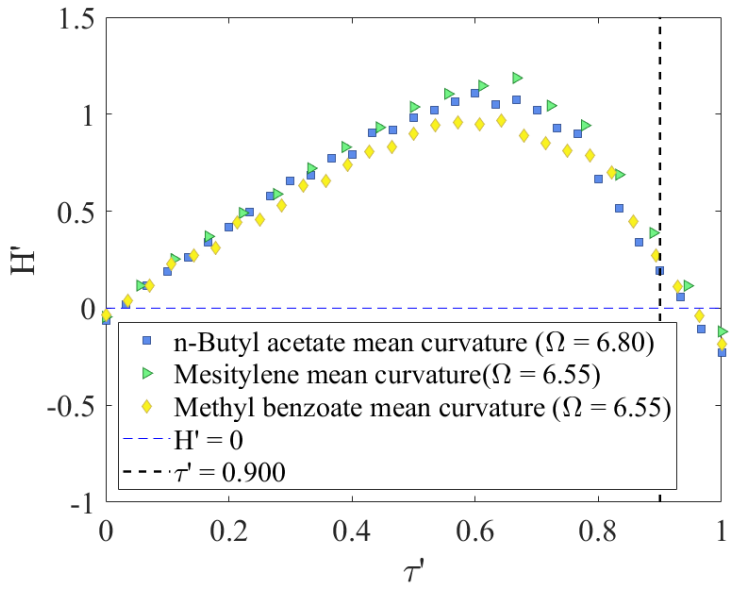


Figure 3.32: The evolutions of the mean curvature at the centre of the U-shaped profiles with the similar values of Ω shown in Fig 3.30.

droplet with $\Omega = 6.55$. The mean curvature remains a linear rise until the moment $\tau' = 0.556$. After reaching the only peak at the moment $\tau' = 0.667$, the mean curvature drops monotonically and turns to be negative at $\tau' = 0.960$ approximately.

What is more, the evolution of the mean curvature of the n-butyl acetate droplet with $\Omega = 6.80$, shown in the blue squares, rises linearly until the moment $\tau' = 0.556$, plateaus from$\tau' = 0.600$ to $\tau' = 0.667$,and falls monotonically showing a negative value at $\tau' = 0.967$.

The yellow diamonds represent the evolution of the mean curvature of the methyl benzoate droplet with $\Omega = 6.55$. Likewise, the linear rise continues between $\tau' = 0$ and $\tau' = 0.536$. At the moment $\tau' = 0.643$, the mean curvature is at the only peak, indicating the meniscus is the curviest one; and soon it plummets to a negative value at the moment $\tau' = 0.960$.

Also, the heights at the centre of the profiles, shown in Fig 3.34, behave in the similar way that all the U-shaped profiles experience two different sorts of linear drop before it touches down. The first linear decrease takes up three fifths of the total duration approximately and the beginning moment of the second linear decrease starts at the moment $\tau' \approx 0.760$.

The green triangles stay a linear drop until $\tau' = 0.667$; the falling rate slows

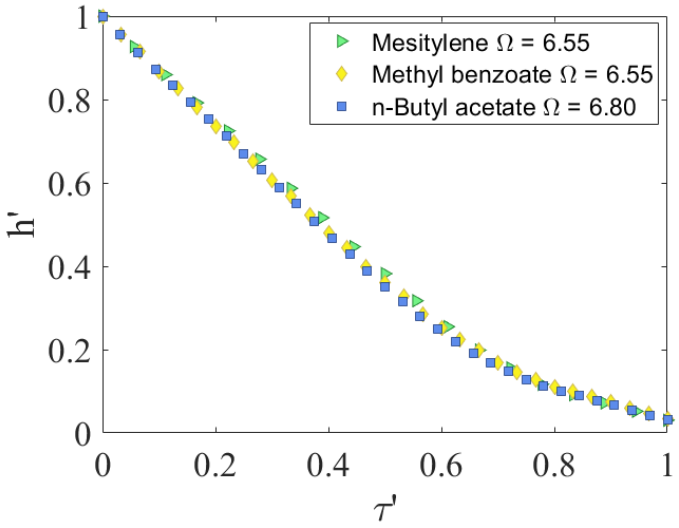


Figure 3.33: The evolutions of the height at the centre of the U-shaped profiles with the similar Ω's.

since then and follow the other linear drop at the moment $\tau' = 0.767$, the falling rate of which is not as fast as that at the beginning. The height yellow stars are the result of the methyl benzoate droplet, which follow the first sort of the linear drop until the moment $\tau' = 0.633$ and the other linear drop appears at the moment $\tau' = 0.767$. The blue squares also show the first linear drop until the moment $\tau' = 0.594$ and follows the other linear change from the moment $\tau' = 0.750$, after a period for adjustment continuing for $0.180\tau'$, approximately.

## 3.7 Effectiveness of Ω

In this section, the experimental results of pure droplets evaporating in cylindrical wells, Sec 3.7.1, the impact from the temperature of a substrate on the shape of profile, Sec 3.7.2.

In brief, according to the experimental results, the parameter, Ω, is proven effective to predict a shape of a profile from the evaporation of a droplet printed in a shallow cylindrical well. Although rising the temperature of a substrate will lower the surface tension of a droplet, leading to the decrease of the value of Ω, the viscosity and evaporation rate of the droplet grow at the same time, further complicating the evaporation. The results of mesitylene droplets evaporating on substrates with

temperature set at 45.00°C and methyl droplets evaporating on substrates with temperature set at 50.00°C, confirm the effectiveness of Ω in the prediction about the shape of a profile.

### 3.7.1 Profiles of Different Solvents

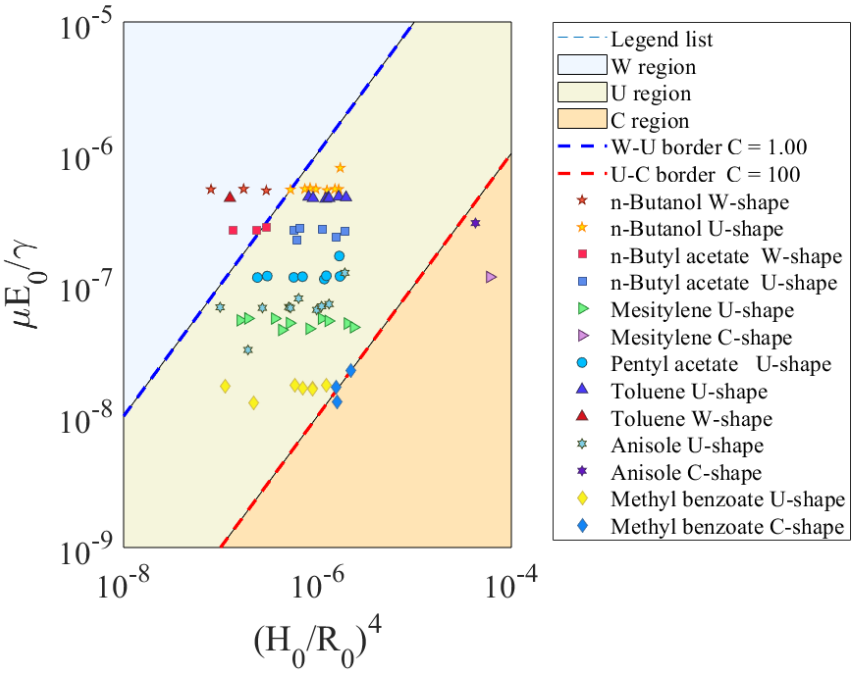


Figure 3.34: The experimental results suggesting the borders dividing W (sky blue region)/U areas(the jade region in the middle), and U/C areas(the orange region) are where the values of Ω are 1.00 and 100, respectively.

The profiles of different solvents used in this study are shown in Fig 3.34, in which only the profiles of toluene, n-butanol and n-butyl acetate show W-shaped profiles and the C-shaped profiles are from methyl benzoate, mesitylene and anisole. Here, a profile is distinguished by its evolution of the height and mean curvature at the centre, as illustrated in the preceding sections.

If the height evolution of a profile at the centre decreases following a exponential curve as a line in a semi-log plot as shown in Fig 3.25, then the profile is defined as a W-shaped profile. In addition, if the height of a profile evolves linearly until the disjoining pressure is non-negligible which is usually before the moment $\tau' = 0.900$, the profile is regarded as a C-shaped profile. For a height evolution at the centre

decreases linearly for the first few moments and turns to be a curve later during evaporation, the height evolution is regarded as a U-shaped profile.

The mean curvature at the centre for C-shaped profiles rises linearly, whereas that of W-shaped profiles have turning points with an initial value smaller than zero (a dimple at $\tau' = 0$); the mean curvature of U-shaped profiles shows a linear increases but after a specific moment, it begins to drop and, sometimes, ends with a negative value due to the impact from the disjoining pressure.

To test the effectiveness of Ω in the prediction of a profile, I conducted the experiments systematically by choosing the solvents with the evaporation rates ranging from 420 pl/s (toluene in the wells with radii of 75.0 $\mu$m) to 6.02 pl/s (methyl benzoate in the wells with radii of 75.0 $\mu$m) and the cylindrical wells with aspect ratios ranging from 1.20/75.0 to **2.50/25.0**.

According to the experimental results, only n-butanol, n-butyl acetate, toluene and methyl benzoate show different profiles; hence, the results from them are critical to verify the effectiveness of Ω. Moreover, mesitylene, pentyl acetate (CAS number: 628-63-7), and anisole droplets mainly appear to be U-shaped profiles, although there exist two C-shaped profiles in the wells whose aspect ratios are 2.20/25.0 (mesitylene, the only purple triangle with $\Omega = 524$) and 2.02/25.0 (anisole, the only purple hexagon with $\Omega = 144$), respectively.

The height evolutions of at the centre of the n-butanol droplets, n-butyl acetate droplets and methyl benzoate droplets are presented in Fig 3.35, Fig 3.36 and Fig 3.38, respectively.

In Fig 3.35, the minimum value of Ω from the U-shaped profiles of n-butanol droplets is 0.994, while the maximum of the W-shaped profiles is 0.568, as is shown in Fig 3.36b where the W-shaped profiles show the lines in the semi-log plot and the U-shaped profile with $\Omega = 0.994$ appears to be a curve. The results in Fig 3.35c and Fig 3.35d are the U-shaped profiles of n-butanol showing two sorts of linear decreases during evaporation.

The height evolutions of the n-butyl acetate droplets presented in Fig 3.34, are shown in Fig 3.36. Similarly, the W-shaped profiles of n-butyl acetate shown in Fig 3.36a and Fig 3.36b show the exponential decreases while the U-shaped profiles

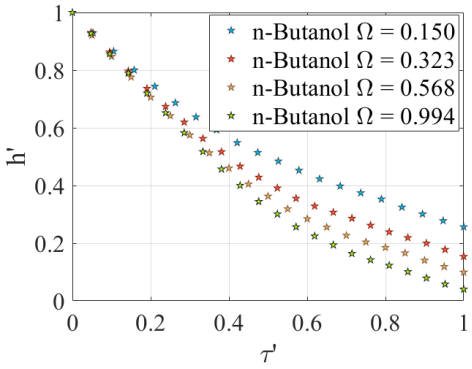


(a) The evolutions of the height at the centre of the W-shaped profiles of n-butanol droplets and the U-shaped profile with Ω = 0.994.

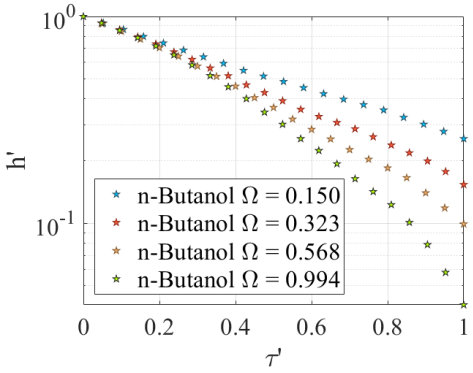


(b) The evolutions of the height at the centre of the W-shaped profiles of n-butanol droplets shown in the semi-log plot.

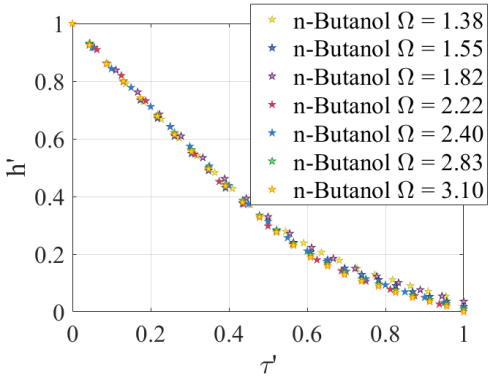


(c) The evolutions of the height at the centre of the U-shaped profiles of n-butanol droplets in which the minimum value of Ω is 0.994.

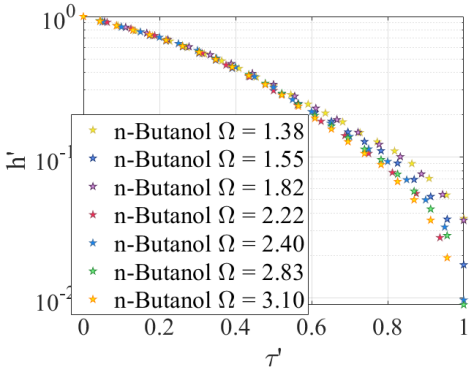


(d) The evolutions of the height at the centre of the U-shaped profiles of n-butanol droplets shown in the semi-log plot.

Figure 3.35: The evolutions of the height at the centre of the profiles from the n-butanol droplets shown in Fig 3.34.

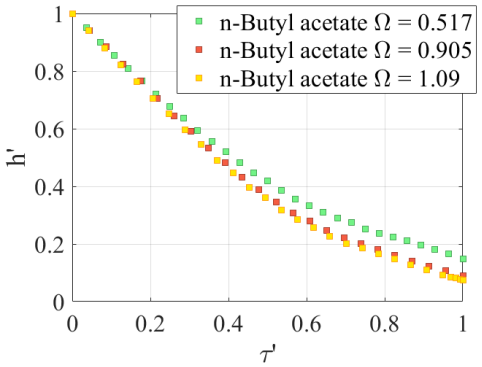


(a) The evolutions of the height at the centre of the W-shaped profiles of n-butyl acetate droplets with the maximum of Ω's being 1.09.

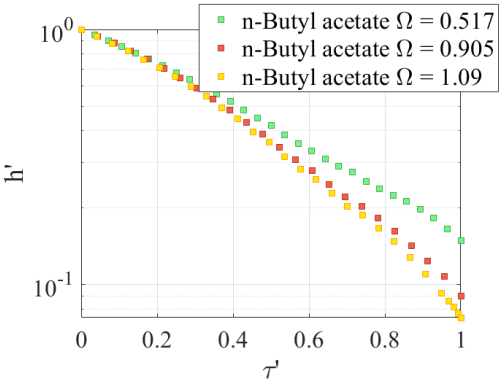


(b) The evolutions of the height at the centre of the W-shaped profiles of n-butyl acetate droplets shown in the semi-log plot.

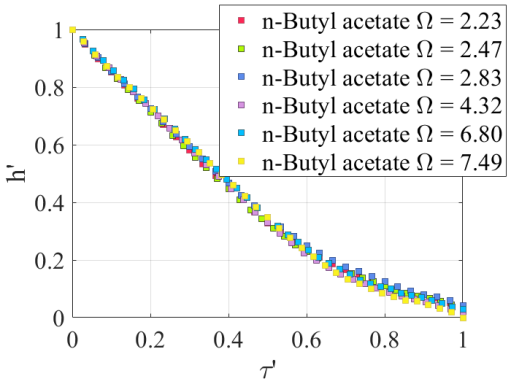


(c) The evolutions of the height at the centre of the U-shaped profiles of n-butyl acetate droplets with the minimum of Ω's being 2.23.

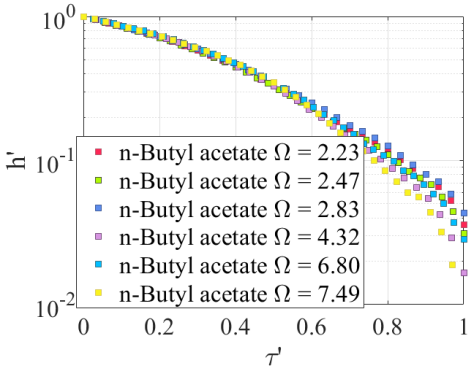


(d) The evolutions of the height at the centre of the U-shaped profiles of n-butyl acetate droplets shown in the semi-log plot.

Figure 3.36: The evolutions of the height at the centre of the profiles from the n-butyl acetate droplets shown in Fig 3.34.

in Fig 3.36c and Fig 3.36d bear two linear decreases as U-shaped profile has. The minimum value of Ω of the U-shaped profiles is 2.23, while the maximum value of Ω of the W-shaped profiles is 1.09.

The contribution of the disjoining pressure, Π in Eq 3.7.1, at the total pressure on the liquid-air interface of the U-shaped profile with $\Omega = 2.23$, is given in Fig 3.37, in which the Hamaker constant ($A_{132}$) is $-4.246 \times 10^{-20}$ J approximately [170], so that the disjoining pressure is negligible until the moment $\tau' = 0.900$. Afterwards, the disjoining pressure seems to challenge the Laplace pressure from the moment $\tau' \approx 0.950$. Therefore, $\tau' = 0.900$ is set as the end moment to distinguish the shape of a profile.

$$\Pi = -\frac{H_a}{6\pi h^3} \tag{3.7.1}$$

where

$$H_a = A_{132} \approx A_{33} - A_{13} \tag{3.7.2}$$

and

$$A_{13} = \sqrt{A_{11}A_{33}} \tag{3.7.3}$$

where the subscripts 1, 2 and 3 of $A$ denote ITO, air and n-butyl acetate, respectively [170].

The height evolutions of the methyl benzoate droplets in Fig 3.34 are presented in Fig 3.38. The U-shaped profiles show the two sorts of linear decreases until the touch-down moment with a period of transition at $0.500 < \tau' < 0.700$; the maximum value of the $\Omega'$s of the U-shaped profiles is 76.6, while the minimum value of the $\Omega'$s of the C-shaped profiles is 93.2. However, the results from the C-shaped profiles only present a linear decrease until the disjoining pressure plays an important role in the total pressure after the moment $\tau' = 0.900$.

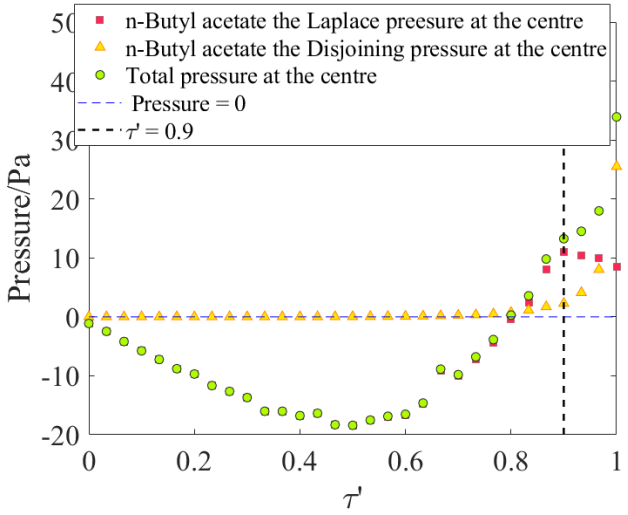


Figure 3.37: The pressure at the centre on the liquid-air interface of the U-shaped profile of n-butyl acetate with $\Omega = 2.23$.

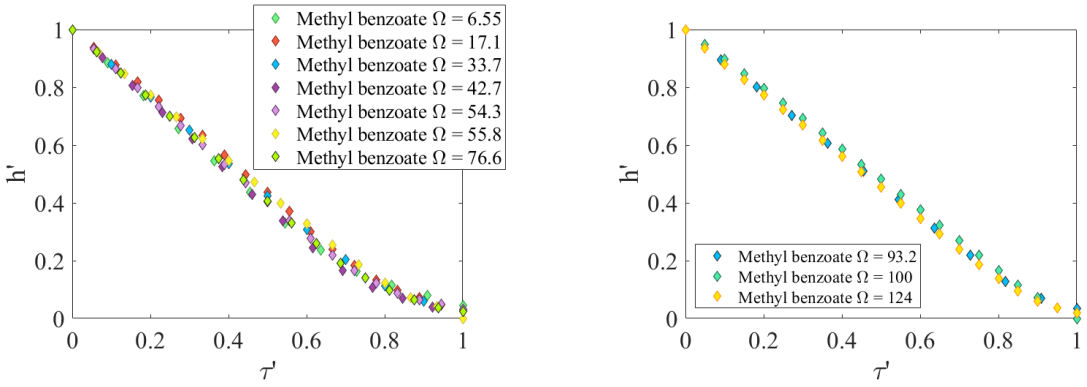


(a) The height evolution at the centre of the U-shaped profiles of methyl benzoate droplets with the maximum of the Ω's being 76.6.

(b) The height evolution at the centre of the C-shaped profiles of methyl benzoate droplets with the minimum of the Ω's being 93.2.

Figure 3.38: The evolutions of the height at the centre of the profiles from the methyl benzoate droplets shown in Fig 3.34.

### 3.7.2 The Impact from Temperature on Profiles

Temperature plays a significant role in the shape of a profile, which not only changes evaporation rate but also shifts the viscosity and surface tension of a solvent. With the increase of temperature, the evaporation rate of a solvent will rise based on the surge of its vapour pressure [149], while the values of viscosity and surface tension will fall [171] [172], leading to a complex balance between these three different factors which is indicated by the change of Ω since it combines the effects that result from evaporation rate, viscosity and surface tension altogether.

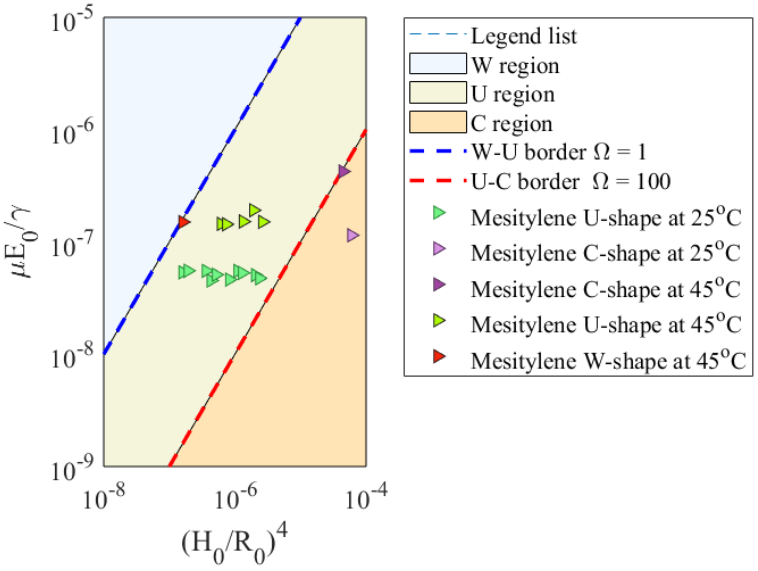


Figure 3.39: The experimental results of mesitylene at the temperature of 25.00°C and 45.00°C, respectively.

Mesitylene and methyl benzoate were chosen as the candidates to investigate the impact from temperature on the shapes of profiles. The temperature of the Peltier stage in the setup, shown in Fig 2.3, was set at 25.00 ± 0.50°C, 35.00 ± 0.50°C, 45.00 ± 0.50°C and 55.00 ± 0.50°C, respectively, for the experiments of mesitylene, while it was 50.00± 0.50°C for methyl benzoate droplets to further verify the impact from the temperature.

All the experiments were carried out with the ambient temperature and relative humidity recorded as 25.10 ± 0.11°C and 29.58 % ± 0.50 %, respectively. The surface tension and viscosity of mesitylene at the temperatures higher than 25.00°C is estimated by extending the data from the literature [149] [171] [173], as given in Fig

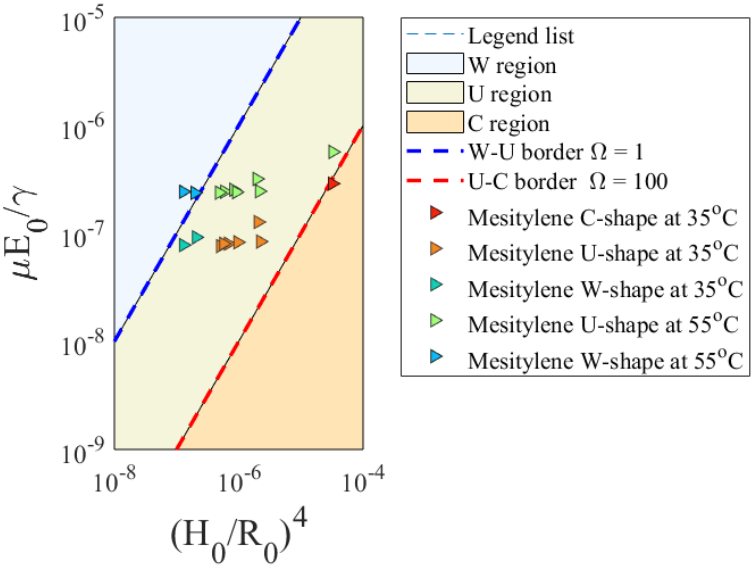


Figure 3.40: The experimental results of mesitylene at the temperature of 35.00°C and 55.00°C, respectively.

3.41a and Fig 3.41b.

The experimental results of mesitylene at the temperatures of 25.00 ± 0.50°C, 35.00 ± 0.50°C, 45.00 ± 0.50°C and 55.00 ± 0.50°C are shown in Fig 3.41. The mesitylene droplets mainly show U-shaped profiles even under the highest temperature, 55.00 ± 0.50°C, though W-shaped profiles appear when the aspect ratios of wells are 1.42/75.0 and 1.60/75.0, respectively.

When the temperature is 25.00 ± 0.50°C, the profiles of mesitylene appear to be U-shaped profiles except in the well with the aspect ratio of 1.90/25.0, shown in the purple triangle. Likewise, the only C-shaped profiles of mesitylene at the temperatures of 35.00 ± 0.50°C and 45.00 ± 0.50°C are found in the well with the aspect ratio of 1.90/25.0, as shown in the purple triangles in Fig 3.39 and the red triangle in Fig 3.40.

Unlike what happens to the well with the aspect ratio of 1.90/25.0 under the temperature of 25.00 ± 0.50°C, 35.00 ± 0.50°C and 45.00 ± 0.50°C, there is a U-shaped profile emerging when the temperature was set at 55.00 ± 0.50°C ( one of the green triangles in Fig 3.40).

On the other hand, W-shaped profiles only appear when the temperature is higher than 25.00°C. Under the temperatures of 35.00 ± 0.50°C and 55.00 ± 0.50°C,

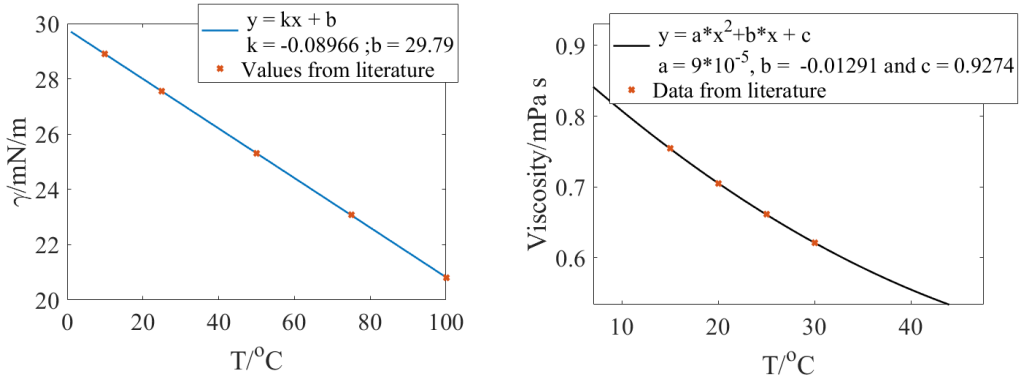


(a) The surface tension of mesitylene changing with temperature; the orange crosses are the data from the literature [149] while the blue line is a linear fit.

(b) The viscosity of mesitylene changing with temperature. The orange crosses are the data from the literature [149] while the black curve is a parabolic fit.

Figure 3.41: The surface tension and viscosity of mesitylene at different temperatures from the literature [149] [171] [173] and the fit curves.

the W-shaped profiles of mesitylene, shown in the cyan triangles for $35.00 \pm 0.50$°C and navy triangles for $55.00 \pm 0.50$°C, appear when the aspect ratios of wells are 1.42/75.0 and 1.60/75.0, while under the temperatures of $45.00 \pm 0.50$°C, the aspect ratio is 1.50/75.0.

As is mentioned before, temperature contributes to the change of the three factors, namely evaporation rate, viscosity and surface tension. For instance, the evaporation rate of mesitylene at 45.00°C is 135 pl/s approximately, while it is only 39.5 pl/s at 25.00 °C; in addition, the viscosity and surface tension of mesitylene increase from 0.507 mPa s and 25.76 mN/m (at 45.00°C) to 0.661 mPa s and 27.55 mN/m (at 25.00°C), respectively [174]. Therefore, the combination of these three factors increases by $9.7 \times 10^{-8}$ from 25.00°C to 45.00°C as shown in Eq 3.7.4 and 3.7.5. With the rise of temperature, the capillary number increases so that the value of Ω plummets, accordingly. In consequence, U-shaped profiles turn to W-shaped profiles and C-shaped profiles turn to U-shaped profiles.

$$\frac{\mu E_0}{\gamma} = 5.4 \times 10^{-8} \quad T_{sub} = 25.00 \pm 0.50°C \tag{3.7.4}$$

$$\frac{\mu E_0}{\gamma} = 1.5 \times 10^{-7} \quad T_{sub} = 45.00 \pm 0.50°C \tag{3.7.5}$$

where $T_sub$ is the temperature of a substrate.

The results show that rising the temperature of a substrate is an effective way to change the shape of a profile from a C-shaped profile to a U-shaped profile, or even, a U-shaped profile to a W-shaped profile.

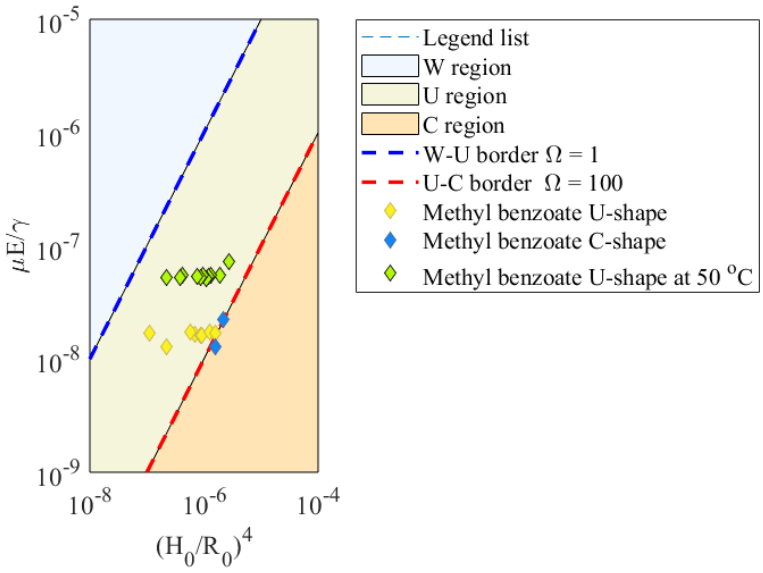


Figure 3.42: The comparison of the results of methyl benzoate droplets at the temperatures of 25.00 ± 0.50°C and 50.00 ± 0.50°C, respectively.

The experimental results of methyl benzoate droplets at 50.00±0.50°C are shown in Fig 3.42 where we can find that the profiles are only U-shaped even in the wells in which methyl benzoate droplets are C-shaped profiles under the temperature of 25.00 °C.

The evaporation rate of methyl benzoate is 31.0 pl/s under the temperature of 50.00 ± 0.50°C which is almost five times as much as it is at 25.00°C (6.10 pl/s) and is large enough to overcome the change of the property at the different temperatures, leading to the shapes of profiles become the U-shaped profiles with larger flat bottoms when the droplets touch down, as is shown in Eq 3.7.6 and 3.7.7, in which the capillary number of methyl benzoate increases from $1.7\times10^{-8}$ to $5.4\times10^{-8}$. Hence. the value of Ω at 50.00 $°C$ decreases substantially, which agrees with the fact that the profiles under the higher temperature have flatter bottoms when the droplets are about to touch down at the base and the flat bottoms emerges earlier in an evaporation process, if the number of Ω is smaller.

$$\frac{\mu E}{\gamma} = 1.7 \times 10^{-8} \quad T_{sub} = 25.00 \pm 0.50°C \tag{3.7.6}$$

$$\frac{\mu E}{\gamma} = 5.4 \times 10^{-8} \quad T_{sub} = 50.00 \pm 0.50°C \tag{3.7.7}$$

where $T_{sub}$ means the temperature of a substrate, patterned with cylindrical wells, controlled by the Peltier stage.

In conclusion, when the temperature of a substrate increases, the viscosity and surface tension of mesitylene and methyl benzoate will fall, but the evaporation rates will rise. The change of the capillary number depends on the degree that the viscosity, surface tension and vapour pressure change with the temperature. For methyl benzoate, once the temperature rises from 25.00 °C to 50.00 °C, the extent of the rise of evaporation rate is large enough to dominate the change of the ratio $\mu/\gamma$ so that the capillary number rises which means that the impact from the viscosity on the internal flow in the liquid becomes more significant, levelling the cap-like shape into a flat bottom; thus the profiles located at C-region at 25.00 °C enter into U-region at 50.00 °C.

# CHAPTER 4

## Binary Solvents: New Profiles and its Features

No matter in industry or academia, binary systems, ternary systems or even more complex ones are most common for the purpose of achieving flat and uniform layers [175].

In this chapter, I mainly pay attention to the new shapes emerging from binary systems and how these shapes relate to the theoretical evaporation rate when the solvents obey Raoult's law. With reference to the shapes, besides C-shaped profiles, U-shaped profiles and W-shaped profiles, the new shapes of profiles include M-shaped profile, spreading profile, bell-shaped profile and lopsided profile, which result from surface tension gradients and, therefore, the Marangoni flow inside the droplet.

Due to the preferential evaporation of the more volatile solvent, there emerges a gradient of the more volatile solvent along the direction of the r-axis, which changes the surface tension and viscosity at a position. The refractive index and the analysis of the error in experiment owing to the preferential evaporation is introduced in Sec 2.5. The evaporation rate of a binary solvent system in a cylindrical well is illustrated in Sec 4.1. Also, Marangoni flow arises because of the surface tension gradient and the strength of Marangoni flow is indicated by Ma, the Marangoni number. In the end, the results from the solvents with similar surface tension are given in Sec 4.2.

As viscosity also plays an important role in the evaporation process of pure solvent droplet, shown in the parameter $\Omega$, three different groups of binary mixtures are designed to investigate the influence from viscosity by choosing different mass fractions; meanwhile, the impact from the aspect ratio of a well on evaporation is also researched.

## 4.1 Evaporation Rate of a Binary Mixture Droplet in a Cylindrical Well

Based on the definition of evaporation rate $dm/dt$ that is shown in Eq 3.1.3, the expression of evaporation rate for a binary droplet is

$$-\frac{dm}{dt} = \iint_S (\mathbf{J}_{m1} + \mathbf{J}_{m2}) \cdot d\mathbf{S} = \iint_S (\mathbf{J}_{m1} + \mathbf{J}_{m2}) \cdot \mathbf{n} dS \tag{4.1.1}$$

where $\mathbf{J}_{m1}$ and $\mathbf{J}_{m2}$ denote the fluxes of component 1 and component 2, respectively. Hence, the evaporation rate of a binary mixture may be regarded as the combination of two fluxes

$$\frac{dm}{dt} = \frac{dm_1}{dt} + \frac{dm_2}{dt} \tag{4.1.2}$$

where

$$-\frac{dm_1}{dt} = \iint_S \mathbf{J}_{m1} \cdot \mathbf{n} dS \tag{4.1.3}$$

$$-\frac{dm_2}{dt} = \iint_S \mathbf{J}_{m2} \cdot \mathbf{n} dS \tag{4.1.4}$$

Applying the FEM result of $dm/dt$ achieved by Hu and Larson to the individual component in a binary mixture, as we have done to a pure solvent droplet in Eq

3.1.5, the expressions of $dm_1/dt$ and $dm_2/dt$ are [1]

$$-\frac{dm_1}{dt} = \frac{4D_1\,(1-R_{h1})\,R\,p_{v1}M_{w1}}{R_cT_c} \qquad \theta \sim 0 \tag{4.1.5}$$

$$-\frac{dm_2}{dt} = \frac{4D_2\,(1-R_{h2})\,R\,p_{v2}M_{w2}}{R_cT_c} \qquad \theta \sim 0 \tag{4.1.6}$$

where $p_{v1}$ and $p_{v2}$ are the partial vapour pressures of solvent 1 and solvent 2 respectively.

If each component in a binary mixture obeys Raoult's law, as shown in Eq 4.1.7 and Eq 4.1.8, namely the partial vapour pressure equal to the product of the mole fraction by the vapour pressure of the pure component, then the mixture is an ideal solution. [176]

$$p_{v1} = p^0_{v1}x_1 \tag{4.1.7}$$

$$p_{v2} = p^0_{v2}x_2 \tag{4.1.8}$$

However, if components differ in molecular structures, its vapour pressures will have deviation from Raoult's law [87], such as the mixture of toluene and n-butanol.

Assuming that component 1 and component 2 comply with Raoult's law, the evaporation rate of a binary mixture written in the loss of volume are

$$-\frac{dV_1}{dt} = \frac{4D_1\,(1-R_{h1})\,R\,p^0_{v1}x_1M_{w1}}{R_cT_c\;\rho_1} \tag{4.1.9}$$

$$-\frac{dV_2}{dt} = \frac{4D_2\,(1-R_{h2})\,R\,p^0_{v2}x_2M_{w2}}{R_cT_c\;\rho_2} \tag{4.1.10}$$

where $R_{h1}$ and $R_{h2}$ are the concentrations of component 1 and component 2 in the vapour phase far from the space over the binary mixture droplet, and the values of them are zero, when there are no open sources of the solvents in the ambience nearby the setup. Thus, the total evaporation rate of this mixture is

$$-\frac{dV}{dt} = 4R\frac{D_1p^0_{v1}x_1M_{w1}\,\rho_2 + D_2p^0_{v2}x_2M_{w2}\,\rho_1}{R_cT_c\rho_1\rho_2} \tag{4.1.11}$$

from which we can find that the evaporation rate of a binary droplet depends on the diffusion coefficients, densities, mole fractions and vapour pressures of the solvents, if it is an ideal solution, the radius of a cylindrical well and the temperature which is controlled by the Peltier stage. As a binary droplet evaporates, the mole fractions of the components may change due to the preferential evaporation of the more volatile solvent. According to the volume loss rates expressed in Eq 4.1.9 and Eq 4.1.10, the changing rate of the amount of substance for the two solvents are

$$-\frac{dn_{m1}}{dt} = \frac{4D_1 R\, p_{v1}^0 x_1}{R_c T_c} \tag{4.1.12}$$

$$-\frac{dn_{m2}}{dt} = \frac{4D_2 R\, p_{v2}^0 x_2}{R_c T_c} \tag{4.1.13}$$

let

$$C_1 = \frac{4D_1 R\, p_{v1}^0}{R_c T_c} \tag{4.1.14}$$

$$C_2 = \frac{4D_2 R\, p_{v2}^0}{R_c T_c} \tag{4.1.15}$$

$$\frac{C_1}{C_2} = \frac{D_1 p_{v1}^0}{D_2 p_{v2}^0} \tag{4.1.16}$$

in which $D_1$, $R$, $p_{v1}^0$,$p_{v2}^0$, $R_C$ and $T_c$ remain fixed during the evaporation; therefore, we have

$$-\frac{dn_{m1}}{dt} = C_1 x_1 \tag{4.1.17}$$

$$-\frac{dn_{m2}}{dt} = C_2 \left(1 - x_1\right) \tag{4.1.18}$$

$$-\frac{dn_{mt}}{dt} = \left(C_1 - C_2\right) x_1 + C_2 \tag{4.1.19}$$

where $n_{mt}$ is the sum of the amount of substance of component 1 and component 2.

$$n_{mt} = n_{m1} + n_{m2} \tag{4.1.20}$$

if $C_1 \approx C_2$ or $C_2 >> |C_1 - C_2|\, x_1$, the evaporation rate of a binary mixture droplet will be similar to that of a pure droplet. According to the definition of mole fraction of a substance, namely $x_1 = n_{m1}/(n_{m1} + n_{m2})$, we have

$$dx_1 = d\left(\frac{n_{m1}}{n_{m1} + n_{m2}}\right) \tag{4.1.21}$$

that is

$$dx_1 = \frac{1}{n_{m1} + n_{m2}} dn_{m1} + \frac{-n_{m1}}{(n_{m1} + n_{m2})^2} d\left(n_{m1} + n_{m2}\right) \tag{4.1.22}$$

Since $n_{m1}$ and $n_{m2}$ are changing as a binary droplet evaporates as shown above, we can find

$$-\left(n_{m1} + n_{m2}\right)^2 dx_1 = \left(C_1 n_{m2} + C_2 n_{m1}\right) x_1 dt - C_2 n_{m1} dt \tag{4.1.23}$$

that is

$$dx_1 = \frac{(C_2 - C_1)(1 - x_1)x_1}{n_{m1} + n_{m2}} dt \tag{4.1.24}$$

integrating both sides, we have

$$x_1 = \frac{1}{1 + P_1 e^{P_2 t}} \tag{4.1.25}$$

where

$$P_1 = \frac{1 - x_1^0}{x_1^0} \tag{4.1.26}$$

$$P_2 = (C_1 - C_2) \int \frac{1}{n_{mt}} dt \tag{4.1.27}$$

Since the initial mole fraction of a component is always smaller than 1, $P_1 > 0$ holds, showing that the evolution of $x_1$ bears the similarities with a logistic curve. When $(C_2 - C_1)$ is larger than 0, component 2 evaporates faster and the mole fraction

of component 2 falls following a path of a logistic curve.

To investigate the impact from the values of $C_1$ and $C_2$ on a binary droplet evaporating in a cylindrical well, here I show the theoretical results of the cases where $C_1/C_2$ are equal to 0.01, 0.1, 1, 10 and 100, respectively. Pentyl acetate is chosen as the reference solvent, denoted as component 2, while component 1 is defined here by changing the amount of diffusion coefficient of pentyl acetate to adjust the ratio of $C_1/C_2$.

In order to calculate $C_2$ and the evaporation curve(Volume-time), the depth and radius of the host well are assumed to be 2.00 $\mu$m and 75 $\mu$m, respectively, with the initial volume of a binary droplet set as much as the volume of the cylindrical well. The mass ratio of component 1 and component 2 at the initial moment is 1:1 and each component obeys Raoult's law; the results including the evolutions of mole fractions and volumes are presented in Fig 4.1 and Fig 4.2 in which the component in a binary mixture with the higher value of $C$ evaporates faster.

More details about the value of diffusion coefficient of component 1 and component 2 are given in Table 4.1.

| Solvent | Vapour pressure kPa | Diffusion coefficient in air $\times 10^{-2}$cm$^2$/s | $-dV/dt$ pl/s | $R_0$ $\mu$m | $H_0$ $\mu$m | $\frac{C_1}{C_2}$ |
|---|---|---|---|---|---|---|
| Pentyl acetate$*$ | 0.60 | 0.0610 | 6583 | 75 | 2.00 | 0.01 |
| Pentyl acetate | 0.60 | 0.610 | 658.3 | 75 | 2.00 | 0.1 |
| Pentyl acetate$*$ | 0.60 | 6.10 | 65.83 | 75 | 2.00 | 1.0 |
| Pentyl acetate$*$ | 0.60 | 61.0 | 6.583 | 75 | 2.00 | 10 |
| Pentyl acetate$*$ | 0.60 | 610 | 0.6583 | 75 | 2.00 | 100 |

Table 4.1: Diffusion coefficient in air of pentyl acetate changed (marked with $*$) to adjust the value of $C_1/C_2$; for example, to achieve the result when $C_1/C_2 = 0.1$, the diffusion coefficient of pentyl acetate is decreased to $6.10\times10^{-3}$ cm$^2$/s, while the original data of pentyl acetate is $6.10\times10^{-2}$cm$^2$/s which is chosen as component 2 in the mixtures [149] [177].

When $C_1/C_2 = 1$, the mole fractions of component 1 and component 2 remain constant until the droplet evaporates completely; at the same time, the evaporation rate of the droplet at different moments is double as much as that of either component in the mixtures, namely component 1 or component 2, which suggests

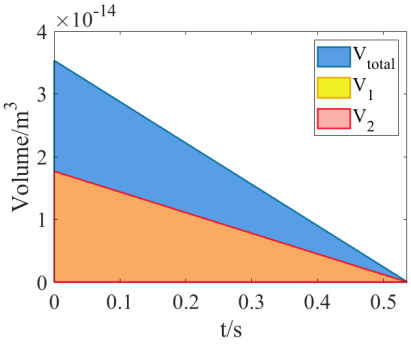


(a) The evolution of volume of a mixture in which $C_1/C_2 = 1$

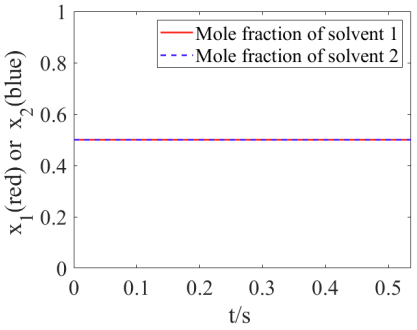


(b) The evolutions of mole fraction of a mixture in which $C_1/C_2 = 1$

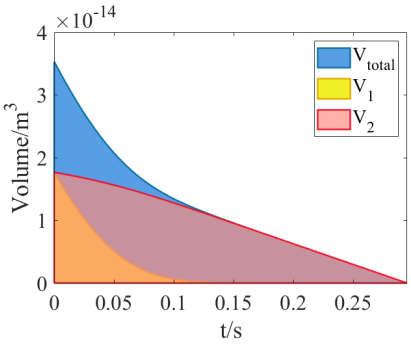


(c) The evolution of volume of a mixture in which $C_1/C_2 = 10$

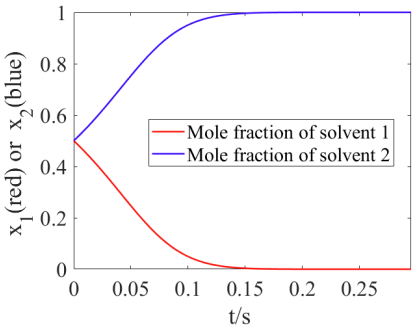


(d) The evolution of mole fraction from a mixture in which $C_1/C_2 = 10$

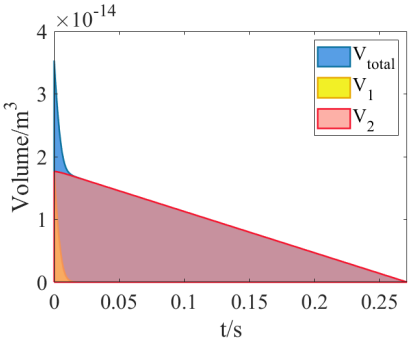


(e) The evolution of volume of a mixture in which $C_1/C_2 = 100$

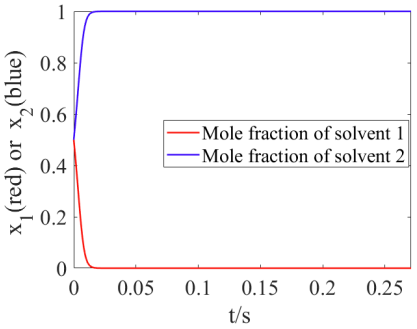


(f) The evolution of mole fraction from a mixture in which $C_1/C_2 = 100$

Figure 4.1: The Evolution of volume and composition of binary droplets whose mass ratios are 1:1 at the initial moment, while the values of $C_1/C_2$ are 1:1 , 1:10 and 1:100, respectively.

that the mixture whose value of $C_1/C_2$ is 1, behaves identically to a pure droplet of component 1, as shown in Fig 4.1a and Fig 4.1b.

In Fig 4.1c and Fig 4.1e, it can be seen that component 1, which is the more volatile component in the mixtures, leaves the droplet earlier than component 2 does, although the two components have the same mass at the initial moment; what is more, the larger the value of $C_1/C_2$ is, the faster component 1 dries up, as compared in Fig 4.1a , Fig 4.1c and Fig 4.1e. Also, the mole fraction of component 1 plummets more quickly than component 2 does, and this tendency becomes more apparent if the value of $C_1/C_2$ is larger, as shown in Fig 4.1b, Fig 4.1d and Fig 4.1f.

In Fig 4.1f the mole fraction of component 1 approaches zero when $t = 0.012$ s approximately; therefore, the droplet behaves like a pure droplet of component 2 afterwards, leading to the fixed value of evaporation rate, which is represented by the slope of $V_{total}$ in Fig 4.1e. It indicates that $C_1/C_2$ can be taken as a means to verifying the degree of how much a binary mixture droplet behaves differently from a pure droplet; in other words, the larger the value of $C_1/C_2$ is, the more analogously a binary droplet will behave like a pure droplet during evaporation.

Likewise, the evolutions of the volume and mole fraction of the binary mixtures with $C_1/C_2 = 0.1$ and $C_1/C_2 = 0.01$, respectively, are shown in Fig 4.2.

For the cases of $C_1/C_2 = 0.1$ and $C_1/C_2 = 0.01$, component 1 evaporates more slowly than component 2 does, as indicated in Fig 4.2a and 4.2c, where the yellow areas represent the volume of component 1 at different moments. Since component 1 is the less volatile component indicated by the value of $C_1/C_2$, the droplets of $C_1/C_2 = 0.1$ and $C_1/C_2 = 0.01$, contain more and more component 1 counted in mole fraction, as shown in Fig 4.2b and Fig 4.2d, and finally the whole droplets resemble to pure droplets of component 1.

The triple overlapped areas in Fig 4.2a and Fig 4.2c, which are located before the evaporation rate turns to a fixed value, are related to the value of $C_1/C_2$. If the magnitude of $log_{10}(C_1/C_2)$ becomes larger, the proportion of the triple overlapped will shrink. When $C_1/C_2 = 0.1$, the volume change turns to be linear from the moment 1.20 s while the total duration is 2.92 s; however, if $C_1/C_2 = 0.01$, the total duration is 27.1 s with the moment when volume change becomes linear at $t = 1.30$

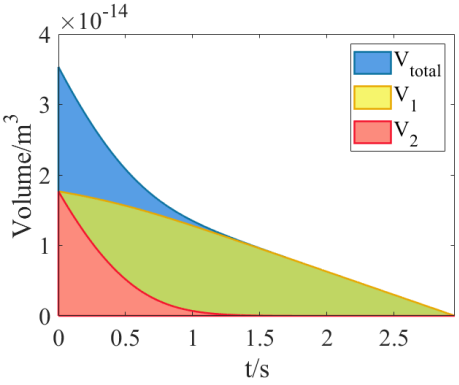


(a) The evolution of volume from a mixture in which $C_1 : C_2 = 0.1$

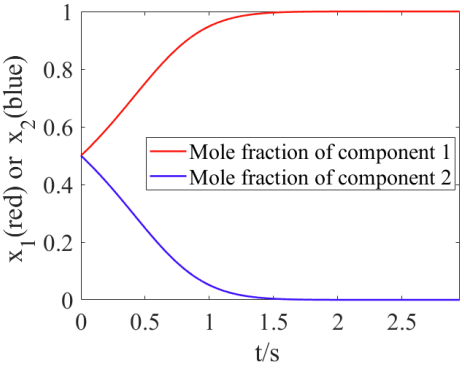


(b) The evolution of mole fraction from a mixture in which $C_1/C_2 = 0.1$

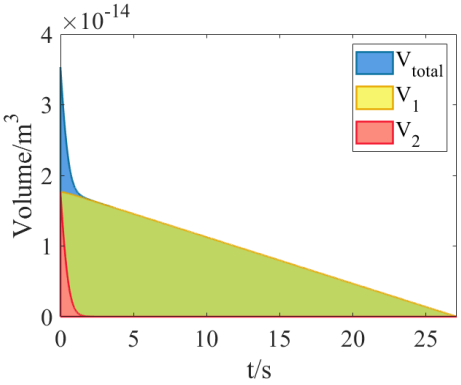


(c) The evolution of mole fraction from a mixture in which $C_1/C_2 = 0.01$

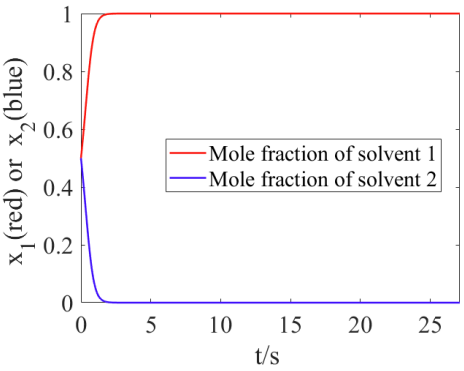


(d) The evolution of mole fraction from a mixture in which $C_1/C_2 = 0.01$

Figure 4.2: The Evolution of volume and compositions of binary droplets whose mass ratios are 1:1 at the initial moment, when $C_1/C_2 = 0.1$ and $C_1/C_2 = 0.01$, respectively.

s.

Although the duration of evaporation differs in the cases of $C_1/C_2 = 100$ and $C_1/C_2 = 0.01$, the more volatile component disappears at the same proportion of the duration, 0.013/0.271 for $C_1/C_2 = 100$ and 1.30/27.1 for $C_1/C_2 = 0.01$. Thus, when considering the impact from the value of $C_1/C_2$ on the preferential evaporation, it is reasonable to regard the more volatile component as component 1 in the analysis shown in this chapter.

### 4.1.1 Evaporation of n-Butanol and n-Butyl Acetate

| Mixture | n-butyl acetate g ($m_1$) | n-butanol g ($m_2$) | $m_1/m_2$ | $C_1/C_2$ | $H_0$ $\mu$m | R $\mu$m | Profile shapes |
|---|---|---|---|---|---|---|---|
| 1 | 2.7009 | 0.30010 | 9.0000 | 1.51 | 2.00 | 75.0 | W |
| 2 | 1.5209 | 1.5002 | 1.0138 | 1.51 | 2.15 | 75.0 | W |
| 3 | 0.32000 | 2.7050 | 0.11830 | 1.51 | 2.10 | 75.0 | W |

Table 4.2: Details of the results of the binary solvents shown in Fig 4.3.

The binary solvent system of n-butanol and n-butyl acetate has the ratio $C_1/C_2$ of 1.51. To investigate the influence of mass ratio, the mass ratios of n-butyl acetate and n-butanol are set at 9.0000, 1.0138 and 0.11830, as given in Table 4.2 in which the profiles from the binary solvents showed W-shaped profiles.

The theoretical volume change of the the binary solvent with $m_1/m_2 = 9.0000$ is identical to the result from experiment, as shown in Fig 4.3a; furthermore, the mole fractions shown in Fig 4.3b illustrate that the mole fraction of n-butyl acetate is decreasing while that of n-butanol increases, which is due to the preferential of the more volatile solvent, n-butyl acetate, in the binary solvent; however, the amount of n-butyl acetate is the majority component until the droplet touches down.

In spite of the slight differences, the theoretical volume changes of the binary solvent with $m_1/m_2 = 1.10138$ and 0.11830 agree mostly with the experiment results shown in Fig 4.3c and Fig 4.3d. The evaporation rates of the both groups are lower than the predicted values, indicating that either component in the binary systems evaporates more slowly. Assuming that diffusion coefficients in air do not change,

the vapour pressures of n-butanol and n-butyl acetate are lower than them in the pure droplets.

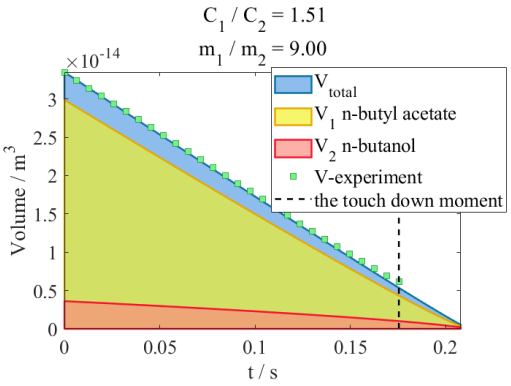


(a) The evolution of the volumes from the mixture of n-butyl acetate and n-butanol in which $C_1 : C_2 = 1.51$ and $m_1 : m_2 = 9.00$.

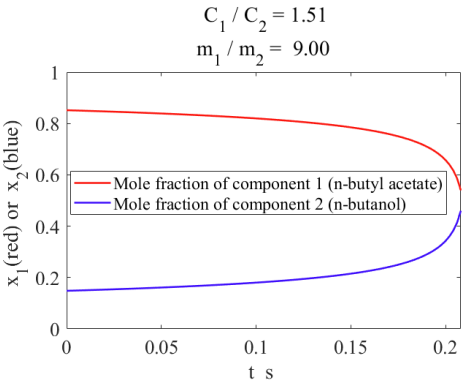


(b) The evolution of the mole fractions from the mixture of n-butyl acetate and n-butanol in which $C_1 : C_2 = 1.51$ and $m_1 : m_2 = 9.00$.

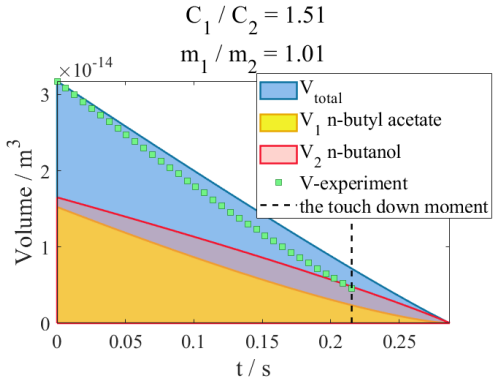


(c) The evolution of the volumes from the mixture of n-butyl acetate and n-butanol in which $C_1 : C_2 = 1.51$ and $m_1 : m_2 = 1.01$.

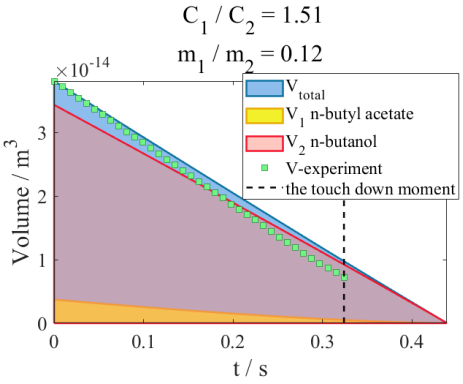


(d) The evolution of the volumes from the mixture of n-butyl acetate and n-butanol in which $C_1 : C_2 = 1.51$ and $m_1 : m_2 = 0.12$.

Figure 4.3: The comparisons of the theoretical results of the binary systems containing n-butanol and n-butyl acetate and its experiment results.

In conclusion, according to the results shown in Fig 4.1 and Fig 4.2, we can find that the preferential evaporation of the more volatile component exists in a binary droplet when the components are assumed to obey Raoult's law and evaporate at different rates. The existence of preferential evaporation induces that the changes of the properties of a binary droplet with time. Locally, the concentration of the more volatile component at the contact line which is pinned at the brim of a cylindrical well, may not be equal with its concentration at the centre of the well; if the velocity of the internal flow is not large enough to bring the more volatile component from

the centre to the contact line to compensate the loss due to evaporation, there will emerge a new internal flow because of the appearance of surface tension gradient, which is also known as the Marangoni effect. The direction of the Marangoni flow depends on the difference of the surface tension and moves from the area with lower surface tension to the area with the higher one.

In Fig 4.1 and Fig 4.2, I assume that the contact line is fixed and there is no new contact line appearing during evaporation; however, once a droplet has touched town on the base, a new contact line or two will emerge so that the evaporation rate changes. Thus, the result about the evaporation rate of a binary solvent is only reliable to predict the evaporation rate of a binary droplet before it reaches the touch-down moment.

In 4.3d, the theoretical evaporation rate of the binary droplet of n-butyl acetate and n-butanol with mass ratio of 9.0000 agrees with the experiment result, while the theoretical evolutions of the mole fractions are shown in Fig 4.3b suggesting that the droplet becomes richer and richer in the less volatile solvent, n-butanol. Since the difference of the surface tensions of the single solvents is only 0.05 mN/m, the Marangoni flow may not dominate and the capillary flow due to evaporation plays a key role in the internal flow; therefore, the shapes of the profiles are W-shaped. The experiment results of volume changes in Fig 4.3c and Fig 4.3d are lower than that of the theoretical results, which result from the negative deviation of the binary system as the attraction between n-butanol and n-butyl acetate becomes stronger when the amount of n-butanol increases.

If $C_1 - C_2 > 0$ and $\gamma_1 - \gamma_2 > 0$ hold, namely the more volatile solvent has the higher surface tension, or $C_1 - C_2 < 0$ and $\gamma_1 - \gamma_2 < 0$, that is the less volatile solvent has the lower surface tension, are true, then the value of $(\gamma_1 - \gamma_2)(C_1 - C_2)$ is positive; therefore, the evolution of surface tension decreases and appears to be the reverse of a logistic curve.

However, when $C_1 - C_2 < 0$ and $\gamma_1 - \gamma_2 > 0$ exist, namely the less volatile solvent has the higher surface tension, or $C_2 - C_1 > 0$ and $\gamma_1 - \gamma_2 < 0$, that is the more volatile solvent has the lower surface tension, hold, the surface tension in the binary solvent increases and appears to be logistic-curve-like. Therefore, the surface

tension does not change with time if components in a binary system have the same surface tension or the same evaporation rate or if one of the component does not exist any more, $x_1 = 0$ or $x_2 = 0$; and, in these cases, the Marangoni effect will not emerge in the binary systems.

Here, I assume the strength of the Marangoni flow is related to the degree of the preferential evaporation, so that the typical definition of the Marangoni number, Ma,

$$Ma = \frac{R\Delta\gamma}{\mu D} \tag{4.1.1}$$

where $\Delta\gamma$ is the surface tension difference due to the preferential evaporation, is transferred to

$$\Delta\gamma = \frac{\partial_t \gamma R}{u_r} \tag{4.1.2}$$

where $u_r$ is the velocity along the r-direction

$$Ma = \frac{R^2 \partial_t \gamma}{\mu h u_r^2} = \frac{R^2}{\mu h u_r^2} \frac{(\gamma_1 - \gamma_2)(C_2 - C_1)(1 - x_1)x_1}{n_{m1} + n_{m2}} \tag{4.1.3}$$

In terms of the impact induced by the mole fraction of a component, the Marangoni effect is the most acute when $x_1 = 0.5$ as indicated by $(1 - x_1)x_1$; furthermore, the Marangoni effect becomes more obvious with the increase of the difference of evaporation rate or surface tension. Also, the geometrical feature of a host well contributes to the Marangoni effect as well; the lower an aspect ratio of a well is, the stronger the Marangoni effect will be.

Moreover, when $d\gamma/dt > 0$ so that $Ma > 0$, the more volatile solvent has the lower surface tension, and the Marangoni flow moves towards the contact line [106]; if $d\gamma/dt < 0$, the more volatile solvent has the lower surface tension, and the Marangoni flow points towards the centre of a droplet, in which case $Ma < 0$.

## 4.2 New Profiles Emerging from Binary Droplets

Apart from W-shaped profile, U-shaped profile and C-shaped profile found from the evaporation of pure droplets in swallow cylindrical wells, there are four new kinds of profiles appearing, namely bell-shaped profile, M-shaped profile, lopsided profile and spreading profile.

In each subsection, a new profile is illustrated, following the itinerary:

1. what is the definition of a new shape of profile?
2. an example of this sort of profile and its geometrical features;
3. when does the new shape of profile occur?

The characteristic time, $\tau'$, for the experiments of binary droplets is selected at the moment when the height at the centre of a profile is equal to the depth of its host well.

### 4.2.1 Bell-shaped Profile

Bell-shaped profile, which has a bell-shaped meniscus shown in Fig 4.4a, whether it remains for long or short, is a new sort of profile found in this work. When the meniscus of a droplet appears to be bell-shaped with the height at the centre higher than the depth of its well, the majority of the droplet near the centre is concave down, while the height profile near the brim of its host well is concave up, which is clearly reflected by the sign of the mean curvature along the direction of radius. The principal curvatures, mean curvature and Gaussian curvature of the meniscus shown in Fig 4.4a, is presented in Fig 4.4b. It clearly shows that the sign of the mean curvature is negative in the region where $0 \leq r < 62.5\mu$m and positive in $r > 62.5\mu$m which only accounts for 16.7%. The sign change of the mean curvature along the direction of radius is the main difference between a bell-shaped profile and a spherical cap.

Therefore, according to the definition of the Laplace pressure in Eq 2.4.4, that the pressure decreases monotonically from the centre to the edge means the internal flow in a bell-shaped profile is joined by the gradient of the Laplace pressure.

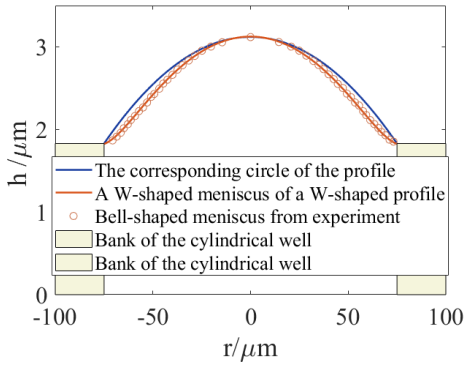


(a) An example of bell-shaped meniscus from the binary droplet comprising 0.9400 g (28.66%) anisole and 2.110 g (71.34%) mesitylene, evaporating in the cylindrical well with depth and radius of 1.81 $\mu$m and 75.0 $\mu$m, respectively.

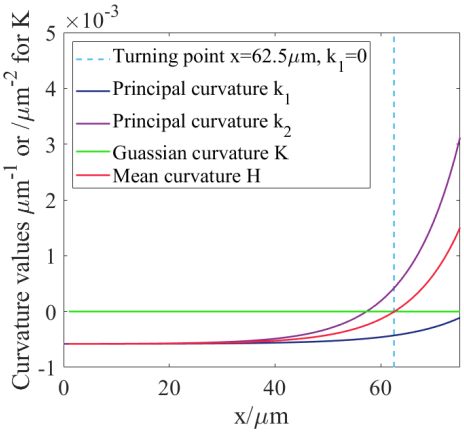


(b) The principal curvatures, mean curvature and Gaussian curvature along the direction of radius of the meniscus, shown in Fig 4.4a.

Figure 4.4: A bell-shaped meniscus of the binary droplet of anisole and mesitylene and its geometrical features. The sign of mean curvature is negative within the region $0 \leq r < 62.5$ $\mu$m, as the meniscus in the region is concave down; however, the mean curvature rises to be positive in the region $r > 62.5\mu$m, showing the distinction from a spherical cap.

The experiment result of the binary droplet comprising 0.9400 g (28.66%) anisole and 2.110 g (71.34%) mesitylene, while evaporating in the cylindrical well with depth and radius of 1.81 $\mu$m and 75.0 $\mu$m, is shown in Fig 4.5. The values of $\Omega$'s for anisole and mesitylene are 4.42 and 6.76, respectively, if they are not mixed. In the solvent system, $C_1 - C_2 > 0$ and $\gamma_1 - \gamma_2 > 0$ hold, which means $d\gamma/dt$ of the entire system is negative, with the subscript 1 and 2 representing anisole and mesitylene, respectively. As a result, the solutal Marangoni flow moves towards the centre, bending the liquid-vapour interface into a bell-like shape.

The bell-shaped meniscus appears at the moment $t = 0.730$ s, although the majority still resembles to a spherical cap; afterwards, the menisci are bell-shaped until $t = 1.21$ s. The bell-shaped meniscus disappears from the moment $t = 1.45$ s and afterwards the profiles emerges to be a U-shaped profile with a wide bottom when the droplet touches down.

To focus on the evaporation process before the touch-down moment, the experiment results shown in the characteristic time scale are presented in Fig 4.6a, where the negative value of $\tau'$ means a specific moment when the height at the centre is

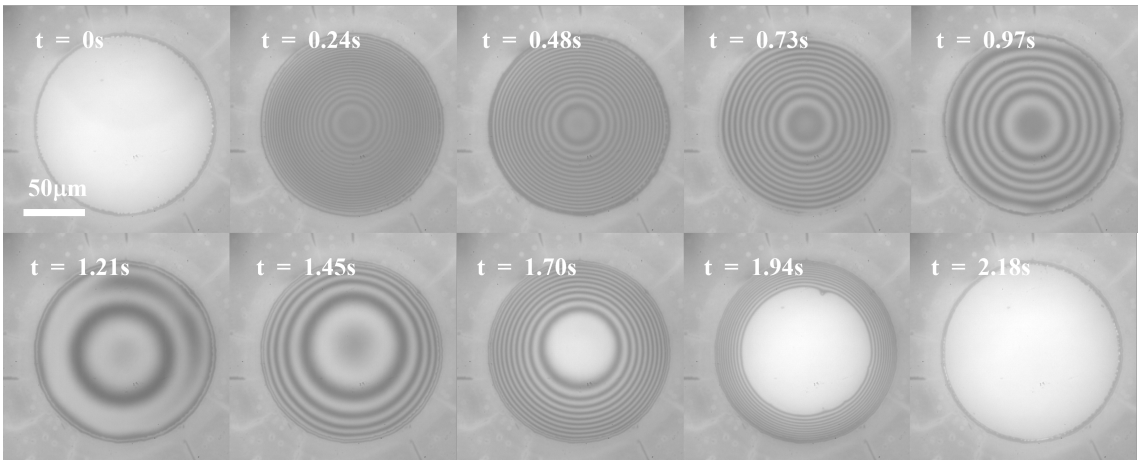


Figure 4.5: The experiment result of the bell-shaped profile emerging from the binary droplet comprising 0.9400 g (28.66%) anisole and 2.110 g (71.34%) mesitylene, evaporating in the cylindrical well with depth and radius of 1.81 $\mu$m and 75.0 $\mu$m.

higher than the depth of its well. The first moment is chosen when the noise from the background on the fringes is small enough to be overcome so that the fringes are recognisable by the code. For instance, the first moment of the binary droplet of anisole and mesitylene, $\tau' = -1.07$, shown in Fig 4.6a is $t = 0.510$ s.

The height profiles of the results shown in Fig 4.6a are given in Fig 4.6b. The meniscus appears to be bell-shaped at $\tau' = -0.840$, as shown in the light blue asterisks near the top; afterwards, the bell-shaped meniscus remains until $\tau' = 0.310$. At the moment $\tau' = 1.00$, the droplet touches down with a wide bottom located at $-37.4\mu\text{m} < r < 37.4\mu\text{m}$, shown in the brick red asterisks at the bottom. Hence, when the meniscus does not appear to be bell-shaped, it evolves as a U-shaped profile, ending up with a wide touch-down area.

The height evolution at the centre, counted in $\tau'$, is presented in Fig 4.7a which shows that the height at the centre decreases linearly until $\tau' = 0.750$ ,despite the height higher than the depth of its well between $\tau' = -1.07$ and $\tau' = 0$. In addition, the evolution of the mean curvature at the centre rises almost linearly until $\tau' = 0.750$ when it peaks, as shown in Fig 4.7b, although the value of it staggers near $\tau' = 0$. The mean curvature drops intermediately after $\tau' = 0.750$, suggesting that the height profile at the centre becomes flatter and flatter as it evolves.

The experiment results prove that bell-shaped profiles mainly appear when $d\gamma/dt < 0$, namely $Ma < 0$. For example, the binary systems of anisole and mesitylene,

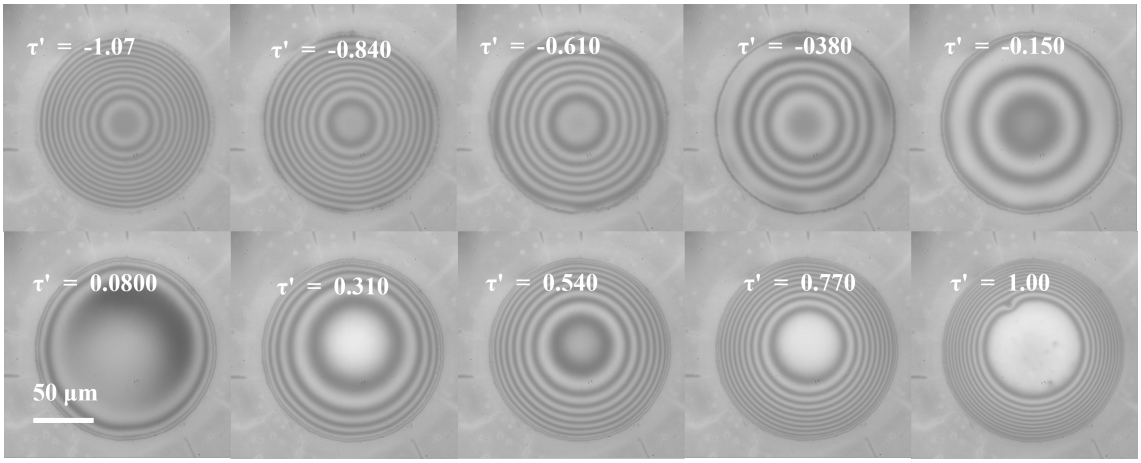


(a) The experiment result of the bell-shaped profile shown in Fig 4.5, counted in the characteristic time $\tau'$.

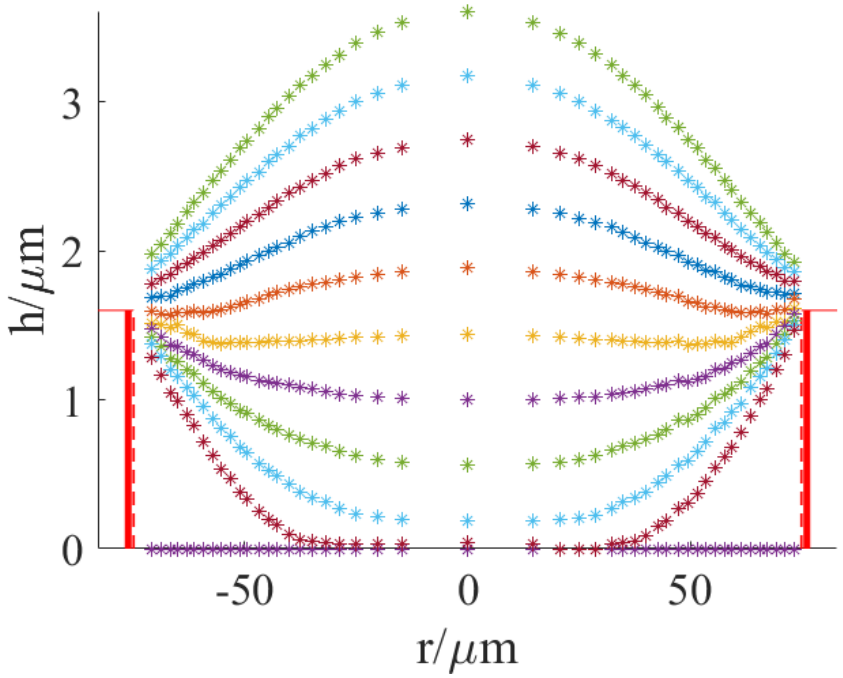


(b) The reconstructed profile of the bell-shaped profile shown in Fig 4.5.

Figure 4.6: The evolution of the bell-shaped profile counted in the characteristic time, $\tau'$ before the droplet touches down. The experiment results counted in $\tau'$ is shown in Fig 4.6a with the time difference of $\Delta t = 0.125$ s or $\Delta\tau' = 0.230$, and the corresponding height profiles are presented in Fig 4.6b.

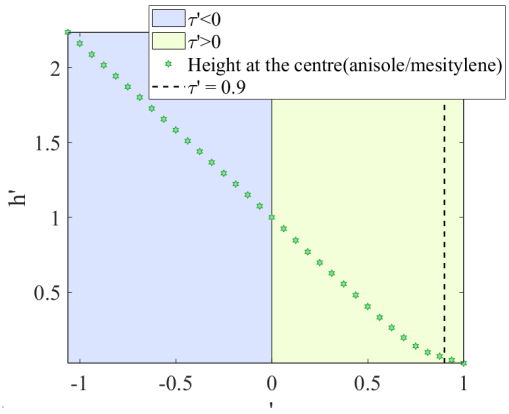


(a) The evolution of the height at the centre of the bell-shaped profile shown in Fig 4.6a.

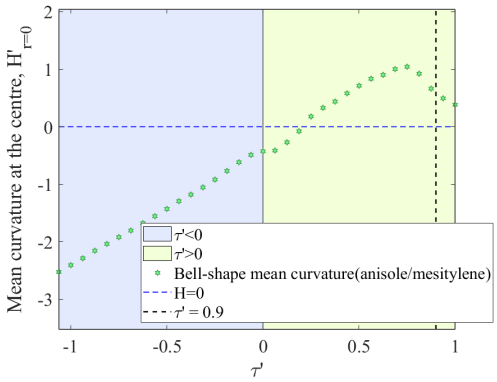


(b) The evolution of the mean curvature at the centre of the bell-shaped profile.

Figure 4.7: The evolutions of the height and the mean curvature at the centre of the bell-shaped profile.

pentyl acetate and anisole or toluene and n-butanol show bell-shaped profiles in cylindrical wells with the aspect ratio ranging from 1.50/75.0 to 3.20/75.0.

### 4.2.2 M-shaped profile

M-shaped profile is another new sort of profiles found from the evaporation of binary droplets. Once a height profile shows an M-shaped meniscus,namely a local minimum near the centre with two peaks located between the centre and edge, resembling to the capital letter M, the profile is defined as an M-shaped profile; therefore, an M-shaped profile may end up with a spherical cap, a wide bottom at the centre(like a U-shaped profile does) or even a small dimple near the centre(as a U-shaped profile will appear) until it touches down.

In Fig 4.8, an M-shaped meniscus and its curvatures along the direction of radius are presented, respectively. The M-shaped meniscus is from the binary droplet containing 1.905 g (94.85%) toluene and 0.1035 g (5.150%) n-butanol while evaporating in a cylindrical well with the depth and radius of 2.41 $\mu$m and 75.0 $\mu$m, respectively; and, therefore, the values of $\Omega$'s for toluene and n-butanol are 2.32 and 2.25, respectively.

In the solvent system, $C_1 - C_2 > 0$ and $\gamma_1 - \gamma_2 > 0$ seems to hold, according to the property of an ideal mixture, which means $d\gamma/dt$ of the entire system is negative

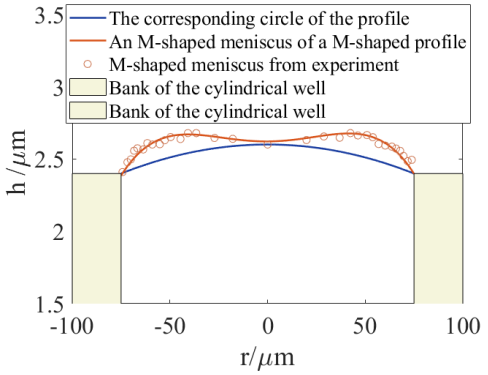


(a) An example of M-shaped meniscus from the binary droplet comprising 1.905 g (94.85%) toluene and 0.1035 g (5.150%) n-butanol, evaporating in the cylindrical well with depth and radius of 2.41 $\mu$m and 75.0 $\mu$m, respectively.

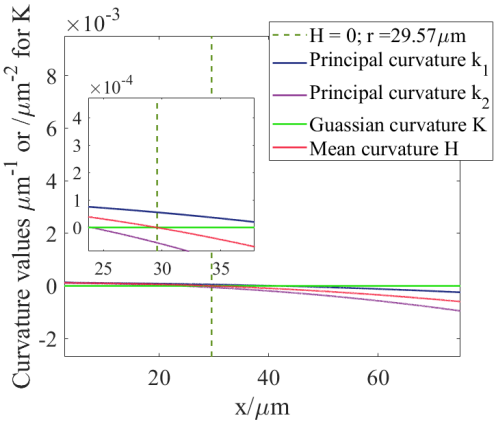


(b) The principal curvatures, mean curvature and Gaussian curvature along the direction of radius of the M-shaped meniscus, shown in Fig 4.8a.

Figure 4.8: An M-shaped meniscus of a binary droplet of toluene and n-butanol and its geometrical features.

too, with the subscripts 1 and 2 representing toluene and n-butanol, respectively. However, the mixture of toluene and n-butanol is non-ideal so that the degree of the non-ideality also contributes to the appearance of a profile. In fact, when n-butanol is dilute in the mixture, its vapour pressure increases to 13.77 kpa which is higher than that of toluene, and, therefore, $C_1 - C_2 < 0$.

In consequence, the sign of $d\gamma/dt$ is positive while the solutal Marangoni flow moves towards the contact line and the droplet remains in the well. However, when the mass fraction of n-butanol increases to 10% approximately, the evaporation rate of toluene is faster than that of n-butanol so that $C_1 - C_2$ turns to be positive and profiles become bell-shaped. More information is shown in Sec 4.3. The application of the non-ideality of a solvent system may prove effective to fabricate a flat layer as the Marangoni effect changes direction while evaporating.

The orange dots are the results from the experiment, while the orange curve is the fit curve so as to obtain the curvatures shown in Fig 4.8b, and the blue curve is the corresponding spherical cap passing the height at the centre and the brim of the well. The distinction between the blue curve and the orange curve shows the clear difference of the M-shaped meniscus and a spherical cap, which is also suggested by the results of the curvatures in Fig 4.8b. The mean curvature at the centre is the

double of the second derivative of the height profile, $h''$, as the centre of the surface of revolution remains an elliptic point.

However, M-shaped meniscus shows a drastically large value of the first principal curvature, $k_1 = h'/r$, at the direction of the parallels, as shown in the navy curve in Fig 4.8b, since the inflection point of the orange curve is close to the point $r = 0$. Hence, the mean curvature near the centre is far higher than anywhere else on the profile, so that the Laplace pressure drags the flow from the edge towards the centre. At the point $r = 29.6\mu$m, the mean curvature is zero, since the two principal curvatures have the same amplitude, but difference signs.

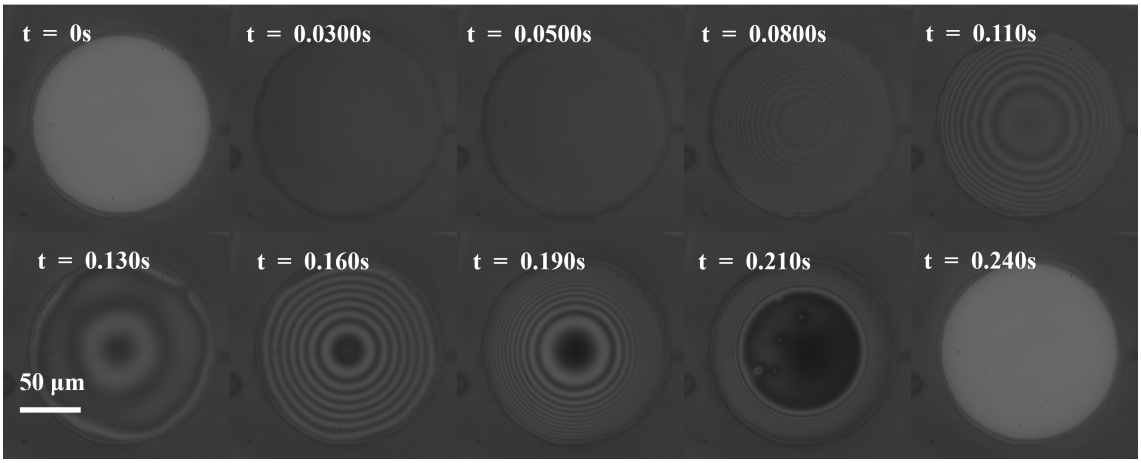


Figure 4.9: The experiment results of M-shaped profile of the binary droplet comprising 1.905 g (94.85%) toluene and 0.1035 g (5.150%) n-butanol, evaporating in a cylindrical well with depth and radius of 2.41 $\mu$m and 75.0 $\mu$m, respectively.

The experiment results of the M-shaped profiles at different moments are shown in Fig 4.9. The initial moment, $t = 0$ s, is the moment when the droplet is jetted by a print-head, recorded by the high speed camera. The menisci at the moments from $t = 0.0300$ s to $t = 0.110$ s can be well-fit with spherical caps; however, the M-shaped meniscus appears at $t = 0.130$ s and evolves until $t = 0.190$ s when the meniscus resembles to a spherical cap again. At the moment $t = 0.210$ s, the profile is about to touch down with a wide bottom showing near the centre. The duration of the evaporation is 0.240 s.

In order to concentrate on the evolution of the profile before the touch-down moment, the experiment results are analysed with the characteristic time, $\tau'$, as

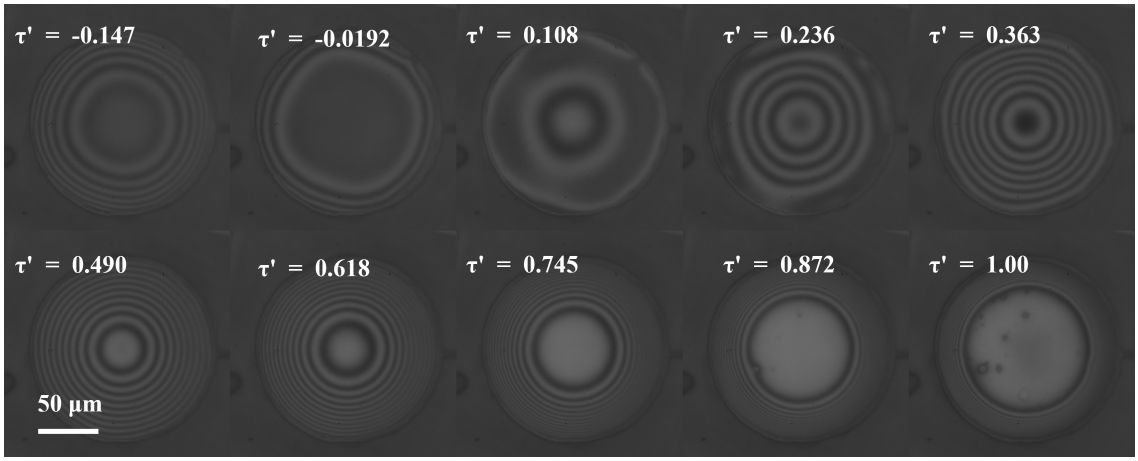


(a) The experiment result of the M-shaped profile shown in Fig 4.5, counted in the characteristic time $\tau'$.

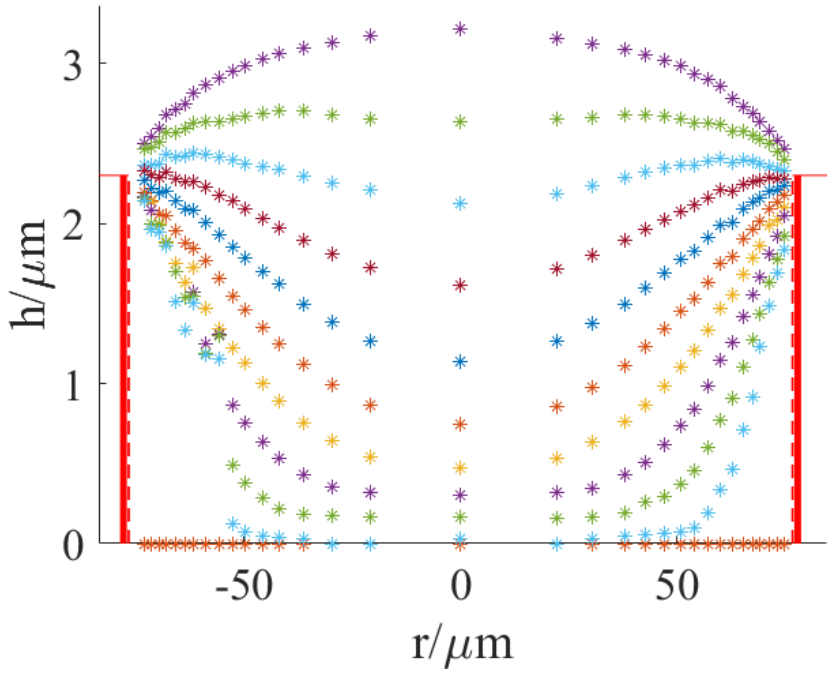


(b) The reconstructed profile of the M-shaped profile shown in Fig 4.10a.

Figure 4.10: The evolution of the M-shaped profile counted in the characteristic time, $\tau'$ before the droplet touches down.

shown in Fig 4.10a, where the $\tau' = -0.147$ denotes $t = 0.113$ s recorded by the camera, while $\tau' = 1.00$ is $t = 0.208$ s. The height profiles at each moment shown in Fig 4.10a are reconstructed in Fig 4.10b with the purple asterisks at the top representing the result at $\tau' = -0.147$ and the light blue ones at the bottom of $\tau' = 1.00$.

The light green asterisks shows that the meniscus deviates from a spherical cap at the moment $\tau' = -0.0192$, while at $\tau' = 0.108$, the meniscus is an obvious M-shaped one with the height at the centre appears to be a local minimum which is just below the depth of the well. Having been evolving as an M-shaped profile, the meniscus at the moment $\tau' = 0.363$ shows a local minimum at the centre as well, shown in the dark blue asterisks. However, at $\tau' = 0.490$, the meniscus appears to be a spherical shape and the features of an M-shaped meniscus never appears again. Instead, the height profile evolves like a pure droplet showing a W-shaped profile, touching down with a small dimple near the centre.

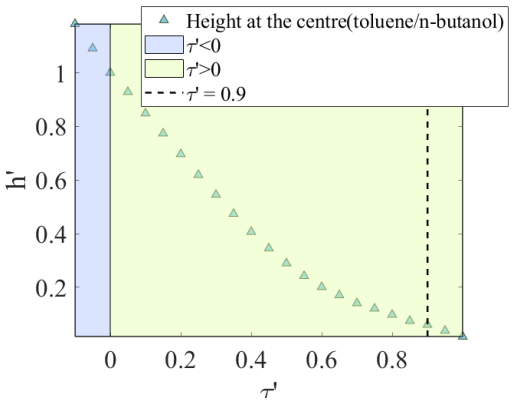


(a) The evolution of the height at the centre of the M-shaped profile shown in Fig 4.10a.

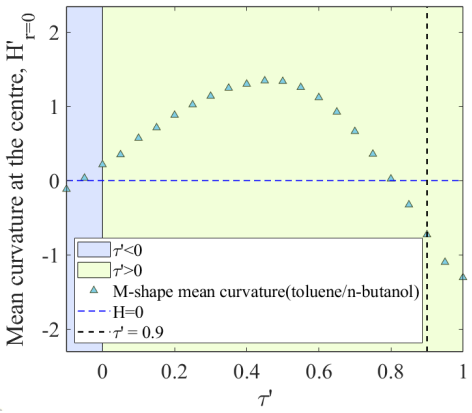


(b) The evolution of the mean curvature at the centre of the M-shaped profile.

Figure 4.11: The evolutions of the height and the mean curvature at the centre of the M-shaped profile.

The evolutions of the height and the mean curvature at the centre are shown in Fig 4.11. The height at the centre decreases linearly until $\tau' = 0.440$, and since then, the M-shaped meniscus on the profile disappears; in the mean time, the mean curvature rises and reaches the only peak at the same moment. Afterwards, the height drops not as quick and seems to enter the other mode of linear declining,

while the mean curvature turns out to be 0 at the moment $\tau' = 0.800$. The negative value of the mean curvature at $\tau' = 0.900$ indicates the profile is a W-shaped one when its M-shaped features disappear, as there is a small dimple near the centre which is shown by the dark fringe at then centre at the moment $\tau' = 1.00$ in Fig 4.10b.

From experiments, M-shaped profiles emerge when $d\gamma/dt > 0$ is true, namely $Ma > 0$; though the Marangoni flow moves towards the contact line, strengthening the flow which moves to the contact line anyway due to evaporation and counteracting the flow due to the pressure difference on the liquid-air interface, the liquid of a M-shaped profile still manages to stay within the well.

### 4.2.3 Spreading profile

Spreading profile is another new sort of profiles found in this work. For most droplets, the liquid mainly stay within the brim of a well properly and the height profile evolves while the contact line is anchored. However, for a spreading profile, the contact line is no longer fixed at the brim of a well; instead, the contact line is moving and expanding as the droplet spreads, leading to the increase of evaporation rate. The degree of the expansion of a contact line may vary, but in this work such profiles are classified as spread profiles.

An example of spreading profile is given in Fig 4.12 which shows the evaporation process of the binary droplet comprising 1.009 g (49.51%)n-butanol and 1.029 g (50.49%) n-pentyl acetate in a cylindrical well with depth and radius of 2.40 $\mu$m and 75.0$\mu$m; and the values of $\Omega$'s for n-butanol and n-pentyl acetate are 2.21 and 8.19, respectively. In addition, $C_1 - C_2$ is a positive value while $\gamma_1 - \gamma_2$ is negative with the subscripts 1 and 2 denoting n-butanol and n-pentyl acetate, respectively. Therefore, the sign of $d\gamma/dt$ in the solvent system is positive while the solutal Marangoni flow moves towards the contact line so rapidly that the droplet spreads out.

The spreading ends at the moment $t = 0.265$ s; and afterwards, the droplet evolves like a W-shaped profile with the appearance of a small dimple at the centre when the droplet touches down, as presented in Fig 4.12a. Furthermore, the states of the droplet before the spreading ends, is given in Fig 4.12b. The spreading mainly

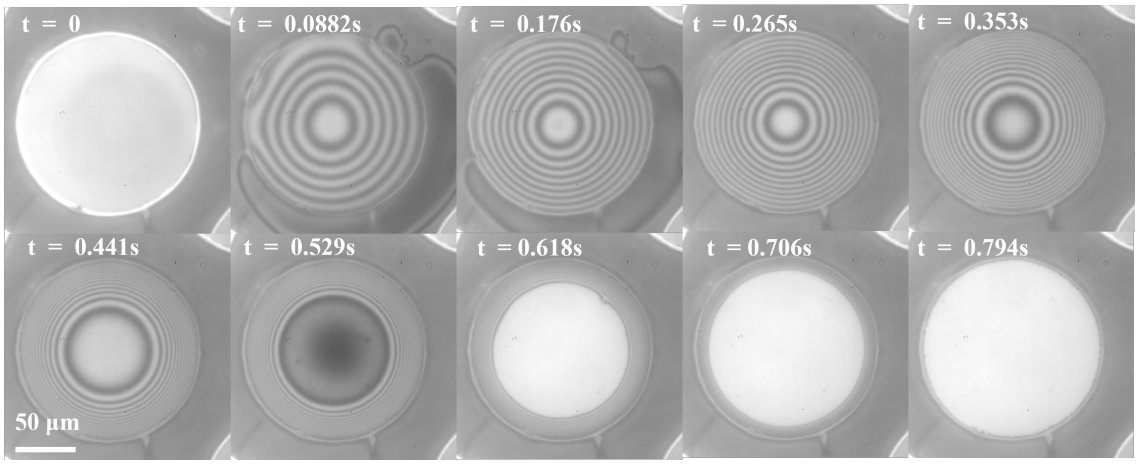


(a) The experiment result of the spreading profile of the binary droplet containing 1.009 g (49.51%) n-butanol and 1.029 g (50.49%) n-pentyl acetate evaporating in the well with depth and radius of 2.40 $\mu$m and 75.0 $\mu$m, respectively.

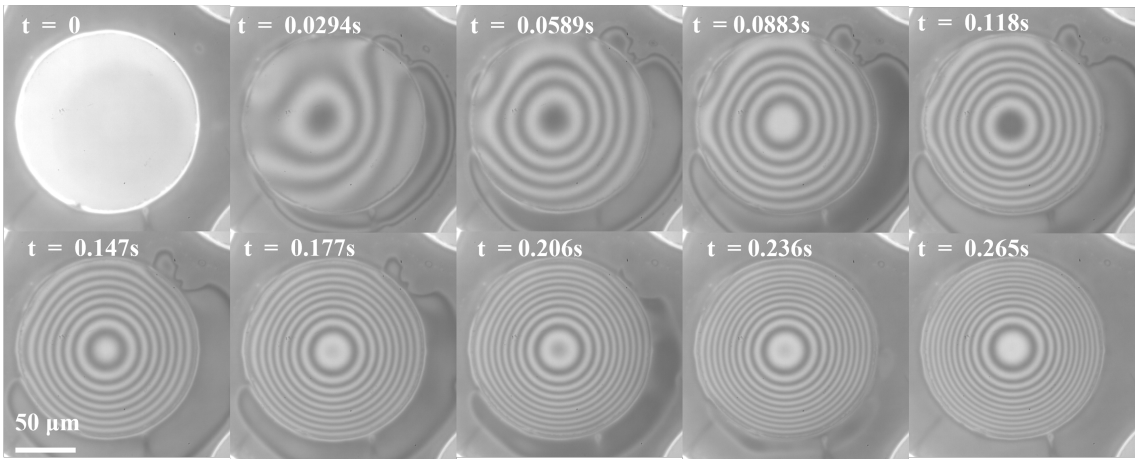


(b) The moments when the contact line of the droplet spreads (0 s $\leq t <$ 0.147 s) and returns back to the brim of the well (0.147 s $\leq t <$ 0.265 s).

Figure 4.12: A spreading profile from the binary droplet of 1.009 g (49.51%) n-butanol and 1.029 g (50.49%) n-pentyl acetate evaporating in the well with depth and radius of 2.40 $\mu$m and 75.0 $\mu$m, respectively.

occurs at the right-down area, whereas the contact line begins to move back to the brim of the well at the moment $t = 0.147$ s and is completely back to the well at $t = 0.265$ s. The other spreading profile presented in Fig 4.13, shows a flat-disk

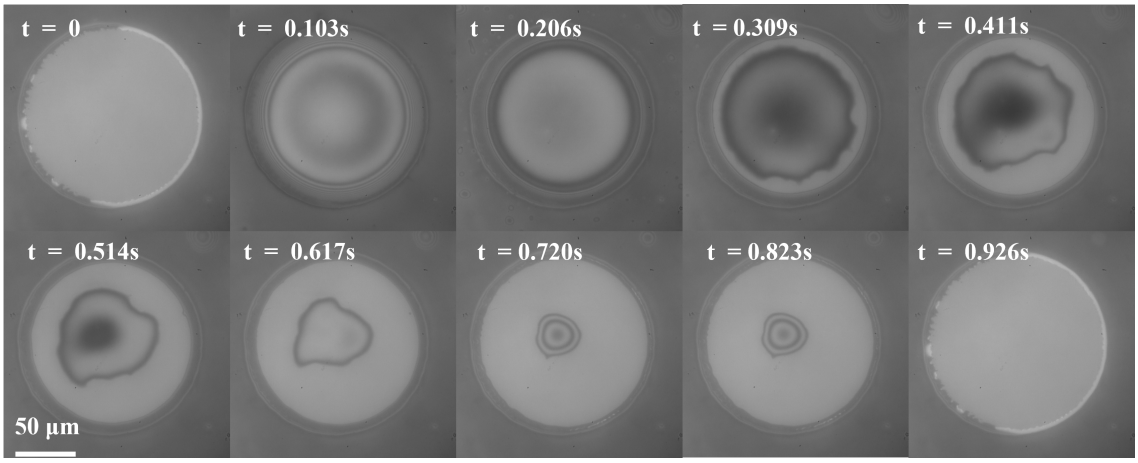


(a) A spreading profile of the binary droplet containing 69.69% n-butyl acetate and 30.31% methyl benzoate.

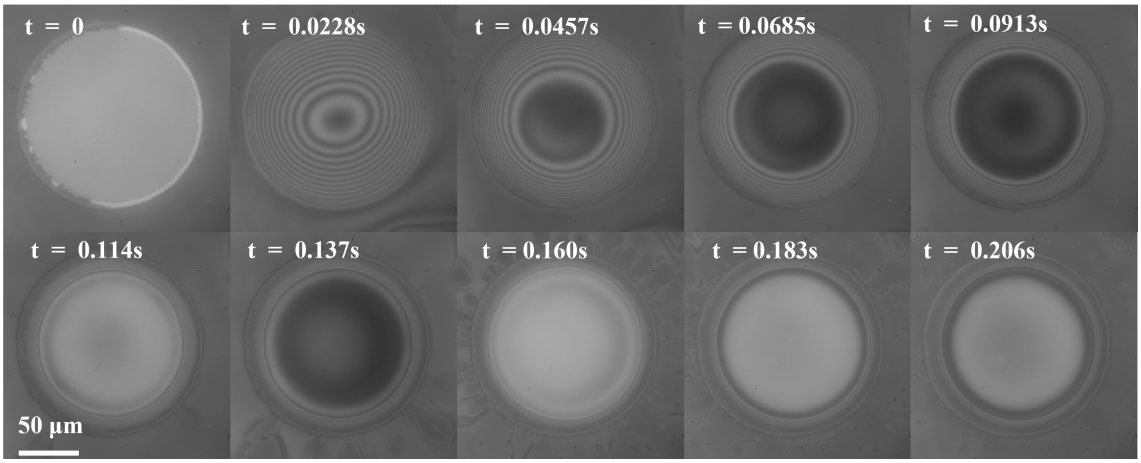


(b) The moments before $t = 0.206$ s when the spreading process ends.

Figure 4.13: The experiment result of the binary droplet of n-butyl acetate and methyl benzoate.

at the moments $t = 0.103$ s and $t = 0.206$ s. When the droplet touches down, the inner part of liquid becomes to be a spherical cap shape until the droplet dries up thoroughly, as shown in Fig 4.13a. The drying of the inner liquid takes up the majority of the evaporation time, suggesting that the inner liquid is rich in methyl benzoate, the less volatile component.

The fringes of the profile at the moments until the disappearance of the spreading of contact line are presented in Fig 4.13b. The height profile at the centre becomes

flattened from $t = 0.0457$ s, while the droplet spreads. However, the flattened area keeps growing and reaches the largest area at $t = 0.160$ s, which almost accounts for the entire area of the well. The inner part separates from the liquid which attaches to the brim of the well at $t = 0.183$ s the moment when the droplet is about to touch down. In the end, the droplet touches down at the base, while the inner part appears to be a rather flattened shape.

The value of $d\gamma/dt$ for a spreading profile is larger than 0, similar to an M-shaped profile, but the Marangoni flow in a spreading profile seems to reach an extreme degree that the liquid no longer stays in the well but is dragged out of a well and may not come back to the well until it totally dries up.

### 4.2.4 Lopsided profile

Lopsided profile is the only symmetry-breaking shape found in this study. At the early stage of a lopsided profile, the meniscus may appear to be bell-shaped; however, as evaporating goes on, the meniscus turns to be askew, slightly or drastically, and the unbalanced shape remains until the droplet touches down. In some severe cases, droplets showing lopsided profiles, rupture as soon as the menisci appear to be bell-shaped. Although there is a bell-shaped meniscus showing on a lopsided profile for some moments, the meniscus appears to be lopsided and never returns to be symmetrical; therefore, lopsided profile is defined as a new sort of profiles in this work.

To analyse a lopsided profile and reconstruct the menisci, two directions are chosen, direction A, on which the slope on a profile is steepest, and direction B that is orthogonal to direction A. The menisci at both directions of a lopsided profile of the binary droplet comprising 1.421 g (68.93%) anisole and 0.641 g mesitylene evaporating in a cylindrical well with depth and radius of 1.91 $\mu$m and 75 $\mu$m, is shown in Fig 4.14. The profile on the direction A in Fig 4.14a is where the slope has the largest value, along which the meniscus is positive askew, which means the lowest point of the meniscus is at the point where $r < 0$ $\mu$m, with the slope on the left half much steeper than the right half; while the profile on Direction B, which shows the symmetrical shape, orthogonal to the direction A, remains symmetric. The

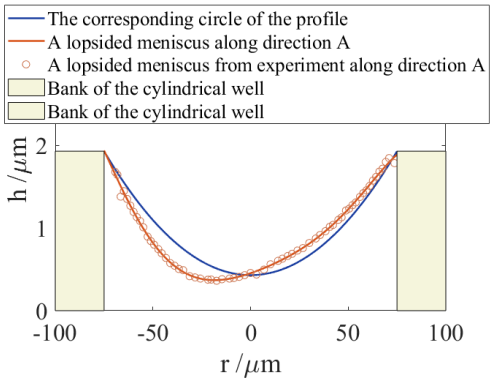


(a) The blue curve is the corresponding spherical cap passing the brim of the well(banks) and the height profile at $r = 0$ $\mu$m, while the orange dots and the orange curve are from experiment and its fitted curve, respectively.

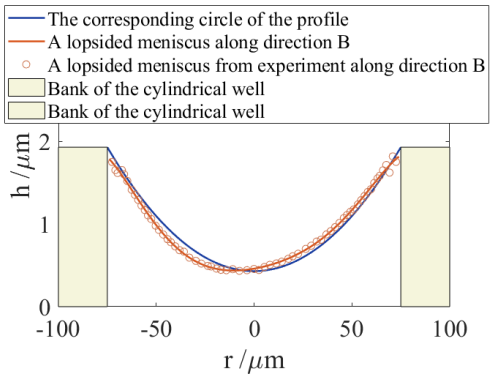


(b) Similarly, the blue curve if the same corresponding spherical cap as shown in Fig 4.14a, since the height at the centre is the same on any directions. The orange dots and curve are the results from the experiment and its fitted curve.

Figure 4.14: An example of lopsided meniscus from the binary droplet comprising 1.421 g (68.93%) anisole and 0.6406 g (31.07%) mesitylene, evaporating in the cylindrical well with depth and radius of 1.93 $\mu$m and 75.0 $\mu$m, respectively.

meniscus on direction B is almost a spherical cap, suggesting that surface tension on the interface still dominates the shape on direction B. The striking difference of a profile along different directions is the feature of a lopsided profile, which clearly distinguishes it from the other sorts of profiles.

The experiment result of the binary droplet is shown in Fig 4.15. The meniscus of the droplet resembles to a spherical cap until $t = 1.48$ s; however, the meniscus is bell-shaped at $t = 1.85$ s before it turns out to be a lopsided meniscus at $t = 2.22$ s; since then, the meniscus is askew until the touch-down moment at $t = 2.59$ s. Although the meniscus is not symmetrical when it touches down, the evolution of the meniscus shows that the profile attempts to regain symmetry while the new contact line at the base is receding to the brim of the well, as shown in the fringes at $t = 2.95$ s.

Likewise, the experiment result is also shown in the characteristic time on both directions in Fig 4.16. The meniscus are symmetrical until $\tau' = 0.200$ and the meniscus is bell-shaped from $\tau' = -0.400$. However, the meniscus becomes slightly asymmetrical at $\tau' = 0.200$ with the minimum point situated at the left-bottom area; although the location of the minimum moves towards the centre as the droplet

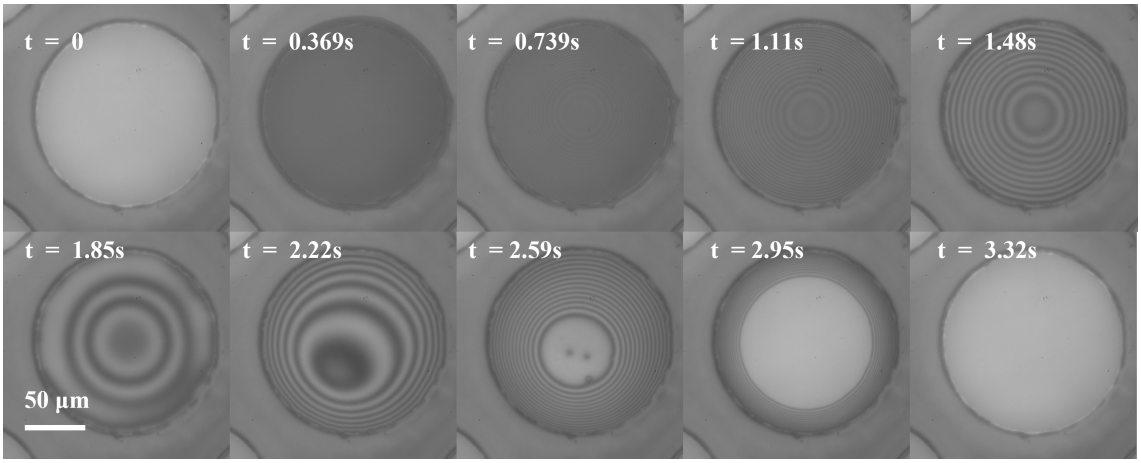


Figure 4.15: The experiment results of a lopsided profile of the binary droplet comprising 1.421 g (68.93%) anisole and 0.6406 g (31.07%) mesitylene, evaporating evaporating in the cylindrical well with depth and radius of 1.93 $\mu$m and 75.0 $\mu$m, respectively.

evaporates, it stays at the same region until it touches down at $\tau' = 1.00$, as shown in Fig 4.16a.

The height profiles along direction A and direction B are shown in Fig 4.16d and Fig 4.16d, respectively, with the exact directions shown in Fig 4.16b and Fig 4.16e. The meniscus at the moment $\tau' = -0.800$ is shown in the light green dots at the top in Fig 4.16d and Fig 4.16e, while the red asterisks at the bottom are the meniscus at the touch-down moment.

The lopsided meniscus first appears at the moment $\tau' = 0.200$ as the local minima on the yellow asterisks are not equal to each other on direction A. The minimum values are 1.66 $\mu$m and 1.73 $\mu$m at $r = -43.8$ $\mu$m and $r = 41.6$ $\mu$m, respectively; afterwards, the only minimum on the profile are at the locations $r = -34.4$ $\mu$m, $r = -26.1$ $\mu$m and $r = -19.6$ $\mu$m at the moment $\tau' = 0.400$, $\tau' = 0.600$ and $\tau' = 0.800$, respectively. When it touches down on direction A, the touch area is located in -34.4 $\mu$m $< r <$ 12.9 $\mu$m; however, the touch-down area on direction B is located in -26.4 $\mu$m $< r <$ 25.9$\mu$m.

The evolutions of the height and the mean curvatures (both directions) at the centre are presented in Fig 4.17, in which the red dashed line is at the moment $\tau' = 0.200$ when the meniscus becomes lopsided.

The height evolution shows the linear decrease until $\tau' = 0.200$, the symmetry-

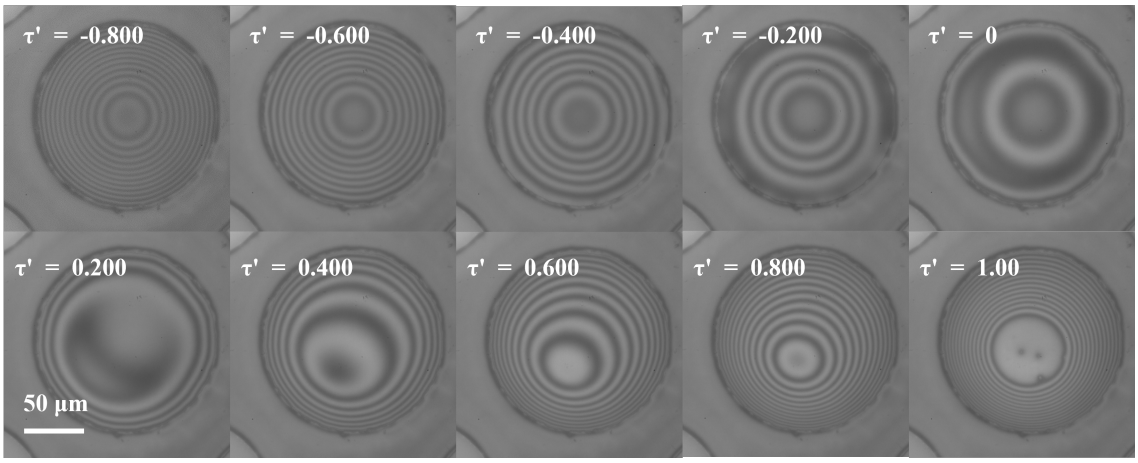


(a) The experiment result counted in $\tau'$ of the lopsided profile in Fig 4.15.

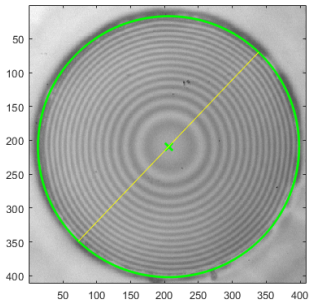

(b) Direction A to analyse the height profile

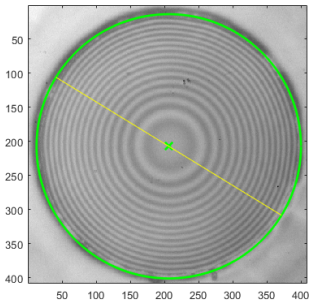

(c) Direction B to analyse the height profile

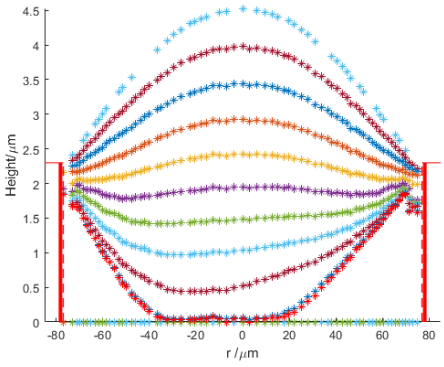


(d) The height profile along direction A from $\tau' = -0.800$ to $\tau' = 1.00$

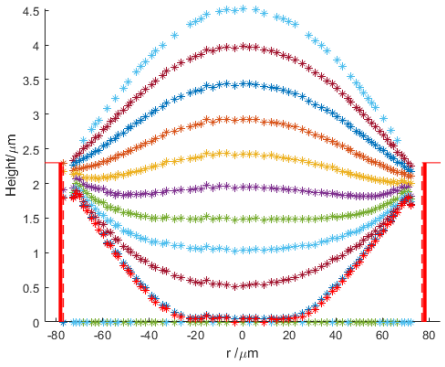


(e) The height profile along direction B from $\tau' = -0.800$ to $\tau' = 1.00$

Figure 4.16: The experiment result of the lopsided profile shown in the characteristic time from $\tau' = -0.800$ to $\tau' = 1.00$, respectively.

.

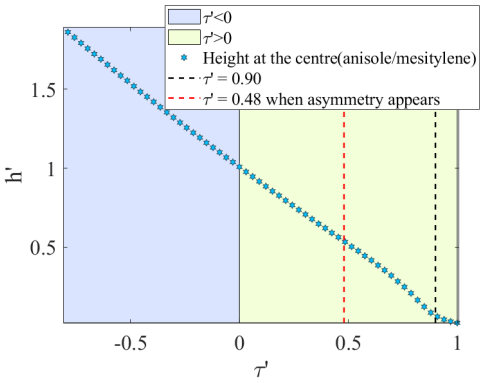


(a) The evolution of the height at the centre of the lopsided profile shown in Fig 4.16a.

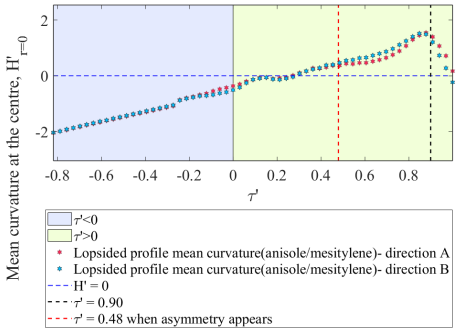


(b) The evolution of the mean curvature at the centre of the lopsided profile.

Figure 4.17: The evolutions of the height and the mean curvature at the centre of the lopsided shaped profile.

breaking moment, as indicated by the pink dashed line in Fig 4.17a; in addition, the profile is bell-shaped until $\tau' = 0.200$ since the bell-shaped meniscus appears and remains until the symmetry breaks. From the moment $\tau' = 0.200$ to $\tau; = 0.900$, the height at the centre seems to deviate from the linear decline.

The mean curvature at both directions are presented in the blue and red stars in Fig 4.17b. The evolutions show the identical tendencies, though the red asterisks are higher than the blue ones at the region $-0.12 < \tau' < 0.12$. Apart from that, the mean curvatures on the directions meet again at $\tau' = 0.200$ and since then the mean curvature on direction B is higher than that on direction A, suggesting that the meniscus on direction B at the centre is more uneven and the asymmetry begins at from this moment.

## 4.3 Non-ideal Binary Droplets

Toluene and n-butanol are chosen as the candidate solvents to investigate the behaviour of non-ideal binary droplets evaporating in cylindrical wells. The binary system shows positive deviation from the ideal binary solvent systems which obey Raoult's law, as shown in Fig 4.18 [178], since the interaction of toluene and n-butanol is less stronger than that between the pure solvents [179] [180] [181].

The total vapour pressure of the mixture rises until $x \approx 0.194$ and plummets

dramatically afterwards. When the mole fraction of n-butanol is 0.0977, the total vapour pressure is then 8.467 kpa. Assuming that the majority of the liquid, toluene, obeys Raoult's law and the other component, n-butanol, follows Henry's law [87] [182] [183], we will find that the vapour pressure of n-butanol is 13.77 kpa while that of toluene is only 7.893 kpa which is significantly lower, and hence, the less volatile solvent. In this case, the more volatile component is n-butanol rather than toluene; and the value of $d\gamma/dt$ is positive, the Marangoni flow moves towards the contact line along the r-direction. Therefore, in theory, the profiles appearing from the binary system which is dilute in n-butanol will show M-shaped profiles or spreading profiles.

However, when the mole fraction of n-butanol increases to 0.451, the total vapour pressure is then 8.034 kpa; if the vapour pressure of toluene also obeys Raoult's law, the vapour pressure of n-butanol is 4.131 kpa which is lower than that of toluene, so that the more volatile solvent in the mixture is toluene instead of n-butanol. Thus, the value of $d\gamma/dt$ is negative and the Marangoni flow points towards the centre of a droplet with the profiles appearing to be bell-shaped or lopsided.

Though the data was measured at 313.15 K [178], the prediction is still valid when the temperature does not vary much [184]. The analysis shows that the direction of the Marangoni flow may change with the concentration of a component when the vapour pressure of a mixture has a positive deviation.

A binary droplet containing 1.905 g (94.85%) toluene and 0.1035 g (5.150%) n-butanol in the well with depth and radius of 2.41 $\mu$m and 75.0 $\mu$m, respectively, shows an M-shaped profile as presented in Fig 4.19a. At the moment $\tau' = -0.258$. the meniscus resembles to a spherical cap still; however, it turns to be flattened at $\tau' = -0.117$, which is shown in the purple asterisks near the top in Fig 4.19c; although the height at the centre becomes to be a local minimum from $\tau' = 0.0219$ and remains the minimum on the meniscus until the droplet touches down, there are two local maxima on the 2D height profile near the brim of the well at $r = -52.9$ $\mu$m and $r = 53.3$ $\mu$m at the moment $\tau' = 0.0219$, generating an M-shaped meniscus at this moment. After then, the evolution of the meniscus is similar to a U-shaped profile, whose profile touches down with a wide bottom and the height at the centre

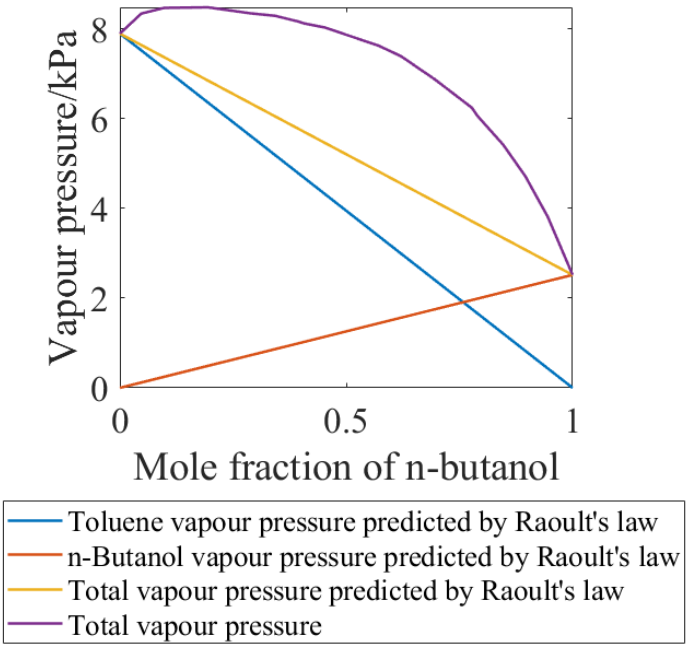


Figure 4.18: Vapour pressure of the mixture of n-butanol and toluene at 313.15 K. The purple line represents the data from literature, while the yellow line is the total pressure predicted by Raoult's law with the blue line and the orange line denoting the pressure of toluene and n-butanol, respectively. [178]

shows two linear decreasing patterns, though the evaporation rate is changing as the components have different vapour pressures.

When the concentration of n-butanol increases to 0.6014 g (29.91%), the profile appears to be a bell-shaped profile, as presented in Fig 4.19b. Likewise, the height details at each moment are given in Fig 4.19d. At the moment $\tau' = -0.161$, the meniscus is bell-shaped as is shown in the yellow asterisks at the top; later, the bell-shaped meniscus begins to wane and only appears to be a smaller bell-shape at $\tau' = -0.0323$ whereas the feature of bell-shaped disappears from the moment $\tau' = 0.0968$ when the profile starts to evolve like a U-shaped profile. A wide bottom near the centre begins to appear at the moment $\tau' = 0.613$, ranging from $r = -20.6$ $\mu$m to $r = 21.6$ $\mu$m; since then, the flat bottom keeps growing while the droplet evaporates, and the touch-down area ranges from $r = -49.6$ $\mu$m to $r = 49.6$ $\mu$m, as shown in the red asterisks at the bottom in Fig 4.19d. The meniscus at each moment is plotted with the same time difference, so that the blank area between each two menisci is proportional to the volume change, indicating that the evaporation rate

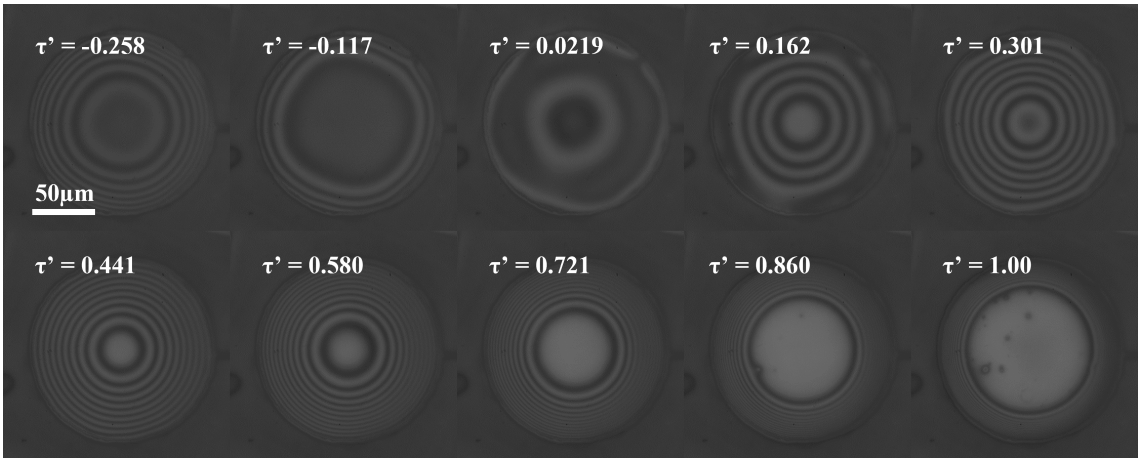


(a) M-shaped profile from the binary droplet of 1.905 g (94.85%) toluene and 0.1035 g (5.150%) n-butanol in the well with depth and radius of 2.41 $\mu$m and 75.0 $\mu$m.

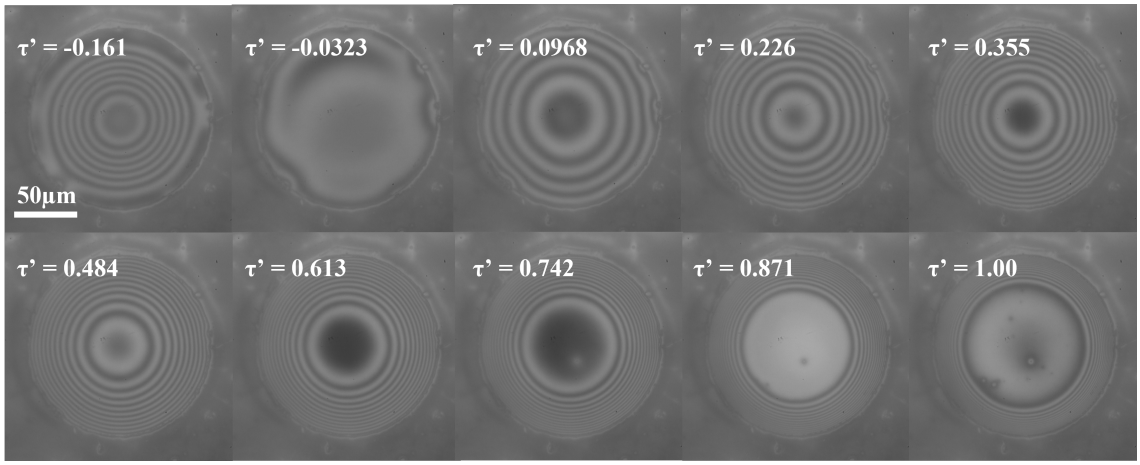


(b) Bell-shaped profile from the binary droplet of 1.409 g (70.09%) toluene and 0.6014 g (29.91%) n-butanol in the well with depth and radius of 2.33 $\mu$m and 75.0 $\mu$m.

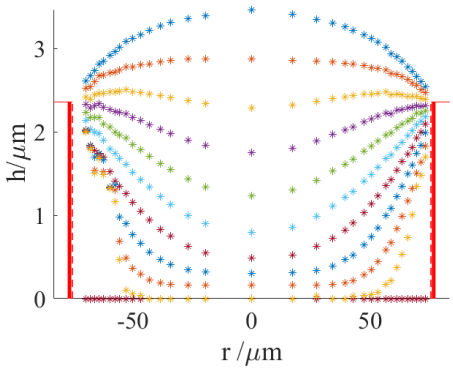


(c) The height profile of the M-shaped profile

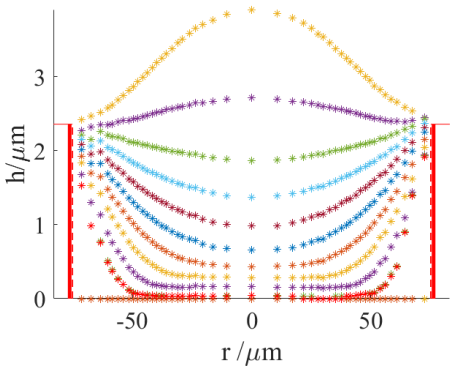


(d) The height profile of the bell-shaped profile.

Figure 4.19: The experiment results of the binary droplets of toluene and n-butanol (I).

decreases during evaporation.

Another bell-shaped profile from the binary droplet of 1.067 g (51.35%) toluene and 1.010 g (48.65%) n-butanol is shown in Fig 4.20a with the height profiles reconstructed in Fig 4.20c. At the moment $\tau' = -0.167$, the meniscus is a bell-shaped one as shown in the yellow asterisks in Fig 4.20c; the feature of bell-shaped weakens at the moment $\tau' = -0.037$. The height at the centre becomes flattened at the moment $\tau' = 0.611$ with the flat area located between $r = -17.7$ $\mu$m and $r = 16.4$ $\mu$m; afterwards, the flat bottom grows and touches down in the area -51.5 $\mu$m $\leq r \leq$ 51.5 $\mu$m at the moment $\tau' = 1.00$ shown in green asterisks at the bottom.

Reducing the amount of toluene to 0.2142 g (10.61%), the binary droplet of toluene and n-butanol shows a U-shaped profile, as presented in Fig 4.20b and Fig 4.20d; the flat bottom emerges at the moment $\tau' = 0.417$, ranging from $r = -17.8$ $\mu$m to $r = -16.7$ $\mu$m, as shown in the brick red asterisks. When the droplet touches down, there is a small dimple at the centre, located at $-37.1$ $\mu$m $\leq r \leq 36.5$ $\mu$m, which only emerges after $\tau' > 0.900$ mainly because of the rise of disjoining pressure.

The height evolutions at the centre of the binary droplets, pure toluene and pure n-butanol are shown in Fig 4.21. The bell-shaped profiles shown in the blue and purple squares have the same decreasing modes and they join the rest of the height evolutions from the moment $\tau' = 0.585$, showing a linear decreasing tendency. The height evolution of the M-shaped profile is similar to those of the U-shaped profiles until $\tau' = 0.170$; since then, it slowly joins bell-shaped profiles at $\tau' = 0.452$. The U-shaped profiles end the first linear decrease at $\tau' = 0.434$ and begins the second linear decrease from $\tau' = 0.585$.

The evolutions of the mean curvature at the centre of the binary droplets and its pure droplets are presented in Fig 4.23. The mean curvatures of the profiles are all negative at the moment $\tau' = -0.250$, suggesting that the profiles at the centre are all concave up.

At the moment $\tau' = 0$, the M-shaped profile has a positive value, which results from the profile being concave down as a local minimum on the profile; while the mean curvatures of the other profiles at $\tau' = 0$ are almost 0. Surprisingly, the mean curvature of the binary droplet containing 10.61% toluene (the red squares) has the

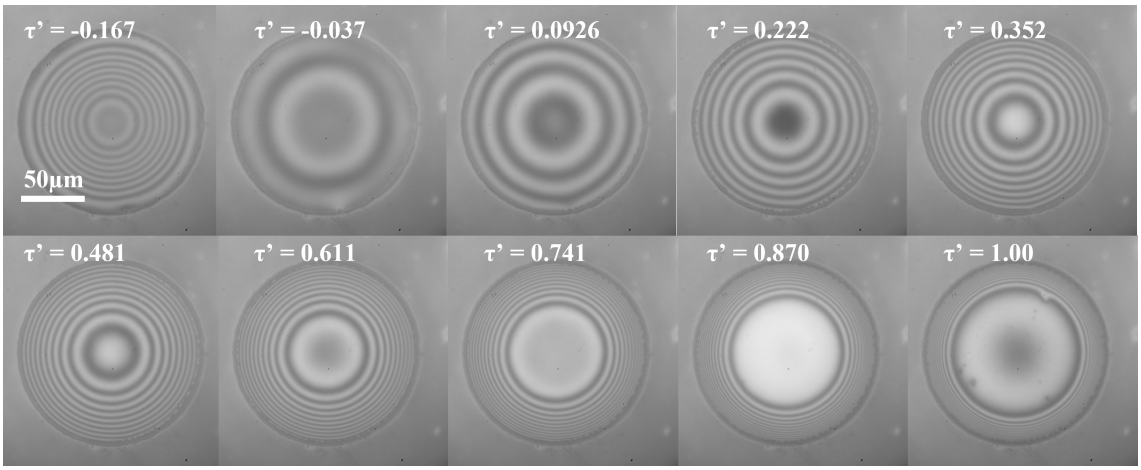


(a) Bell-shaped profile from the binary droplet of 1.067 g (51.35%) toluene and 1.010 g (48.65%) n-butanol in the well with depth and radius of 2.28 $\mu$m and 75.0 $\mu$m, respectively.

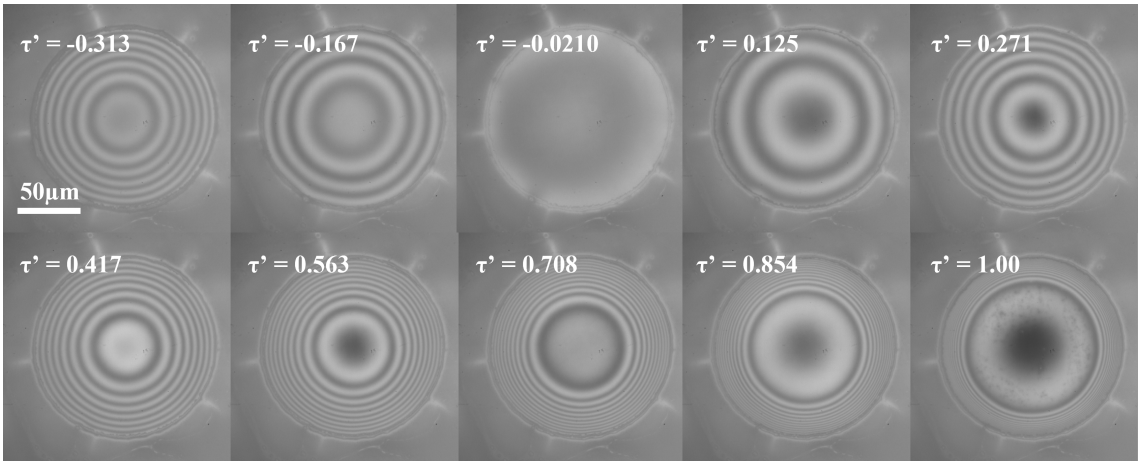


(b) U-shaped profile from the binary droplet of 0.2142 g (10.61%) toluene and 1.806 g (89.39%) n-butanol in the well with depth and radius of 2.36 $\mu$m and 75.0 $\mu$m, respectively.

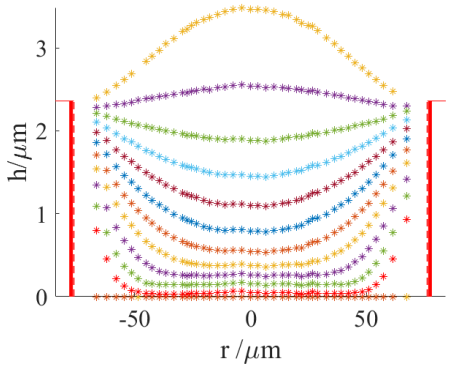


(c) The height profile of the bell-shaped profile.

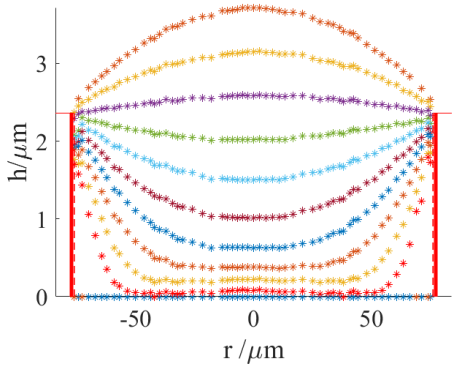


(d) The height profile of the U-shaped profile.

Figure 4.20: The experiment results of the binary droplets of toluene and n-butanol (II).

.

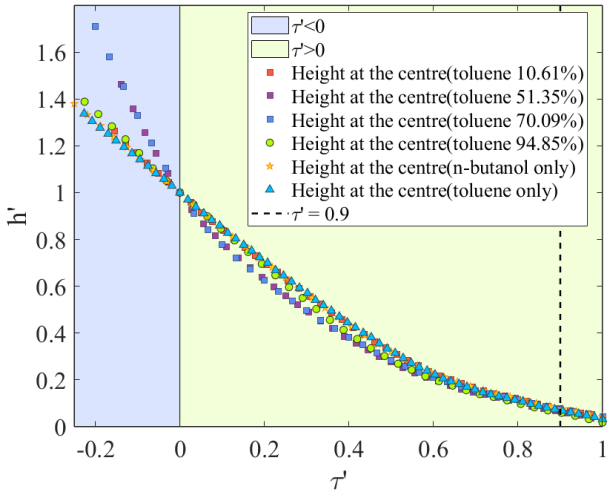


Figure 4.21: The evolution of the height at the centre of the binary droplets of toluene and n-butanol and the pure droplets of toluene and n-butanol, respectively.

same evolution pattern with that of the pure n-butanol (the yellow star).

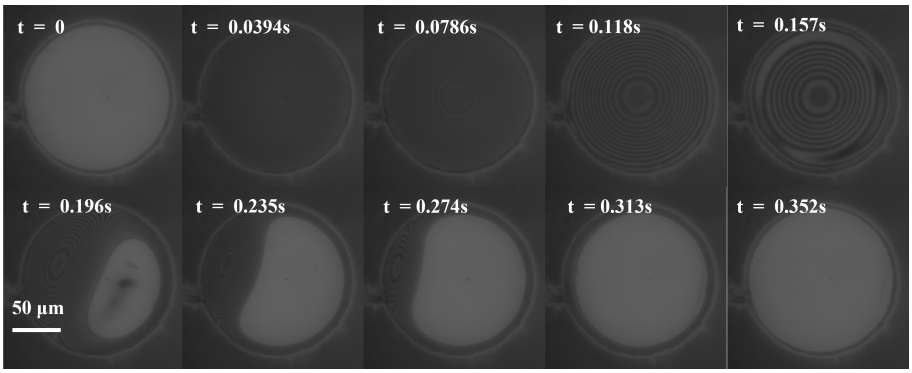


Figure 4.22: Lopsided profile from the binary droplet of 1.824 g (89.54%) toluene and 0.2130 g (10.46%) in the well with the radius and depth of 2.45 $\mu$m and 75.0 $\mu$m, respectively.

As much as showing the same trend before $\tau' = 0.370$, the bell-shaped profile of the binary droplet of 70.09% toluene, plotted in the blue squares, seems to follow the evolution of that of the pure toluene (the light blue triangles) from $\tau' = 0.370$, while the bell-shaped profile of binary droplet of 51.35% toluene, turns to the trend of the pure n-butanol slowly. Apart from turning to be positive at $\tau' = -0.0641$ which is different from the other profiles, the mean curvature of the M-shaped profile keeps rising until $\tau' = 0.484$ and joins the change of the pure toluene at $\tau' = 0.581$.

The binary droplet of 1.824 g (89.54%) toluene and 0.2130 g (10.46%) shows a lopsided profile in cylindrical wells with the aspect ratio ranging from 1.6/75 to

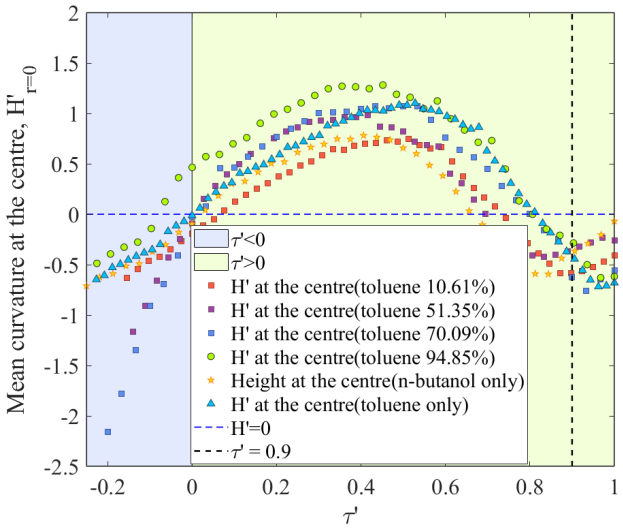


Figure 4.23: The evolution of the mean curvature at the centre of the profiles of the binary droplets, pure toluene and pure n-butanol.

2.9/75. Since there is too much noise in the height profile of the droplet printed in the cylindrical well with the depth and radius of 2.45 $\mu$m and 75.0 $\mu$m, respectively, which is shown in Fig 4.22, especially near the upper left corner where the fringes are too congested to be detected, the height profile emerging from the cylindrical well with the depth and radius of 1.96 $\mu$m and 75.0 $\mu$m, respectively, is shown in Fig 4.24 instead.

The lopsided profile shown in Fig 4.24a, remains symmetric until $\tau' = 0.0821$ with the occurrence of the symmetry-breaking between $\tau' = -0.101$ and $\tau' = 0.0821$. As a result, there is a local minimum emerging near the upper-left region of the height profile, though the other local minimum appears when the droplet is about to touch down, as shown in the dark fringes near the centre at the moment $\tau' = 0.816$ and $\tau' = 1.00$.

The directions on which the slope of the height profile decreases slowest, Direction A and fastest, Direction B, are presented in Fig 4.24b and Fig 4.24c, respectively. Accordingly, the height profiles on both directions are reconstructed in Fig 4.24d and Fig 4.24d. On Direction A, the height profile is symmetric while on Direction B the height profile is askew, suggesting that the meniscus are no longer circular symmetry but reflection symmetry with the diameter of the well on Direction B being the axis of symmetry.

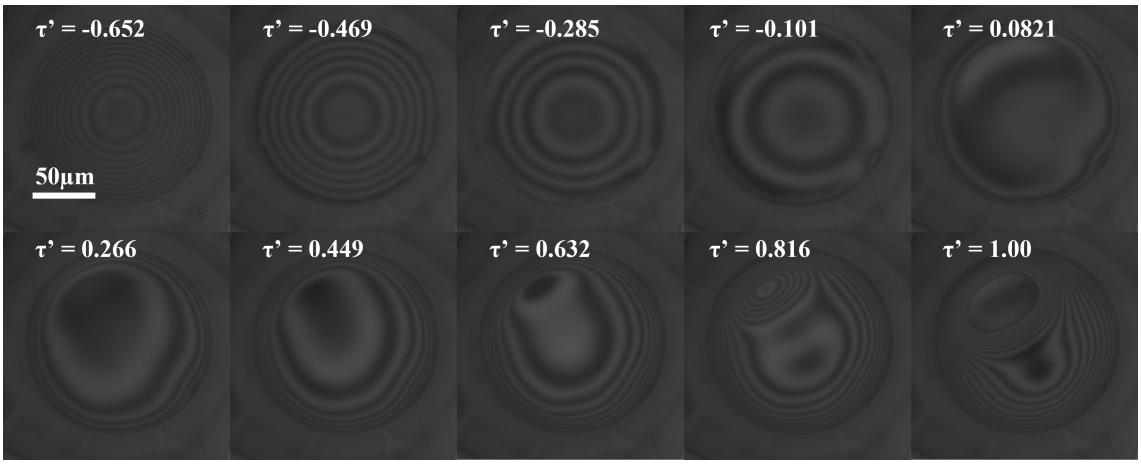


(a) Lopsided profile from the binary droplet of 1.824 g (89.54%) toluene and 0.2130 g (10.46%) n-butanol in the well with depth and radius of 1.96 $\mu$m and 75.0 $\mu$m, respectively.

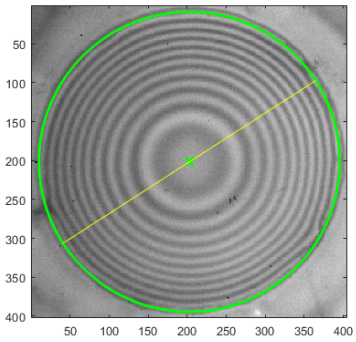

(b) Direction A to detect the profile

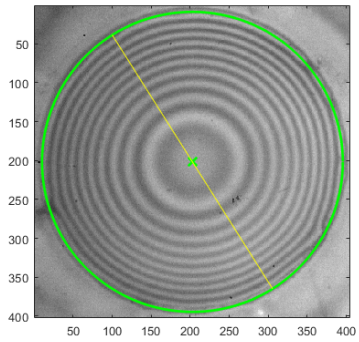

(c) Direction B to detect the profile

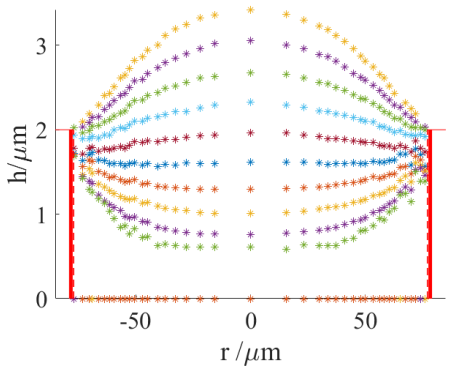


(d) The height profile of the lopsided profile along direction A.

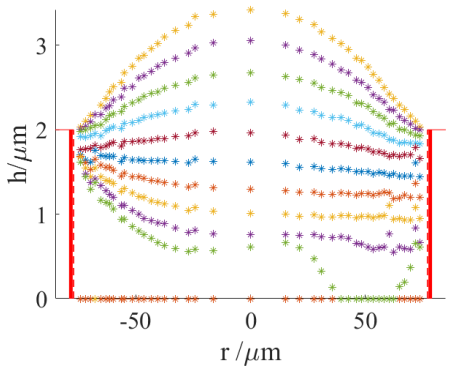


(e) The height profile of the lopsided profile along direction B.

Figure 4.24: The experiment result of the lopsided profile and its height profiles reconstructed along the directions that the slopes are most and least steep. At the moment $\tau' = 0.266$, the symmetry breaks on direction B, as shown in the dark blue asterisks in Fig 4.24e, and the touch-down area is located in 39.8 $\mu$m $\leq r \leq$ 60.6 $\mu$m; meanwhile the height profile on direction A remains symmetrical.

.

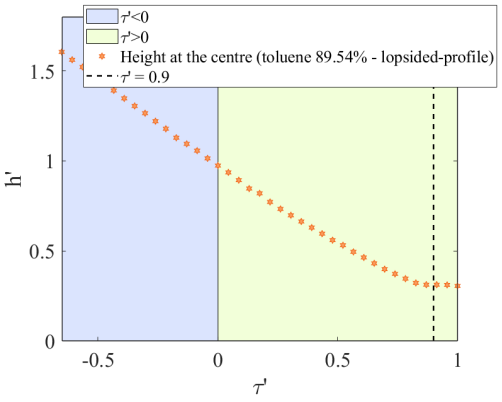


(a) The evolution of the height at the centre of the lopsided profile in Fig 4.24.

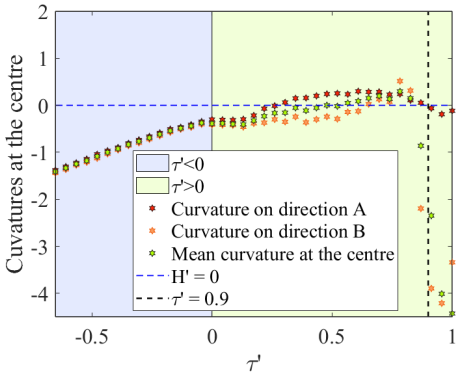


(b) The evolution of the mean curvature at the centre.

.

Figure 4.25: The evolutions of height and curvature at the centre of the lopsided profile.

.

The evolution of the height at the centre, presented in Fig 4.25b, shows that the height decreases almost linearly until the moment $\tau' = 0.826$; after then the height at the centre almost keeps the same the value before it touches down. The height at the centre evolves the same in any direction and it does not provide much information to distinguish a lopsided profile from symmetrical profiles.

In Fig 4.25, the curvatures on the directions and the mean curvature show the same evolution before $\tau' = 0.0870$, indicating that the profile is symmetrical. However, the curvature on Direction A (the symmetrical direction) rises faster than that on Direction B afterwards and remains positive until $\tau' = 0.900$. The different values of the curvatures indicate that the internal flows due to the Laplace pressure are also different on the directions.

## 4.4 Doughnut Profile after Touch-down

Apart from bell-shaped profile, M-shaped profile, spreading profile and lopsided profile which emerges from a non-ideal mixture, there is a doughnut-shaped profile, which has a torus liquid deposit appearing from binary solvent systems when it touches down at the base and is receding towards the edge of a well. However, unlike the other profiles appearing while droplets do not touch down, doughnut-

shaped profiles only turn up when a droplet touches down and the newly-emerging contact line is receding towards the edge of a well.

The evolution of a doughnut-shaped profile is presented in Fig 4.26. At $\tau' = 1.10$ the doughnut ring, which is a part of the top of a torus, shown in the inner dark fringe near the centre, is separated from the main part of the liquid droplet. In the mean time, the other part of the mixture keeps moving towards the edge of the well until $\tau' = 1.15$. At $\tau' = 1.20$, liquid only exists at the doughnut ring, suggesting that the doughnut ring is rich in the less volatile solvent of the mixture, mesitylene. The values of $\Omega$'s for mesitylene and n-butyl acetate are 24.6 and 4.46, respectively.

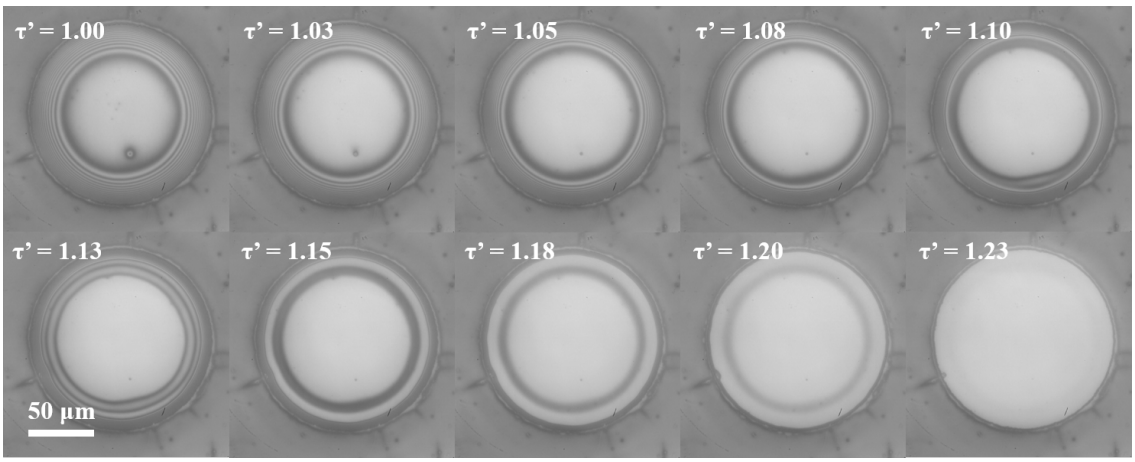


Figure 4.26: Doughnut-shaped profile of the binary mixture of mesitylene(49.98% in mass, 1.5001g) and n-butyl acetate (50.02% in mass, 1.5012g), evaporating in a well with the depth and radius of 2.50 $\mu$m and 75.0 $\mu$m, respectively.

# CHAPTER 5

# Conclusion

## 5.1 Conclusion

In Chapter 2, I have analysed the error due to the existence of an extra thin ITO layer which is widely used in fabricating a device. The result shows that the error is 7 nm approximately and does not have a serious impact on the further geometrical analysis, since the error is the same at each point. In addition, I have also analysed the error in the experiment of an evaporating binary droplet, since the refractive index of a binary system changes while a binary droplet is evaporating; the error, 6% approximately, depends on the difference of the refractive indices of the components in a binary system.

The code written to calculate the error is listed in Appx 1.1. Also, the height profile of an evaporating droplet is reconstructed at a moment, based on the merit of the axial symmetry; the mean curvature, Gaussian curvature and principal curvatures of a surface are proved effective to distinguish the shapes of different height profiles.

In Chapter 3, I have introduced three different sorts of height profiles, namely W-shaped profile, U-shaped profile and C-shaped profile, emerging when pure droplets

evaporating in cylindrical wells with aspect ratio ranging from 1.00/75.0 to 3.20/75.0. The evolution of the mean curvature at the centre is key to recognise the shape of a profile; in addition, the evolution of the height at the centre also shows different tendencies. All the shapes are distinguished before $\tau' = 0.90$ when the disjoining pressure is about to contribute the pressure difference over the liquid-air interface. Furthermore, I have shown how to anticipate the evaporation rate of a pure droplet in a cylindrical well. The results prove the effectiveness of a parameter $\Omega = (\sigma\epsilon^4)/(\mu E_0)$, which is also defined as enhanced capillary number [95], to predicting the shape of a profile from a pure droplet evaporating in a cylindrical well. Also, W-shaped profile or U-shaped profile will appear when the temperature of a substrate increases. The deposits from the dilute polystyrene solution show that a W-shaped profile will leave a W-shaped deposit while a deposit from a U-shaped profile has a relative flat bottom near the centre with the majority of the deposit near the contact line as the internal flow only comprises the capillary flow due to evaporation.

In Chapter 4, I have calculated the theoretical evaporation rate of an ideal binary droplet in a cylindrical well, showing that the evaporation rate of the entire system does not change linearly if the components have different evaporation rates, assuming that the droplet obeys Raoult's law; the results in Eq 4.1.25 and Fig 4.1f show that the evolution of mole fractions follows a logistic-curve-like tendencies. Furthermore, I have also deduced the evolution of surface tension in a binary system; since the surface tension gradient along the r-direction results from the preferential evaporation ultimately, the definition of $Ma$ in this study is defined as shown in Eq 4.1.3. Although the exact value of $Ma$ is no longer easily calculated like what I have done with $\Omega$ for pure droplets, the sign of $Ma$ indicates the direction of the Marangoni flow which inevitably induces four new shapes, bell-shaped profile, lopsided-profile, M-shaped profile and spreading profile; the first two profiles appear when $Ma < 0$, whereas the two other profiles emerge if $Ma > 0$. I have also explained the geometrical features of the four new profiles and the way to distinguish them. The non-ideal binary system of toluene and n-butanol bears positive deviation from Raoult's law, that is when the concentration of n-butanol is low, n-butanol

in fact evaporates faster than toluene; however, while we increase the concentration of n-butanol, toluene will be the more volatile solvent, so that the profiles are M-shaped when the system is dilute in n-butanol, but become lopsided or bell-shaped when it is growing rich in n-butanol. Therefore, in practical use, an ink in industry shall be carefully prepared while selecting proper solvents and the concentration of the different components matters especially when they combine a mixture having positive deviation from Raoult's law.

## 5.2 Future Work

In this work, the influence of the aspect ratio has been investigated; however, pixels that are the wells on a substrate to hold ink and generate specific pattern, are not always cylindrical [185] [186] [187]; most of them are stadium-like and do not have a flat base [188]. Hence, the future work may endeavour to research the height profiles in wells with different shapes and upgrade the parameter [189] [190], $\Omega$, for the new scenarios. There may appear a shape with W-shaped on the one principal direction and U-shaped or C-shaped on the other principal direction; in this case, the evolution of the height at the centre could be critical to decide the shape of a profile since it is the same at any direction and may turn out to be unique for different profiles as well.

What is more, one direction of the shape may be designed to be much longer than the other side, almost turning a well to be a groove [191] [192] [193], and the evaporation process may involve Rayleigh-Plateau instability on the longer side direction [194] [195] [196]. The merit is that the volumes of the sub-droplets generated due to Rayleigh-Plateau instability may follow specific rules based on the gradient of surface tension and evaporation rate. The distance between each groove will be a critical factor, if there are more than two grooves [197].

Moreover, in industry, most pixels which mostly are wells with irregular shapes the degree of which depends on the accuracy of photolithography, have the banks not developed perpendicularly. In this case, the contact line may not be fixed and is likely to move during evaporation. For an evaporating droplet, the receding

angle is not always the same as the Young's contact angle as the receding contact angle increases with the volatility and decreases if the thickness of the wetting film increases [198] [199].

When a droplet overfills a well with the apparent contact angle $\theta_{ap}$ larger then $\theta_0 + \alpha$, in which $\theta_0$ and $\alpha$ are the contact angle of a droplet and the slope of a bank, a droplet will spread out, as is shown in Fig 5.1a, according to Gibbs pinning criterion [200] [201].

However, when a droplet recedes, it may remain concave-down if its receding angle is larger than $\alpha$; but the meniscus of a droplet will turn to be concave-up when the receding angle is smaller than $\alpha$, as is shown in Fig 5.1b. Future work of this project may attempt to find proper angles for different solvent systems so as to achieve desired results, and to update the parameter $\Omega$ to adapt to the new scenarios.

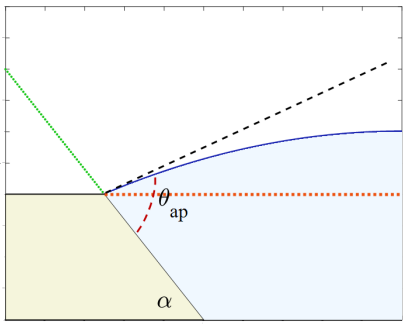


(a) The case of advancing leftwards, when the apparent contact angle $\theta_{ap}$ is larger than $\alpha + \theta_0$, while the meniscus is concave down.

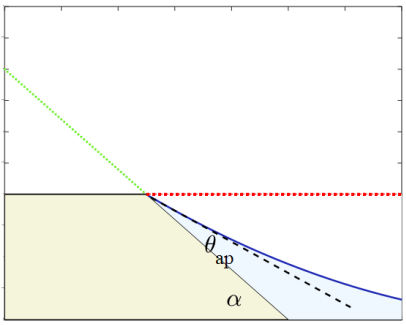


(b) The case of receding downwards, when the receding angle is smaller than $\alpha$, while the meniscus is concave up. The blue region is the liquid part.

Figure 5.1: The possible cases of de-pinning contact lines, where $\theta_0$ is the contact angle of a droplet on a flat surface, $\theta_{ap}$ is the apparent contact angle of a droplet and $\alpha$ is the slope of a bank.

.

If the mechanism of the process is well-understood, the application of printing electronics may find even more possible ways to design the structure of a device. Regarding thin, printed films, future study should attempt to develop a quantitative method to measure its thickness and uniformity, especially when a layer is as thick as 50 nm. My thought is that we could try to analyse the light intensity from the

fringes of three-beam interference in which the final reflection is from polymer-air interface instead of droplet-air interface.

When the aspect ratio of a well is not so small as I have used in this work, pure droplets may appear to be C-shaped profiles as $\Omega$ contains the item $\epsilon^4$ which means a small change of $h$ or $R$ has a much greater impact on the shape of a profile than the property of a pure solvent droplet. If a droplet is seeded with particles which do not change the evaporation process, the particles will mostly deposit near the contact line as the coffee-ring effect still dominates.

For binary droplets or multiple-component droplets, the Marangoni effect, thermal or solutal, has considerable effect on profiles [74]. The contact angle may change during evaporation when preferential evaporation occurs, as is already found in ethanol-water droplets [71], leading to a even more complex situations for droplets evaporating in shallow, sloped wells.

Also, I have only investigated the droplets which are generated by printing one droplet only. However, in the real world, the volume of a droplet from an ink-jet printer usually ranges from 3 to 6 pl [202], so that it takes four to six droplets to merge and fill a blank well entirely [203] [204]. The location of the droplets and the merging period may contribute to the final result and shapes as the last droplet may not have the same concentration with the first one [205] [206], generating a surface tension gradient along some direction. Therefore, the strategy including the locations of a series of droplets, the time difference between each droplet, the volumes of droplets and the geometrical features of a well, is fundamental and shall be fully exploited so that the synergistic effects of the factors aforementioned can be maximised to fabricate a device with the best performance possible.

# Bibliography


[1] H. Hu and R. G. Larson, "Evaporation of a sessile droplet on a substrate," *The Journal of Physical Chemistry B*, vol. 106, no. 6, pp. 1334–1344, 2002. 1, 1.3, 1.3, 1.4, 3.1, 4.1

[2] H. Hu and R. G. Larson, "Analysis of the effects of marangoni stresses on the microflow in an evaporating sessile droplet," *Langmuir*, vol. 21, no. 9, pp. 3972–3980, 2005. 1, 1.3, 1.3, 1.3, 1.3, 3.1

[3] J. Kang, J. B.-H. Tok, and Z. Bao, "Self-healing soft electronics," *Nature Electronics*, vol. 2, no. 4, pp. 144–150, 2019. 1.1

[4] S. Khan, L. Lorenzelli, and R. S. Dahiya, "Technologies for printing sensors and electronics over large flexible substrates: A review," *IEEE Sensors Journal*, vol. 15, no. 6, pp. 3164–3185, 2014. 1.1

[5] J. A. Lewis and B. Y. Ahn, "Three-dimensional printed electronics," *Nature*, vol. 518, no. 7537, pp. 42–43, 2015. 1.1

[6] Y. Khan, A. Thielens, S. Muin, J. Ting, C. Baumbauer, and A. C. Arias, "A new frontier of printed electronics: flexible hybrid electronics," *Advanced Materials*, vol. 32, no. 15, pp. 1905279(1)–1905279(11), 2020. 1.1

[7] E. B. Secor, B. Y. Ahn, T. Z. Gao, J. A. Lewis, and M. C. Hersam, "Rapid and versatile photonic annealing of graphene inks for flexible printed electronics," *Advanced Materials*, vol. 27, no. 42, pp. 6683–6688, 2015. 1.1

[8] M. K. Choi, J. Yang, T. Hyeon, and D.-H. Kim, "Flexible quantum dot light-emitting diodes for next-generation displays," *npj Flexible Electronics*, vol. 2, no. 1, pp. 1–14, 2018. 1.1

[9] S. Ma, Y. Kumaresan, A. S. Dahiya, and R. Dahiya, "Ultra-thin chips with printed interconnects on flexible foils," *Advanced Electronic Materials*, vol. 8, no. 5, p. 2101029, 2022. 1.1

[10] D. Jiang, Z. Chu, J. Peng, and W. Jin, "Screen-printed biosensor chips with prussian blue nanocubes for the detection of physiological analytes," *Sensors and Actuators B: Chemical*, vol. 228, pp. 679–687, 2016. 1.1

[11] Y. Wang, C. Chen, H. Xie, T. Gao, Y. Yao, G. Pastel, X. Han, Y. Li, J. Zhao, K. Fu, *et al.*, "3d-printed all-fiber li-ion battery toward wearable energy storage," *Advanced Functional Materials*, vol. 27, no. 43, pp. 1703140(4)–1703140(5), 2017. 1.1

[12] A. M. Gaikwad, D. A. Steingart, T. Nga Ng, D. E. Schwartz, and G. L. Whiting, "A flexible high potential printed battery for powering printed electronics," *Applied Physics Letters*, vol. 102, no. 23, pp. 104–108, 2013. 1.1

[13] D. Maurya, S. Khaleghian, R. Sriramdas, P. Kumar, R. A. Kishore, M. G. Kang, V. Kumar, H.-C. Song, S.-Y. Lee, Y. Yan, *et al.*, "3d printed graphene-based self-powered strain sensors for smart tires in autonomous vehicles," *Nature communications*, vol. 11, no. 1, pp. 1–10, 2020. 1.1

[14] S. Cinti and F. Arduini, "Graphene-based screen-printed electrochemical (bio) sensors and their applications: Efforts and criticisms," *Biosensors and Bioelectronics*, vol. 89, pp. 107–122, 2017. 1.1

[15] Z. Zhu, H. S. Park, and M. C. McAlpine, "3d printed deformable sensors," *Science advances*, vol. 6, no. 25, pp. eaba5575(2)–eaba5575(5), 2020. 1.1

[16] R. Su, S. H. Park, X. Ouyang, S. I. Ahn, and M. C. McAlpine, "3d-printed flexible organic light-emitting diode displays," *Science advances*, vol. 8, no. 1, p. eabl8798, 2022. 1.1

[17] Y. Yao, Y. Chen, K. Wang, N. Turetta, S. Vitale, B. Han, H. Wang, L. Zhang, and P. Samorì, "A robust vertical nanoscaffold for recyclable, paintable, and flexible light-emitting devices," *Science advances*, vol. 8, no. 10, pp. eabn2225(3)–eabn2225(4), 2022. 1.1

[18] C. Wei, W. Su, J. Li, B. Xu, Q. Shan, Y. Wu, F. Zhang, M. Luo, H. Xiang, Z. Cui, *et al.*, "A universal ternary-solvent-ink strategy toward efficient inkjet-printed perovskite quantum dot light-emitting diodes," *Advanced Materials*, vol. 34, no. 10, pp. 2107798(3)–2107798(15), 2022. 1.1

[19] D. C. Kim, H. Yun, J. Kim, H. Seung, W. S. Yu, J. H. Koo, J. Yang, J. H. Kim, T. Hyeon, and D.-H. Kim, "Three-dimensional foldable quantum dot light-emitting diodes," *Nature Electronics*, vol. 4, no. 9, pp. 671–680, 2021. 1.1

[20] T. Meng, Y. Zheng, D. Zhao, H. Hu, Y. Zhu, Z. Xu, S. Ju, J. Jing, X. Chen, H. Gao, *et al.*, "Ultrahigh-resolution quantum-dot light-emitting diodes," *Nature Photonics*, vol. 16, no. 4, pp. 297–303, 2022. 1.1

[21] H. Sirringhaus, T. Kawase, R. Friend, T. Shimoda, M. Inbasekaran, W. Wu, and E. P. Woo, "High-resolution inkjet printing of all-polymer transistor circuits," *Science*, vol. 290, no. 5499, pp. 2123–2126, 2000. 1.1

[22] Y. Yu, J. Li, S. A. Solomon, J. Min, J. Tu, W. Guo, C. Xu, Y. Song, and W. Gao, "All-printed soft human-machine interface for robotic physicochemical sensing," *Science Robotics*, vol. 7, no. 67, pp. eabn0495(3)–eabn0495(6), 2022. 1.1

[23] A. J. Hart and A. Rao, "How to print a 3d object all at once," *Science*, vol. 363, no. 6431, pp. 1042–1043, 2019. 1.1

[24] P. Tian, V. Bulovic, P. Burrows, G. Gu, S. Forrest, and T. Zhou, "Precise, scalable shadow mask patterning of vacuum-deposited organic light emitting devices," *Journal of Vacuum Science & Technology A: Vacuum, Surfaces, and Films*, vol. 17, no. 5, pp. 2975–2981, 1999. 1.1

[25] X. Cheng and L. J. Guo, "A combined-nanoimprint-and-photolithography patterning technique," *Microelectronic Engineering*, vol. 71, no. 3-4, pp. 277–282, 2004. 1.1

[26] W. Shen, X. Zhang, Q. Huang, Q. Xu, and W. Song, "Preparation of solid silver nanoparticles for inkjet printed flexible electronics with high conductivity," *Nanoscale*, vol. 6, no. 3, pp. 1622–1628, 2014. 1.1

[27] J.-A. Pan and D. V. Talapin, "3d-printing nanocrystals with light," *Science*, vol. 377, no. 6610, pp. 1046–1047, 2022. 1.1

[28] Y. Wu, J. Ren, S. Zhang, and S. Wu, "Nanosphere-aggregation-induced reflection and its application in large-area and high-precision panchromatic inkjet printing," *ACS applied materials & interfaces*, vol. 12, no. 9, pp. 10867–10874, 2020. 1.1

[29] T. Driessen and R. Jeurissen, "Drop formation in inkjet printing," *Fundamentals of Inkjet Printing: The Science of Inkjet and Droplets*, pp. 93–116, 2016. 1.1

[30] D. Lohse, "Fundamental fluid dynamics challenges in inkjet printing," *Annual review of fluid mechanics*, vol. 54, pp. 349–382, 2022. 1.1, 1.2, 1.2, 1.3.2

[31] S. K. Wilson and H.-M. DAmbrosio, "Evaporation of sessile droplets," *Annual Review of Fluid Mechanics*, vol. 55, 2023. 1.1

[32] Q. Zhang, Q. Jin, A. Mertens, C. Rainer, R. Huber, J. Fessler, G. Hernandez-Sosa, and U. Lemmer, "Fabrication of bragg mirrors by multilayer inkjet printing," *Advanced Materials*, vol. 34, no. 33, pp. 2201348(4)–2201348(9), 2022. 1.1

[33] P. Calvert, "Inkjet printing for materials and devices," *Chemistry of materials*, vol. 13, no. 10, pp. 3299–3305, 2001. 1.1

[34] L. Nayak, S. Mohanty, S. K. Nayak, and A. Ramadoss, "A review on inkjet printing of nanoparticle inks for flexible electronics," *Journal of Materials Chemistry C*, vol. 7, no. 29, pp. 8771–8795, 2019. 1.1

[35] J. Kwon, Y. Takeda, K. Fukuda, K. Cho, S. Tokito, and S. Jung, "Three-dimensional, inkjet-printed organic transistors and integrated circuits with 100% yield, high uniformity, and long-term stability," *ACS nano*, vol. 10, no. 11, pp. 10324–10330, 2016. 1.1

[36] M. Gao, L. Li, and Y. Song, "Inkjet printing wearable electronic devices," *Journal of Materials Chemistry C*, vol. 5, no. 12, pp. 2971–2993, 2017. 1.1

[37] H. Kim, J. I. Jang, H. H. Kim, G.-W. Lee, J. A. Lim, J. T. Han, and K. Cho, "Sheet size-induced evaporation behaviors of inkjet-printed graphene oxide for printed electronics," *ACS Applied Materials & Interfaces*, vol. 8, no. 5, pp. 3193–3199, 2016. 1.1

[38] Z.-J. Zhao, S.-H. Shin, S. Y. Lee, B. Son, Y. Liao, S. Hwang, S. Jeon, H. Kang, M. Kim, and J.-H. Jeong, "Direct chemisorption-assisted nanotransfer printing with wafer-scale uniformity and controllability," *ACS nano*, vol. 16, no. 1, pp. 378–385, 2022. 1.1

[39] Y. Zhang, S. Zheng, F. Zhou, X. Shi, C. Dong, P. Das, J. Ma, K. Wang, and Z.-S. Wu, "Multi-layer printable lithium ion micro-batteries with remarkable areal energy density and flexibility for wearable smart electronics," *Small*, vol. 18, no. 5, pp. 2104506(3)–2104506(8), 2022. 1.1

[40] M. Xie, L. Lian, X. Mu, Z. Luo, C. E. Garciamendez-Mijares, Z. Zhang, A. López, J. Manríquez, X. Kuang, J. Wu, *et al.*, "Volumetric additive manufacturing of pristine silk-based (bio) inks," *Nature Communications*, vol. 14, no. 1, pp. 210–215, 2023. 1.1

[41] C. Chen, J. Chen, H. Han, L. Chao, J. Hu, T. Niu, H. Dong, S. Yang, Y. Xia, Y. Chen, *et al.*, "Perovskite solar cells based on screen-printed thin films," *Nature*, pp. 1–6, 2022. 1.1

[42] T.-L. Hsieh, S. Garoff, and R. D. Tilton, "Marangoni spreading time evolution and synergism in binary surfactant mixtures," *Journal of Colloid and Interface Science*, vol. 623, pp. 685–696, 2022. 1.1

[43] P. Johansson, G. Galliéro, and D. Legendre, "How molecular effects affect solutal marangoni flows," *Physical Review Fluids*, vol. 7, no. 6, pp. 064202–064212, 2022. 1.1

[44] Y. Xiao, N. M. Ribe, Y. Zhang, Y. Pan, Y. Cao, and H. C. Shum, "Generation of fermats spiral patterns by solutal marangoni-driven coiling in an aqueous two-phase system," *Nature Communications*, vol. 13, no. 1, pp. 7206–7211, 2022. 1.1

[45] J. Ryu, H. S. Ko, and H. Kim, "Vapor absorption and marangoni flows in evaporating drops," *Langmuir*, vol. 38, no. 7, pp. 2185–2191, 2022. 1.1

[46] S. D. Hoath, *Fundamentals of inkjet printing: the science of inkjet and droplets*. John Wiley & Sons, 2016. 1.2

[47] H. Dong, W. W. Carr, and J. F. Morris, "An experimental study of drop-on-demand drop formation," *Physics of fluids*, vol. 18, no. 7, pp. 072102(1)–072102(2), 2006. 1.2

[48] J. Lemarchand, N. Bridonneau, N. Battaglini, F. Carn, G. Mattana, B. Piro, S. Zrig, and V. Noël, "Challenges, prospects, and emerging applications of inkjet-printed electronics: A chemist's point of view," *Angewandte Chemie International Edition*, vol. 61, no. 20, pp. e202200166(2)–e202200166(3), 2022. 1.2

[49] T. Driessen, P. Sleutel, F. Dijksman, R. Jeurissen, and D. Lohse, "Control of jet breakup by a superposition of two rayleigh–plateau-unstable modes," *Journal of fluid mechanics*, vol. 749, pp. 275–296, 2014. 1.2

[50] B. N. Diggs-McGee, E. L. Kreiger, M. A. Kreiger, and M. P. Case, "Print time vs. elapsed time: A temporal analysis of a continuous printing operation for additive constructed concrete," *Additive Manufacturing*, vol. 28, pp. 205–214, 2019. 1.2

[51] S. Hoath, S. Jung, and I. Hutchings, "A simple criterion for filament break-up in drop-on-demand inkjet printing," *Physics of Fluids*, vol. 25, no. 2, pp. 021701(7)–021701(8), 2013. 1.2

[52] S. Ma, F. Ribeiro, K. Powell, J. Lutian, C. Møller, T. Large, and J. Holbery, "Fabrication of novel transparent touch sensing device via drop-on-demand inkjet printing technique," *ACS applied materials & interfaces*, vol. 7, no. 39, pp. 21628–21633, 2015. 1.2

[53] J. Castrejón-Pita, G. Martin, S. Hoath, and I. Hutchings, "A simple large-scale droplet generator for studies of inkjet printing," *Review of Scientific Instruments*, vol. 79, no. 7, pp. 075108(3)–075108(8), 2008. 1.2

[54] A. Lee, K. Sudau, K. H. Ahn, S. J. Lee, and N. Willenbacher, "Optimization of experimental parameters to suppress nozzle clogging in inkjet printing," *Industrial & engineering chemistry research*, vol. 51, no. 40, pp. 13195–13204, 2012. 1.2

[55] G. H. McKinley and M. Renardy, "Wolfgang von ohnesorge," *Physics of Fluids*, vol. 23, no. 12, pp. 127101(4)–127101(5), 2011. 1.1, 1.2

[56] H. Schlichting and K. Gersten, *Boundary-layer theory*. Springer Science & Business Media, 2003. 1.2, 3.2, 3.2, 3.2

[57] N. Rott, "Note on the history of the reynolds number," *Annual review of fluid mechanics*, vol. 22, no. 1, pp. 1–12, 1990. 1.2

[58] S. Y. Misyura, "The effect of weber number, droplet sizes and wall roughness on crisis of droplet boiling," *Experimental Thermal and Fluid Science*, vol. 84, pp. 190–198, 2017. 1.2

[59] J. E. Seebergh and J. C. Berg, "Dynamic wetting in the low capillary number regime," *Chemical Engineering Science*, vol. 47, no. 17-18, pp. 4455–4464, 1992. 1.2

[60] N. D. Patil, J. Shaikh, A. Sharma, and R. Bhardwaj, "Droplet impact dynamics over a range of capillary numbers and surface wettability: Assessment of moving contact line models and energy budget analysis," *Physics of Fluids*, vol. 34, no. 5, pp. 052119(2)–052119(5), 2022. 1.2

[61] B. Derby, "Inkjet printing of functional and structural materials: fluid property requirements, feature stability, and resolution," *Annual Review of Materials Research*, vol. 40, pp. 395–414, 2010. 1.2

[62] H.-Y. Jun, S.-J. Kim, and C.-H. Choi, "Ink formulation and printing parameters for inkjet printing of two dimensional materials: A mini review," *Nanomaterials*, vol. 11, no. 12, pp. 3441(1)–3441(7), 2021. 1.2

[63] B. Derby, "Additive manufacture of ceramics components by inkjet printing," *Engineering*, vol. 1, no. 1, pp. 113–123, 2015. 1.2

[64] P. C. Duineveld, M. M. De Kok, M. Buechel, A. Sempel, K. A. Mutsaers, P. Van de Weijer, I. G. Camps, T. Van de Biggelaar, J.-E. J. Rubingh, and E. I. Haskal, "Ink-jet printing of polymer light-emitting devices," in *Organic Light-Emitting Materials and Devices V*, vol. 4464, pp. 59–67, SPIE, 2002. 1.2

[65] R. Reitz and S. Lin, "Drop and spray formation from a liquid jet," *Annu. Rev. Fluid Mech*, vol. 30, pp. 85–89, 1998. 1.2

[66] D. Kong, Y. Wang, S. Huang, B. Zhang, Y. V. Lim, G. J. Sim, P. Valdivia y Alvarado, Q. Ge, and H. Y. Yang, "3d printed compressible quasi-solid-state nickel–iron battery," *Acs Nano*, vol. 14, no. 8, pp. 9675–9686, 2020. 1.3

[67] R. D. Deegan, O. Bakajin, T. F. Dupont, G. Huber, S. R. Nagel, and T. A. Witten, "Capillary flow as the cause of ring stains from dried liquid drops," *Nature*, vol. 389, no. 6653, pp. 827–829, 1997. 1.3, 1.3

[68] R. D. Deegan, "Pattern formation in drying drops," *Physical review E*, vol. 61, no. 1, pp. 475–476, 2000. 1.3

[69] C. Diddens, Y. Li, and D. Lohse, "Competing marangoni and rayleigh convection in evaporating binary droplets," *Journal of fluid mechanics*, vol. 914, 2021. 1.3, 1.3

[70] K. Sefiane, "Patterns from drying drops," *Advances in colloid and interface science*, vol. 206, pp. 372–381, 2014. 1.3

[71] H. Tan, C. Diddens, A. A. Mohammed, J. Li, M. Versluis, X. Zhang, and D. Lohse, "Microdroplet nucleation by dissolution of a multicomponent drop in a host liquid," *Journal of fluid mechanics*, vol. 870, pp. 217–246, 2019. 1.2, 1.3, 5.2

[72] R. Picknett and R. Bexon, "The evaporation of sessile or pendant drops in still air," *Journal of colloid and Interface Science*, vol. 61, no. 2, pp. 336–350, 1977. 1.3, 1.3

[73] D. Hu and H. Wu, "Volume evolution of small sessile droplets evaporating in stick-slip mode," *Physical Review E*, vol. 93, no. 4, pp. 042805(3)–042805(6), 2016. 1.3

[74] A. A. Pahlavan, L. Yang, C. D. Bain, and H. A. Stone, "Evaporation of binary-mixture liquid droplets: The formation of picoliter pancakelike shapes," *Physical review letters*, vol. 127, no. 2, pp. 024501(8)–024501(9), 2021. 1.3, 1.3.1, 1.3.2, 1.3.2, 1.3.2, 3.2, 5.2

[75] H. W. Morse, "On evaporation from the surface of a solid sphere. preliminary note," in *Proceedings of the American Academy of Arts and Sciences*, vol. 45, pp. 363–367, JSTOR, 1910. 1.3, 3.1

[76] H. Y. Erbil, G. McHale, and M. Newton, "Drop evaporation on solid surfaces: constant contact angle mode," *Langmuir*, vol. 18, no. 7, pp. 2636–2641, 2002. 1.3

[77] R. W. Coutant and E. C. Penski, "Experimental evaluation of mass transfer from sessile drops," *Industrial & Engineering Chemistry Fundamentals*, vol. 21, no. 3, pp. 250–254, 1982. 1.3

[78] R. D. Deegan, O. Bakajin, T. F. Dupont, G. Huber, S. R. Nagel, and T. A. Witten, "Contact line deposits in an evaporating drop," *Physical review E*, vol. 62, no. 1, pp. 756–760, 2000. 1.3, 1.4

[79] C. Diddens, "Detailed finite element method modeling of evaporating multicomponent droplets," *Journal of Computational Physics*, vol. 340, pp. 670–687, 2017. 1.3

[80] S. K. Wilson and B. R. Duffy, "Mathematical models for the evaporation of sessile droplets," *Drying of Complex Fluid Drops: Fundamentals and Applications*, vol. 14, pp. 47–52, 2022. 1.3

[81] X. Du and R. Deegan, "Ring formation on an inclined surface," *Journal of Fluid Mechanics*, vol. 775, pp. R3(2)–R3(12), 2015. 1.3

[82] S. Morris, "On the contact region of a diffusion-limited evaporating drop: a local analysis," *Journal of fluid mechanics*, vol. 739, pp. 308–337, 2014. 1.3

[83] O. Carrier, N. Shahidzadeh-Bonn, R. Zargar, M. Aytouna, M. Habibi, J. Eggers, and D. Bonn, "Evaporation of water: evaporation rate and collective effects," *Journal of Fluid Mechanics*, vol. 798, pp. 774–786, 2016. 1.3

[84] A. Oron, S. H. Davis, and S. G. Bankoff, "Long-scale evolution of thin liquid films," *Reviews of modern physics*, vol. 69, no. 3, p. 931, 1997. 1.3, 3.2

[85] A. Marchand, J. H. Weijs, J. H. Snoeijer, and B. Andreotti, "Why is surface tension a force parallel to the interface?," *American Journal of Physics*, vol. 79, no. 10, pp. 999–1008, 2011. 1.3, 1.3.1

[86] P. G. de Gennes, *Soft interfaces: the 1994 Dirac memorial lecture*. Cambridge University Press, 1997. 1.3

[87] P. Atkins, P. W. Atkins, and J. de Paula, *Atkins' physical chemistry*. Oxford university press, 2014. 1.3.1, 2.4.2, 3.1, 3.1, 3.1, 4.1, 4.3

[88] P.-G. De Gennes, F. Brochard-Wyart, D. Quéré, *et al.*, *Capillarity and wetting phenomena: drops, bubbles, pearls, waves*, vol. 315. Springer, 2004. 1.3.1, 3.3.1

[89] C. W. Extrand, "Meniscus formation in a vertical capillary tube," *Langmuir*, vol. 38, no. 7, pp. 2346–2353, 2022. 1.3.1

[90] I. Cantat, "Liquid meniscus friction on a wet plate: Bubbles, lamellae, and foams," *Physics of Fluids*, vol. 25, no. 3, pp. 031303(5)–031303(8), 2013. 1.3.1

[91] L. D. Landau and E. M. Lifshitz, *Fluid Mechanics: Landau and Lifshitz: Course of Theoretical Physics, Volume 6*, vol. 6. Elsevier, 2013. 1.3.1

[92] C. K. Batchelor and G. Batchelor, *An introduction to fluid dynamics*. Cambridge university press, 2000. 1.3.1

[93] M. R. Moore, D. Vella, and J. M. Oliver, "The nascent coffee ring: how solute diffusion counters advection," *Journal of Fluid Mechanics*, vol. 920, pp. A54(3)–A54(15), 2021. 1.3.1, 3.2

[94] M. R. Moore, D. Vella, and J. M. Oliver, "The nascent coffee ring with arbitrary droplet contact set: an asymptotic analysis," *Journal of Fluid Mechanics*, vol. 940, 2022. 1.3.1, 3.2

[95] C. N. Kaplan and L. Mahadevan, "Evaporation-driven ring and film deposition from colloidal droplets," *Journal of Fluid Mechanics*, vol. 781, p. R2, 2015. 1.3.1, 1.3.2, 3, 3.2, 5.1

[96] A. D. Carrithers, M. J. Brown, M. Z. Rashed, S. Islam, O. D. Velev, and S. J. Williams, "Multiscale self-assembly of distinctive weblike structures from evaporated drops of dilute american whiskeys," *ACS nano*, vol. 14, no. 5, pp. 5417–5425, 2020. 1.3.2

[97] M. Gugliotti, M. S. Baptista, and M. J. Politi, "Surface tension gradients induced by temperature: the thermal marangoni effect," *Journal of chemical education*, vol. 81, no. 6, pp. 824–826, 2004. 1.3.2

[98] B. Zeng, K. L. Chong, Y. Wang, C. Diddens, X. Li, M. Detert, H. J. Zandvliet, and D. Lohse, "Periodic bouncing of a plasmonic bubble in a binary liquid by competing solutal and thermal marangoni forces," *Proceedings of the National Academy of Sciences*, vol. 118, no. 23, pp. e2103215118(3)–e2103215118(5), 2021. 1.3.2

[99] L. Thayyil Raju, C. Diddens, Y. Li, A. Marin, M. N. Van Der Linden, X. Zhang, and D. Lohse, "Evaporation of a sessile colloidal water–glycerol droplet: Marangoni ring formation," *Langmuir*, vol. 38, no. 39, pp. 12082–12094, 2022. 1.3.2

[100] H. Kim, F. Boulogne, E. Um, I. Jacobi, E. Button, and H. A. Stone, "Controlled uniform coating from the interplay of marangoni flows and surface-adsorbed macromolecules," *Physical review letters*, vol. 116, no. 12, pp. 124501(1)–124501(3), 2016. 1.4, 1.3.2

[101] X. Xu, J. Luo, and D. Guo, "Criterion for reversal of thermal marangoni flow in drying drops," *Langmuir*, vol. 26, no. 3, pp. 1918–1922, 2010. 1.3.2

[102] S. Shiri, S. Sinha, D. A. Baumgartner, and N. J. Cira, "Thermal marangoni flow impacts the shape of single component volatile droplets on thin, completely wetting substrates," *Physical Review Letters*, vol. 127, no. 2, pp. 024502(3)–024502(9), 2021. 1.3.2

[103] H. Hu and R. G. Larson, "Marangoni effect reverses coffee-ring depositions," *The Journal of Physical Chemistry B*, vol. 110, no. 14, pp. 7090–7094, 2006. 1.3.2

[104] Z. S. Davidson, Y. Huang, A. Gross, A. Martinez, T. Still, C. Zhou, P. J. Collings, R. D. Kamien, and A. Yodh, "Deposition and drying dynamics of liquid crystal droplets," *Nature communications*, vol. 8, no. 1, pp. 1–7, 2017. 1.3.2

[105] L. Scriven and C. Sternling, "The marangoni effects," *Nature*, vol. 187, no. 4733, pp. 186–188, 1960. 1.3.2

[106] D. A. Baumgartner, S. Shiri, S. Sinha, S. Karpitschka, and N. J. Cira, "Marangoni spreading and contracting three-component droplets on completely wetting surfaces," *Proceedings of the National Academy of Sciences*, vol. 119, no. 19, pp. e2120432119(3)–e2120432119(6), 2022. 1.3.2, 4.1.1

[107] A. Marin, R. Liepelt, M. Rossi, and C. J. Kähler, "Surfactant-driven flow transitions in evaporating droplets," *Soft Matter*, vol. 12, no. 5, pp. 1593–1600, 2016. 1.3.2

[108] D.-O. Kim, A. Rokoni, P. Kaneelil, C. Cui, L.-H. Han, and Y. Sun, "Role of surfactant in evaporation and deposition of bisolvent biopolymer droplets," *Langmuir*, vol. 35, no. 39, pp. 12773–12781, 2019. 1.3.2

[109] J. R. Trantum, M. L. Baglia, Z. E. Eagleton, R. L. Mernaugh, and F. R. Haselton, "Biosensor design based on marangoni flow in an evaporating drop," *Lab on a Chip*, vol. 14, no. 2, pp. 315–324, 2014. 1.3.2

[110] A. Marin, S. Karpitschka, D. Noguera-Marín, M. A. Cabrerizo-Vílchez, M. Rossi, C. J. Kähler, and M. A. R. Valverde, "Solutal marangoni flow as the cause of ring stains from drying salty colloidal drops," *Physical review fluids*, vol. 4, no. 4, pp. 041601(3)–041601(10), 2019. 1.3.2

[111] T. Li, A. Kar, and R. Kumar, "Marangoni circulation by uv light modulation on sessile drop for particle agglomeration," *Journal of Fluid Mechanics*, vol. 873, pp. 72–88, 2019. 1.3.2

[112] A. D. Nikolov, D. T. Wasan, A. Chengara, K. Koczo, G. A. Policello, and I. Kolossvary, "Superspreading driven by marangoni flow," *Advances in colloid and interface science*, vol. 96, no. 1-3, pp. 325–338, 2002. 1.3.2

[113] S. Deodhar, S. P. Thampi, and M. G. Basavaraj, "Drops spreading on fluid surfaces: Transition from laplace to marangoni regime," *Physical Review Fluids*, vol. 6, no. 11, pp. L112001(1)–L112001(15), 2021. 1.3.2

[114] H.-H. Wei, "Marangoni-enhanced capillary wetting in surfactant-driven superspreading," *Journal of Fluid Mechanics*, vol. 855, pp. 181–209, 2018. 1.3.2

[115] D. Lohse and X. Zhang, "Physicochemical hydrodynamics of droplets out of equilibrium," *Nature Reviews Physics*, vol. 2, no. 8, pp. 426–443, 2020. 1.3.2

[116] R. Van Gaalen, H. Wijshoff, J. Kuerten, and C. Diddens, "Competition between thermal and surfactant-induced marangoni flow in evaporating sessile droplets," *Journal of colloid and interface science*, vol. 622, pp. 892–903, 2022. 1.3.2

[117] P. Kolliopoulos, K. S. Jochem, L. F. Francis, and S. Kumar, "Capillary flow of evaporating liquid solutions in open rectangular microchannels," *Journal of Fluid Mechanics*, vol. 938, pp. A22(3)–A22(5), 2022. 1.3.2

[118] S. Kalliadasis, A. Kiyashko, and E. Demekhin, "Marangoni instability of a thin liquid film heated from below by a local heat source," *Journal of Fluid Mechanics*, vol. 475, pp. 377–408, 2003. 1.3.2

[119] O. S. Pak, J. Feng, and H. A. Stone, "Viscous marangoni migration of a drop in a poiseuille flow at low surface péclet numbers," *Journal of fluid mechanics*, vol. 753, pp. 535–552, 2014. 1.3.2

[120] T. Kajiya, W. Kobayashi, T. Okuzono, and M. Doi, "Controlling the drying and film formation processes of polymer solution droplets with addition of small amount of surfactants," *The Journal of Physical Chemistry B*, vol. 113, no. 47, pp. 15460–15466, 2009. 1.4, 1.4

[121] P. Kant, A. L. Hazel, M. Dowling, A. B. Thompson, and A. Juel, "Controlling droplet spreading with topography," *Physical Review Fluids*, vol. 2, no. 9, pp. 094002(3)–094002(13), 2017. 1.4

[122] D. Van Dam and J. Kuerten, "Modeling the drying of ink-jet-printed structures and experimental verification," *Langmuir*, vol. 24, no. 2, pp. 582–589, 2008. 1.4, 1.4

[123] L. Wang, M. H. Lee, J. Barton, L. Hughes, and T. W. Odom, "Shape-control of protein crystals in patterned microwells," *Journal of the American Chemical Society*, vol. 130, no. 7, pp. 2142–2143, 2008. 1.4

[124] E. Berthier, J. Warrick, H. Yu, and D. J. Beebe, "Managing evaporation for more robust microscale assays part 1. volume loss in high throughput assays," *Lab on a Chip*, vol. 8, no. 6, pp. 852–859, 2008. 1.4

[125] M. C. Park, J. Y. Hur, K. W. Kwon, S.-H. Park, and K. Y. Suh, "Pumpless, selective docking of yeast cells inside a microfluidic channel induced by receding meniscus," *Lab on a Chip*, vol. 6, no. 8, pp. 988–994, 2006. 1.4

[126] V. Dugas, J. Broutin, and E. Souteyrand, "Droplet evaporation study applied to dna chip manufacturing," *Langmuir*, vol. 21, no. 20, pp. 9130–9136, 2005. 1.4

[127] H. Nakao, S. Tokonami, T. Hamada, H. Shiigi, T. Nagaoka, F. Iwata, and Y. Takeda, "Direct observation of one-dimensional plasmon coupling in metallic nanofibers prepared by evaporation-induced self-assembly with dna," *Nanoscale*, vol. 4, no. 21, pp. 6814–6822, 2012. 1.4

[128] R. H. Cole, S.-Y. Tang, C. A. Siltanen, P. Shahi, J. Q. Zhang, S. Poust, Z. J. Gartner, and A. R. Abate, "Printed droplet microfluidics for on demand dispensing of picoliter droplets and cells," *Proceedings of the National Academy of Sciences*, vol. 114, no. 33, pp. 8728–8733, 2017. 1.4

[129] K. T. Hjelt, R. van den Doel, W. Lubking, and M. J. Vellekoop, "Measuring liquid evaporation from micromachined wells," *Sensors and Actuators A: Physical*, vol. 85, no. 1-3, pp. 384–389, 2000. 1.6, 1.4, 1.4

[130] C.-T. Chen, C.-L. Chiu, C.-Y. Hsu, Z.-F. Tseng, and C.-T. Chuang, "Inkjet-printed polymeric microstructures in $n$-sided regular polygonal cavities," *Journal of microelectromechanical systems*, vol. 20, no. 4, pp. 1001–1009, 2011. 1.4

[131] L. Van den Doel, K. Hjelt, I. Young, and L. Van Vliet, "Monitoring the evaporation process of liquid samples in sub-nanoliter vials," in *5th Annual Conference of the Advanced School for Computing and Imaging, Heijen, NL, June 15-17*, Citeseer, 1999. 1.4

[132] C.-T. Chen, C.-Y. Hsu, C.-L. Chiu, and C.-T. Chuang, "Polygonal microstructures self-assembled from evaporating picoliter droplets in micro cavities," in *2010 IEEE 5th International Conference on Nano/Micro Engineered and Molecular Systems*, pp. 1025–1028, IEEE, 2010. 1.4

[133] C.-T. Chen, C.-C. Chieng, and F.-G. Tseng, "Uniform solute deposition of evaporable droplet in nanoliter wells," *Journal of Microelectromechanical Systems*, vol. 16, no. 5, pp. 1209–1218, 2007. 1.4, 3.3.1

[134] C.-T. Chen, F.-G. Tseng, and C.-C. Chieng, "Evaporation evolution of volatile liquid droplets in nanoliter wells," *Sensors and Actuators A: Physical*, vol. 130, pp. 12–19, 2006. 1.4, 3.3.1, 3.3.2

[135] I. Young, R. Moerman, L. Van Den Doel, V. Iordanov, A. Kroon, H. Dietrich, G. Van Dedem, A. Bossche, B. Gray, L. Sarro, *et al.*, "Monitoring enzymatic

reactions in nanolitre wells," *Journal of Microscopy*, vol. 212, no. 3, pp. 254–263, 2003. 1.7, 1.4

[136] N. S. Lynn, C. S. Henry, and D. S. Dandy, "Evaporation from microreservoirs," *Lab on a Chip*, vol. 9, no. 12, pp. 1780–1788, 2009. 1.4

[137] A. Babaie and B. Stoeber, "Concentration field evolution during the drying of a thin polymer solution film near the contact line," *Langmuir*, vol. 31, no. 33, pp. 9033–9040, 2015. 1.8, 1.4

[138] A. Babaie and B. Stoeber, "Viscous flow separation caused by the marangoni effect in competition with capillary flow," *Physics of Fluids*, vol. 27, no. 7, pp. 071702(2)–071702(12), 2015. 1.4

[139] A. Babaie, *Flow physics during the drying of a thin polymer solution film near the contact line*. PhD thesis, University of British Columbia, 2015. 1.4

[140] A. Babaie, S. Madadkhani, and B. Stoeber, "Evaporation-driven low reynolds number vortices in a cavity," *Physics of Fluids*, vol. 26, no. 3, pp. 033102(11)–033102(12), 2014. 1.4

[141] B. Rieger, L. Van den Doel, and L. Van Vliet, "Ring formation in nanoliter cups: Quantitative measurements of flow in micromachined wells," *Physical Review E*, vol. 68, no. 3, p. 036312, 2003. 1.4, 1.4, 3.3.1, 3.3.2, 3.3.2, 3.3.2

[142] H.-M. D'ambrosio, T. Colosimo, B. R. Duffy, S. K. Wilson, L. Yang, C. D. Bain, and D. E. Walker, "Evaporation of a thin droplet in a shallow well: theory and experiment," *Journal of Fluid Mechanics*, vol. 927, pp. A43(1)–A43(13), 2021. 1.9, 1.4, 1.4, 3.1, 3.3.1, 3.3.2, 3.3.2

[143] B. K. Kazmierski, L. Yang, E. L. Talbot, C. D. Bain, L. W. Tan, and D. Walker, "Inkjet printing onto patterned substrates," in *NIP & Digital Fabrication Conference*, vol. 2016, pp. 170–174, Society for Imaging Science and Technology, 2016. 1.4

[144] B. Kazmierski, *The Drying of Inkjet Printed Drops on Patterned Substrates*. PhD thesis, Durham University, 2018. 1.4, 2.4.2

[145] H. Wong, S. Morris, and C. Radke, "Three-dimensional menisci in polygonal capillaries," *Journal of Colloid and Interface Science*, vol. 148, no. 2, pp. 317–336, 1992. 1.4, 1.10

[146] J. Wang and J. Fukai, "Evaporation rate profiles from a liquid in a cylindrical hole," *Journal of Chemical Engineering of Japan*, vol. 51, no. 1, pp. 49–52, 2018. 1.4

[147] S. Price, *Modelling the Evaporation of a Binary Droplet in a Well*. PhD thesis, Durham University, 2023. 1.4

[148] M. Born and E. Wolf, *Principles of optics: electromagnetic theory of propagation, interference and diffraction of light*. Elsevier, 2013. 2.2, 2.3, 2.3, 2.3, 2.3, 2.5

[149] D. R. Lide, *CRC handbook of chemistry and physics*, vol. 85. CRC press, 2004. 2.1, 2.5, 2.5, 3.1, 3.2, 3.7.2, 3.7.2, 3.41a, 3.41b, 3.41, 4.1

[150] J. C. R. Reis, I. M. Lampreia, Â. F. Santos, M. L. C. Moita, and G. Douhéret, "Refractive index of liquid mixtures: theory and experiment," *ChemPhysChem*, vol. 11, no. 17, pp. 3722–3733, 2010. 2.1

[151] M. Baum, I. Alexeev, M. Latzel, S. H. Christiansen, and M. Schmidt, "Determination of the effective refractive index of nanoparticulate ito layers," *Optics Express*, vol. 21, no. 19, pp. 22754–22761, 2013. 2.1

[152] E. Hecht, *Optics*. Pearson Education India, 2012. 2.3, 2.3, 2.5

[153] S. Ross, *A first course in probability*. Pearson, 2010. 2.3

[154] D. Bertsekas and J. N. Tsitsiklis, *Introduction to probability*, vol. 1. Athena Scientific, 2008. 2.3

[155] M. P. Do Carmo, *Differential geometry of curves and surfaces: revised and updated second edition*. Courier Dover Publications, 2016. 2.4.2, 2.4.2, 2.4.2

[156] T. J. Willmore, *An introduction to differential geometry*. Courier Corporation, 2013. 2.4.2

[157] J. Diez, R. Gratton, L. Thomas, and B. Marino, "Laplace pressure driven drop spreading," *Physics of Fluids*, vol. 6, no. 1, pp. 24–33, 1994. 2.4.2

[158] C. S. Sharma, C. Stamatopoulos, R. Suter, P. R. von Rohr, and D. Poulikakos, "Rationally 3d-textured copper surfaces for laplace pressure imbalance-induced enhancement in dropwise condensation," *ACS applied materials & interfaces*, vol. 10, no. 34, pp. 29127–29135, 2018. 2.4.2

[159] S. Ljunggren and J. C. Eriksson, "Minimal surfaces and winsor iii microemulsions," *Langmuir*, vol. 8, no. 5, pp. 1300–1306, 1992. 2.4.2

[160] S. Sternberg, *Lectures on differential geometry*, vol. 316. American Mathematical Soc., 1999. 2.4.2

[161] W. Heller, "Remarks on refractive index mixture rules," *The Journal of Physical Chemistry*, vol. 69, no. 4, pp. 1123–1129, 1965. 2.5

[162] R. Francesconi and S. Ottani, "Correlation of density and refraction index for liquid binary mixtures containing polyglycols. use of the group contributions in the lorentz–lorenz, gladstone–dale and vogel equations to evaluate the density of mixtures," *Journal of molecular liquids*, vol. 133, no. 1-3, pp. 125–133, 2007. 2.5

[163] N. P. Holmes, H. Munday, M. G. Barr, L. Thomsen, M. A. Marcus, A. D. Kilcoyne, A. Fahy, J. van Stam, P. C. Dastoor, and E. Moons, "Unravelling donor–acceptor film morphology formation for environmentally-friendly opv ink formulations," *Green Chemistry*, vol. 21, no. 18, pp. 5090–5103, 2019. 3.1

[164] H. Tyrrell, "The origin and present status of fick's diffusion law," *Journal of chemical education*, vol. 41, no. 7, pp. 397–399, 1964. 3.1

[165] I. Langmuir, "The evaporation of small spheres," *Physical review*, vol. 12, no. 5, pp. 368–369, 1918. 3.1

[166] O. A. Oleinik and V. N. Samokhin, *Mathematical models in boundary layer theory*. Routledge, 2018. 3.2

[167] J. Padday, A. Pitt, and R. Pashley, "Menisci at a free liquid surface: surface tension from the maximum pull on a rod," *Journal of the Chemical Society, Faraday Transactions 1: Physical Chemistry in Condensed Phases*, vol. 71, pp. 1919–1931, 1975. 3.3.1

[168] C.-T. Chen, F.-G. Tseng, and C.-C. Chieng, "Evaporation evolution of volatile liquid droplets in nanoliter well array," in *The 13th International Conference on Solid-State Sensors, Actuators and Microsystems, 2005. Digest of Technical Papers. TRANSDUCERS'05.*, vol. 1, pp. 812–815, IEEE, 2005. 3.3.1, 3.3.1, 3.3.2

[169] B. Dai, L. G. Leal, and A. Redondo, "Disjoining pressure for nonuniform thin films," *Physical Review E*, vol. 78, no. 6, pp. 061602(3)–061602(5), 2008. 3.6.1

[170] J. N. Israelachvili, "Intermolecular and surface forces," *ACADEMIC PR*, 1992. 3.7.1, 3.7.1

[171] R. H. Ewell and H. Eyring, "Theory of the viscosity of liquids as a function of temperature and pressure," *The Journal of Chemical Physics*, vol. 5, no. 9, pp. 726–736, 1937. 3.7.2, 3.7.2, 3.41

[172] S. Mayer, "Dependence of surface tension on temperature," *The Journal of Chemical Physics*, vol. 38, no. 8, pp. 1803–1808, 1963. 3.7.2

[173] J. A. Al-Kandary, A. S. Al-Jimaz, and A.-H. M. Abdul-Latif, "Viscosities, densities, and speeds of sound of binary mixtures of benzene, toluene, o-xylene, m-xylene, p-xylene, and mesitylene with anisole at (288.15, 293.15, 298.15, and 303.15) k," *Journal of Chemical & Engineering Data*, vol. 51, no. 6, pp. 2074–2082, 2006. 3.7.2, 3.41

[174] M. S. Hossain, S. Akhtar, and F. Verpoort, "Densities and dynamic viscosities of alicyclic cyclohexane with toluene, o-xylene, and mesitylene at t=(303.15 to 323.15) k and atmospheric pressure," *Journal of Chemical & Engineering Data*, vol. 63, no. 6, pp. 1885–1895, 2018. 3.7.2

[175] W. e. a. Zhu, "Nanoparticle contact printing with interfacial engineering for deterministic integration into functional structures," *Science advances*, vol. 8, no. 43, p. 4869, 2023. 4

[176] E. Guggenheim, "The theoretical basis of raoult's law," *Transactions of the Faraday Society*, vol. 33, pp. 151–153, 1937. 4.1

[177] G. Lugg, "Diffusion coefficients of some organic and other vapors in air," *Analytical Chemistry*, vol. 40, no. 7, pp. 1072–1077, 1968. 4.1

[178] D. Knuth, "Chemical engineering and material research information centre." 4.3, 4.18

[179] R. W. Kugel, "Raoult's law: Binary liquid-vapor phase diagrams: A simple physical chemistry experiment," *Journal of chemical education*, vol. 75, no. 9, pp. 1125(3)–1125(5), 1998. 4.3

[180] M. McGlashan, "Deviations from raoult's law," *Journal of Chemical Education*, vol. 40, no. 10, p. 516, 1963. 4.3

[181] G. Calingaert and L. B. Hitchcock, "The application of the phase rule to the calculation of liquid and vapor compositions in binary systems. deviations from raoult's law for hydrocarbon mixtures1," *Journal of the American chemical Society*, vol. 49, no. 3, pp. 750–765, 1927. 4.3

[182] F. L. Smith, A. H. Harvey, *et al.*, "Avoid common pitfalls when using henry's law," *Chemical engineering progress*, vol. 103, no. 9, pp. 33–39, 2007. 4.3

[183] W. M. Meylan and P. H. Howard, "Bond contribution method for estimating henry's law constants," *Environmental Toxicology and Chemistry: An International Journal*, vol. 10, no. 10, pp. 1283–1293, 1991. 4.3

[184] M.-J. Huron and J. Vidal, "New mixing rules in simple equations of state for representing vapour-liquid equilibria of strongly non-ideal mixtures," *Fluid Phase Equilibria*, vol. 3, no. 4, pp. 255–271, 1979. 4.3

[185] G. Zabow, "Reflow transfer for conformal three-dimensional microprinting," *Science*, vol. 378, no. 6622, pp. 894–898, 2022. 5.2

[186] J. Hong, Y. Jin, Y. Jin, J. Chen, Y. Li, and J. Chen, "Coalescence dynamics of a droplet impacting on a rectangular pixel for inkjet printing," *Langmuir*, pp. 725–726, 2022. 5.2

[187] K. Li, T. Li, T. Zhang, H. Li, A. Li, Z. Li, X. Lai, X. Hou, Y. Wang, L. Shi, *et al.*, "Facile full-color printing with a single transparent ink," *Science advances*, vol. 7, no. 39, pp. eabh1992(3)–eabh1992(6), 2021. 5.2

[188] Y. Liu, M. Zheng, B. OConnor, J. Dong, and Y. Zhu, "Curvilinear soft electronics by micromolding of metal nanowires in capillaries," *Science Advances*, vol. 8, no. 46, pp. eadd6996(5)–eadd6996(9), 2022. 5.2

[189] T. Haldar, T. Wollandt, J. Weis, U. Zschieschang, H. Klauk, R. T. Weitz, J. N. Burghartz, and M. Geiger, "High-gain, low-voltage unipolar logic circuits based on nanoscale flexible organic thin-film transistors with small signal delays," *Science Advances*, vol. 9, no. 1, p. eadd3669, 2023. 5.2

[190] Y.-T. Xu, C. Yuan, B.-Y. Zhou, Z. Li, J. Hu, P. Lin, W.-W. Zhao, H.-Y. Chen, and J.-J. Xu, "Silicon solar cell-enabled organic photoelectrochemical transistor optoelectronics," *Science China Materials*, pp. 1–9, 2023. 5.2

[191] A. Malijevskỳ and A. O. Parry, "Condensation and evaporation transitions in deep capillary grooves," *Journal of Physics: Condensed Matter*, vol. 26, no. 35, pp. 355003(4)–355003(6), 2014. 5.2

[192] Q. Cao, Z. Cui, and W. Shao, "Optimization method for grooved surface structures regarding the evaporation heat transfer of ultrathin liquid films at the nanoscale," *Langmuir*, vol. 36, no. 11, pp. 2802–2815, 2020. 5.2

[193] S. Kachel, Y. Zhou, P. Scharfer, C. Vrančić, W. Petrich, and W. Schabel, "Evaporation from open microchannel grooves," *Lab on a Chip*, vol. 14, no. 4, pp. 771–778, 2014. 5.2

[194] K. Khare, M. Brinkmann, B. M. Law, E. L. Gurevich, S. Herminghaus, and R. Seemann, "Dewetting of liquid filaments in wedge-shaped grooves," *Langmuir*, vol. 23, no. 24, pp. 12138–12141, 2007. 5.2

[195] J. Bostwick and P. Steen, "Stability of constrained cylindrical interfaces and the torus lift of plateau–rayleigh," *Journal of fluid mechanics*, vol. 647, pp. 201–219, 2010. 5.2

[196] M. Dokowicz and W. Nowicki, "Morphological transitions of droplets wetting a series of triangular grooves," *Langmuir*, vol. 32, no. 28, pp. 7259–7264, 2016. 5.2

[197] L. Zhao, C. Li, J. Xu, and W. Wu, "Fabrication of suspended periodic nanostructure by focused ion beam induced material migration and rayleigh-plateau instability," in *2013 13th IEEE International Conference on Nanotechnology (IEEE-NANO 2013)*, pp. 582–585, IEEE, 2013. 5.2

[198] C. Poulard, O. Bnichou, and A. M. Cazabat, "Freely receding evaporating droplets," *Langmuir*, vol. 19, no. 21, pp. 8828–8834, 2003. 5.2

[199] G. Guna and C. P. M. Cazabat, "The contact angle of droplets evaporating at ambient temperature," *Applied Mathematics Research eXpress*, vol. 2006, pp. 1–17, 2006. 5.2

[200] Y. Tsoumpas, S. Dehaeck, M. Galvagno, A. Rednikov, and P. Colinet, "Non-equilibrium gibbs' criterion for completely wetting volatile liquids," *Langmuir*, vol. 30, no. 40, pp. 11847–52, 2014. 5.2

[201] H. Kusumaatmaja, J. M. Yeomans, and M. L. Blow, "Imbibition through an array of triangular posts," 2009. 5.2

[202] X. Li, Z. Xue, X. Chen, X. Qiao, G. Mo, W. Bu, B. Guan, and T. Wang, "Printable assemblies of perovskite nanocubes on meter-scale panel," *Science Advances*, vol. 8, no. 45, pp. eadd1559(3)–eadd1559(4), 2022. 5.2

[203] O. Song, D. Rhee, J. Kim, Y. Jeon, V. Mazánek, A. Söll, Y. A. Kwon, J. H. Cho, Y.-H. Kim, Z. Sofer, *et al.*, "All inkjet-printed electronics based on electrochemically exfoliated two-dimensional metal, semiconductor, and dielectric," *npj 2D Materials and Applications*, vol. 6, no. 1, pp. 1–12, 2022. 5.2

[204] H. W. Tan, Y. Y. C. Choong, C. N. Kuo, H. Y. Low, and C. K. Chua, "3d printed electronics: Processes, materials and future trends," *Progress in Materials Science*, p. 100945, 2022. 5.2

[205] E. Oropeza-Guzman, M. Rios-Ramirez, and J. C. Ruiz-Suarez, "Leveraging the coffee ring effect for a defect-free electroformation of giant unilamellar vesicles," *Langmuir*, vol. 35, no. 50, pp. 16528–16535, 2019. 5.2

[206] Y. Jin, J. Chen, Z. Yin, Y. Li, and M. Huang, "Positioning error limit for the last droplet deposition into a microcavity in the manufacture of printed oleds," *Langmuir*, vol. 37, no. 31, pp. 9396–9404, 2021. 5.2

# CHAPTER 1

# Appendix

All the code is written with Matlab 2020b.

## 1.1 Three-beam Interference

```
clear all
z=453:1:477;
h_droplet= 0:.1:4000;                    %unit:nm
h_ITO=50;                                %unit:nm
FWHM=9.3623;                             % delta lamda in the
    expression of coherence length
Refractive_index_1=1.5200;               %glass
Refractive_index_2=1.9842;               %ITO
Refractive_index_3=1.3941;               %Droplet_   n-butyl
   acetate
Refractive_index_4=1.0003;               %Air
```

```
sigma_1=3.9785;                         % with filter_ Data
   from Teresa and Lisong
mu_1=464.50;                             %unit:nm with filter_
    Data from Teresa and Lisong

sigma_2=9.3414 ;                        %without filter Data
   from Teresa and Lisong
mu_2=465.70;                            %unit:nm without
   filter, Data from Teresa and Lisong

wave_length_distribution_1 =normpdf(z,mu_1,sigma_1);    %
   unit:nm with filter_ Data from Teresa and Lisong
wave_length_distribution_2 =normpdf(z,mu_2,sigma_2);    %
   unit:nm with filter_ Data from Teresa and Lisong

wave_length_of_the_source_1 = mu_1;       %unit:nm   with
    filter    Data from Teresa and Lisong
Wave_number_1 = 2 * pi / wave_length_of_the_source_1;
        %2pi/lamda,

color_p = [236, 138, 91;12, 112, 104; 220, 94, 75]/255; %
   set any colour for your curves or dots
% plot(z,wave_length_distribution_1,'Marker','o','color',
   color_p(1,:),'linewidth',1) %
   light_distribution_with_filter
wave_length_of_the_source_2 = mu_2;       %unit:nm   with
    filter    Data from Teresa and Lisong
Wave_number_2 = 2 * pi / wave_length_of_the_source_2;
        %2pi/lamda
```

```
Ref_12= (Refractive_index_1 - Refractive_index_2)^2 / (
   Refractive_index_1 + Refractive_index_2)^2;
Ref_23= (Refractive_index_2 - Refractive_index_3)^2 / (
   Refractive_index_2 + Refractive_index_3)^2;
Ref_34= (Refractive_index_3 - Refractive_index_4)^2 / (
   Refractive_index_3 + Refractive_index_4)^2;

Tran_12 = 4 * Refractive_index_1 * Refractive_index_2/((
   Refractive_index_1 + Refractive_index_2)^2);
Tran_23 = 4 * Refractive_index_2 * Refractive_index_3/((
   Refractive_index_2 + Refractive_index_3)^2);
Tran_34 = 4 * Refractive_index_3 * Refractive_index_4/((
   Refractive_index_3 + Refractive_index_4)^2);


%Light_1 Lr; Light_2  Ltrt; Light_3   Lttrtt
Path_S_12=2* Refractive_index_2 * h_ITO;
                                    %path_difference
   between Light1 and Ligh2
Phase_D_12= 2 * pi / wave_length_of_the_source_1 *
   Path_S_12 + pi ;        %Phase_difference_delta



Path_S_13=2* Refractive_index_2 * h_ITO + 2 *
   Refractive_index_3 * h_droplet;
                           %path_difference
```

```
Phase_D_13= 2 * pi / wave_length_of_the_source_1 *(
   Path_S_13 ) + pi  ;

Path_S_23= 2 * Refractive_index_3 * h_droplet;
                                %path_difference
Phase_D_13= 2 * pi / wave_length_of_the_source_1 *(
   Path_S_13 ) + pi ;

%% To calculat the maximum of the total light intensity
   when the intensity of the light beam is at the highest
    and the lowest respectively
I_max = normpdf(mu_1,mu_1,sigma_1)
I_min = normpdf(mu_1 - 3*sigma_1,mu_1,sigma_1)

 % loght_intensity_induced_from__the_max_intenisty
I_max = normpdf(mu_1,mu_1,sigma_1)
% Phase_D_12_max= 2 * pi / wave_length_of_the_source_1 *
   Path_S_12 + pi;
% Phase_D_13_max= 2 * pi / wave_length_of_the_source_1 *(
    Path_S_13 ) + pi;
% Phase_D_13_max= 2 * pi / wave_length_of_the_source_1 *(
    Path_S_13 ) + pi;
% I_alpha_1 in the thesis
I_total_1_max = I_max * (Ref_12 + Tran_12 * Tran_12 *
   Ref_23  + Tran_12 * Tran_12 * Tran_23 * Tran_23 *
   Ref_34 );
I_total_2_max = -2 * I_max* Tran_12 * (Ref_12 * Ref_23)
   ^0.5 * cos( 2 * pi /mu_1 * Path_S_12 );

N_1_max = 2 * I_max * Tran_12 ^2 * Tran_23 * (Ref_23 *
   Ref_34)^0.5 ;
```

```
N_2_max = -2 * I_max * Tran_12  * Tran_23 * (Ref_12 *
   Ref_34)^0.5 * cos( 2 * pi / mu_1 *  Path_S_12);
N_3_max = 2 * I_max * Tran_12 * Tran_23 * (Ref_12 *
   Ref_34)^0.5 * sin( 2 * pi / mu_1 *  Path_S_12) ;

N_max=((N_1_max + N_2_max)^2 + N_3_max ^2 )^0.5;

tan_theta_max_num = (Ref_12)^0.5 * sin( 2 * pi / mu_1 *
   Path_S_12)
tan_theta_max_den = Tran_12 *(Ref_23)^0.5 - (Ref_12 )^0.5
    * cos( 2 * pi / mu_1 *  Path_S_12)
tan_theta_max = tan_theta_max_num / tan_theta_max_den

%
theta_max= atan(tan_theta_max);

I_total_3_max = N_max*cos((2 * pi /mu_1 * Path_S_23 )-
   theta_max);
I_total_max = I_total_1_max +I_total_3_max +
   I_total_2_max;
height_differnence = theta_max * mu_1;  % the error from
   the monotonic light

%  loght_intensity_induced_from__the_min_intenisty

I_total_1_min = I_min * (Ref_12 + Tran_12 * Tran_12 *
   Ref_23  + Tran_12 * Tran_12 * Tran_23 * Tran_23 *
   Ref_34 );
I_total_2_min = -2 * I_min* Tran_12 * (Ref_12 * Ref_23)
   ^0.5 * cos( 2 * pi /mu_1 * Path_S_12 );
```

```
N_1_min = 2 * I_min * Tran_12 ^2 * Tran_23 * (Ref_23 *
   Ref_34)^0.5 ;
N_2_min = -2 * I_min * Tran_12  * Tran_23 * (Ref_12 *
   Ref_34)^0.5 * cos( 2 * pi / mu_1 *  Path_S_12);
N_3_min = 2 * I_min * Tran_12 * Tran_23 * (Ref_12 *
   Ref_34)^0.5 * sin( 2 * pi / mu_1 *  Path_S_12) ;

N_min=((N_1_min + N_2_min)^2 + N_3_min ^2 )^0.5;

tan_theta_min_num = (Ref_12)^0.5 * sin( 2 * pi / mu_1 *
   Path_S_12)
tan_theta_min_den = Tran_12 *(Ref_23)^0.5 - (Ref_12 )^0.5
    * cos( 2 * pi / mu_1 *  Path_S_12)
tan_theta_min = tan_theta_min_num / tan_theta_min_den

%
theta_min= atan(tan_theta_min);

I_total_3_min = N_min*cos((2 * pi /mu_1 * Path_S_23 )-
   theta_min);
I_total_min = I_total_1_min +I_total_3_min +
   I_total_2_min;


h_error_max = theta_max * mu_1 / 4/ pi /
   Refractive_index_3
h_error_min = theta_max * (mu_1 - 3*sigma_1) / 4/ pi /
   Refractive_index_3
h_error_max_plus = theta_max * (mu_1 + 3*sigma_1) / 4/ pi
    / Refractive_index_3
```

```
%% To define the function for the further calculation

% clear all
f = @(x,y) x * cos(y) ;
sigma_vis = 3.9786;
mu_vis = 464.50;
% lamda_=453:0.1:476;  %52.5642:0.1:476.4358;
% wave_number = 2*pi / lamda
i_0 = @(x,y) normpdf(x,mu_vis,sigma_vis);
I_total_1_fun = @(x,y) normpdf(x,mu_vis,sigma_vis) *  (
   Ref_12 + Tran_12 * Tran_12 * Ref_23  + Tran_12 *
   Tran_12 * Tran_23 * Tran_23 * Ref_34 );
I_total_1_fun(464.50);
% % plot(x,I_total_1_fun,x,i_0);
I_total_2_fun =@(x,y) -2 * normpdf(x,mu_vis,sigma_vis)*
   Tran_12 * (Ref_12 * Ref_23)^0.5 * cos( 2 * pi /x *
   Path_S_12 );
I_total_2_fun(464.50);

N_1_max_fun =@(x,y) 2 * normpdf(x,mu_vis,sigma_vis) *
   Tran_12 ^2 * Tran_23 * (Ref_23 * Ref_34)^0.5  ;
N_2_max_fun = @(x,y) -2 * normpdf(x,mu_vis,sigma_vis) *
   Tran_12  * Tran_23 * (Ref_12 * Ref_34)^0.5 * cos( 2 *
   pi/x *Path_S_12);
N_3_max_fun = @(x,y) 2 * normpdf(x,mu_vis,sigma_vis) *
   Tran_12 * Tran_23 * (Ref_12 * Ref_34)^0.5 * sin( 2 *
   pi / x *  Path_S_12) ;
%  N_1_max_fun(464.50)
%   N_2_max_fun(464.50)
%    N_3_max_fun(464.50)
```

```
N_max_fun = @(x,y) ((N_1_max_fun(x) + N_2_max_fun(x)).^2
   + N_3_max_fun(x) .^2 ).^0.5;
N_max_fun(464.50)
% % plot(x,I_total_1_fun,x,i_0,x,I_total_2_fun);
tan_theta_max_fun =@(x,y) (Ref_12 )^0.5 * sin( 2 * pi / x
    * 2* Refractive_index_2 * h_ITO)/( Tran_12 *(Ref_23 )
   ^0.5 - (Ref_12 )^0.5 * cos( 2 * pi / x * 2*
   Refractive_index_2 * h_ITO)  )
tan_theta_max_fun (464.50)

theta_max_fun =@(x,y) atan(tan_theta_max_fun(x));
 theta_max_fun (464.50)
% %
I_total_3_max_fun =@(x,y) N_max_fun(x) * cos((2 * pi /x *
    2 * Refractive_index_3 * y )- theta_max_fun(x))
I_total_3_max_fun(464.50,1)
I_total_max_fun =@(x,y) normpdf(x,mu_vis,sigma_vis) * (
   Ref_12 + Tran_12 * Tran_12 * Ref_23  + Tran_12 *
   Tran_12 * Tran_23 * Tran_23 * Ref_34 ) + N_max_fun(x)
   * cos((2 * pi /x * 2 * Refractive_index_3 * y )-
   theta_max_fun(x)) -2 * normpdf(x,mu_vis,sigma_vis)*
   Tran_12 * (Ref_12 + Ref_23)^0.5 * cos( 2 * pi /x *
   Path_S_12 );
 %% This part is set to calculate exact result of the
    function I(k,S);
%  b=1:20:2000
Left_border = mu_vis - 3 * sigma_vis;
Right_border = mu_vis + 3 * sigma_vis;
c=0;
I_total_max_fun =@(x,y) normpdf(x,mu_vis,sigma_vis) * (
   Ref_12 + Tran_12 * Tran_12 * Ref_23  + Tran_12 *
```

```
   Tran_12 * Tran_23 * Tran_23 * Ref_34 ) + N_max_fun(x)
   * cos((2 * pi /x * 2 * Refractive_index_3 * y )-
   theta_max_fun(x)) -2 * normpdf(x,mu_vis,sigma_vis)*
   Tran_12 * (Ref_12 + Ref_23)^0.5 * cos( 2 * pi /x *
   Path_S_12 );
I_total_max_fun(1,c);
d=[];
d_d=[];
d_d_d=[];
% light_intensity=[]
height_of_droplet = 0;
k=Left_border
% filename_4=['light_intensity_surf2','.dat']; % save
   file %together 05-08-20 zhida
% fp_in=fopen(filename_4,'a+');
 while k <= Right_border
     step_2=1;
%      package=[];
%
%      package=I_total_max_fun(k,c);
%
%      light_intensity=[light_intensity; package];
        while height_of_droplet<9999

              c = height_of_droplet;
              s=[];
              s= I_total_max_fun(k,c);
              d_d = [d_d;s];

%               fprintf(fp_in,'\n ');
%               fprintf(fp_in,'%12.8f', s);
```

```
                step_1=5;
                height_of_droplet = height_of_droplet +
                    step_1;
            end
        lamda=k;
        height_of_droplet=0;
        d_d_d = [d_d_d,d_d];
        d_d=[];
        k = k + step_2;
 end
%  fclose(fp_in);
 %% This part is to calculate the 2D plot of I(S) which
    combines the entire intensity from different k at
    each point
Left_border = mu_vis -3 * sigma_vis;
Right_border = mu_vis + 3 * sigma_vis;
lig_int=[];
total_int_unit=[];
height_of_droplet=0;
k =Left_border;
while height_of_droplet<10000

        c = height_of_droplet;

        total_int_single=0;
%               s=[];
%               s= I_total_max_fun(k,c);
%               d_d = [d_d;s]
%               d_d_d = [d_d_d,d_d];
%               d_d=[];
              while k <= Right_border
```

```
                step_2=1;
                package=[];
                package=I_total_max_fun(k,c);
                lig_int = [lig_int;package];
                total_int_single= total_int_single +
                   package;
                k = k + step_2;
            end
    total_int_unit=[total_int_unit;total_int_single];
    k = Left_border
    step_1 = 1;
    height_of_droplet = height_of_droplet + step_1;
end
%% plot  Light_intensity_ against_ optical_path
optical_path=0:step_1:9999
figure
color_p = [06, 138, 241 ;12, 112, 104;106,30,205]/255; %
   set any colour for your curves or dots
plot(optical_path, total_int_unit,'color',color_p(1,:),'
   linewidth',1);
xlabel('Height of droplet (nm)');
ylabel('Relative Light Intensity');
title('L(h,\lambda)n-Butyl acetate');
legend('Relative Light Intensity');
```

## 1.2 Geometrical Features of a Profile

```
%% this code is to calculate the mean curvature at the
   centre point of a profile;
clear all
```

```
toluene_ten
toluene_fifty
toluene_seventy
toluene_ninety_five
toluene_ninety_lopsided_a
toluene_ninety_lopsided_b


colour_i = 20;
color_p = [255,228,181;240,247,255;
   240,105,040;100,249,237;
   245,245,220;200,100,50;200,191,255;110,105,30;255,215,0;176,196
    %set any colour for your curves or dots
color_q = [154,28,246;240,248,255;
   240,255,240;100,149,137;
   145,145,220;100,100,100;10,191,255;190,95,90;155,215,0;76,096,2


% edge colours for dots
colour_s=[139,32,14;255,138,0;157, 77, 95; 27, 59,
   126;38, 140, 53;85, 40, 92;207, 186, 79;68, 115,
   162;39,80,93;98, 50, 52;54, 50, 98; 67, 76, 36 ;73,
   44, 109;     134, 90, 45;82, 50, 83;34, 36, 30; 52,
   23, 20; 242, 93, 13]/255;
% face colours for dots
colour_t=[245,92,66;255,229,0;253, 38, 85;92, 139,
   235;114, 243, 133;214, 148, 225; 249, 242, 31;19, 133,
    246; 0,190,255; 215, 20, 30;74, 58, 248;128, 206,
   229; 100, 24, 195;     234, 172, 108;  160, 68,
   162;175, 250, 5 ;245, 37, 10;250, 155, 92  ]/255;
color_area = [94, 184, 247;224, 255, 168;224, 255,
   168;231, 206, 253; 251, 152, 213;172, 192, 252]/255
color_line=[117,107,177]/255;
```

```
set(gca,'fontname','times')  % Set it to times
%n-butanol w-1; n-butanol-U-2 n-butyl acetate W-3 U-4;
   mesitylene U-5 C-6;
%methyl benzoate u-7 c-8

%% toluene_ten_n_butanol
length_toluene_ten_n_butanol_time=length(
   toluene_ten_n_butanol_time);
t_count=1
radii_from_fit=[0:0.01:1];
k_2=[]
figure
while t_count <= length_toluene_ten_n_butanol_time

     if t_count < 20
        toluene_ten_n_butanol_height_t =
           toluene_ten_n_butanol_height(1:end,t_count)
        fitbobject_toluene_ten_n_butanol = fit(
           toluene_ten_n_butanol_radii,
           toluene_ten_n_butanol_height_t,'1/a*exp(a*x+b)
            + 1/(a)*exp(-a*x+b) +c*x^2 + d','StartPoint',
            [12.85, 0.2, 2.61 -1.6]);%[12.85, 0.2, 19.61
           -1.6]
    %   fitbobject_toluene_ten_n_butanol = fit(
      toluene_ten_n_butanol_radii,
      toluene_ten_n_butanol_height_t,'poly6');
        [hr_test, hrr_test] = differentiate(
           fitbobject_toluene_ten_n_butanol,
           radii_from_fit)
     elseif t_count >= 20
         toluene_ten_n_butanol_height_t =
```

```
            toluene_ten_n_butanol_height(1:end,t_count)
        fitbobject_toluene_ten_n_butanol = fit(
           toluene_ten_n_butanol_radii,
           toluene_ten_n_butanol_height_t,'1/a*exp(a*x+b)
            + 1/(a)*exp(-a*x+b) +c*x^2 + d','StartPoint',
            [12.85, 1.2, 2.61-t_count*0.35 -1.6]);%
           [12.85, 0.2, 19.61 -1.6]
%    fitbobject_toluene_ten_n_butanol = fit(
   toluene_ten_n_butanol_radii,
   toluene_ten_n_butanol_height_t,'poly6');
     [hr_test, hrr_test] = differentiate(
        fitbobject_toluene_ten_n_butanol,
        radii_from_fit)
 end

s1= 'toluene_ten_n_butanol at t/t_d='
i_moment=round(toluene_ten_n_butanol_time(t_count),3)
   ;
s2= string(i_moment);
s3= '';
s_title=strcat(s1,s2,s3);

plot(fitbobject_toluene_ten_n_butanol,
   toluene_ten_n_butanol_radii,
   toluene_ten_n_butanol_height_t)
xlabel('r /\mu m');
ylabel('h /\mu m ');
title('h-r toluene_ten_n_butanol profile fitting
   curve');
legend('Location','northwestoutside')
hold on
```

```
    hrr_0 = hrr_test(1);
    k_2=[k_2,hrr_0];

    t_count = t_count +1
end
%


k_2_tran=transpose(k_2)
k_1 = 0
k_2_toluene_ten_n_butanol=k_2_tran*(1);
H_toluene_ten_n_butanol=(k_2_toluene_ten_n_butanol)
figure
plot(toluene_ten_n_butanol_time,H_toluene_ten_n_butanol)



%%  binary_curvature_toluene_fifty_n_butanol
length_toluene_fifty_n_butanol_time=length(
   toluene_fifty_n_butanol_time);
t_count=1
radii_from_fit=[0:0.01:1];
k_2=[]
figure
stage_1 = 6

while t_count <=  length_toluene_fifty_n_butanol_time

     if t_count < stage_1
        toluene_fifty_n_butanol_height_t =
           toluene_fifty_n_butanol_height(1:end,t_count)
```

```
        fitbobject_toluene_fifty_n_butanol = fit(
           toluene_fifty_n_butanol_radii,
           toluene_fifty_n_butanol_height_t,'1/a*exp(a*x+
           b) + 1/(-a)*exp(-a*x+b) +c*x^2 + d','
           StartPoint', [12.85, -0.2, 0.6 -0.6]);%[12.85,
            0.2, 19.61 -1.6]
%       fitbobject_toluene_fifty_n_butanol = fit(
   toluene_fifty_n_butanol_radii,
   toluene_fifty_n_butanol_height_t,'poly4');
        [hr_test, hrr_test] = differentiate(
           fitbobject_toluene_fifty_n_butanol,
           radii_from_fit)
     elseif t_count >= stage_1
         toluene_fifty_n_butanol_height_t =
            toluene_fifty_n_butanol_height(1:end,t_count)
        fitbobject_toluene_fifty_n_butanol = fit(
           toluene_fifty_n_butanol_radii,
           toluene_fifty_n_butanol_height_t,'1/a*exp(a*x+
           b) + 1/(a)*exp(-a*x+b) +c*x^2 + d','StartPoint
           ', [12.85, 1.2, 2.61-t_count*0.35 -1.6]);%
           [12.85, 0.2, 19.61 -1.6]
    %   fitbobject_toluene_fifty_n_butanol = fit(
      toluene_fifty_n_butanol_radii,
      toluene_fifty_n_butanol_height_t,'poly6');
         [hr_test, hrr_test] = differentiate(
           fitbobject_toluene_fifty_n_butanol,
           radii_from_fit)
     end

    s1= 'toluene_fifty_n_butanol at t/t_d='
    i_moment=round(toluene_fifty_n_butanol_time(t_count)
```

```
        ,3);
    s2= string(i_moment);
    s3= '';
    s_title=strcat(s1,s2,s3);

    plot(fitbobject_toluene_fifty_n_butanol,
       toluene_fifty_n_butanol_radii,
       toluene_fifty_n_butanol_height_t)
    xlabel('r /\mu m');
    ylabel('h /\mu m ');
    title('h-r toluene_fifty_n_butanol profile fitting
       curve');
    legend('Location','northwestoutside')
    hold on
    hrr_0 = hrr_test(1);
    k_2=[k_2,hrr_0];

    t_count = t_count +1
end
%


k_2_tran=transpose(k_2)
k_1 = 0
k_2_toluene_fifty_n_butanol=k_2_tran*(1);
H_toluene_fifty_n_butanol=(k_2_toluene_fifty_n_butanol)
figure
plot(toluene_fifty_n_butanol_time,
   H_toluene_fifty_n_butanol)
%%  binary_curvature_toluene_seventy_n_butanol
length_toluene_seventy_n_butanol_time=length(
```

```
   toluene_seventy_n_butanol_time);
t_count=1
radii_from_fit=[0:0.01:1];
k_2=[]
figure
stage_1 = 10

while t_count <=  length_toluene_seventy_n_butanol_time

     if t_count < stage_1
        toluene_seventy_n_butanol_height_t =
           toluene_seventy_n_butanol_height(1:end,t_count
           )
        fitbobject_toluene_seventy_n_butanol = fit(
           toluene_seventy_n_butanol_radii,
           toluene_seventy_n_butanol_height_t,'poly8')%
           '1/a*exp(a*x+b) + 1/(-a)*exp(-a*x+b) +c*x^2 +
           d','StartPoint', [52.85, -10.2, 0.6 -1.6])
           ;%[12.85, 0.2, 19.61 -1.6]
    %   fitbobject_toluene_seventy_n_butanol = fit(
      toluene_seventy_n_butanol_radii,
      toluene_seventy_n_butanol_height_t,'poly6');
        [hr_test, hrr_test] = differentiate(
           fitbobject_toluene_seventy_n_butanol,
           radii_from_fit)
     elseif t_count >= stage_1
         toluene_seventy_n_butanol_height_t =
            toluene_seventy_n_butanol_height(1:end,
            t_count)
        fitbobject_toluene_seventy_n_butanol = fit(
           toluene_seventy_n_butanol_radii,
```

```
        toluene_seventy_n_butanol_height_t,'1/a*exp(a*
        x+b) + 1/(a)*exp(-a*x+b) +c*x^2 + d','
        StartPoint', [12.85, 1.2, 2.61-t_count*0.35
        -1.6]);%[12.85, 0.2, 19.61 -1.6]
%   fitbobject_toluene_seventy_n_butanol = fit(
   toluene_seventy_n_butanol_radii,
   toluene_seventy_n_butanol_height_t,'poly6');
    [hr_test, hrr_test] = differentiate(
        fitbobject_toluene_seventy_n_butanol,
        radii_from_fit)
 end

s1= 'toluene_seventy_n_butanol at t/t_d='
i_moment=round(toluene_seventy_n_butanol_time(t_count
   ),3);
s2= string(i_moment);
s3= '';
s_title=strcat(s1,s2,s3);

plot(fitbobject_toluene_seventy_n_butanol,
   toluene_seventy_n_butanol_radii,
   toluene_seventy_n_butanol_height_t)
xlabel('r /\mu m');
ylabel('h /\mu m ');
title('h-r toluene_seventy_n_butanol profile fitting
   curve');
legend('Location','northwestoutside')
hold on
hrr_0 = hrr_test(1);
k_2=[k_2,hrr_0];
```

```
    t_count = t_count +1
end
%
%
k_2_tran=transpose(k_2)
k_1 = 0
k_2_toluene_seventy_n_butanol=k_2_tran*(1);
H_toluene_seventy_n_butanol=(
   k_2_toluene_seventy_n_butanol)
figure
plot(toluene_seventy_n_butanol_time,
   H_toluene_seventy_n_butanol)

%%  binary_curvature_toluene_ninety_five_n_butanol
length_toluene_ninety_five_n_butanol_time=length(
   toluene_ninety_five_n_butanol_time);
t_count=1
radii_from_fit=[0:0.01:1];
k_2=[]
figure
stage_1 = 26

while t_count <=
   length_toluene_ninety_five_n_butanol_time

     if t_count < stage_1
        toluene_ninety_five_n_butanol_height_t =
           toluene_ninety_five_n_butanol_height(1:end,
           t_count)
%          fitbobject_toluene_ninety_five_n_butanol = fit(
   toluene_ninety_five_n_butanol_radii,
```

```
   toluene_ninety_five_n_butanol_height_t,'1/a*exp(a*x+b)
    + 1/(-a)*exp(-a*x+b) +c*x^2 + d','StartPoint', [2.85,
    -10.2, 0.6 -1.6]);%[12.85, 0.2, 19.61 -1.6]
      fitbobject_toluene_ninety_five_n_butanol = fit(
         toluene_ninety_five_n_butanol_radii,
         toluene_ninety_five_n_butanol_height_t,'poly6');
        [hr_test, hrr_test] = differentiate(
           fitbobject_toluene_ninety_five_n_butanol,
           radii_from_fit)
     elseif t_count >= stage_1
         toluene_ninety_five_n_butanol_height_t =
            toluene_ninety_five_n_butanol_height(1:end,
            t_count)
        fitbobject_toluene_ninety_five_n_butanol = fit(
           toluene_ninety_five_n_butanol_radii,
           toluene_ninety_five_n_butanol_height_t,'1/(a)*
           exp(a*x+b) + 1/(a)*exp(-a*x+b) +c*x^2 + d','
           StartPoint', [12, 1.2, 1, -3]);%[12.85, 0.2,
           19.61 -1.6]
%       fitbobject_toluene_ninety_five_n_butanol = fit(
   toluene_ninety_five_n_butanol_radii,
   toluene_ninety_five_n_butanol_height_t,'poly4');
        [hr_test, hrr_test] = differentiate(
           fitbobject_toluene_ninety_five_n_butanol,
           radii_from_fit)
     end

     s1= 'toluene_ninety_five_n_butanol at t/t_d='
     i_moment=round(toluene_ninety_five_n_butanol_time(
        t_count),3);
     s2= string(i_moment);
```

```
    s3= '';
    s_title=strcat(s1,s2,s3);

    plot(fitbobject_toluene_ninety_five_n_butanol,
       toluene_ninety_five_n_butanol_radii,
       toluene_ninety_five_n_butanol_height_t)
    xlabel('r /\mu m');
    ylabel('h /\mu m ');
    title('h-r n anisole-mesitylene M-shaped profile
       fitting curve');
    legend('Location','northwestoutside')
    hold on
    hrr_0 = hrr_test(1);
    k_2=[k_2,hrr_0];

    t_count = t_count +1
end
%

%
k_2_tran=transpose(k_2)
k_1 = 0
k_2_toluene_ninety_five_n_butanol=k_2_tran*(1);
H_toluene_ninety_five_n_butanol=(
   k_2_toluene_ninety_five_n_butanol)
figure
plot(toluene_ninety_five_n_butanol_time,
   H_toluene_ninety_five_n_butanol)


%%  binary_curvature_pure_n_butanol
```

```
length_pure_n_butanol_time=length(pure_n_butanol_time);
t_count=1
radii_from_fit=[0:0.01:1];
k_2=[]
figure
stage_1 = 58

while t_count <=  length_pure_n_butanol_time

     if t_count < stage_1
        pure_n_butanol_profile_t = pure_n_butanol_profile
           (1:end,t_count)
%          fitbobject_pure_n_butanol = fit(
   pure_n_butanol_radii,pure_n_butanol_profile_t,'1/a*exp
   (a*x+b) + 1/(-a)*exp(-a*x+b) +c*x^2 + d','StartPoint',
    [2.85, -10.2, 0.6 -1.6]);%[12.85, 0.2, 19.61 -1.6]
       fitbobject_pure_n_butanol = fit(
          pure_n_butanol_radii,pure_n_butanol_profile_t,'
          poly6');
          [hr_test, hrr_test] = differentiate(
             fitbobject_pure_n_butanol,radii_from_fit)
     elseif t_count >= stage_1
          pure_n_butanol_profile_t =
             pure_n_butanol_profile(1:end,t_count)
%          fitbobject_pure_n_butanol = fit(
   pure_n_butanol_radii,pure_n_butanol_profile_t,'1/(a)*
   exp(a*x+b) + 1/(a)*exp(-a*x+b) +c*x^2 + d','StartPoint
   ', [-12, 1.2, 1, -3]);%[12.85, 0.2, 19.61 -1.6]
       fitbobject_pure_n_butanol = fit(
          pure_n_butanol_radii,pure_n_butanol_profile_t,'
          poly4');
```

```
        [hr_test, hrr_test] = differentiate(
           fitbobject_pure_n_butanol,radii_from_fit)
     end

    s1= 'pure_n_butanol at t/t_d='
    i_moment=round(pure_n_butanol_time(t_count),3);
    s2= string(i_moment);
    s3= '';
    s_title=strcat(s1,s2,s3);

    plot(fitbobject_pure_n_butanol,pure_n_butanol_radii,
       pure_n_butanol_profile_t)
    xlabel('r /\mu m');
    ylabel('h /\mu m ');
    title('h-r of pure_n_butanol fitting curve');
    legend('Location','northwestoutside')
    hold on
    hrr_0 = hrr_test(1);
    k_2=[k_2,hrr_0];

    t_count = t_count +1
end
%

%
k_2_tran=transpose(k_2)
k_1 = 0
k_2_pure_n_butanol=k_2_tran*(1);
H_pure_n_butanol=(k_2_pure_n_butanol)
figure
plot(pure_n_butanol_time,H_pure_n_butanol)
```

```
%%  binary_curvature_pure_toluene
length_pure_toluene_time=length(pure_toluene_time);
t_count=1
radii_from_fit=[0:0.01:1];
k_2=[]
figure
stage_1 = 30

while t_count <=  length_pure_toluene_time

     if t_count < stage_1
        pure_toluene_profile_t = pure_toluene_profile(1:
           end,t_count)
        fitbobject_pure_toluene = fit(pure_toluene_radii,
           pure_toluene_profile_t,'1/a*exp(a*x+b) + 1/(-a
           )*exp(-a*x+b) +c*x^2 + d','StartPoint', [2.85,
            -10.2, 0.6 -1.6]);%[12.85, 0.2, 19.61 -1.6]
%        fitbobject_pure_toluene = fit(pure_toluene_radii,
   pure_toluene_profile_t,'poly6');
        [hr_test, hrr_test] = differentiate(
           fitbobject_pure_toluene,radii_from_fit)
     elseif t_count >= stage_1
         pure_toluene_profile_t = pure_toluene_profile(1:
            end,t_count)
        fitbobject_pure_toluene = fit(pure_toluene_radii,
           pure_toluene_profile_t,'1/(a)*exp(a*x+b) + 1/(
           a)*exp(-a*x+b) +c*x^2 + d','StartPoint', [12,
           1.2, 1, -3]);%[12.85, 0.2, 19.61 -1.6]
%        fitbobject_pure_toluene = fit(pure_toluene_radii,
```

```
   pure_toluene_profile_t,'poly4');
        [hr_test, hrr_test] = differentiate(
           fitbobject_pure_toluene,radii_from_fit)
     end

     s1= 'pure toluene at t/t_d='
     i_moment=round(pure_toluene_time(t_count),3);
     s2= string(i_moment);
     s3= '';
     s_title=strcat(s1,s2,s3);

     plot(fitbobject_pure_toluene,pure_toluene_radii,
        pure_toluene_profile_t)
     xlabel('r /\mu m');
     ylabel('h /\mu m ');
     title('h-r pure toluene profile fitting curve');
     legend('Location','northwestoutside')
     hold on
     hrr_0 = hrr_test(1);
     k_2=[k_2,hrr_0];

     t_count = t_count +1
end
%

%
k_2_tran=transpose(k_2)
k_1 = 0
k_2_pure_toluene=k_2_tran*(1);
H_pure_toluene=(k_2_pure_toluene)
figure
```

```
plot(pure_toluene_time,H_pure_toluene)


%% to plot mean curvature at the centre at different
   moments
colour_i = 20;
color_p = [255,228,181;240,248,255;
   240,255,240;100,249,237;
   245,245,220;200,200,200;200,191,255;110,105,30;255,215,0;176,196
    %set any colour for your curves or dots
color_q = [255,228,181;240,248,255;
   240,255,240;100,149,137;
   245,245,220;100,100,100;10,191,255;210,105,30;155,215,0;76,096,

% color_p = [255,228,181;240,248,255;
   240,255,240;100,149,237;245,245,220;100,100,100]/255;
color_area = [94, 184, 247;224, 255, 168;224, 255,
   168;231, 206, 253; 251, 152, 213;172, 192, 252]/255
color_line=[117,107,177]/255;
figure

toluene_n_butanol_time =[toluene_ten_n_butanol_time;
   toluene_fifty_n_butanol_time;
   toluene_seventy_n_butanol_time;
   toluene_ninety_five_n_butanol_time;pure_toluene_time;
   pure_n_butanol_time]

time_min = min(toluene_n_butanol_time)

area_left_x = time_min
area_right_y = 1
```

```
area_top_y = 2
area_bottom_y = -2.5
axis tight
% fill /tau<0
fill_left_x=[area_left_x -0 0 area_left_x];
fill_left_y=[area_bottom_y area_bottom_y area_top_y
   area_top_y]
fill(fill_left_x, fill_left_y, color_area(6,:),'FaceAlpha
   ',.33,'DisplayName','\tau''<0');
% % fill /tau>0
hold on
fill_right_x=[0 area_right_y area_right_y 0];
fill_right_y=[area_bottom_y area_bottom_y area_top_y
   area_top_y];
fill(fill_right_x, fill_right_y, color_area(2,:),'
   FaceAlpha',.43,'DisplayName','\tau''>0');
%fill area ends


plot(toluene_ten_n_butanol_time, H_toluene_ten_n_butanol,
   's','MarkerSize',6,'MarkerEdgeColor', colour_s(1,:),'
   MarkerFaceColor',colour_t(1,:),'displayname','Height
   at the centre(toluene 10.61%)')
hold on

plot(toluene_fifty_n_butanol_time,
   H_toluene_fifty_n_butanol,'s','MarkerSize',6,'
   MarkerEdgeColor', colour_s(15,:),'MarkerFaceColor',
   colour_t(15,:),'displayname','Height at the centre(
   toluene 51.35%)')
```

```
hold on

plot(toluene_seventy_n_butanol_time,
   H_toluene_seventy_n_butanol,'s','MarkerSize',6,'
   MarkerEdgeColor', colour_s(4,:),'MarkerFaceColor',
   colour_t(4,:),'displayname','Height at the centre(
   toluene 70.09%)')
hold on

plot(toluene_ninety_five_n_butanol_time,
   H_toluene_ninety_five_n_butanol,'o','MarkerSize',6,'
   MarkerEdgeColor', colour_s(16,:),'MarkerFaceColor',
   colour_t(16,:),'displayname','Height at the centre(
   toluene 94.85%)')
hold on

plot(pure_n_butanol_time, H_pure_n_butanol,'p','
   MarkerSize',6,'MarkerEdgeColor', colour_s(2,:),'
   MarkerFaceColor',colour_t(2,:),'displayname','Height
   at the centre(n-butanol only)')
hold on

plot(pure_toluene_time, H_pure_toluene,'^','MarkerSize'
   ,6,'MarkerEdgeColor', colour_s(9,:),'MarkerFaceColor',
   colour_t(9,:),'displayname','Height at the centre(
   toluene only)')
hold on

baseline_x_left = -0.25
baseline_x_right = 1
baseline_x=[baseline_x_left :0.05:baseline_x_right]
```

```
baseline_dots_number=length(baseline_x)
baseline_ones=ones(baseline_dots_number,1)
baseline_y=0*baseline_ones

plot(baseline_x,baseline_y,'b--','linewidth',1,'
   displayname','H=0')
hold on

baseline_y_top = 2
baseline_y_bottom =  -2.5

baseline_y_ver=[baseline_y_bottom:0.01:baseline_y_top]
baseline_dots_number_y=size(baseline_y_ver);
baseline_ones=ones(baseline_dots_number_y(2),1)
baseline_x_ver=0.9*baseline_ones
%
plot(baseline_x_ver,baseline_y_ver,'k--','linewidth',1.5,
   'displayname','\tau'' = 0.9')
hold on
axis tight
% xlim([-0.25 1])
% ylim([-5*10^-4  10*10^-4])
legend('Location','southwest')
xlabel('\tau'''','fontsize',18);
ylabel('Mean curvature at the centre, H''_r_=_0','
   fontsize',18);
% title('Mean curvature of different shapes at r = 0');
set(gca,'fontname','times','fontsize',14)  % Set it to
   times
```

## 1.3 Evaporation Rate of a Binary Droplet

```
%% the code in this file is written to calculate x_1 n_1
   in a numerical way
clear all
colour_s = [139,32,14;255,138,0;157, 77, 95; 27, 59,
   126;38, 140, 53;85, 40, 92;207, 186, 79;68, 115,
   162]/255;
% face colours for dots
colour_t = [245,92,66;255,229,0;253, 38, 85;92, 139,
   235;114, 243, 133;214, 148, 225; 249, 242, 31;19, 133,
    246]/255;

% n_butyl_acetate_n_butanol_volume_data
t_exp = importdata('t_experiment1.dat')
V_exp_raw = importdata('V_experiment1.dat')
V_exp = V_exp_raw/10^15

colour_line_x=[251, 22, 14; 62, 14, 251]/255;
%colour_line 1 _ for dv/dt total; colour_line_2 for dv/
   dt_1
frame_rate = 500 %fps

% solvent 1 mesitylene
% D_1 = 0.0663 *10^(-4) % unit m^2/s
% mass_1=1.5*10^(-3) %unit kg
% density_1=861.5 % unit kg/m^3
% p_0_v_1 = 330  %unit Pa
% M_w_1 = 120.91 *10^(-3) % unit kg/mo
%
%
```

```
% % % solvent 1 pentyl acetate
% D_1 = 0.0061 *10^(-4) % unit m^2/s 0.061 from the
   literature
% mass_1=1.5*10^(-3) %unit kg
% density_1=876 % unit kg/m^3
% p_0_v_1 = 600  %unit Pa
% M_w_1 = 130.19 *10^(-3) % unit kg/mol

% % solvent 1 mesitylene
% D_1 = 0.0663 *10^(-4) % unit m^2/s
% mass_1=2.1101*10^(-3) %unit kg
% density_1=861.5 % unit kg/m^3
% p_0_v_1 = 330  %unit Pa
% M_w_1 = 120.191 *10^(-3) % unit kg/mol

% solvent 1 n-butyl acetate
D_1 = 0.0672 *10^(-4)% unit   m^2/s
mass_1 = 1  *10^(-3) %unit kg
p_0_v_1 = 1660 %unit Pa
M_w_1 = 116.16 *10^(-3) % unit kg/mol
density_1 = 882.5 % unit kg/m^3

% solvent 2 n-butanol
D_2 = 0.0861 *10^(-4) % unit m^2/s
mass_2=0.5*10^(-3) %unit kg
p_0_v_2 = 860  %unit Pa
M_w_2 = 74.12 *10^(-3) % unit kg/mol
density_2=809.8 % unit kg/m^3
% % solvent 2 anisole
% D_2 = 0.0729 *10^(-4)% unit   m^2/s
% mass_2 = 0.9400  *10^(-3) %unit kg
```

```
% p_0_v_2 = 470 %unit Pa
% M_w_2 = 108.138 *10^(-3) % unit kg/mol
% density_2 = 994 % unit kg/m^3

% solvent 2 n-butyl acetate
% D_2 = 0.0672 *10^(-4)% unit   m^2/s
% mass_2 = 2.7  *10^(-3) %unit kg
% p_0_v_2 = 1660 %unit Pa
% M_w_2 = 116.16 *10^(-3) % unit kg/mol
% density_2 = 882.5 % unit kg/m^3

% R_c gas constant
R_c = 8.314  % unit m3_Pa_K_-1_mol_-1
% T_ temperature of the substrate
T_c = 298.15 % unit K

%
% % solvent 2 pentyl acetate
% D_2 = 0.061 *10^(-4)% unit   m^2/s
% mass_2 = 1.5  *10^(-3) %unit kg
%
% density_2 = 876 % unit kg/m^3
% p_0_v_2 = 600 %unit Pa
% M_w_2 = 130.19 *10^(-3) % unit kg/mol
%
% % R_c gas constant
% R_c = 8.314  % unit m3_Pa_K_-1_mol_-1
% % T_ temperature of the substrate
% T_c = 298.15 % unit K

% radius of a well
```

```
R_of_well = 75*10^(-6); % unit m
% height of a well
H_of_well= 1.6*10^(-6);  % unit m

V_cap = 0;
% volume of a blank well
mass_ratio_1 = mass_1/(mass_1 + mass_2);
mass_ratio_2 = mass_2/(mass_1 + mass_2);

Volume_ratio_1 = mass_1/density_1/(mass_1/density_1 +
   mass_2/density_2);
Volume_ratio_2 = mass_2/density_2/(mass_1/density_1 +
   mass_2/density_2);

% V_t_0 = pi * R_of_well^2 * H_of_well + V_cap % unit m
   ^-3
V_t_0 = V_exp(1);
% volume_M_shaped_profile(1) %45.44075*10^(-15)  % from
   experiment m^3

v_t_0_s_1 = V_t_0 * Volume_ratio_1;
v_t_0_s_2 = V_t_0 * Volume_ratio_2;
% constants C1 and C2
C_1 = 4* D_1 * R_of_well * p_0_v_1 / R_c /T_c;  %
C_2 = 4* D_2 * R_of_well * p_0_v_2 / R_c /T_c;

% evaporation rate of pure solvents
d_v_d_t_1_pure = C_1 * M_w_1/density_1;  % unit m^3/s
d_v_d_t_2_pure = C_2 * M_w_2/density_2;  % unit m^3/s

% x_1 x_2: the mole fractions of the solvents
```

```
n_1 = mass_1 / M_w_1;
n_2 = mass_2 / M_w_2;

n_total = n_1 + n_2;
x_1 = n_1 / n_total;
x_2 = n_2 / n_total;

step_t = 1/frame_rate % unit s;
V_t = V_t_0;

x_t_total_1 = [];
x_t_total_2 = [];
t_count = 0;
t_total = [];
x_1_t = x_1;
x_2_t = x_2;

V_1_t= v_t_0_s_1;
V_2_t= v_t_0_s_2;
n_1_t = n_1;
n_2_t = n_2;
n_1_t_total = [];
n_2_t_total = [];


V_t_total = [];
V_1_t_total = [];
V_2_t_total = [];

while V_t > 0
```

```
d_V_1_dt = d_v_d_t_1_pure * x_1_t;

d_V_2_dt = d_v_d_t_2_pure * x_2_t;

V_t_total = [V_t_total,V_t];

V_1_t_total = [V_1_t_total,V_1_t];

V_2_t_total = [V_2_t_total,V_2_t];

x_t_total_1=[x_t_total_1,x_1_t];

x_t_total_2=[x_t_total_2,x_2_t];

t_total = [t_total; t_count];

t_count = t_count + step_t;

V_t= V_t - d_V_1_dt * step_t - d_V_2_dt * step_t

V_1_t =  V_1_t - d_V_1_dt * step_t;

V_2_t =  V_2_t - d_V_2_dt * step_t;

n_1_t = V_1_t * density_1 / M_w_1;

n_1_t_total =[n_1_t_total ; n_1_t]

n_2_t = V_2_t * density_2 / M_w_2;

n_2_t_total =[n_2_t_total ; n_2_t]
```

```
    x_1_t = n_1_t /(n_2_t +n_1_t );

    x_2_t = n_2_t /(n_2_t +n_1_t );

end

if find(n_1_t_total<0) < length(n_1_t_total)

    t_sequence = find(n_1_t_total<0) - 1;

    V_1_t_total = V_1_t_total(1:t_sequence);

    V_2_t_total = V_2_t_total(1:t_sequence);

    t_total = t_total(1:t_sequence);

    V_t_total = V_t_total(1:t_sequence);

    x_t_total_1 = x_t_total_1(1:t_sequence);

    x_t_total_2 = x_t_total_2(1:t_sequence);

end

if V_1_t_total(end)<0

    V_1_t_total = V_1_t_total(1:end-1);

    V_2_t_total = V_2_t_total(1:end-1);
```

```
    t_total = t_total(1:end-1);

    V_t_total = V_t_total(1:end-1);

    x_t_total_1 = x_t_total_1(1:end-1);

    x_t_total_2 = x_t_total_2(1:end-1);
end

if V_2_t_total(end)<0

    V_1_t_total = V_1_t_total(1:end-1);

    V_2_t_total = V_2_t_total(1:end-1);

    t_total = t_total(1:end-1);

    V_t_total = V_t_total(1:end-1);

    x_t_total_1 = x_t_total_1(1:end-1);

    x_t_total_2 = x_t_total_2(1:end-1);
end
%%
% this part is to get the duration of evaporation
t_total_length = length(t_total);
t_final = t_total(t_total_length);
figure
plot(t_total,x_t_total_1,'-','Color', colour_line_x(1,:),
   'linewidth',1.5,'DisplayName','Mole fraction of
   component 1 (n-butyl acetate)')
```

```
hold on
plot(t_total,x_t_total_2,'-','Color', colour_line_x(2,:),
   'linewidth',1.5,'DisplayName','Mole fraction of
   component 2 (n-butanol)')
xlabel('t  s ',FontSize=14);
ylabel('x_1(red) or  x_2(blue) ', FontSize=14);
ylim([0 1]);
xlim([0 t_final]);
legend('location','northeast');

% to write the title
s1= ' C_1 / C_2 = ' ;
C1_C2 = round(C_1/ C_2,2);
s2= string(C1_C2);
s3= 'm_1 / m_2 =  ';
mass_ratio = round(mass_1/mass_2,2);
s4= string(mass_ratio);

s_1 = s1 + s2;
s_2 = s3 + s4;
s_title=strcat(s1,s2,s3,s4);

title({s_1 s_2});
set(gca,'fontname','times','fontsize',14)  % Set it to
   times
% legend('x_1 (pentyl acetate) - t ','x_2 (anisole) - t
   ','Location','northeastoutside');
%%
colour_line=[87, 158, 229; 252, 139, 125;176, 252,
   34;243, 228, 53; 242, 240, 38]/255;
colour_edge=[13, 115, 160;244, 21, 46;109, 160, 13;77,
```

```
   75, 56;232, 168, 2]/255;
% edge colours for dots
colour_s=[139,32,14;255,138,0;157, 77, 95; 27, 59,
   126;38, 140, 53;85, 40, 92;207, 186, 79;68, 115,
   162;39,80,93;98, 50, 52;54, 50, 98; 67, 76, 36 ;73,
   44, 109;     134, 90, 45;82, 50, 83;34, 36, 30; 52,
   23, 20;81, 63, 47;36, 71, 66; 51, 61, 51;28, 38,
   29]/255;
% face colours for dots
colour_t=[245,92,66;255,229,0;253, 38, 85;92, 139,
   235;114, 243, 133;214, 148, 225; 249, 242, 31;19, 133,
    246; 0,190,255; 215, 20, 30;74, 58, 248;128, 206,
   229; 100, 24, 195;     234, 172, 108;  160, 68,
   162;175, 250, 5 ;245, 37, 10; 240, 136, 36;17, 208,
   180;160, 254, 118; 13, 185, 248]/255;


figure
x = t_total;
Y = V_t_total;
Y_1 = V_1_t_total;
Y_2 = V_2_t_total
area(x,Y,'FaceColor',colour_line(1,:),'EdgeColor',
   colour_edge(1,:),'LineWidth',1.5,FaceAlpha = 0.68)
% a(1).FaceColor = [0.22 0.6 0.5];
% a(1).EdgeColor = [0.13 0.08 0.18];
hold on
area(x,Y_1,'FaceColor',colour_line(5,:),'EdgeColor',
   colour_edge(5,:),'LineWidth',1.5,FaceAlpha = 0.68);
hold on
area(x,Y_2,'FaceColor',colour_line(2,:),'EdgeColor',
   colour_edge(2,:),'LineWidth',1.5,FaceAlpha = 0.68);
```

```
hold on

% plot(time_M_shaped_profile,volume_M_shaped_profile)
plot(t_exp,V_exp,'s','MarkerEdgeColor', colour_s(5,:),'
   MarkerFaceColor',colour_t(5,:),'DisplayName','V-
   experiment')
hold on
% to plot the line of t of which the value is equal to
   touch-down moment
V_exp_raw = V_exp*10^15;
baseline_y_top = V_exp_raw(1);
baseline_y_bottom =  0;
baseline_y_ver = [baseline_y_bottom:0.1:baseline_y_top];
baseline_y_ver = baseline_y_ver/10^15;

baseline_dots_number_y = size(baseline_y_ver);
baseline_ones = ones(baseline_dots_number_y(2),1);
baseline_x_1 = t_exp(end);
baseline_x_ver = baseline_x_1 * baseline_ones;
%
plot(baseline_x_ver,baseline_y_ver,'k--','linewidth',1.5,
   'displayname','the touch-down moment ')
hold on
% fill_bot_x=[10^-7 10^-4 10^-4];
% fill_bot_y=[10^-9 10^-9 10^-6];
% fill(fill_bot_x,fill_bot_y,color_p(1,:),'DisplayName','
   C area');
% fill areas
ylabel('Volume m^3');
xlabel('t s');
xlim([0 t_final]);
```

```
ylim([0 V_t_0]);
% to write the title
s1= ' C_1 / C_2 = ' ;
C1_C2 = round(C_1/ C_2,2);
s2= string(C1_C2);
s3= 'm_1 / m_2 = ';

mass_ratio = round(mass_1/mass_2,3);
s4= string(mass_ratio);

s_1 = s1+s2;
s_2 = s3+s4;
s_title=strcat(s1,s2,s3,s4);
title({s_1  s_2});

legend({'V_t_o_t_a_l','V_1 n-butyl acetate','V_2 n-
   butanol','V-experiment','the touch down moment',})
set(gca,'fontname','times','fontsize',13)  % Set it to
   times
hold off
```